DEVELOPMENT OF THE MOLECULAR LEVEL DESCRIPTON FOR NICKEL(II)-BASED LIGAND-EXCHANGE THERMOCHROMISM

by

Matthew Scott Queen

A dissertation submitted in partial fulfillment
of the requirements for the degree

of

Doctor of Philosophy

in

Chemistry

MONTANA STATE UNIVERSITY
Bozeman, Montana

July 2014

ACKNOWLEDGEMENTS

I would first like to thank my advisor, Robert Szilagyi, for allowing me to work on this project throughout my graduate studies. It has been a great learning experience both on a scientific and personal level.

I am also grateful to all the former members of the Szilagyi group, especially Travis Harris, and Logan Giles. I really appreciated the time Travis and I spent reading and discussing in a joint effort to better understand computational chemistry. Logan patiently guided me through XAS data collection and data workup. It was always a fun experience, and I truly hope to someday collect data with him again.

I would also like to acknowledge two close friends. The first is Brooks Marshall. Brooks has an infectious passion for all things science. His door was always open, and his phone was always on, ready to discuss any unexplained phenomenon the world had to offer. He is also a great ski partner. We scared off many a third member of our ski parties with our skin track banter about quantum mechanics. The second person is Dr. Phil Stimac. Phil was a great source of outside motivation and encouragement throughout my graduate work. I value him both as a professional advisor and a friend.

I would like to thank my wife Amy for supporting me throughout my graduate studies. She anchors the Ship of Fools that is the Queen family through the roughest of waters. I would also like to thank my parents, Jim and Sue Queen, who have supported me in every crazy decision I have ever made.

TABLE OF CONTENTS

TABLE OF CONTENTS – CONTINUED

TABLE OF CONTENTS – CONTINUED

LIST OF TABLES

Table Page

LIST OF TABLES – CONTINUED

Table Page

LIST OF TABLES – CONTINUED

Table Page

LIST OF FIGURES

Figure Page

LIST OF FIGURES – CONTINUED

Figure Page

LIST OF FIGURES – CONTINUED

Figure Page

LIST OF FIGURES – CONTINUED

Figure Page

LIST OF FIGURES – CONTINUED

Figure Page

LIST OF FIGURES – CONTINUED

Figure Page

LIST OF FIGURES – CONTINUED

Figure Page

LIST OF FIGURES – CONTINUED

Figure Page

ABSTRACT

Coordination compound-based nickel(II) thermochromic systems rely on a temperature-dependent equilibrium shift between different coordination environments of the central nickel ion. These systems are found in thermochromic "smart windows" that tint reversibly in response to temperature increases in their environment providing the benefit of energy savings in commercial and private buildings. Despite the stoichiometrically simple equilibrium for these ligand exchange systems, there is a complex and delicate network of chemical interactions that determine the color, and thermodynamic performance. Accurate computational modeling of nickel(II) ligand exchange thermochromic systems is an important first step in the direction of understanding the parameter space that determines whether a given metal ligand system is thermochromic, the color of the high and low temperature species, the temperature at which the system will change color. The research presented in this dissertation uses experimental results to evaluate theoretical models. Core and valence electronic spectroscopies probe the ground and excited state electronic structures of high temperature nickel(II) thermochromic chromophores which range from the very covalent nickel tetrathiocyclotetradecane thiocrownether to the highly ionic nickel dibromodi(1-pentylbenzimidazole)nickel(II). The experimental electronic structures of these high temperature species combined with experimental ligand exchange thermodynamics are used to guide the evaluation of computational modeling methods in search of methods that reproduces the experimental observables. It is found that commercially relevant nickel(II) thermochromism takes place on an extremely flat potential energy surface governed by ion pairing, hydrogen bonding and dispersion interactions. The modeling of these surfaces requires the explicit consideration of ion pairing and solvent-solute interactions.

CHAPTER 1

INTRODUCTION

Chromogenic Phenomena and Smart Window Technology

The energy demands of our modern lives rely on the utilization of fossil fuels that emit greenhouse gases. With alternative fuel sources still being developed, energy conservation is a realistic short-term goal toward reducing emissions. The majority of residential, industrial, and commercial buildings use energy to power heating, ventilation, and air conditioning (HVAC) systems. Heat gain through windows is typically responsible for over half the load on these HVAC systems.[1] Moreover, this window heat gain is responsible for roughly 30% of the entire US building energy usage (~4.1×10^{15} Btu $year^{-1}$). This is equivalent to the energy obtained from burning 51 million tons of coal. To reduce energy usage due to solar heat gain, windows need to respond to a typical day's heating and cooling demand profiles. This principle governs the design of "smart windows"[2] that can respond to changes in their environment.

Chromogenic phenomena occur when there is a change in the color of a substance or system of substances due to external stimuli. The color of a chromic substance emerges due to the absorption of light by the substance's valence electrons. Therefore, the change in its color can be correlated with a change in valence electron structure, and consequently with system's chemical composition and molecular structure.[3] For a chromogenic phenomenon to be useful in "smart window" technology, it needs to change color reversibly in response to the cooling and heating needs of buildings.

Various chromogenic phenomena can be defined on the basis of the external stimuli that induce color change. Photochromism describes a color change triggered by exposure to light (usually in the UV energy range, 10-400 nm).[4] Photochromic systems can be doped directly into glass as in silver halide nanoparticle systems,[5] or incorporated into a polymer as in the ring-opening reactions of oxazines[6] or naphthopyran.[7] Both glass and polymer systems have been successfully incorporated into eyeglass technology,[8, 9] but have limited application in "smart windows" due to the temperature dependence of the chemical kinetics of the decoloring reaction. The kinetically controlled reverse reaction becomes thermally enabled as temperature rises. For example, the rates of the coloring and decoloring reactions of most oxazines are already equal at 70 ºC,[10] but windows in direct sunlight can reach temperatures in excess of 100 ºC.[11] At these temperatures, the reverse reaction becomes faster and UV light from direct sun exposure cannot maintain the colored state of the window.

Electrochromism is a process where a system changes color in response to a change in applied electric potential. An extensively studied inorganic electrochromic material is tungsten trioxide thin film.[12] An example of the electrochemical reduction that takes place in one type of electrochromic thin film is described by Equation 1.1

$$\underset{\text{Colorless}}{WO_3} + xM^+ + xe^- \rightleftharpoons M_xW^{VI}_{(1-x)}\underset{\text{Deep blue}}{W^V_xO_3} \qquad (1.1)$$

where $M^+ = H^+$, Li^+, Na^+, or K^+ and e^- denotes electrons. In this system, a change in the applied electric potential across the WO_3 thin film reduces the oxidation state of a number of tungsten sites that is proportional to the cation concentration, applied electric potential,

and film thickness.[12] These changes create the possibility for photon absorption via a proposed intervalence charge transfer between covalently linked W^{V} and W^{VI} sites.[13] Electrochromic smart windows require control instrumentation that switch voltages on and off in response to changes in the light intensity or heat load. An example for these type of control systems in electrochromic technology can be seen in the automatic dimming mirrors in cars and light trucks.[14] Within the mirrors an electrochromic dimming process is signaled when light hits a photo diode secured to the back of the mirror which applies a voltage to the mirror surface causing it to dim.

Thermochromism, the subject of this dissertation, is a process where a system changes color in response to a change in temperature. An advantage of using thermochromic (TC) systems in "smart window" technology is their response to solar heating which is the source of the heat gain that necessitate the use HVAC systems. For a TC system to be successfully incorporated into a "smart window" technology it needs to be nearly colorless at ambient temperatures, manifest a uniform gray tint in a ~20-80 ºC temperature range, and be stable across the temperature range that a window operates ~0-100 ºC.[11]

Two well-studied organic TC systems with industrial relevance are Leuco dyes, and spiropyrans. Leuco dyes are weak acids that change color reversibly as a function of pH. To incorporate these dyes into TC systems the acid dye and a dissociable salt are dispersed into a solid fatty alcohol (e.g. dodecanol, or octadecanol) matrix. The matrix undergoes a phase change from solid to liquid at ~20 °C and the salt dissociates. The

increased salt concentration changes the pH of the system which effects the color of the dye.[15]

The thermally controlled ring opening of spiropyrans causes a change in a molecule's light absorption. A specific example is di-β-naphthospiran

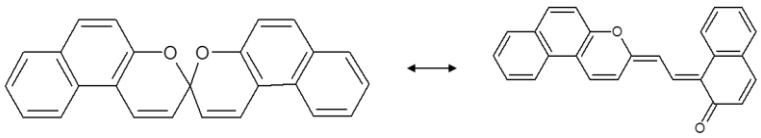

(1.2)

The molecule is colorless at ambient temperatures in benzene, but turns blue-violet when boiled at 80 ºC.[16] The color change is the result of the thermally controlled ring opening of the bond between the spiro-carbon and the ring oxygen.[17] The low transition temperatures and poor stability of both the Luco dyes and spiropyran systems eliminate their use in smart window technology.

Vanadium dioxide (VO_2) is an inorganic thermochromic material that has a solid-solid phase transition at 68 °C.[15] At temperatures below 68 °C, vanadium dioxide transmits infrared light. Above 68 °C, vanadium dioxide undergoes a semiconductor-to-metal phase transition, that makes the material infrared reflective. This feature makes VO_2 potentially useful in smart coatings for buildings and cars. A thin film of VO_2 applied to the exterior of a window allows transmission of visible light while blocking the infrared; this reduces warming of the building. Inorganic materials are generally much more resistant to photo-induced decomposition than organic materials, but they do not block visible light that is partially responsible for thermal heating.

Ligand exchange thermochromic (LETC) systems are based on coordination chemistry, ligand exchange processes, where the coordination environment of a central

metal ion changes as a function of temperature. These systems display good color and performance over the desired 0-100 ºC operating temperature range, and show good stability over 30 years of simulated use.[3] Another advantage of these systems is the possibility for tuning the color while maintaining TC activity. This dissertation summarizes our current efforts in using theoretical chemical methods and a broad range of spectroscopic tools towards understanding the molecular level details of LETC processes that contribute to the rationalized design of better performing materials.

Inorganic Ligand Exchange Thermocromism

The only commercially available LETC "smart windows" rely on Ni(II) coordination complexes to tint polyvinylbutyral films. These films are separated and pressed between two sheets of glass and assembled as shown in Figure 1.1.[3]

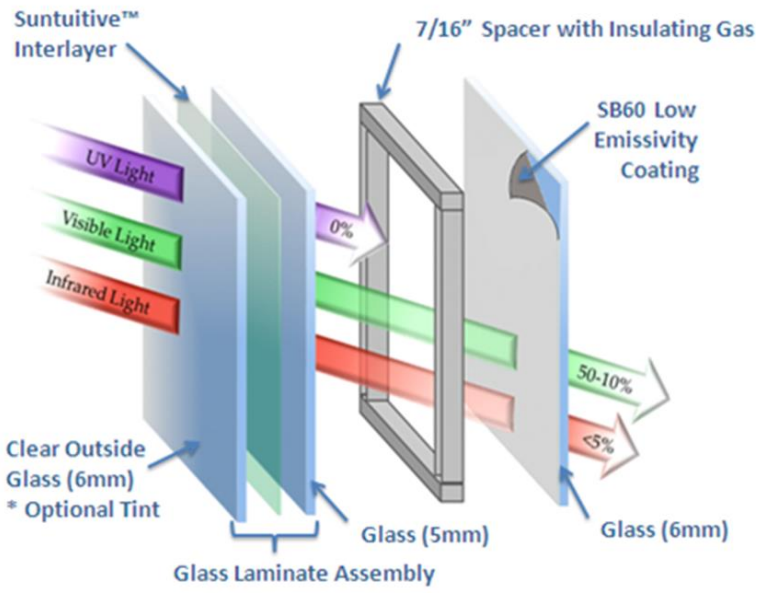

Figure 1.1 Suntuitive™ Interlayer smart window technology assemblies (adapted from Pleotint.com website, last accessed: 3/25/2014)

The chemical equilibrium process that takes place in the LETC film at a constant temperature is described by general Equation 1.3.

$$[M(l\varepsilon L)_6]^x + 4\ h\varepsilon L^y \leftrightarrow [M(h\varepsilon L)_4]^z + 6\ l\varepsilon L \quad (1.3)$$

$$\Delta G_{rxn} = \Delta H^0 - T\Delta S^0 + RTln\left(\frac{Q}{Q^0}\right) \quad (1.4)$$

where M is the metal ion at the center of the coordination complex (in the case of commercial LETC "smart windows" M= Ni^{2+} , but M=Co^{2+}, Fe^{3+} systems are also known).[18] The identity of the lεL (low epsilon ligand) and hεL (high epsilon ligand) define the color of the coordination complexes at ambient and elevated temperatures respectively. The $[M(l\varepsilon L)_6]^x$ corresponds to the low colored (molar extinction coefficient < 10 L $mole^{-1}$ cm^{-1} in the visible range) species formed at ambient temperatures, while the $[M(h\varepsilon L)_4]^z$ is the highly colored (extinction coefficient > 50 L $mole^{-1}$ cm^{-1} in the visible range) species formed at elevated temperatures. The value of ΔH^0 in Equation 1.4 is determined by the metal ligand bonding, the bonding in the free ligands, and the interactions of the complexes and ligands with the polymer matrix. The ΔS^0 term is determined by the difference in structure and composition of the six and four coordinate complexes, as well as the counter ion/polymer matrix reorganization. As the magnitude of the ΔS^0 term increases, the temperature range required for the system to fully change color decreases.[3] Increasing or decreasing the concentration of lεL and hεL affects the thermodynamics of the system via the reaction quotient $\left(\frac{Q}{Q^0}\right)$ term. This term accounts for the systems deviation from its standard state concentration Q^0, which is, in the case of solutes in solution, usually 1 bar and 1 M ideal solutions (no solute-solute interactions). The effect can be utilized when empirically designing TC systems via Le Chatelier's

principle. In the design process the hεL is added gradually to a solution of M^{z-y} metal ion until the highly colored $[M(heL)_4]^z$ complex appears (forcing equilibrium to the right). This solution is then decolorized by titrating in excess lεL to form the $[M(lεL)_6]^x$ (forcing the equilibrium to the left).

The current commercial "smart window" technology from Pleotint LLC uses a three-layered system to form their Suntuitive™ Interlayer (Figure 1.1). TC tinting blue and orange Ni(II) layers are divided by a clear separator. The orange layer is contains a Ni(II), proprietary diol (lεL), and a 3:1 ratio of iodide to pyridine derivative (hεL) . The blue layer contains Ni(II), a proprietary diol (leL), 2:2 ratio of bromide to imidazole derivative (hεL), and a 3:1 ratio of bromide to imidazole derivative (hε L). The two layers together provides a uniform gray appearance when heated. The combined transmission spectrum of an example two layers system at temperatures ranging from 24 ºC to 75 ºC is shown in Figure 1.2.

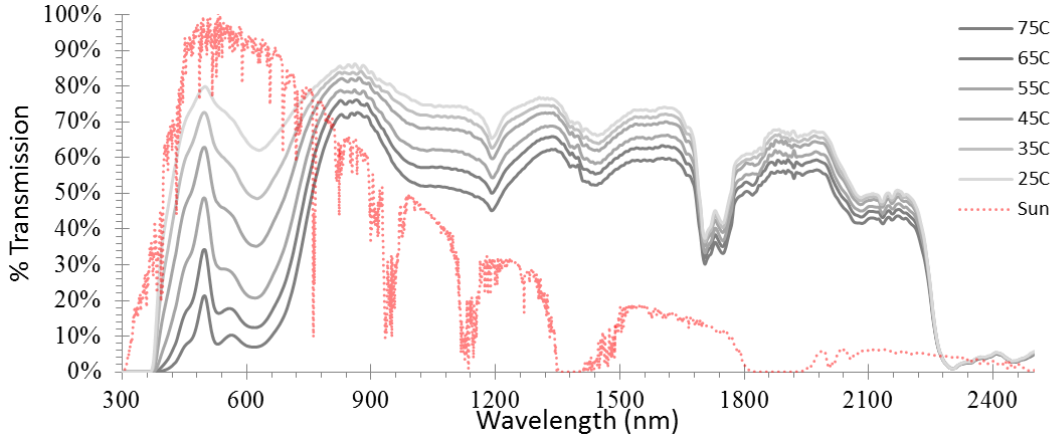

Figure 1.2 Transmittance spectra of the Suntuitive™ Interlayer laminate (composition given in text) placed between two 3-mm clear glass substrates at glass temperatures ranging from 25 to 75 ºC along with the solar spectrum of the in the UV, visible, and near infrared energy regions. Spectra provided by Pleotint LLC.

LETC “smart windows” presently cost roughly ten times the amount of a similar double pained window. There are two technological solutions that would enable a considerable cost reduction. The first is to decrease the number of TC films needed to give the tinted window a gray appearance when heated. To accomplish this, a $[M(heL)_{4\text{-}5}]^{z+/-}$ complex is needed that absorbs energies across the peak of the solar radiation spectrum (Figure 1.2).

The yet to be designed $[M(heL)_{4\text{-}5}]^{z+/-}$ compound must also retain the thermodynamic properties (ΔH^0, ΔS^0) necessary for the ligand exchange to take place between 60-100 ºC. The second means to reduce the cost of TC windows is to decrease the concentration of active ingredients needed to tint the window upon heating. To do this, $[M(heL)_{4\text{-}5}]^{z+/-}$ complexes are needed with larger molar extinction coefficients and thus greater light absorption. To understand how greater light absorption can be achieved a deeper understanding of the origin of light absorption in the currently available LETC systems are needed.

The origins of the colors of currently available LETC “smart windows” lie in the electronic structures of the chromophores. In general, the ambient temperature species in nickel based LETC ($[Ni(l\varepsilon L)_6]^x$) have a formally Ni^{2+} center surrounded by six lεLs (less if bridging ligands such as diols or triols are used). The Ni^{2+} ions have 5 d orbitals that are split by the octahedral field of σ interacting ligands. Two sets of molecular orbitals (MO) with t_{2g} and e_g symmetries are formed. Figure 1.3A is an MO diagram illustrating the octahedral splitting the $[Ni(l\varepsilon L)_6]^x$.

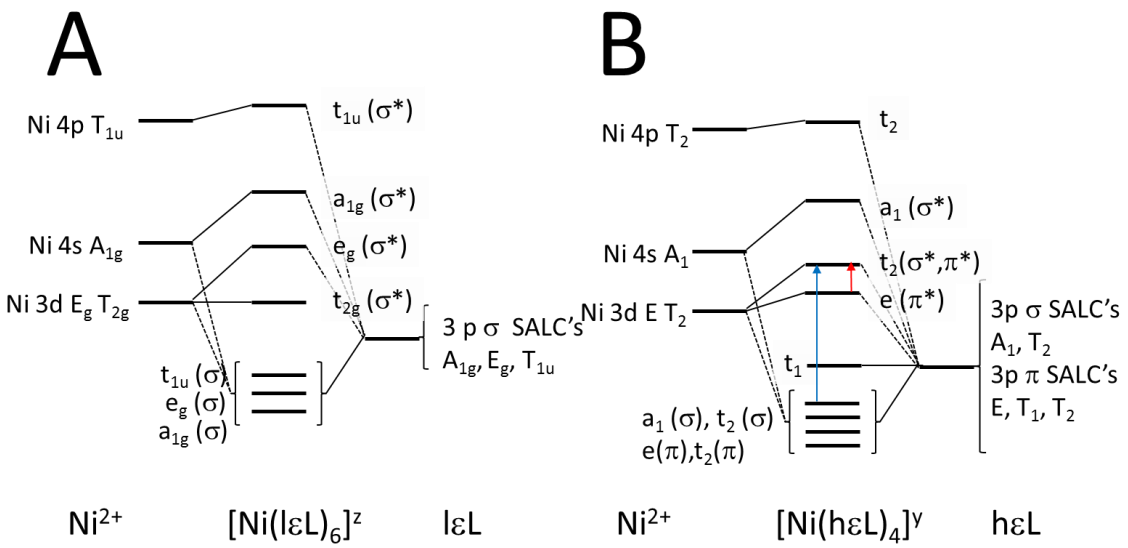

Figure 1.3 A) MO diagram of general O_h $[Ni(l\varepsilon L)_6]^y$ complex with sigma donating ligands B) MO diagram of idealized T_d $[Ni(h\varepsilon L)_4]^z$ with π and σ donating ligands (model for $[NiX_4]^{2-}$ complexes where X=Cl, Br, or I) d→d transitions are noted by the red arrow going from the occupied e MOs to the partially occupied t_2 MOs.

When the electrons in the octahedral field interact with visible light the resulting d→d valence electron excitations conserve gerade symmetry with respect to inversion and are therefore Laporte forbidden.[19] The extinction coefficients of the forbidden transitions are around 1-10 dm^3 mol^{-1} cm^{-1}. When heated, the Ni^{2+} ions exchange ligands with their surroundings forming $[M(h\varepsilon L)_4]^z$ complexes. The 5 Ni d orbitals in the newly formed $[M(h\varepsilon L)_4]^z$ are split by a tetrahedral ligand field into MOs with t_2 and e symmetries (Figure 1.3B). The magnitude of the ligand field splitting determines the energy of the d→d electronic absorption (red arrow Figure 1.4B) and thus the color of the $[M(h\varepsilon L)_4]^z$ complex. Most $[M(h\varepsilon L)_4]^z$ complexes have visible d→d excitations with extinction coefficients around 100-400 dm^3 $mol^{-1}cm^{-1}$.

The origin of the absorption intensity difference between $[M(l\varepsilon L)_6]^x$ and $[M(h\varepsilon L)_4]^z$ can be explained using MO theory. The lack of center of symmetry in the tetrahedral ($[M(h\varepsilon L)_4]^z$) complex allows for configuration interaction (CI) mixing of the ligand np→Ni charge transfer (CT) excited states (blue arrow in Figure 1.4B). The ligand to metal charge transfer excitations (LMCT) have extinction coefficients upwards of 10,000 to 50,000 $dm^3\ mol^{-1}\ cm^{-1}$. The extent to which the LMCT states CI mix with the Ni d→d transitions determines the Ni d→d excitation intensity.

An example of CI mixing of LMCT states into d→d transitions is seen in the increasing transition intensity across the $[NiX_4]^{2+}$ series where X = Cl, Br, and I (Figure 1.4).

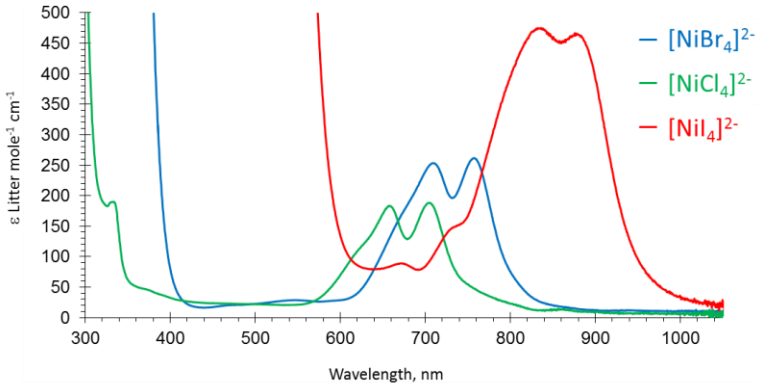

Figure 1.4UV-Vis spectra for the $[NiX_4]^{2+}$ series (where X = Cl, Br, and I) in γ-butyrolactone (GBL). Spectra were taken by sonicating tetrabutylammoniumhalide to saturation with 1.0 and 0.5 mM $Ni(ClO_4)_2•6H_2O$

The decrease in energy of the LMCT transitions (high energy shoulder) across the $[NiX_4]^{2-}$ series (~330 nm, ~400nm, and ~600 nn for $[NiCl_4]^{2-}$, $[NiBr_4]^{2-}$, and $[NiI_4]^{2-}$ respectively) is seen in spectra in Figure 1.4. The same trend is shown schematically in the MO diagrams of Figure 1.4 (dashed arrows). The LMCT transition energy is a

function of the effective nuclear charge of the halide ion. As the effective nuclear charge increases across the series ($Cl^- < Br^- < I^-$) so does the energy of the np atomic orbitals that form σ bonding MOs with the Ni d orbitals.

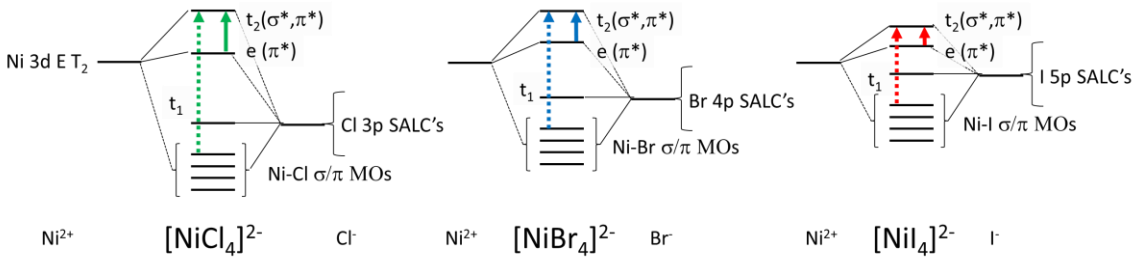

Figure 1.5 MO diagrams for the $[NiX_4]^{2-}$ series showing the relationship between the LMCT energy (dashed arrow) and d→d energy (solid arrow) as a function of effective nuclear charge of the halide ions which increases as $Cl^- < Br^- < I^-$.

Lower LMCT energies result in better energy overlap between LMCT states and Ni d→d states (solid arrows Figure 1.5), which increases the probability for CI mixing. The CI mixing of the dipole allowed LMCT states increases the intensity of the d→d transitions in going from $[NiCl_4]^{2-}$, $[NiBr_4]^{2-}$, to $[NiI_4]^{2-}$.

The $[NiX_4]^{2-}$ series defines a range of transition energies and intensities with two extremes of d→d transitions (low energy and low intensity), and LMCT transitions (high energy and high intensity). The continuum can be stretched beyond the high and low limits with the introduction of ligands with low lying antibonding orbitals capable of accepting electron density, such as triphenylphosphines (PPh_3). PPh_3 ligands, with their low lying P-C σ* orbitals, have high energy high intensity metal to ligand charge transfer (MLCT) transitions (Figure 1.6 A and B). MLCT states with the correct overlap can CI

mix into Ni d→d transitions to increase intensity (Figure 1.6 A). When MLCT and LMCT balance their respective CI coefficients within the d→d states there is the possibility for ligand to ligand charge transfer (LLCT) (Figure 1.6 B).

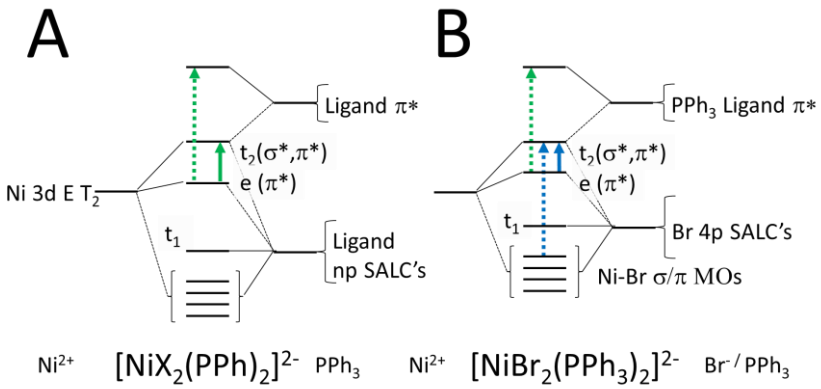

Figure 1.6 A) Metal to ligand charge transfer to π^* ligand based orbitals. B) Ligand to ligand charge transfer representation.

However, there is a fundamental problem with simply selecting highly colored complexes on the basis of charge transfer excitations or transition broadening for LETC. The increased energy of the ligand np orbitals required for low energy LMCT states, or broad d→d transitions, leads to stronger metal ligand bonding. Stronger metal ligand bonds increases ΔH^0. LETC coloration can only remain spontaneous (i.e. ΔG_{rxn} remains negative) if the $T\Delta S^0$ term or the concentration of lεL (used to increase RTlnQ) counteract the increased bond enthalpy. To understand the difficulty of balancing these terms we need to take a closer look at the thermodynamics that govern the color change in currently available smart windows.

The 100-400 $dm^3\ mol^{-1}\ cm^{-1}$ molar extinction coefficients associated with d→d transitions and the 1 mm path lengths dictated by the window design[3] necessitate the 0.1

moles nickel ion per kg of polymer concentrations. To get a T_{cross}, of below 70 °C, three and five-fold excess hεL and lεL concentrations are needed respectively. The ions are dissolved in a solid polymer matrix (Butvar® B-90 polyvinyl butyral resin). The unconventional, high viscosity, low dielectric, organic solvation environment creates non-ideal solution conditions, where the chemical interactions between the various solute molecules cannot be neglected (Equation 1.5). The enthalpy associated with metal ligand bonding is no longer the only enthalpic contribution to the ΔG_{rxn} for the LETC process. Now the enthalpy associated with ion pairing, and H-bonding interactions between dissociated lεLs must be considered as well (Equation 1.5).

$$\Delta G_{rxn} = \Delta H^0 + \Delta H_{interaction} - T\Delta S^0 + RTln\frac{[Products\,]}{[Reactants\,]} \qquad (1.5)$$

To account for these interactions the concentrations within the reaction quotient need to be listed in terms of their activities, which are effective concentrations. This effective concentration is calculated by multiplying the molar concentration by an activity coefficient (γ), defined by Equation 1.6

$$\gamma = e^{\frac{\Delta H_{interaction}}{RT}} \qquad (1.6)$$

This definition is really just the $\Delta H_{interaction}$ in a form that allows for its incorporation into the logarithm. There, the $\Delta H_{interaction}$ adjust the reaction free energy by increasing or reducing the concentration of species in the reaction quotient.

As detailed above, the color and thermodynamics of LETC systems depend on the identity and concentration of the metal, hεLs, lεLs, their counterions, and the solvent choice. This dependence leads to an experimental parameter space so complex, that

currently no theoretical method can predict either the color or the thermodynamics of a thermochromic system without actually performing the experiment. Even with experimental results in hand, the interpretation of the observations using theoretical methodologies is challenging. This is evident when considering even the most fundamental LETC systems. The simplest LETC system, in terms of components, consist of an equilibrium between octahedral $[Ni(H_2O)_6]^{2+}$ and tetrahedral $[NiCl_4]^{2-}$ in water. This system is prepared so that the final solution is 1mM in $Ni(ClO_4)\bullet 6H_2O$ and 5.6 M in Me_4NCl. The use of $[Me_4N]^+$ as a counter ion to the chloride is critical for this system to show TC behavior.[20] Chloride sources such as HCl, LiCl, NaCl, and Et_4NCl do not allow for the tetrachloronickelate species even in highly concentrated (pressurized systems > 10 M) solutions at 110 °C.[20] It is proposed that the ~5M concentrated $[Me_4N]^+$ counterion (with inter TMA^+ - Cl^- ion distances of 0.5nm) leads to decreased chloride water induced dipole interactions, thus decreased Cl^- hydration. The decreased hydration increases the Cl^- ability to bind Ni^{2+} but to date no theoretical model has described the experimental results.[18]

Quantum Mechanical Model for Nickel-based LETC

The development of a quantum mechanical model of nickel LETC requires a fundamental understanding of the connection between color and thermodynamics. The approach used in this dissertation to explore the connectivity, integrates experiment and theory. To illustrate the approach graphically, a tetrahedron scheme is presented in Figure 1.7.

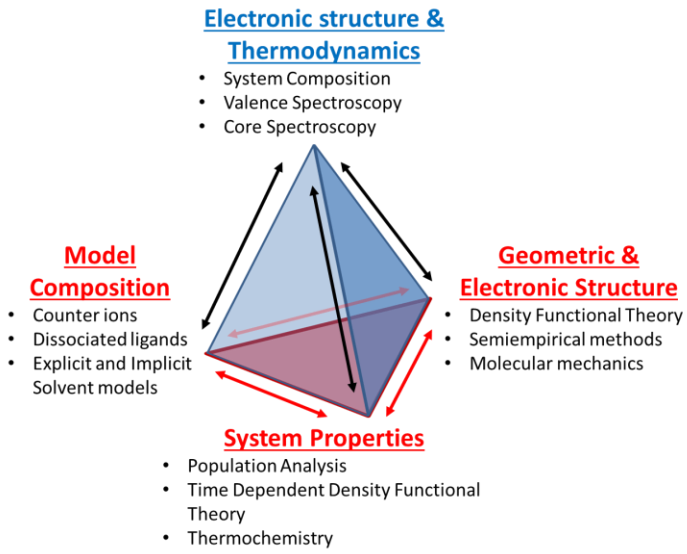

Figure 1.7 Research parameter space used to illustrate the approach used in this dissertation to investigate LETC systems.

Each corner of the tetrahedron features a single component of the overall model, and list below, the methods used to define or derive the component.

The experimental electronic structure and thermodynamics, at the top of the tetrahedron, are defined using valence electron spectroscopy, UV-VIS (described in Chapter 4) and, core electron, S K-edge X-ray absorption spectroscopy (XAS) (described in Chapters 2 and 3), methods. The components of the model at the base of the tetrahedron (noted with red lettering) define the theoretical model chemistry. The validity of the theoretical methods used in any given model must be tested for consistency with the available experimental results (represented by the black arrows connecting top and bottom of the tetrahedron). The interdependence of the theoretical components is represented by the red arrows linking them.

The geometric and electronic structure of LETC chromophores can be calculated using density functional theory (DFT) (described in Chapter 2), semi-empirical methods, and or molecular mechanics (both detailed in Chapter 4). The theoretically predicted properties of the system are calculated with the methods listed at the bottom of the tetrahedron using the theoretical electronic and geometric structure. The methods for calculating system properties include population analysis methods, used to derive orbital properties (detailed in Chapter 2), time-dependent density functional theory (TD-DFT), used to calculate theoretical excitation spectra, and thermochemistry analysis methods, used to calculate ensemble thermochemical properties from a single molecule (both described in Chapter 4). The chemical composition considered in the theoretical model includes all the potential species present in the chemical system as well as the various methods both implicit and explicit for modeling the solvent environment (detailed in Chapter 4).

Research Directions

In this dissertation we seek to create a reliable quantum mechanical model of nickel(II) LETC that that has the potential to probe the connection between color and thermodynamics in the LETC systems. The tetrahedron in Figure 1.8 illustrates the interdependence of theory and experiment that guides the approach used in this dissertation. Experimental characterization directs choices in theoretical modeling of LETC. With this approach in mind, in Chapter 2 XAS is used to define the ground state electronic structure of the LETC chromophore tetrathiacyclotetradecane Ni(II)

($[Ni(ttctd)]^{2+}$). A spectrochemical series of $[Ni(II)S_4]^x$ complexes helps to generalize previously established methods for quantitating S orbital character from pre-edge intensities and S effective nuclear charges. The experimental S orbital characters for the $[Ni(II)S_4]^x$ series are compared to calculated values from a comprehensive set of density functionals to access their accuracy. It is found that DFT overestimates the S character of Ni containing S coordination compounds resulting in an overly covalent M-S bonding picture.

Chapter 3 extends the newly generalized XAS methods developed in Chapter 2 to the ground state electronic structure investigation of the thiourea ligand in Co(II), Ni(II), and Zn(II) coordination complexes. The shortcomings of ground state electronic structure calculations, established in Chapter 2, are used to inform the interpretation of the experimental results that establish metal thiourea complexes as highly ionic compounds.

Chapter 4 uses the results from chapters 2, and 3 to aid in the interpretation of the data from an evaluation of computational modeling techniques applied to an industrially relevant LETC system used in “smart window” technology. In this study experimental valence excitations and thermochemistry of model systems are used to inform the building of computational models. Additional experimental techniques including UV-VIS are correlated with TD-DFT in an effort to select a semi-empirical hybrid density functional to perform a thermochemistry investigation of the thermodynamic properties of the film. To better understand the chemical interactions that dictate the thermodynamics of the LETC system we evaluate the thermochemistry results of models

that are stepwise increased in complexity while simultaneously lowered in level of theory so as to balance computational cost and accuracy.

CHAPTER TWO

ELECTRONIC STRUCTURE OF [Ni(II)S_4] COMPLEXES FROM S K-EDGE X-RAY ABSORPTION SPECTROSCOPY

Contributions of Authors and Co-Authors

Manuscript in Chapter 2

Author: Matt S. Queen

Contributions: Collected and worked up XAS data, carried out and analyzed DFT calculations.

Co-author: Bradley D. Towey

Contributions: Synthesized $Cu(dtc)_2$ and $Ni(dtc)_2$ complexes, collected and worked up XAS data, carried out and analyzed DFT calculations.

Co-author: Kevin A. Murray

Contributions: Carried out and analyzed DFT calculations

Co-author: Brad S. Veldkamp

Contributions: Synthesized $[Ni(ttctd)]^{2+}$ and collected XAS data

Co-author: Harlan J. Byker

Contributions: Provided UV-VIS and thermodynamic data for the $[Ni(ttctd)]^{2+}$ thermochromic system.

Co-author: Robert K. Szilagyi

Contributions: Assisted with the design and execution of the experiment and theoretical calculations. Discussed the results and edited the manuscript at all stages.

Manuscript Information Page

Authors: Matt S. Queen, Bradley D. Towey, Kevin A. Murray,
Brad S. Veldkamp, Harlan J. Byker, Robert K. Szilagyi
Journal: Coordination Chemistry Reviews

Status of Manuscript:
____ Prepared for submission to a peer-reviewed journal
____ Officially submitted to a peer-review journal
____ Accepted by a peer-reviewed journal
_X__ Published in a peer-reviewed journal

Publisher: Elsevier
Date of Submitted: 20 March 2012
Date Accepted: Accepted 28 July 2012
Volume 257, Issue 2, 15 January 2013, Pages 564–578

CHAPTER 2

ELECTRONIC STRUCTURE OF [Ni(II)S_4] COMPLEXES FROM S K-EDGE X-RAY ABSORPTION SPECTROSCOPY

Abstract

The nickel ion has a remarkably rich coordination chemistry among the first-row transition metals. Complexes with sulfur containing ligands are particularly notable, since they can manifest classical/metal-based (innocent) or inverted/ligand-based (noninnocent) behavior depending on the chemical composition of the S-ligands and the coordination geometry. Using sulfur K-edge X-ray absorption spectroscopy (XAS), we established a spectrochemical series for [Ni(II)S4] complexes containing thiolate, aliphatic dithiolate, olefinic and aromatic enedithiolate, conjugated dithiocarbamate, and aliphatic thioether ligands. The pre-edge intensities at the sulfur K-edge follow an increasing trend from tetrathiolate through dithiolate and enedithiolate to tetrathioether. In order to obtain quantitative sulfur orbital compositions from XAS data, we generalized the earlier methods of estimating the sulfur 1s→3p transition dipole integral for a broad range of S-ligands by considering chemical shifts of spectroscopic features due to changes in the sulfur effective nuclear charge and S-ligand coordination to Ni. The XASbased experimental orbital compositions are compared with a comprehensive set of density functional theory-based, electronic structure calculations. The 1,2-dithiolate ligands gave indication of inverted bonding, independently whether the coordinated sulfur centers are connected by constrained single or double C,C bonds. Despite intense

pre-edge features, both dithiocarbamate and thioether complexes can be described with classical inorganic bonding description.

Introduction

Core Excited State Spectroscopy Background

X-ray absorption spectroscopy uses tunable X-rays to excite core electrons in atoms. X-ray absorption spectra can be categorized into edges based on the principle quantum level of the core electrons being excited. The excitation of n=1 electrons give K-edge spectra, while n=2 electrons give L-edge and n=3 M-edges.[21] The binding energies of core electrons vary in energy according to the Bohr model with the Moseley extension (Equation 2.1).[22, 23]

$$E = -Z_{eff}^2 \frac{13.6eV}{n^2} \tag{2.1}$$

Where Z_{eff} is the effective nuclear charge of the atom (Zeff = Z – σ), σ is the screening term and is estimated using Slater's rules, n is the principle quantum energy level occupied by the electron, and 13.6 eV is the binding energy of the 1s electron in the ground state of the hydrogen atom. The dependence of the binding energy on the effective nuclear charge of the atom makes XAS an element specific technique.

"Tender" X-rays (1-3 keV) can be used to excite K-edge transitions in the atoms of potential lεL and hεL (Si/P/S/Cl) used in LETC systems. The pre-edge features of ligand K-edge spectra of coordinated ligands contain information about the ligand character of the metal-ligand bond, and the ligand effective nuclear charge.[24]

Figure1.12A shows the S K-edge spectrum for a nickel tetrathiocyclotetradecane thiocrownether ($[Ni(ttctd)]^{2+}$) (Structure can be seen in Figure 2.1 C) sample in the tender X-ray region.

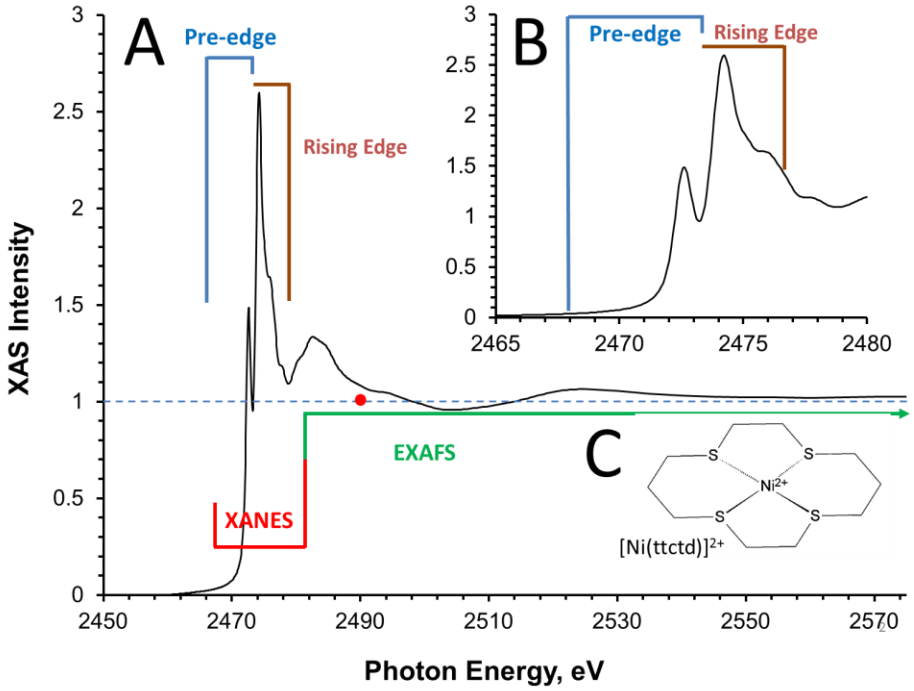

Figure 2.1 A)Normalized S K-edge spectrum taken at beam line 4-3 at Stanford Synchrotron Radiation Lightsource (SSRL). The XANES and EXAFS regions are noted in red and green respectively. B)The XANES region is further divided into the pre- and rising edge regions blue and brown respectively. C) Molecular structure of $[Ni(ttctd)]^{2+}$

All XAS spectra can be broken into two main regions. The lower energy region below the atomic ionization threshold is called the X-ray absorption near-edge structure (XANES) region (Figure 2.1 A red region). The higher energy region above the atomic ionization threshold is called the extended X-ray absorption fine structure (EXAFS) region

(Figure 12 A green region), The features in the XANES region (Figure 2.1B) are the result of core electrons being excited to unoccupied valence orbitals giving rise to bound

excited states. Interpretation of the pre-edge transition intensities, as expressed by pre and rising-edge peak areas, gives insights into the ground-state electronic structure of a molecule. The data oscillations in the EXAFS region are the result of quantum interference between the ionized and back-scattered (by neighboring atoms) wave of a photoelectron. The variation of the periodicity within this region can be transformed from an energy scale to electron momentum space (k), and after Fourier transformation can be used to obtain information about the radial distribution of neighboring atoms.[21]

In this Chapter and Chapter 3 the pre-edge intensities for the S-kedge spectra of coordination complexes will be analyzed to extract experimental molecular orbital coefficients. The orbital coefficients will be reproduced with various levels of density functional theory to find the method that best represents a wide variety of S ligand types.

S K-edge and [Ni(II)S_4] Complexes

Nickel manifests remarkably diverse coordination chemistry.[25] In particular, the Ni(II) oxidation state is of interest due to its $3d^8$ valence electron configuration that can exist in paramagnetic $S = 1$ or diamagnetic $S = 0$ ground states. For four coordinate complexes, these spin states correspond with tetrahedral and square planar coordination geometry, respectively. Notably, the paramagnetic tetrahedral state manifests Jahn–Teller distortion, which renders the symmetry of the [Ni(II)S_4] moiety to be effectively D_{2d}. Furthermore, the large steric bulk of the substituted sulfur ligand (S-ligand) contributes to the elongated Ni-S bond lengths and may lower the symmetry to S_4.[26] For the diamagnetic complexes, the effective symmetry is D_{2h} due to the coordination environment. The spectrochemical series of weak σ- and/or π-donor ligands *versus* the

strong σ-donor and π-acceptor ligands predetermines the central Ni(II) ion's coordination geometry and spin state. This is less straightforward for the family of S-containing ligands with intermediate ligand field strength.

In this comparative study, we focus on homoleptic [Ni(II)S_4] coordination compounds that span both spin states, both coordination geometries, anionic, neutral, and cationic complexes (Scheme 2.1).

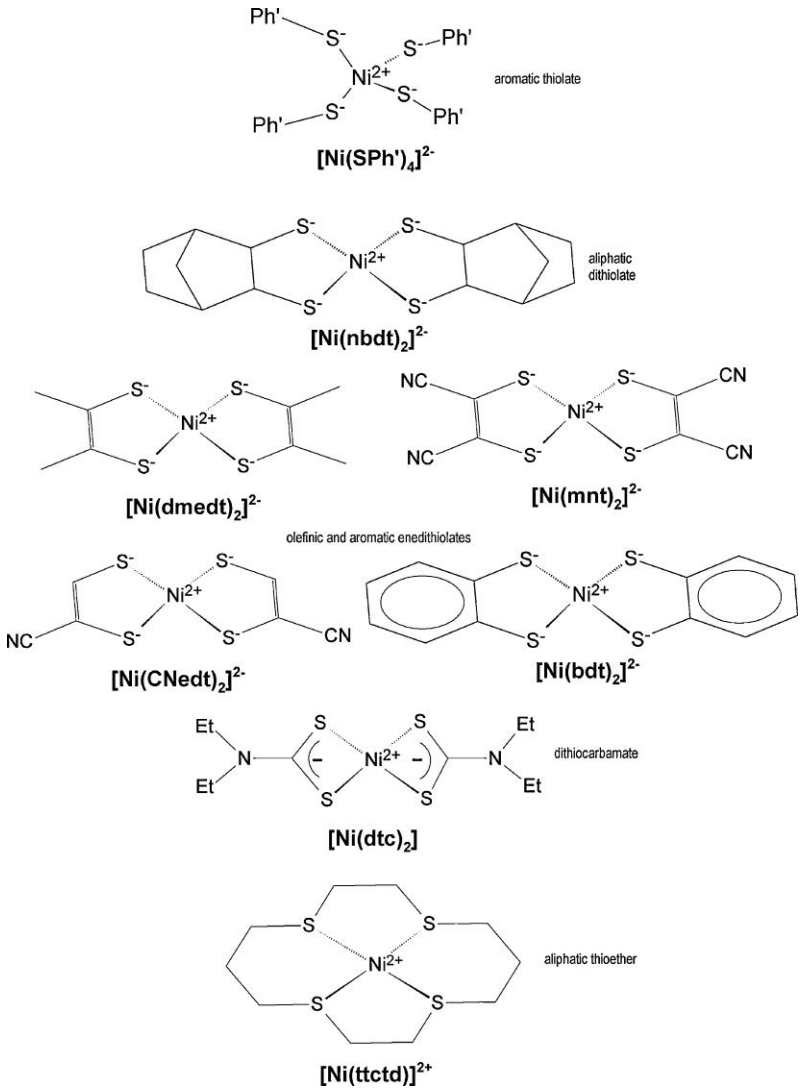

Scheme 2.1 Nickel coordination complexes with various sulfur-ligands and coordination environments

The electronic structure of the high spin, tetrahedral complex $[Ni(II)(SPh')_4]^{2-}$ of this series with aromatic thiolate ligands (S-Ph′ = S-2-Ph-C_6H_4) has already been discussed in detail.[26, 27] This complex can be considered as a representative example for the classical inorganic or normal bonding scenario with unoccupied, degenerate metal d-orbitals ($3d_{xz}$ and $3d_{yz}$ of the t_2-set) lying above the symmetry adapted combination of donor S 3p orbitals in molecular orbital theory or S lone pairs in a valence bond picture. Moreover, the sulfur K-edge X-ray Absorption Near-Edge Spectroscopic (S K-edge XANES) analysis of the $[Ni(II)(SPh')_4]^{2-}$ defined about 33% S 3p character in each of the partially occupied Ni 3d-orbitals.[27] This corresponds to approximately 17% Ni-S bond covalency or a donation of 0.085 electron (e^-) per each ligand from the S lone pairs to each of the electron holes in the Ni-S σ^*/π^*. Another representative example for the remarkable coordination chemistry of S-based ligands is the family of bis(enedithiolate)nickel complexes[28-32] that are also known as bis(dithiolene)nickel complexes. The formal Ni oxidation states of these complex range from II to IV in $[Ni(dmedt)_2]^{2-}$ to $[Ni(dmedt)_2]$, respectively. These square planar complexes manifest ligand-based reactivity[33-35] and inverted bonding[36, 37] that have been collectively referred to in the literature as non-innocent coordination behavior.[38, 39] Advanced electron paramagnetic spectroscopic techniques[31, 40, 41] indicated the non-innocent nature of the formally bis(enedithiolate)nickel(III) complex.

The quantitative analysis of the hyperfine coupling constants defined about 80% spin localization at the central $[NiS_4]$ unit with only about 20% localized on the metal. The inverted contributions from the metal and the ligand to the singly occupied π*-orbital

indicate that in going from a formally Ni(II) complex the one-electron oxidation is ligand- and dominantly S-based. The S K-edge XANES analysis extended the ground state description of the paramagnetic, formally Ni(III) species, to both its reduced (formally Ni(II)) and oxidized (formally Ni(IV)) forms.[37] For all three members of this electron-transfer series with the same, non-aromatic ligands,[42, 43] the ground state bonding description can be described with more than 50% S contribution per electron hole to the redox active, unoccupied frontier orbital. Due to the diamagnetic ground state of the $3d^8$ Ni(II) complex with a single empty d-orbital, and thus the presence of spin up (α) and spin down (β) electron holes, this corresponds to more than 1 electron total S contribution for both spin orbitals. This also translates to more than 25% Ni-S bond covalency or more than 0.25 e^- donation per each enedithiolate ligand per electron hole, which represents close to doubling of covalent bonding relative to the tetrahedral tetrathiolate complex.[27]

Due to the metal-based, innocent electronic structure, the effective and formal oxidation states of the Ni center in a $[Ni(II)(SR)_4]^{2-}$ complex are practically identical. However, this is not true for the non-innocent, enedithiolate Ni complex ($[Ni(dmedt)_2]^{2-}$), where the effective oxidation state is considerably reduced. This remains unchanged throughout the 2-electron electron-transfer series for $[Ni(dmedt)_2]^-$ and $[Ni(dmedt)_2]$. The non-innocent bonding scenario and the corresponding reduction of the Ni effective oxidation state versus its formal Ni(II) state can be rationalized by molecular orbital theory that presents an inverted orbital ordering with the S donor orbitals being at higher energy than the vacant Ni 3d orbital. The efficient σ- and reasonable π-overlap in square planar complexes between the S lone pairs and the vacant Ni 3d orbitals facilitates

intramolecular electron-transfer and contributes to the reduction of the formally Ni(II) to effectively Ni(0) state with concomitant oxidation of the enedithiolate ligands from their thiolate form toward their radical anionic and then further on to their thione form. We extend the previously studied [Ni(II)S_4] complexes with three new members: the bis(1,2-norbornadithiolato)nickel(II) ([Ni(nbdt)$_2$]$^{2-}$), bis(diethyldithiocarbamato) nickel(II) ([Ni(dtc)$_2$]), and the tetrathiacyclotetradecane coordinated nickel(II) ([Ni(ttctd)]$^{2+}$) complexes. These complete a spectrochemical series for the [Ni(II)S_4] motif (Scheme 1) with constrained aliphatic dithiolate, conjugated dithiocarbamate, and aliphatic tetrathioether complexes.

The existence of the latter complex is notable, since only a few thioether ligands coordinate to Ni(II).[44] In addition to its compositional peculiarity, the [Ni(ttctd)]$^{2+}$ complex manifests an ideal behavior in a reversible, ligand exchange-based thermochromic process.[3] The γ-butyrolactone (GBL) solution of the [Ni(ttctd)](ClO_4)$_2$ salt with 30-fold neopentyl glycol (NPG) manifests a reversible color change for the temperature range of 25–100 °C. The solution is almost colorless at low temperature, where the Ni^{2+} ions are coordinated with the NPG ligands. As the temperature increases the [Ni(NPG)$_3$]$^{2+}$ complex converts into [Ni(ttctd)]$^{2+}$ with λ_{max} = 503 nm and $\varepsilon \approx 370$ dm^3 mol^{-1} cm^{-1} in GBL (red color). The estimated thermodynamic parameters for the thermochromic process are ideal due to the large enthalpy (ΔH = 60 kJ mol^{-1}) and large entropy (ΔS = 190 J mol^{-1} K^{-1}) changes.[45]

One of the motivations of the given study is to provide a comprehensive understanding of metal–ligand bonding in Ni(II) coordination complexes with

thermochromic behavior by X-ray absorption spectroscopy and correlated electronic structure calculations. In addition, the exemplary thermochromic behavior of the Ni-thioether complex also serves as an important control for evaluating the Ni-S(thioether) bond covalency.

The X-ray absorption spectroscopy (XAS) probes core-level excitations, yet it can be used to obtain quantitative ground state information.[24] The analysis of the spectroscopic features below the ionization threshold of the S 1s orbitals (~2472 eV) can provide information about the amount of S 3p character in the low lying, unoccupied frontier molecular orbitals. The essential information needed to obtain experimental orbital compositions from experiment is the knowledge of S 1s → 3p transition dipole integral (*I*). This requires the availability of independent spectroscopic information (EPR/ENDOR/ESEEM or XPS for example) about the electronic structure of a given complex. The relevant spectroscopic features in XAS are the well-resolved (pre-edge) and overlapping (rising-edge) features with the ionization threshold (edge jump). Using a dipole expression[46] as shown below, the area or intensity (D_0, eV/absorber) under a given pre-edge or rising-edge feature can be correlated with the amount of S 3 p character per electron hole (α^2, electron hole covalency):

$$D_0 = \frac{1}{3}\frac{h}{N}\alpha^2 I(S1s \rightarrow 3p) \tag{2.1}$$

where *h* represents the number of electron holes in the probed unoccupied orbitals, *N* the number of absorbers, the 1/3 factor is from the *x*, *y*, *z* dependence of the transition dipole expression,[47] and the *I*(S 1s → 3p) is the transition dipole integral (eV) which is the

probability for an excitation of an electron from the sulfur 1s core orbital to the valence S 3p level. Although the core electron dipole integral can be estimated from wave function- or density functional-based calculations,[48] for practical use one needs to consider experimental factors, such as beamline components, detection method, sample preparation protocols, *etc*.[49]

A S 1s → 3p transition dipole moment was first determined for thiolate ligands coordinated to a Cu(II) ion.[50] This was later extended first to sulfide[51] and then to the enedithiolate[37] ligands. A different dipole moment is needed for each S-ligand, since the sulfur 1s orbital energy is inherently linked to the effective nuclear charge (Z_{eff}(S)) seen by the S 1s electron and thus the S atomic charge. An earlier study[52] established a linear relationship between the S atomic charges and the most intense XANES features corresponding to excitations into S-C σ* or S 4p level. This observation allowed for the extension of known dipole integrals to other S-ligands. Overall, there are two conceptually different approaches in the literature for obtaining experimental S 1s → 3p transition dipole integrals for a transition metal complex with vacancy in the d-manifold. The first method[50, 51, 53] used the XAS spectra of S-ligands coordinated to first row transition metals and independent spectroscopic information to assign pre-edge intensities to orbital compositions. The second method compared spectroscopic features of free and coordinated ligands and employed a linear relationship between the S charge as represented by the S 1s → 4p excitation energy positions and the transition dipole integral.[37, 54] The given comprehensive data for Ni(II) coordinated S-ligands provided the opportunity for merging the two approaches and defining a general method for estimating

transition dipole integrals using only XAS data of [Ni(II)S_4] complexes and the corresponding free S-ligands.

An additional implication of our study is the use of experimental electronic structure description to evaluate the accuracy of electronic structure calculations. For Cu(II) complexes,[55] it has been shown that a hybrid functional with approximately 38% Hartree–Fock exchange mixed with Becke 1988 density functional exchange[56] reproduced the experimental orbital composition of the ground state of $[CuCl_4]^{2-}$.[57, 58] The same hybrid functional also provides reasonable electronic structure description of a series of Cu-containing metalloproteins.[59-63] It is important to add here that the appropriate treatment of protein-, crystal-, or solvent-environmental effects in computational modeling is as critical as the selection of the most reasonable density functional.[62-66] Follow up studies investigated the performance of various density functionals for a group of Fe-S clusters and found preference for another hybrid functional with less Hartree–Fock exchange (5%).[67, 68] This functional was essential in predicting the most reasonable composition of the elusive light atoms in Mo-nitrogenase[68] and FeFe-hydrogenase[69] *a priori* to experimental confirmations. Given the success of these empirically developed hybrid functionals, we wish to extend this approach to Ni(II) complexes and thus provide a spectroscopically calibrated method with an optimal saturated basis set for studying the electronic structures of Ni containing metalloenzymes, and organometallic complexes, as well as for designing and optimizing Ni(II)-based thermochromic systems.

Experimental Details

Preparation of Compounds

The Na_2S salt[70] and $Ni(dtc)_2$ complex[71] were prepared and characterized according to literature procedures. The $Li_2(nbdt)$ salt and the corresponding $(Ph_4P)_2Ni(nbdt)_2$ complex were provided by Prof. Michelle Millar, State University of New York, Stony Brook.[72] The tetrathiacyclotetradecane (ttctd) thiocrownether was purchased from Sigma–Aldrich and used without further purification and characterization. An ~5 mM solution of $[Ni(ttctd)]^{2+}$ complex was freshly prepared before the XAS measurements with a slight excess of $Ni(ClO_4)_2$ salt in freshly distilled γ-butyrolactone (GBL). The solid sample was isolated as described in the literature.[44] The XAS spectra of the solution and solid samples were found to be practically identical with negligible distortion in peak amplitudes due to self-absorption effects. All samples measured by us were characterized by comparing their solution and/or solid state UV/vis spectra to literature values.[44, 71, 72]

Sulfur K-edge X-ray Absorption Spectroscopy

The S K-edge data for $[Ni(SPh')_4]^{2-}$,[27] $[Ni(dmedt)_2]^{2-}$,[37] $[Ni(bdt)_2]^{2-}$,[73] and $[Ni(mnt)_2]^{2-}$ [54] were taken from literature. All the other complexes and the corresponding free ligands were either measured at beamline 6-2 ($(Ph_4P)_2Ni(nbdt)_2$ and $Li_2(nbdt)$, $(ClO_4)_2Ni(ttctd)$ and ttctd) or 4-3 ($Ni(dtc)_2$ and Na(dtc)) of the Stanford Synchrotron Radiation Lightsource. Repeated measurements of the samples did not reveal any significant variation among data sets from the different beamlines for solid samples. All

XAS measurements were carried out at room temperature for sample cells that were prepared in nitrogen or argon gas filled glovebox. While mounting the samples at the beamline, they were protected with a few μm thick polypropylene window to eliminate sample degradation due to oxidation or moisture exposure. Sample decomposition was clearly identified by the appearance of the intense sulfate feature at around 2482.5 eV[74]. Spectra with extended energy ranges in Figure 2.1A and B clearly indicate the lack of sulfate in all data considered. The solid samples were ground with boron nitride and pasted onto Kapton tape. Any excess sample was scraped off from the tape to minimize the distortion of peak intensities due to self-absorption effects.[75] The beamlines were optimized to maximize incident beam intensity at the end of the scan (2750 eV). All data presented here were collected with fluorescence detection either using a nitrogen gas purged, multi-element Lytle fluorescence emission detector (EXAFS Co) or a passivated implanted planar silicon detector (PIPS, CANBERRA). Importantly, due to the observed intensity differences between electron yield and fluorescence emission data, the pre-edge intensity analysis and the transition dipole integrals presented here are limited to reasonably thin samples with the latter detection technique.

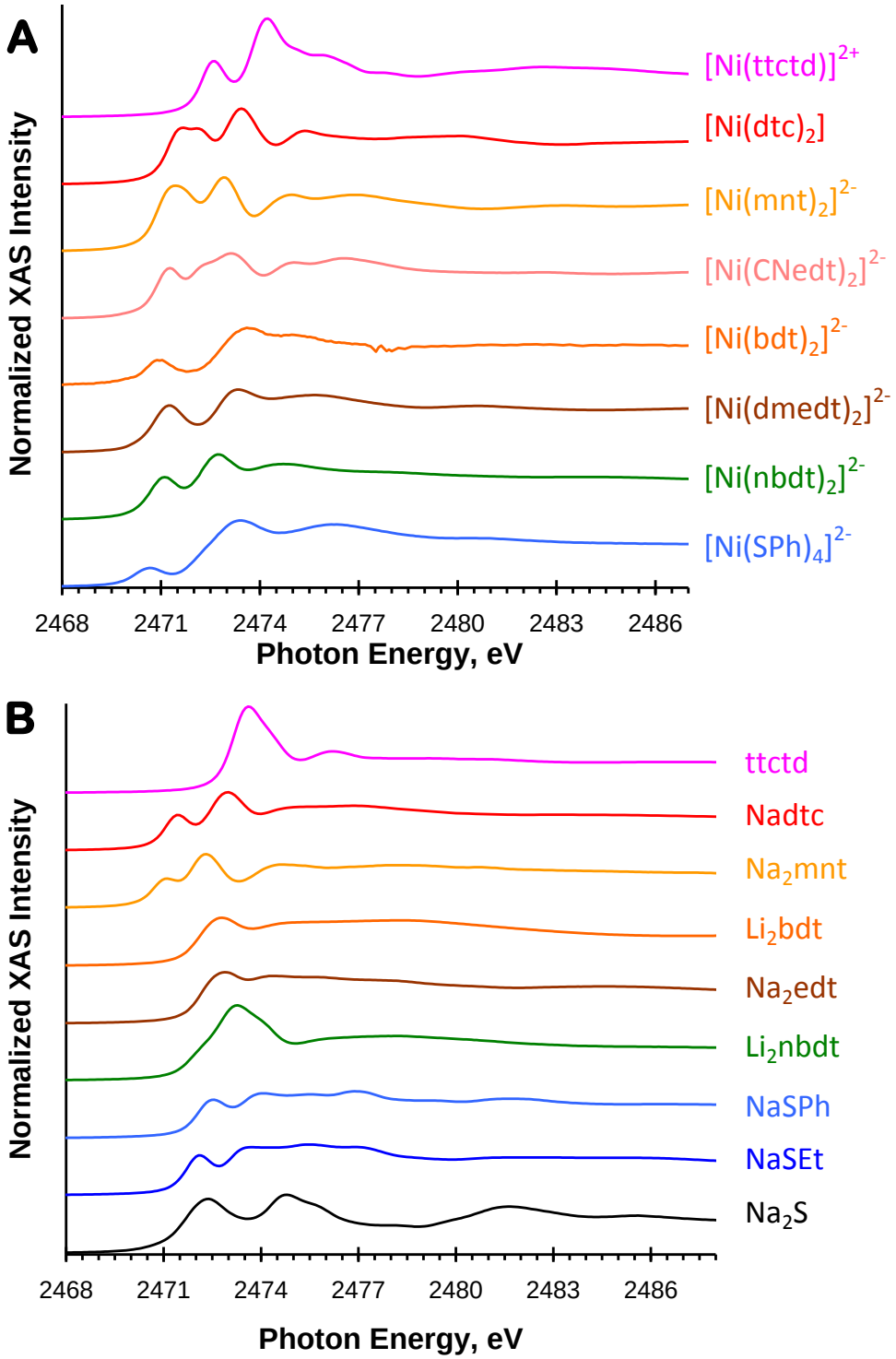

Figure 2.2 A) Full energy range S K-edge spectra for all [Ni(II)S_4] coordination complex and B) Free ligands

XAS Data Normalization and Fitting

All data was background subtracted and normalized using the Automated Data Reduction Protocol developed by Gardenghi.[76] The normalized data were fit using Peak Fit v4.12 (SeaSolve). The details of all fits are shown in Figure 2.3-2.11.

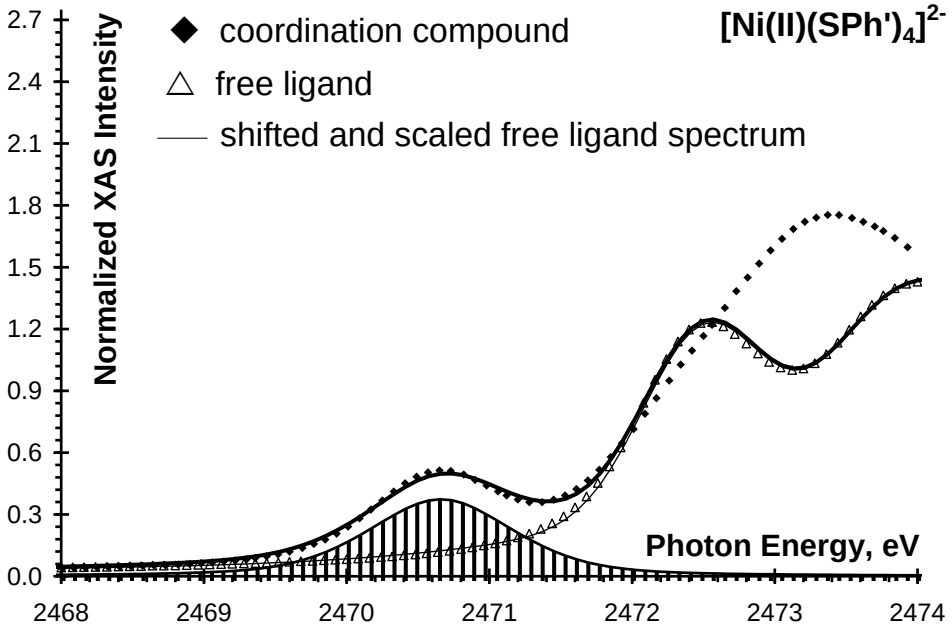

Figure 2.3 Free SPh' ligand fit of the $[Ni(II)(SPh')_4]^{2-}$ spectrum matching the inflection point of the free ligand rising edge to the inflection point of the complex rising edge.

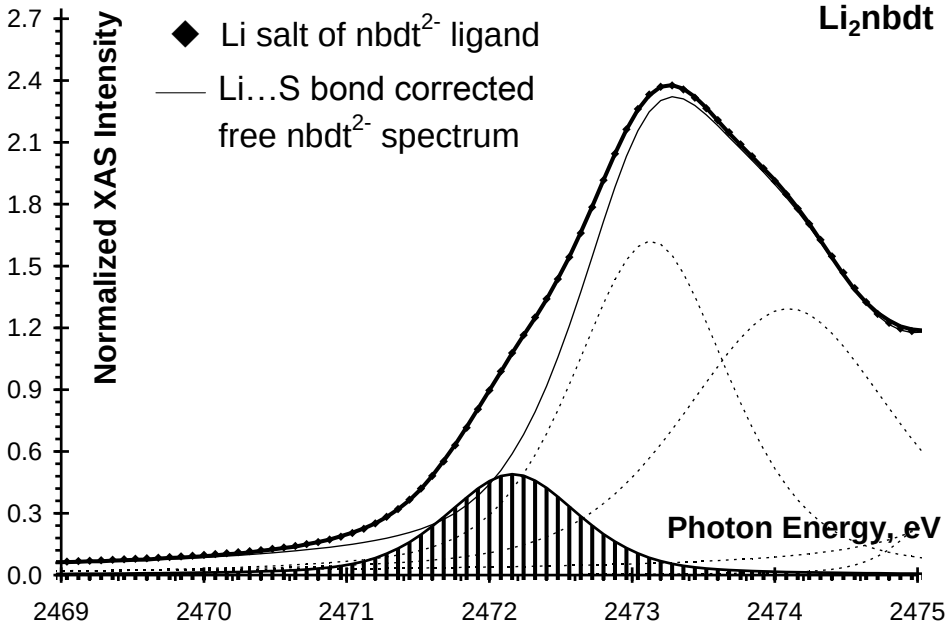

Figure 2.4 Li-S bonding correction by removing the pre-edge feature creating the $nbdt^{2-}$ "free" ligand spectrum for fitting.

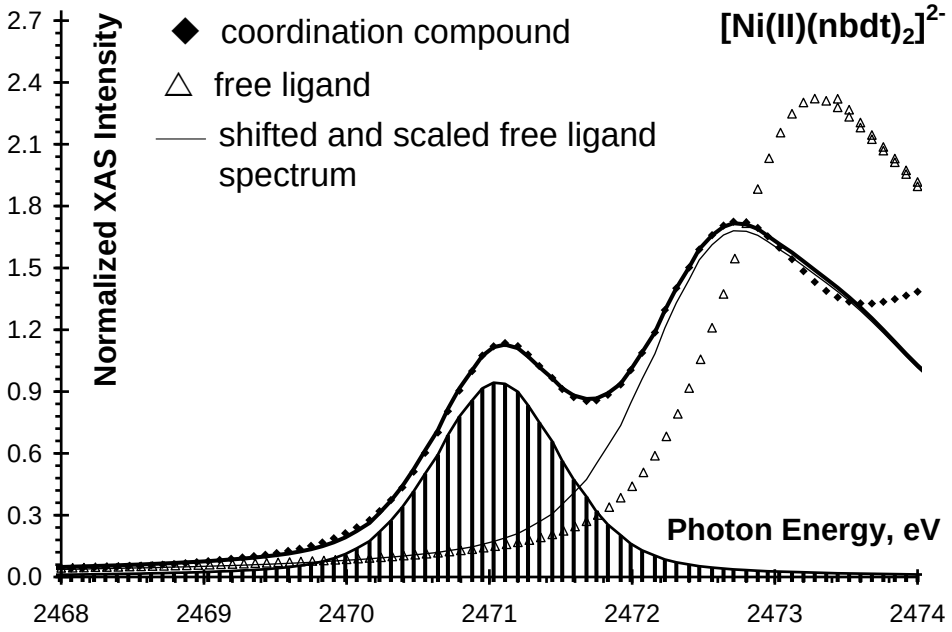

Figure 2.5Fit of the $[Ni(II)(nbdt)_2]^{2-}$ pre-edge feature after rising edge spectrum fittuing with nbd^{2-} "free" ligand.

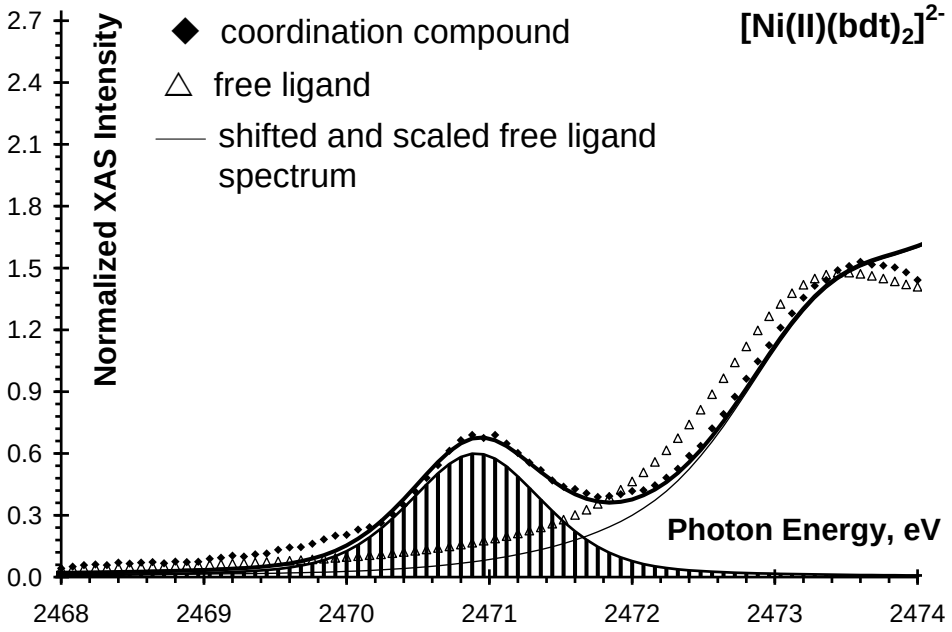

Figure 2.6 Fit of the $[Ni(II)(bdt)_2]^{2-}$ pre-edge feature after fitting the rising edge with the free bdt^{2-} spectrum.

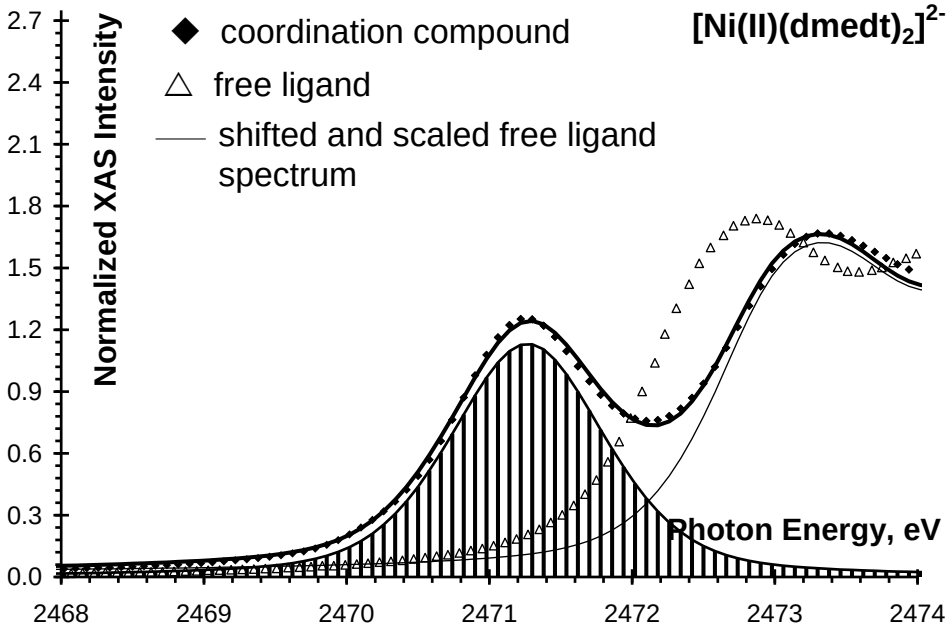

Figure 2.7 Fit of the $[Ni(II)(dmedt)_2]^{2-}$ pre-edge feature after fitting the rising edge with the free $dmedt^{2-}$ spectrum.

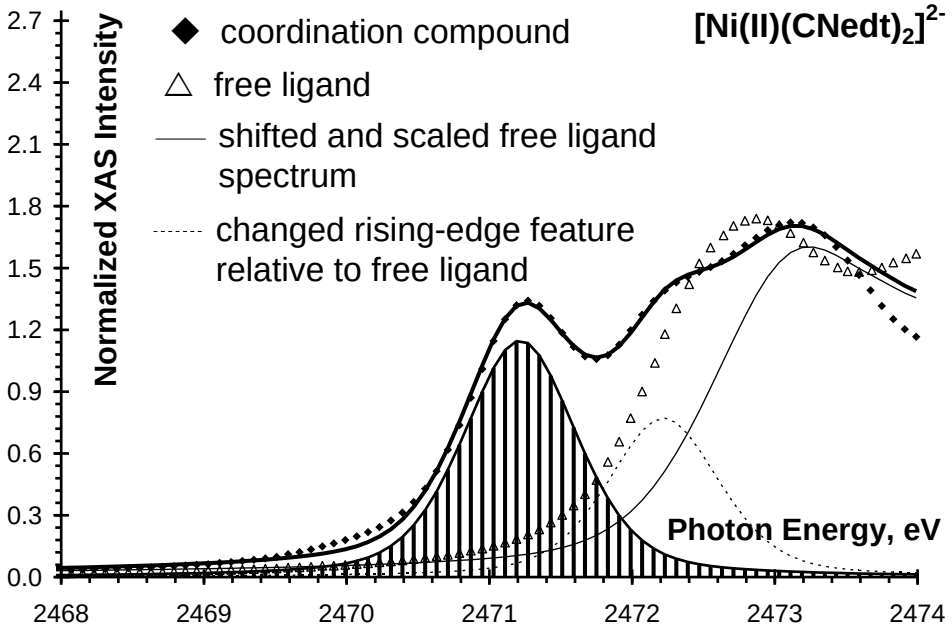

Figure 2.8 Fit of the $[Ni(II)(CNedt)_2]^{2-}$ pre-edge feature after fitting the rising edge with the free $CNedt^{2-}$ spectrum.

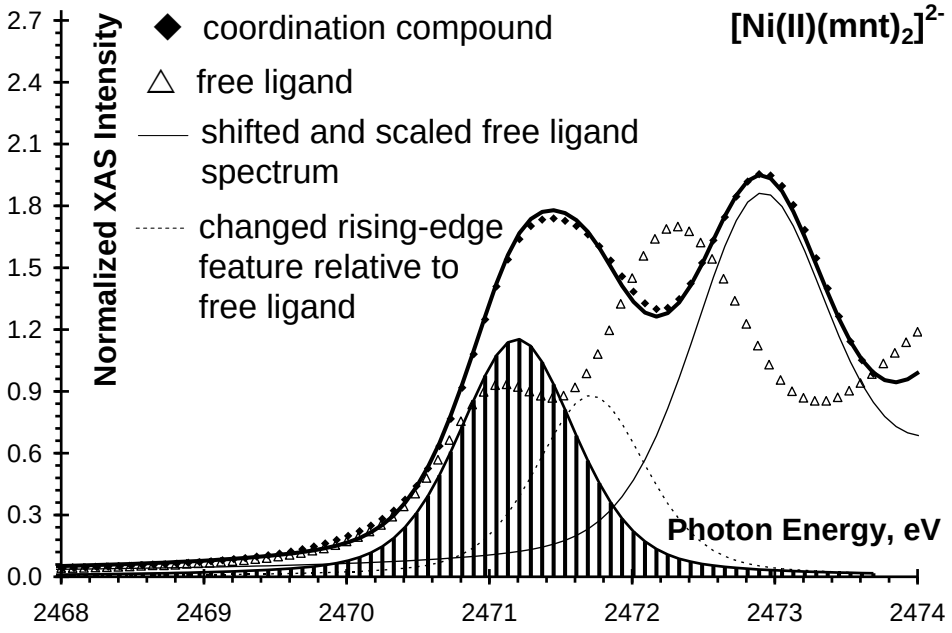

Figure 2.9 Fit of the $[Ni(II)(MNT)_2]^{2-}$ pre-edge feature after fitting the rising edge with the free mnt^{2-} spectrum.

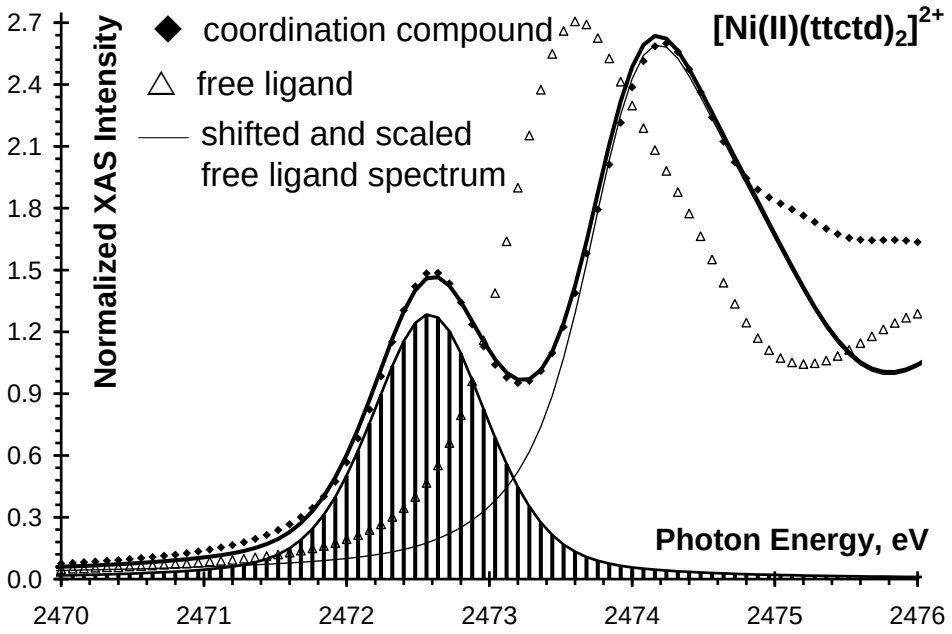

Figure 2.10 Fit of the $[Ni(II)(ttctd)_2]^{2+}$ pre-edge feature after fitting the rising edge with the free ttctd spectrum.

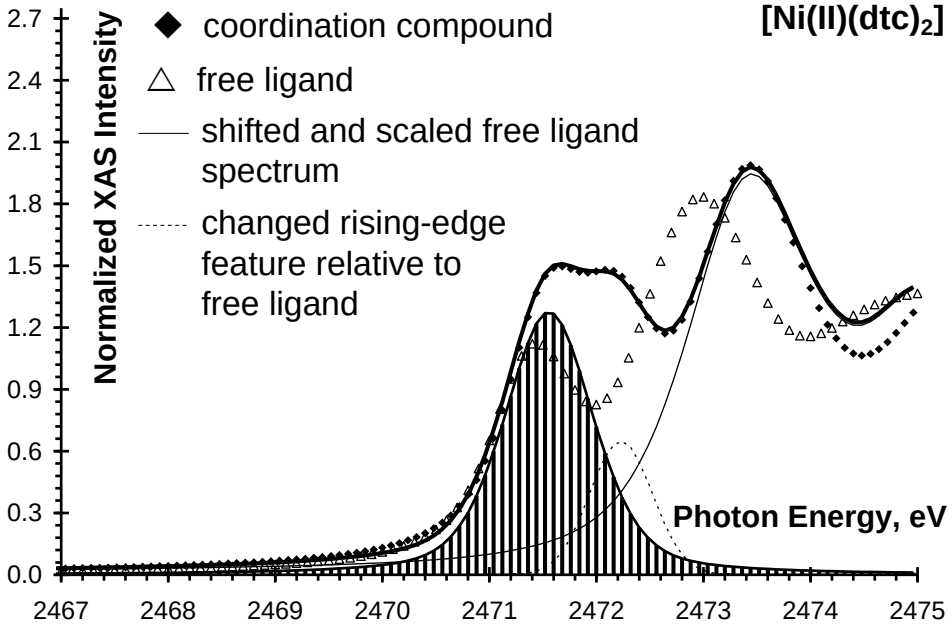

Figure 2.11 Fit of the $[Ni(II)(dtc)_2]$ pre-edge feature after fitting the rising edge with the free ttctd spectrum.

Due to the comprehensive set of spectra for both the Ni(II) complexes and the free ligand salts, we were able to employ a common protocol. All resolved features were fit by pseudo-Voigt lines for non-degenerate excitations below the most intense, S-C σ* features including the S-C π*, and even Li-S σ* orbitals. Transition envelopes were fit using the Gaussian + Lorentzian Amplitude Function in PeakFit with unrestricted Gaussian/Lorentzian mixing ratio, while single or degenerate double electron hole-based excitations were fit with a Gaussian/Lorentzian ratio of 1:1. The corresponding spectroscopic features were subtracted from the free ligand salt spectra to obtain a reasonable rising-edge background for the complexes. Due to the covalent Li-S bonding in Li_2(nbdt) salt, the reference as "free ligand" spectrum is not strictly correct; however, by removing the rising-edge feature we can obtain a reasonable estimate for the free ligand spectrum (Figure 2.4). A free ligand spectrum was fit to create a user defined function, which was then used to subtract C-S σ* transition-based rising-edge and edge-jump features by using the second derivative spectra to align the most intense transitions. The remaining pre-edge (Ni-S bonding) and rising-edge (S-C π* bonding) peaks after the subtraction of the free ligand spectrum were fit with Gaussian/Lorentzian ratio of 1:1 and a linked linewidth of about 1.2 eV. In order to avoid unreasonable distortion and large variations in intensities for ill-resolved features, additional fits were obtained in consecutive steps by gradually allowing for the linewidths, amplitudes, and lastly the energy positions to be altered. The final fits were obtained by relaxing all fit parameters except the Gaussian/Lorentzian mixing ratio.

Electronic Structure Calculations

All electronic structure calculations were performed using Gaussian 09[77] in the presence of a polarizable dielectric environment[78-83] solvent parameters for acetonitrile with a dielectric constant of 35.6 and solvent radius of 1.81 Å. The computational models were created from crystallographic structures ($[Ni(II)(SPh')_4]^{2-}$,[26] $[Ni(II)(nbdt)_2]^{2-}$,[72] $[Ni(II)(dmedt)_2]^{2-}$,[42] $[Ni(II)(bdt)_2]^{2-}$,[84] $[Ni(II)(CNedt)_2]^{2-}$,[85] $[Ni(II)(mnt)_2]^{2-}$,[86, 87] $[Ni(II)(dtc)_2]$,[88] $[Ni(II)(ttctd)]^{2+}$ [44]) and used without structural optimizations. A summary of intramolecular distances and bond angles relevant to the coordination geometry is given in Table 2.1.

Table 2.1 Summary of intramolecular distances and bond angles of crystal structures from literature.

	Ni-S, Å	S···S, Å (intraligand)	S···S, Å (interligand)	S-Ni-S, ° (intraligand)	S-Ni-S, ° (interligand)
$[Ni(SPh')_4]^{2-}$	2.29	3.89	3.66	106	117
$[Ni(nbdt)_2]^{2-}$	2.18	3.08	3.09	90	90
$[Ni(dmedt)_2]^{2-}$	2.18	3.05	3.08	90	89
$[Ni(bdt)_2]^{2-}$	2.17	3.02	3.11	92	88
$[Ni(mnt)_2]^{2-}$	2.20	3.01	3.14	92	88
$[Ni(dtc)_2]$	2.20	2.82	3.39	79	101
$[Ni(ttctd)]^{2+}$	2.18	3.07	3.09	90	90

In order to evaluate the uncertainties in LUMO composition due to the ill-defined crystallographic H atomic positions, the structures of representative examples of the above series were partially optimized. It was determined that changes in the S contributions to the LUMO were less than 0.05 e^- per electron hole. A set of representative exchange and correlation density functionals was chosen according to the rungs of Perdew's ladder of functionals.[89, 90] From the functionals with generalized

gradient approximations (GGA) rung the commonly used BLYP,[56, 91] BP86,[56, 92] mPW,[93] OLYP,[91, 94, 95] PBE,[96] and PW91[96, 97] functionals were employed. The M06L,[98] TPSS,[99] and TPSSLYP1W[100] functionals were selected for representing the metaGGA rung. As a bridge between the two rungs, we used a set of hybrid functionals, that mix Hartree–Fock exchange and thus ionic character into either GGA (B1LYP,[91, 101] B3LYP,[91, 102] BHandHLYP,[91, 103] MPW1K,[104] mPW1PBE,[93, 96] MPW3LYP,[105] MPW1LYP,[106] and O3LYP[91, 107]) or metaGGA (M06,[108] M062X,[108] M06HF,[109, 110] and TPSSh[99]) exchange functionals. We employed the def2-TZVP basis set[111] from the EMSL Gaussian Basis Set Exchange[112, 113] that can be considered saturated for electronic structure and thus orbital compositions. The theoretical total S composition of the unoccupied frontier orbitals corresponding to the Ni-S bonds were obtained from Bader's 'atoms in molecules' population analysis[114-117] using AIMAll program[118] in addition to the conventional Mulliken population analysis (MPA)[119] and Weinhold's Natural population analysis (NPA)[120] as implemented in Gaussian09. The latter two orbital-based methods provided the experimentally comparable S 3p characters.

Similarly to the experimental covalency from XAS as defined by Equation 2.1 the S 3p character of LUMO or S 3p contributions to covalent bonding per electron hole (or per spin orbital) was employed. This is most consistent with a molecular orbital theory-based bonding analysis. The per-hole covalency already takes into account all the contributions from all symmetry allowed S donors. For the diamagnetic complexes, the orbital covalency is simply the double of per-hole covalency. Furthermore, multiplication of the 'per-orbital' values with the number of unoccupied orbitals defines the total sulfur

covalency. Since the Ni(II) complexes have more than one vacant d-electron hole, the upper limit of covalency is 2 e^{-}. Division of the total S covalency by the number of bonds or number of atoms gives the per-bond or per-absorber covalency values that are mainly used in valence-bond theory-based discussions of metal–ligand bonding.

Results and Analysis

S K-edge XANES Analysis of [Ni(II)S_4] Complexes

The comprehensive list of Ni(II) complexes used in the given study includes a paramagnetic (S = 1) tetrahedral $[Ni(SPh')_4]^{2-}$ complex, and a series of diamagnetic (S = 0) square planar dithiolate $[Ni(nbdt)_2]^{2-}$, aliphatic enedithiolate $[Ni(dmedt)_2]^{2-}$, aromatic enedithiolate $[Ni(bdt)_2]^{2-}$, dithiocarbamate $[Ni(dtc)_2]$, and tetrathiocrownether $[Ni(ttcd)]^{2+}$ complexes. Figure 2.12 compares the S K-edge pre-edge and rising-edge features for the above listed complexes. The straightforward molecular orbital picture (Scheme 2.2) of these complexes allows for the assignment of the resolved spectroscopic features below and along the rising-edge.

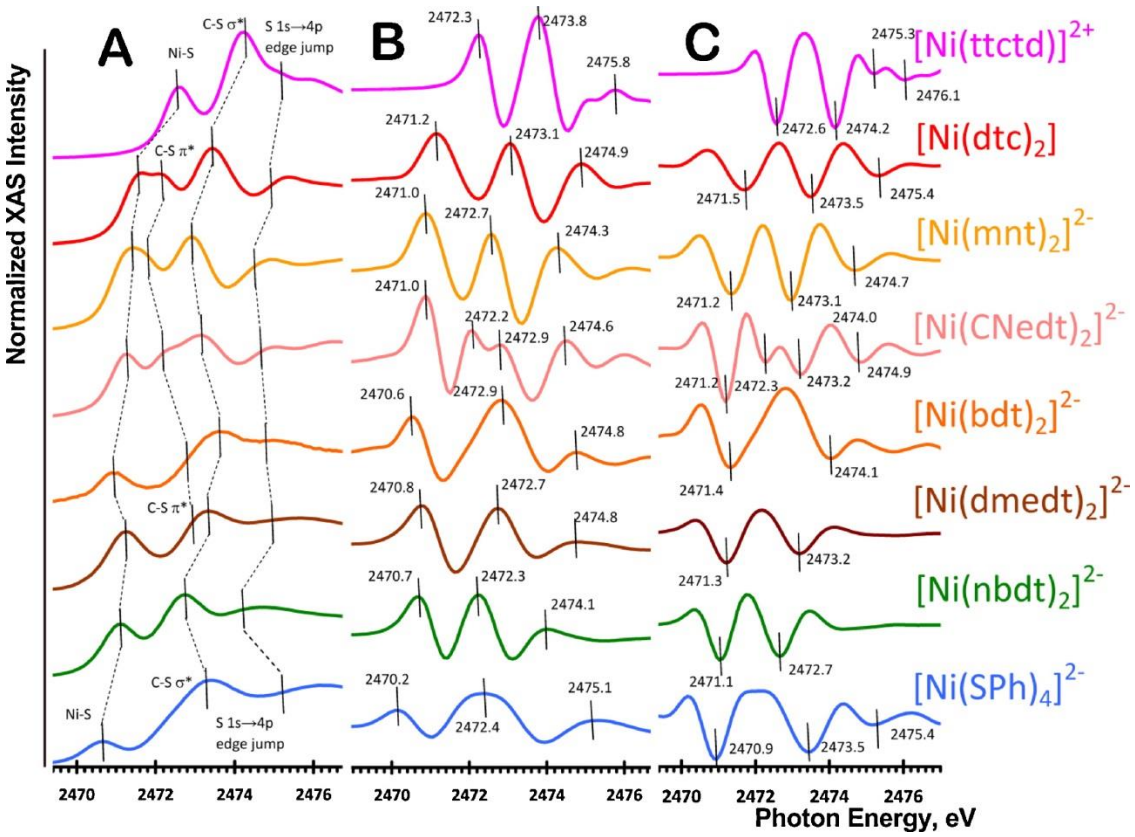

Figure 2.12 Comparison of S K-edge XANES spectra of Ni(II) coordinated S-ligands considered in this work (nbdt = 1-2-norbornadithiolate, edt = ethylenedithiolate, bdt = benzenedithiolate, mnt = maleonitriledithiolate, dtc = diethyldithiocarbamate, ttctd = tetrathiacyclotetradecane) A) normalized data, B) first derivative spectra with inflection points in eV, C) second derivative spectra with peak positions in eV. The S K-edge data for $[Ni(SPh')_4]^{2-}$,[27] $[Ni(dmedt)_2]^{2-}$,[37] $[Ni(bdt)_2]^{2-}$,[73] and $[Ni(mnt)_2]^{2-}$ [54] were taken from literature.

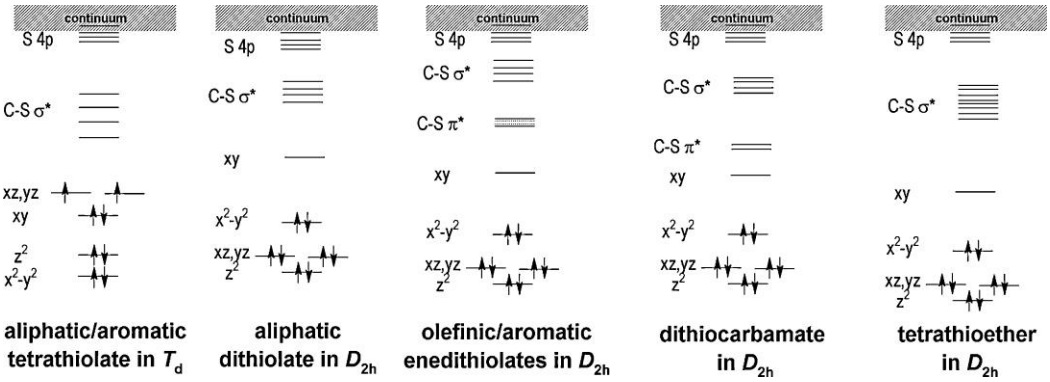

Scheme 2.2

The lowest energy pre-edge feature can be associated with the excitation of the S 1s core electron into the unoccupied, Ni-S antibonding π* or σ* orbitals for the paramagnetic or diamagnetic complexes, respectively. For the $[Ni(dmedt)_2]^{2-}$, $[Ni(bdt)_2]^{2-}$, $[Ni(dtc)_2]$ complexes, the next feature corresponds to the excitations into C-S π* orbitals, followed by the C-S σ* transitions as most intense spectroscopic lines (white lines) for all complexes. The resolution of the S K-edge XAS spectra (~1.2 eV linewidth for single electron excitation) limits unique assignments of any higher lying excitations, but from frontier orbital energy levels it is expected that the S 4p-based bound states will follow with the overlapping edge-jump that corresponds to the ionization threshold of the S 1s orbital into the continuum. The approximate position of the edge jump thus can be estimated from the first inflection point after the C-S σ*-based transitions or the 'white line' feature. Figure 2.12B shows the first derivative spectra, which can be used to obtain the energy positions of inflection points. In general, it is common to correlate the rising-edge inflection points as determined by the first maximum of the first derivative along the rising-edge energy region with the absorber's effective nuclear charge.[121] However, this is only valid for complexes with the same overall electronic structure. In practice, the rising-edge inflection points at the ligand K-edge are only useful for monoatomic/ionic ligands, such as chloride.[47] The comparison of the rising-edge inflection point positions of an aliphatic thiolate coordinated complex to olefinic or aromatic enedithiolate complexes will result in erroneous effective nuclear charge estimates due to the rising-edge originating from a C-S σ* or C-S π* based orbitals, respectively. Figure 2.12C presents the second derivative spectra that can be used to obtain information about the

number of peaks and their energy positions which can guide the fitting procedure and effectively reduce the number of parameters to be fit.

From Figure 2.12C, the pre-edge energy position gradually shifts in going from tetrathiolate, bis(dithiolate), bis(enedithiolate), bis(dithiocarbamate), and tetrathiocrownether coordinated Ni(II) complexes. However, this energy position is affected by both the sulfur effective nuclear charge (ligand-based chemical shift) and the Ni d-manifold energy (coordination-based chemical shift). In going from the tetrathiolate to the dithiolate complex, the dominant change is the change in coordination geometry from tetrahedral to square planar. Therefore, there is positive energy shift in the Ni d-manifold, since the better overlap in the square planar geometry creates a larger ligand field splitting and thus pushes the frontier 3d orbitals to higher energy. In addition, the better overlap allows for greater mixing of the S-based orbitals of the ligand and the vacant metal orbitals. The greater mixing of S 3p with Ni 3d orbitals which is well demonstrated by considerable increase in pre-edge intensity in $[Ni(nbdt)_2]^{2-}$relative to the $[Ni(SPh')_4]^{2-}$ complex. However, the reduced distance of the two S atoms in the bis(dithiolate) complex due to the rigid C-C bond within a constrained cyclic aliphatic framework or the shorter C=C double bond within a olefinic or aromatic enedithiolate and the smaller S···Ni···S bite angle induces a considerable S ↔ S repulsion. This ligand–ligand repulsive interaction raises the energy of the S 1s orbital with respect to those in the tetrahedral Ni-S(thiolate) complex. The effect of the ligand-based chemical shift is most drastic for the thioether complex with the highest Z_{eff}(S) among all $[Ni(II)S_4]$

complexes. This results in a shift to higher energy by approximately 1 eV of the pre-edge feature and the edge jump relative to the dithiocarbamate complex.

In order to carry out the comparison of the pre-edge features, we have chosen to eliminate the rising-edge features using the corresponding uncoordinated ligand salt spectra. Figures 2.2-2.10 show the data points for the coordination complex, free ligands (solid diamonds and hollow triangles, respectively), the shifted/scaled free ligand spectra (thin solid line), the deconvoluted pre-edge feature (shaded pseudo-Voigt feature with 50%/50% mixed Gaussian/Lorentzian line shape), and the sum of the pre-edge feature and shifted free ligand spectra (thick line). Figure 2.13 compares the pre-edge features that correspond only to the S 1s → φ(Ni 3d-S 3p) π* and/or σ* excitation.

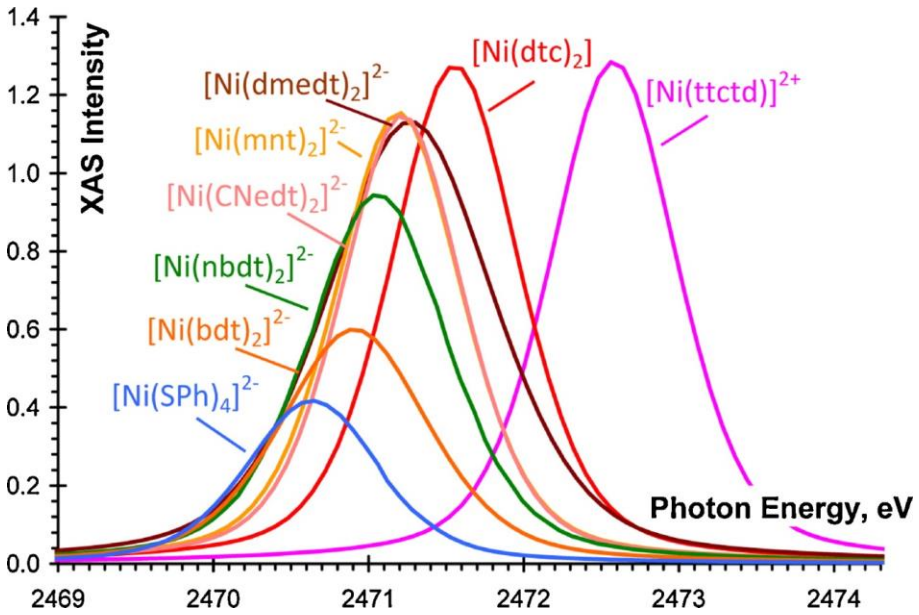

Figure 2.13 Comparison of S K-edge pre-edge features after subtraction of rising-edge features using the free ligand salt spectra (Figures 2.1-2.7).

As defined by the above dipole integral (Equation 2.1), the intensities of these spectroscopic features correspond with the amount of S 3p mixing with the vacant Ni 3d orbital. This is commonly referred to as the Ni-S bond covalency or S contribution to bonding. In order to quantify this information we need to determine a transition dipole moment for each of the complexes.

Table 2.2 summarizes the energy positions, amplitudes, linewidths, and peak intensities that were obtained from fitting the rising-edge corrected, pre-edge features from Figures 2.3-2.11 with a pseudo-Voigt line. The pre-edge energy positions in Table 2.2 already indicate the presence of different S-ligand environment and thus the different nature of the Ni-S bonding. The lowest energy position observed for the pre-edge was measured for the tetrathiolate complex due to the least covalent Ni-S bonding (smallest D_0 values)[27] that corresponds to the most oxidized Ni(II) with the smallest ligand field splitting due to the tetrahedral coordination geometry. The pre-edge features for the dithiolates and enedithiolates can be found in the 2470.9–2471.3 eV energy range, which is about 0.6 eV shifted up in energy relative to the tetrathiolate complex. However, this modest shift actually corresponds to a large reduction of the effective nuclear charge of the Ni(II) due to the considerable S → Ni electron donation as well as the increase in the ligand field splitting due to the square planar coordination environment. The large change is masked by the lower energy position of the edge jump for the square planar complexes by about 1 eV as can be seen in the last column of Table 2.2.

Table 2.2 Fitting results for the pre-edge features in Figure 2.13 and related energy positions from Figure 2.12

Complexes	E, eV[a]	A, -[b]	fwhh, eV[c]	D_0, eV[d]	E_0[C], eV[e]
$[Ni(SPh')_4]^{2-}$[f]	2470.8	0.40	1.10	0.56	2475.1
$[Ni(nbdt)_2]^{2-}$	2471.1	0.95	1.07	1.28	2474.1
$Ni(dmedt)_2]^{2-}$	2471.3	1.13	1.28	1.84	2474.8
$[Ni(bdt)_2]^{2-}$	2471.4	0.60	1.13	0.86	2474.8
$[Ni(CNedt)_2]^{2-}$	2471.2	1.15	0.94	1.37	2474.6
$[Ni(mnt)_2]^{2-}$	2471.3	1.15	0.97	1.40	2474.3
$[Ni(dtc)_2]$	2471.5	1.28	0.99	1.60	2474.9
$[Ni(ttctd)]^{2+}$	2472.6	1.29	0.97	1.59	2475.8

[a]pre-edge peak position; [b] pre-edge peak intensity; [c] half-max full width; [d] normalized, analytical pre-edge peak area; [e] estimated energy position of the edge inflection point; [f] average values are given from the three difference fits shown in Figure 13 that match the published pre-edge intensity in litteature.[27]

There is another considerable stepwise jump in both the pre-edge and the edge jump positions for the dithiocarbamate and the thioether ligand containing complexes.

The pre-edge peak intensities already indicate the amount of S → Ni charge donation as a result of covalent bond formation between the symmetry adapted linear combination of S 3p orbitals and the Ni 3d orbital(s). It is important to note that the peak areas are given as exact analytical areas and not as estimated values from the product of peak amplitude and full width, which is approximately 27% lower. The significant deviation in Ni-S bonding between the tetrahedral and square planar complexes is well represented by the large differences in pre-edge peak intensities. Tying the two thiolates together with a C-C bond in a constrained aliphatic ligand frame drastically increases the pre-edge intensity in $[Ni(nbdt)_2]^{2-}$ (1.28 eV) relative to $[Ni(SPh')_4]^{2-}$ (0.56 eV). Replacing the C-C link between the two adjacent sulfur donors in aliphatic dithiolates

with a shorter and more constrained C=C link in enedithiolates, further increases the pre-edge intensity to the highest value of 1.84 eV for $[Ni(dmedt)_2]^{2-}$ among the listed complexes in Table 2.2. As the peripheral methyl groups of the $[Ni(dmedt)_2]^{2-}$ are stepwise replaced by electron withdrawing cyanide substituents, the pre-edge intensity drops due to delocalization of the S 3p lone pairs into the olefinic conjugated system. Remarkably, this delocalization is also present for the aromatic dithiolate, but to a lesser extent as indicated by the modest change in the pre-edge intensity (0.86 eV) in the $[Ni(bdt)_2]^{2-}$ complex. As we approach the higher energy pre-edge features such those in $Ni(dtc)_2$ and $[Ni(ttctd)]^{2+}$ there are some notable peculiarities. For the former complex, we still see an intense pre-edge feature (1.60 eV) despite the non-ideal S-Ni-S angle (79°) for S lone pair and Ni $3d_{xy}$ overlap and the reduction of the formal oxidation state of the S absorbers. In going from the dtc^- to the ttctd ligand, the pre-edge intensity remains practically the same (1.59 eV), but the S effective nuclear charge is further reduced to formally a neutral S state. The thioether is a weak donor ligand; however, in the given ligand arrangements, the chelating angles (89.7°) are ideal for efficient Ni-SR_2 overlap and therefore S → Ni electron density shift results in covalent Ni-S bonds. The reversible, ligand-exchange thermochromic behavior of the $[Ni(ttctd)]^{2+}$ complex already hints that the covalency will be considerably reduced relative to the enedithiolate complexes, which do not show any thermochromic behavior. Overall, the above trends clearly indicate that the pre-edge intensity itself cannot be the measure of bond covalency when compared for various S-ligands.

In order to obtain S 3p orbital compositions of the Ni-S antibonding orbital from pre-edge intensities at the S K-edge, we need to determine the transition dipole integral or dipole moment for the S 1s → 3p excitation for all ligands and their complexes. From complementarity, this S 3p contribution reflects the S character of the Ni-S bonding orbital. This dipole integral, I (eV), can then be used to convert the normalized intensity (D_0, eV/absorber) to total intensity ($D_0 \times N$, where N is 4 as the number of S absorbers for the series of complexes from Table 2.3, and then to total S 3p character (average S 3p character or covalency × number of electron holes, $\alpha^2 \times h$) as defined by Equation 2.1 Note that the energy dimension of the intensity (D_0) and therefore the dipole integral is due to the integration of peak area defined by a linewidth in eV and dimensionless normalized peak amplitude. The total S 3p character can then be expressed as per-hole or per-bond covalency. The per-hole value has a theoretical maximum of 100%, which in reality cannot be more than about 80% for the given set of S ligands, since each ligand donor orbital may have non-negligible C and H contribution in addition to the Ni character of a given LUMO. Even in the case of an inverted bonding scheme as discussed in literature for enedithiolate ligands[36, 37] there will be about 20% Ni contribution to the LUMO. As discussed above, not all complexes in Table 2.3 with large pre-edge intensities (D_0) are expected to have inverted bonding pictures, and thus the S contributions will be below 50% as a result of the composition and structure of each S-ligand. In order to evaluate the difference between the S-ligands within the complex and their free, ionic forms we considered the S K-edge XAS spectra of a series of S-ligands (Figure 2.14).

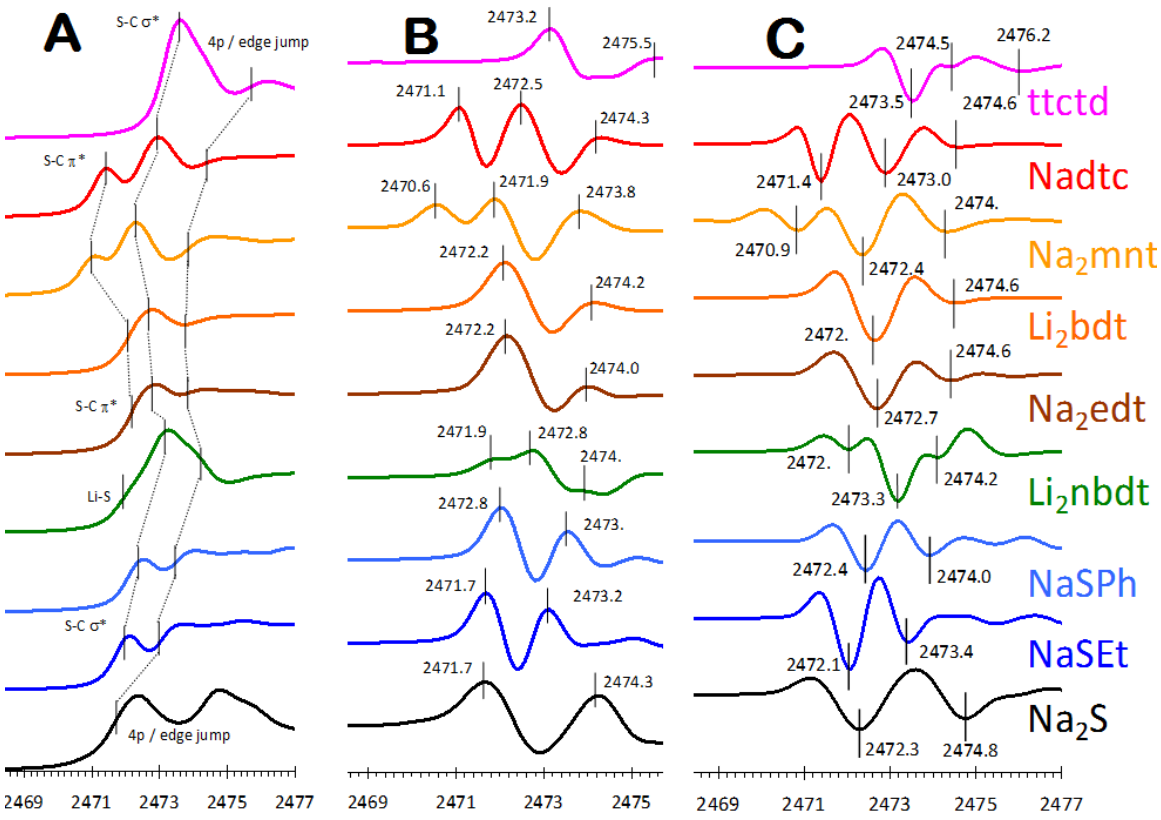

Figure 2.14: Comparison of S K-edge XANES spectra of S-ligands considered in this work. (nbdt = 1-2-norbornadithiolate, edt = ethylenedithiolatem, bdt = benzenedithiolate, mnt = maleonitriledithiolate, dtc = diethyldithiocarmabate, ttctd = (tetrathiacyclotetradecane) A) normalized data, B) 1st derivative spectra with inflection points in eV, C) 2nd derivative spectra with peak positions in eV

S K-edge XANES Analysis of S Ligands

We can separate the effects of ligand-based and coordination-based chemical shifts on the energy positions and intensities of spectroscopic features in Figure 2.12 by comparing the S K-edge spectra of S-ligands in Figure 2.14 The comprehensive set of ligands cover all three important sulfur oxidation states from formally S^{2-} in sulfide to S^{0} in thioether. The enedithiolates can be considered to have a formally S^{1-} charge, however due to conjugation the effective charge is less negative. Similarly, the formal

sulfur charge in the dithiocarbamate ion is $S^{-0.5}$, which is effectively closer to a neutral S(thioether) than to the anionic S(thiolate) due to the extensive delocalization of the out-of-plane π-system involving the lone-pair of the amine N. These qualitative considerations on the basis of valence bond theory are well reproduced by the changes in spectroscopic features as shown in Figure 2.14. With the exception of the two Li^+ salts, all complexes can be considered as in their free ionic form with minimal covalent interactions. Thus, trends in Figure 2.14 describe the ligand-based chemical shifts. It is relevant to the dipole integral discussion and important to point out that consideration of rising-edge features (first maximum of the first derivative spectra along the rising-edge) as the measure of Z_{eff}(S) does not give a chemically acceptable trend. This is due to the different origin (Li-S σ*, S-C σ*, S-C π*, S 4p) of the rising-edge features. The white lines of all S-ligands can be related to the excitation into C-S σ*-based orbital except for the sulfide ligand. However, the origin of the spectroscopic features at the lower energy side of the white lines varies depending on the presence of C-S π* orbitals (in enedithiolates and dithiocarbamate) or covalent interactions between the counter ion and the sulfur (in Li_2(nbdt) and Li_2(bdt) salts).

Figure 2.14 C compares the second derivative spectra that can be used to estimate the peak positions of each rising-edge feature if resolved. It is notable that with the exception of sulfide the feature corresponding to S 4p-based excitations can only be assigned ambiguously. Therefore, we define the energy position of the first inflection point after the last resolved C-S σ* feature to be the experimental measure of the Z_{eff}(S) seen by the S 1s core electron. From a practical peak fitting perspective, this is generally

the lower limit of an energy position where a step function is introduced that represents the ionization threshold or the edge jump. By mapping out the effect of Z_{eff}(S) on the S K-edge XANES features, we are in the position to define the influence of the coordination-based chemical shift for the comprehensive series of Ni(II) complexes.

Development of S 1s → 3p
Transition Dipole Integrals for S-Ligands

The first S 1s → 3p transition dipole integral was developed for the Cu(II) ion coordinated electron-transfer site of plastocyanin and a related model complex.[50] This was further confirmed by a very detailed and comprehensive spectroscopic evaluation of three variants of the Cu(II) site in stellacyanin.[53] The analytical peak intensity of 1.54 eV in Table 2.3 was calculated from the approximated peak intensity of 1.21 eV and applying a 1.27 conversion factor as a difference between the analytical integrated areas and the amplitude × full linewidth approximation. This pre-edge intensity was associated with about 45 ± 3% S 3p character. This agrees well with complementary Cu hyperfine coupling constant analysis from EPR and Cu L-edge spectroscopic features .[122] Notably, since the spectra were obtained for a metalloprotein with other S absorbers that do not contribute to the pre-edge feature, therefore the edge inflection point could not be determined.

The transition dipole integral for a more reduced form of sulfur was obtained from analysis of the pre-edge feature of the $CsFe(III)S_2$ salt with bridging sulfides. The analytical intensity of 3.12 eV corresponds to 42% S 3p character from XPS measurements as analyzed by VBCI model.[51] The corresponding 4p/edge inflection

points are at 2473.6 eV for the complex and 2471.7 eV for the free sulfide ligand. The S K-edge spectrum of the Na_2S salt has two intense features in the 2471–2475 eV region (bottom of Figure 2.14 A); however, the second intense feature can be explained by constructive interference of the scattered and backscattered ionized S 1s core electron (broad undulating EXAFS feature). In going from sulfide to the thiolate (bottom three spectra in Figure 2.14) the edge position is expected to shift toward higher energy due to the increase of the Z_{eff}(S) as the sulfur charge decreases. The sensitivity of the S K-edge technique to ligand-based chemical shifts is well demonstrated by the difference between an aliphatic and aromatic thiolates from the spectra of the NaSPh and NaSEt salts. Continuing to use independent experimental data from XAS measurements, we can define additional entries in Table 2.3. Analysis of ^{33}S and complementary metal hyperfine coupling constants from EPR/ENDOR/ESEEM measurements for the $[Ni(III)(bdt)_2]^-$,[123] $[Ni(III)(dmedt)_2]^-$,[40] $[Cu(II)(mnt)_2]^{2-}$,[31, 123-127] $[Ni(III)(mnt)_2]^-$,[31, 40, 41] and $[Cu(II)(dtc)_2]$ [128, 129] EPR and S K-edge XAS data defines additional transition dipole integrals as shown in Table 2.3. In addition to the above experimentally determined transition dipole integrals, we took into account two additional data points that can be considered as examples for the most oxidized S-ligands that can coordinate to a metal center.[130] These provide critical constraints in developing a ligand-based transition dipole relationship as they mark the upper limit for ligand-based XAS shifts. In Figure 2.14A, the coordination compound-based S 1s → 3p dipole integrals (I^C) are plotted as a function of the edge inflection points (E_0^c) of the complexes relative to that of the

Table 2.3 Comparison of experimental data (XPS or EPR) defining S 1s→3p transition dipole integral (I^C) for S-ligands bound to transition metal ions

Ligand	**Complex**	**D_0, eV[a]**	**N[b]**	**h, [c]**	**α^2, %**	**I^C, eV**	**E_0^C, eV[d]**	**E_0^L, eV [d]**
bridging sulfide	$[Fe(III)S_2]^-$	3.12	2	5	42	8.90	2473.6	2471.7
terminal thiolate	$[^{His}N_2Cu(II)S^{Cys}S^{Met}]^+$	1.54	1	1	45	10.3	n/a [e]	2473.6
olefinic enedithiolate	$[Ni(III)(dmedt)_2]^-$	0.539	4	1	59	13.9	2474.5	2474.1
aromatic enedithiolate (π)	$[Ni(III)(bdt)_2]^-$	0.799	4	1	74	13.0	2474.6	2474.3
conjugated enedithiolate(σ)	$[Cu(II)(mnt)_2]^{2-}$	0.801	4	1	54	17.8	2474.0	2473.8
conjugated enedithiolate(σ)	$[Ni(III)(mnt)_2]^-$	1.05	4	1	60	21.1	2474.4	2473.8
Dithiocarbamate	$[Cu(II)(dtc)_2]$	1.09	4	1	48	27.3	2474.4	2474.3

[a] normalized analytical peak intensity; [b] number of absorbers, [c] number of electron holes, [d] approximate energies of the edge jump inflection points for complexes (C) and ligands (L), [e] in stellacyanin metalloprotein, edge position from the coordinated thiolate is not resolved due to overlapping Cys and Met residues

Na_2S ligand salt (Figure 2.14A 2471.7 eV). Diamond symbols indicate considerable deviations from a linear trend, especially when the mnt^{2-} and the dtc^{-} complexes are considered. This non-linearity is unexpected on the basis of past literature of S K-edge XAS; however, it can be rationalized by considering the cumulative effects of the ligand-based and coordination-based chemical shifts in spectroscopic features due to change in Z_{eff}(S) as a function of Ni-S coordination in addition to differences in S oxidation states and C-S bonding. The ligand-based chemical shifts for the uncoordinated S-ligands are illustrated by the spectroscopic changes in Figure 2.14.

To further explore the relationship between I and Z_{eff}(S) as expressed by experimental edge positions, we need to separate out the effects of coordination-based chemical shifts. As the free ionic S-ligand coordinates to the metal complex, L → M electron donation takes place (hence the covalent M-S bonds) and the S-ligand becomes partially oxidized. The most affected part of the ligand will be the sulfur due to its direct bonding to a metal center and thus the Z_{eff}(S) will increase. Figure 2.15 B represents the illustration for connecting the coordination compound-based dipole integrals (I^C) with the relative edge positions of the uncoordinated S-ligands (E_0^L). The red vertical error bars represent the range for each ligand-based dipole integral (I^L) with the maximum values being I^C for a given ligand/complex. The blue diamonds mark the I^C values and corresponding edge inflection points for the coordination compounds(E_0^c).

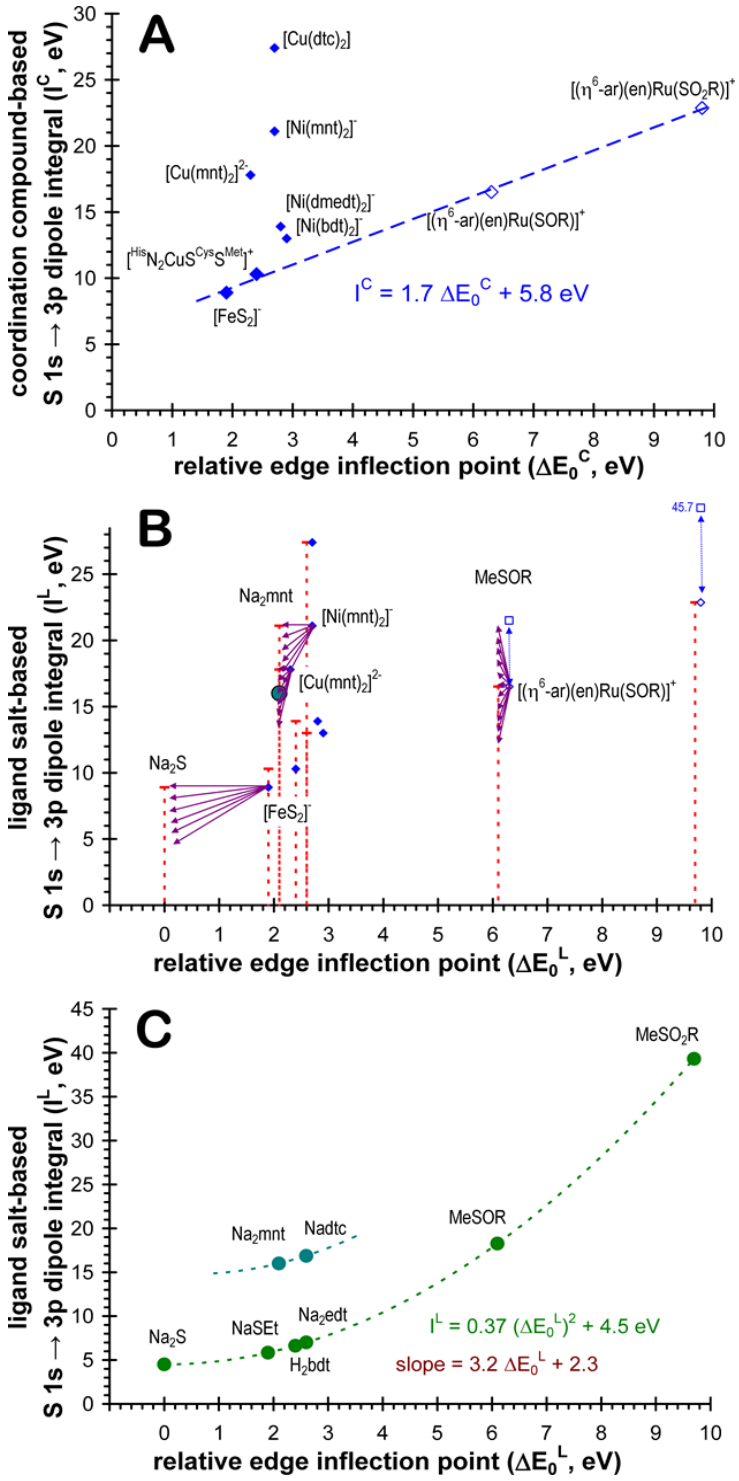

Figure 2.15 Correlation of edge positions relative to Na_2S edge-inflection point (2471.7 eV) and S 1s → 3p dipole integrals (A) ΔE_0^c versus I^c(B) graphical illustration of the development of ligand-based dipole integrals (C) ΔE_0^L versus I^L.

The purple arrows indicate the possible directions for going from the experimental, coordination compound-based (E_0^L, I^C) data points to the corresponding ligand-based (E_0^L, I^L) points. The slope of these arrows will be used later to define the change in the transition dipole integral (I^C–I^L) for a given coordination-based chemical shift (E_0^C, E_0^L). For the most oxidized MeSOR and $MeSO_2R$ ligands, the arrows also point toward greater I^L indicating that we will allow for deviation with positive and negative slopes. The hollow blue rectangles show that acceptable range for the dipole integrals as defined by electronic structure calculations.[130-132]

The experimental data for the $[Cu(II)(mnt)_2]^{2-}$ and $[Ni(III)(mnt)_2]^{-}$ complexes from Table 2.3 provide an opportunity to analytically determine a slope parameter, as introduced above, for taking into account the XAS chemical shift due to Ni-S bond formation. Using the energy difference between the edge positions for the ionic free ligand salt and the complexes, we can estimate a free ionic ligand-based dipole integral (I^L) for a hypothetical free mnt^{2-} ligand that is not involved in any covalent interaction. Equations 2.2a and 2.2b utilize a relationship between the coordination-based chemical shift (E_0^C, E_0^L) and the experimental I^C, such as $I^C = I^L + \text{slope} \times (E_0^C - E_0^L)$.

$$[Cu(II)(mnt)_2]^{2-} : 17.8\ \text{eV} = I^L(mnt)^{2-} + \sigma\text{-slope} \times (2474.0 - 2473.8\ \text{eV}) \qquad (2.2a)$$

$$Ni(III)(mnt)_2]^{2-} : 21.1\ \text{eV} = I^L(mnt)^{2-} + \sigma\text{-slope} \times (2474.4 - 2473.8\ \text{eV}) \qquad (2.2b)$$

Despite the expected difference between the σ and π M-L overlap, from the relative pre-edge intensities in $[Ni(III)(mnt)_2]^{-}$ we can approximate that the Ni(III) receives about the

same amount of electron density (~0.5 e^-/hole) from the S ligands for both π- and σ-holes. The 0.2 eV shift for the Cu(II) complex with a single electron hole in the d-manifold can be correlated with the 0.6 eV shift for the Ni(III) complex with three electron holes. The difference of Equations 2.2b and 2.2a becomes Equation 2.3:

$$16.5 = \sigma\text{-slope} + \pi\text{-slope} \quad (2.3)$$

From a comprehensive TDDFT study for a large set of complexes of the bdt^{2-} ligand,[73] a σ/π slope ratio was obtained to be 1.2. This would give a value of 16.0 eV for $I^L(mnt^{2-})$ (Figure 2.15B, teal dot). Variation of the σ/π slope ratio in the range of 0.5–2.0 would not affect the $I^L(mnt^{2-})$ by more than 0.7 eV (4%). Thus, we can consider the 16.0 ± 0.7 eV to be a reasonable estimate for the free ionic ligand-based S 1s → 3p transition dipole integral for the mnt^{2-} ligand. Due to the lack of the complementary XAS data for any other ligands considered here, this is the only point that marks the ligand-based Z_{eff}(S) as expressed by E_0^L and the corresponding free ionic ligand-based dipole integral for S 1s → 3p core excitation (I^L) that is known to date.

As mentioned above, the data for the ROS^- and RO_2S^- ligands[131, 132] provide a critical upper boundary condition for establishing a relationship between Z_{eff}(S) and the dipole integral. Another reference point for the lower boundary condition is the data for the Na_2S, which represents the most reduced form of a S-ligand. For the specific mathematical relationship for $I^L(E_0^L)$, we propose the use of a second order polynomial for considering the Z_{eff} dependence of the S 1s → 3p transition dipole integral, since we are using energy positions (E_0^C or E_0^L) as the measure of effective nuclear charge. According to the Bohr model[22] with the extension by Moseley[23] that considers electron shielding and use the concept of effective nuclear charge, both the donor core and

acceptor valence electron binding energies are proportional to Z_{eff}^2. This is actually not a novel idea, since similar relationships have already been discussed in literature for a series of first row transition metal K-edges.[133-136] Distortion from linearity can already be observed in the free ligand spectra of Figure 2.15, since as the Z_{eff}(S) increases, the highest energy, resolved bound state excitations overlapping with the ionization threshold. Using the relative energy scale (ΔE_0^L) and taking into account the reference Na_2S being the most reduced S-ligand, we constrained the second order relationship as shown in Equation 2.4

$$I^L = a(\Delta E_0^L)^2 + b(\Delta E_0^L)^2 + c \qquad (2.4)$$

to $b = 0$, which minimizes the ligand-based dipole integral at the sulfide. The maximum value for 'c' is the I^C for the $[FeS_2]^-$ (8.90 eV). In this case the slope parameter for sulfide would be zero (horizontal arrow in Figure 2.15B). The 'a' parameter in Equation 2.4 becomes constrained by the theoretical estimate[130] of the orbital composition of $[Ru(II)\text{-}SOR]^+$ and $[Ru(II)\text{-}SO_2R]^+$ complexes (hollow blue box symbols in Figure 2.15B). In order to extend the known slope parameter for mnt^{2-} ligand defined in Equation 2.3a and 2.3b to the entire series, we evaluated both second order and linear relationships and the data for the oxidized S-ligands ruled out the former. By simultaneously varying the 'a' and 'c' parameters from Equation 2.4, linking the intercept of the linear relationship between the relative edge inflection point and slope parameter to the slope value determined for the Na_2S ligand (lowest energy set of arrows in Figure 2.15 B) we developed a favorable set of parameters that satisfy all boundary

conditions considered above. The resulting uncoordinated S-ligand-based transition dipole integrals as a function of relative edge inflection point are plotted in Figure 2.15C.

There are two data points marked with teal dots in Figure 2.15C that are not on the green dashed lines. These correspond with ligands that contain N atoms, which are conjugated in both σ- and π-orbitals with the S donor orbitals. In both cases, greater fluorescence intensity is observed in XAS measurements than the corresponding unsubstituted hydrocarbon ligands and thus the $I^{L}(\Delta E_0^L)$ relationship needed to be shifted up by about 10 eV. This enhanced fluorescence signal is also expected for pre-edge features for Ni(II)/Cu(II) thiourea and thiohistidine complexes. In the chapter 3 of this dissertation, we plan to evaluate the cause of the excess fluorescence emission channels relative to corresponding unsubstituted ligands by resonant inelastic X-ray scattering at the ligand K-edge energy region.[137]

Experimental S 3p Contributions to the Ni-S Bonds in [Ni(II)S_4] Complexes

The estimated free ligand-based transition dipole integrals from Figure 2.15C can now be used to extrapolate to other ligands with unknown dipole integrals. The second order $I^{L}(E_0^L)$ relationship for the uncoordinated S-ligand provides an estimate for the transition dipole integral for the ligand without being involved in any covalent interaction. The linear slope $(E_0^C - E_0^L)$ relationship defines the change needed for extrapolating to I^{C} from I^{L}. Table 2.4 summarizes the list of parameters used to obtain the transition dipole integrals for the Ni complexes (I^{C}) from their corresponding free ligand value (I^{L}).

Table 2.4: Summary of parameters used to estimate coordination compound-based dipole integrals (I^C) for the studied [Ni(II)S_4] complexes

Complexes	E_0^L, eV [a]	I^L, eV	ΔE, eV [b]	slope [c]	I^C, eV	S 3p, %
$[Ni(SPh')_4]^{2-}$	2473.6	5.8	0.4[d]	13.9	11.4	30
$[Ni(nbdt)_2]^{2-}$	2473.1	5.2	1.0	8.6	13.8	56
$[Ni(dmedt)_2]^{2-}$	2474.1	6.6 [e]	0.7	20.7	21.2	52
$[Ni(bdt)_2]^{2-}$	2474.3	7.0	0.5	23.9	19.0	27
$[Ni(CNedt)_2]^{2-}$	2474.0 [f]	6.4	0.7	18.5	18.4	45
$[Ni(mnt)_2]^{2-}$	2473.8	16.0	0.5	16.4	24.2	35
$[Ni(dtc)_2]$	2474.3	16.9	0.6	23.9	31.2	31
$[Ni(ttctd)]^{2+}$	2475.5	9.8	0.3	48.5	24.4	39

[a] approximate S 1s ionization threshold from Figure 2.12B for the complex and Figure 2.14B for the ligand; [b] chemical shift from the edge inflection point between the coordinated and the free ionic S-ligand as a result of M-S bonding; [c] the slope values for Equation (4) are estimated from the minimal correction to reach the upper limit of dipole integral for a given or similar S-ligand (Figure 2.14c); [d] the chemical shift was determined from the free ligand salt shift in Figure 2.4; [f] the average edge inflection point of Na_2edt and Na_2mnt was used.

The error bar, or uncertainty range, of about 5–7% can be assumed for the dipole integral values due to uncertainties in data collection, normalization, and fitting. There are two exceptions to this as noted by footnotes 'd' to 'f' in Table 2.4. The comparison of free and coordinated aryl thiolate ligands posed a significant challenge as documented in Figure 2.4-2.5 and instead of using the edge-inflection points for the coordination-based chemical shift (1.5 eV) we considered the energy shift used to subtract the free-ligand spectrum from the complex's spectrum (0.4 eV). Furthermore, we did not have data for the corresponding free S-ligand of $[Ni(dmedt)_2]^{2-}$, $[Ni(CNedt)_2]^{2-}$; thus some straightforward approximations had to be made (see Table 2.4 footnotes).

Theoretical Electronic Structure
of $[Ni(II)S_4]$ Complexes Using DFT

A benefit of deriving ground state bonding descriptions from XAS measurements is the direct evaluation of theoretical orbital compositions from the popular density functional theory-based electronic structure calculations. Table 2.4 summarizes the functional dependence of the sulfur character in the LUMOs using a theoretically converged basis set and three population analysis methods. Despite some uncertainties in the ground state spin state for Cu(II) complexes as a function of density functionals,[61, 62] all calculation in Table 2.5 reproduced the ground spin state for the tetrahedral and square planar complexes to be S = 1 and 0, respectively (Table 2.5).

Table 2.5 DFT methods' ability to reproduce the ground spin state for tetrahedral and square planer complexes

S=1/0 gap, eV	GGA	hybrid GGA	metaGGA	hybrid metaGGA	Average
$[Ni(SPh')_4]^{2-}$	0.3	0.3-2.4	0.4-0.5	0.5-2.4	0.7±0.7
S=0/1 gap, eV					
$[Ni(nbdt)_2]^{2-}$	1.2-1.3	0.9-2.8	1.0-1.2	1.1-5.4	1.6±1.2
$[Ni(dmedt)_2]^{2-}$	1.0	0.3-1.0	0.8-1.0	1.0-0.3	0.9±0.2
$[Ni(bdt)_2]^{2-}$	1.1	0.3-1.1	1.0-1.1	1.0-4.1	1.1±0.8
$[Ni(mnt)_2]^{2-}$	0.8-0.9	0.8-2.5	0.8-0.9	0.8-2.6	1.1±0.7
$[Ni(dtc)_2]$	1.3	0.8-1.3	1.1-1.3	0.3-1.2	1.1±0.3
$[Ni(ttctd)]^{2+}$	1.6-1.7	1.0-3.8	1.1-1.6	1.2-1.4	1.6±0.6

It is also important to note that only the Mulliken (MPA) and Weinhold's natural (NPA) population analysis can give S 3p orbital compositions that are directly comparable to experiment, while Bader's atoms in molecules (AIM) method provides total sulfur atomic contributions. The role of the S 3s is negligible for these complexes, thus the results of the latter can be directly compared with the former methods. The range of calculated S contributions to the LUMO varies remarkably as a function of population

analysis method. Generally the MPA method gives the largest deviation from the more comparable NPA and AIM results. In the discussion below, we wish to mainly focus on the AIM results due to our past success in using this more advanced population analysis methods in describing electronic structure of Fe–S clusters.[117]

Table 2.6 Density functional and population analysis method dependence of the Ni-S bonding as expressed by total S contribution (%) to the LUMO for the studied [Ni(II)S_4] complexes (MPA = Mulliken, NPA = Weinhold's natural orbital, AIM = Bader's atoms-in-molecule methods)

	GGA[b]			hybrid GGA[c]			metaGGA[c]			hybrid metaGGA[d]			Overall[e]			I_{DFT}, eV
	MPA	NPA	AIM	MPA	NPA	AIM	MPA	NPA	AIM	MPA	NPA	AIM	MPA	NPA	AIM	AIM
$[Ni(SPh')_4]^{2-}$	26	36-37	33-32	10-26	4-35	22-30	24-25	33	30-48	21-22	23-25	16-26	22±5	28±9	28±9	11
$[Ni(nbdt)_2]^{2-}$	52-54	56-54	49-51	43-54	36-56	40-49	50-53	52-55	47-49	51-39	9-51	39-54	51±4	48±11	46±9	17
$[Ni(dmedt)_2]^{2-}$	58-59	58-59	52	42-58	39-59	40-52	55-57	55-57	48-50	42-57	52	40-48	53±6	55±5	49±8	23
$[Ni(bdt)_2]^{2-}$	57-59	58-59	51-52	51-57	57-49	46-52	56	57	50	56-91	43-63	48	60±11	64±5	50±5	10
$[Ni(mnt)_2]^{2-}$	49-72	52-53	46	41-49	14-52	38-46	46-48	48-51	44	38	12-39	37	49±9	36±17	43±6	26
$[Ni(dtc)_2]$	55-87	61	50-51	48-54	52-61	46-68	52-53	57-59	48-65	45-52	11-57	59-61	54±9	53±14	51±16	13
$[Ni(ttctd)]^{2+}$	52-53	60	49	46-52	42-60	44-49	47-51	55-58	45-47	40-48	11-55	40-45	49±3	53±12	46±5	21

[a] BLYP, BP86, mPW, OLYP, PBE, PW91; [b] B1LYP, BHandHLYP, mPW1PBE, MPWLYP1M, B3LYP, O3LYP, MPW1K, MPW3LYP; [c] M06L, TPSS, TPSSLYP1W; [d] M06, M06-2x, M06-HF, TPSSh functionals; [e] combined uncertainty due to the variation of sulfur orbital composition as a function of density functionals, population analysis method (total for AIM and S 3p for MPA and NPA) and uncertainty in H atomic positions of the crystal structures used

Discussion

With the given systematic study of [Ni(II)S_4] homoleptic coordination complexes we extended the series of classical S-ligands, such as thiolates, aliphatic dithiolates, and enedithiolates to some of the less reduced forms including conjugated dithiocarbamates and thioethers. The XAS data collection and data reduction at the sulfur K-edge are straightforward for these complexes. The pre-edge and rising-edge features can be readily assigned with little uncertainty especially given the possibility of comparing spectroscopic features for a broad series of uncoordinated ligands and their Ni(II) complexes. All square planar complexes can be characterized by intense pre-edge features except for the $[Ni(bdt)_2]^{2-}$ complex (0.9 eV), which is in between the pre-edge areas observed for the tetrahedral (0.5 eV) and square planar complexes (considerably greater than 1 eV). However, the conversion of the pre-edge intensities to actual orbital composition is not straightforward. Despite attempts to find a useful linear relationship between either the complex (E_0^C) or the ligand (E_0^L)-based transition dipole integrals we had to consider a second order relationship between the Z_{eff}(S) and the dipole integrals. We carried out this by using an experimental energy position (white-line position, rising-edge or edge-jump inflection point) for the measure of Z_{eff}, which is the function of Z_{eff}^2 as the experimental measure of sulfur effective nuclear charge. The non-linearity is further supported by the experimental observation (Figure 2.14) that as the sulfur effective nuclear charge increases; the core level excitations go up in energy to such an extent that they overlap with the ionization threshold of the core electron. We found that the first inflection point (E_0) of the XAS spectrum after the last resolved (S 1s → C-S σ*)

feature gives a reasonable experimental estimate for the Z_{eff}(S) in both the complexes and in the free ligands. This is well represented by the shifts of spectroscopic features of the S-ligand series in Figure 2.14 without the presence of significant metal–sulfur covalent bonding (except for the Li salts or protonated ligands). For the sulfide ligand the first intense feature along the rising edge will need to be considered as the measure of the Z_{eff}(S) due to the lack of S-C bonding. Using the currently available data from the literature, we can set up a parabolic relationship for the free ionic ligand-based S 1s → 3p transition dipole integrals as a function of edge position of the S-ligand salt (E_0^L). This relationship was obtained from converting the EPR and XPS-based transition dipole integrals (I^C at E_0^C, Table 2.3) for various M-S complexes to corresponding free ionic S-ligand-based integrals (I^L at E_0^L, Figure 2.15C) by estimating the coordination-based chemical shift in the Z_{eff}(S) due to the formation of the M-S bonds. Considering various boundary conditions obtained from the S K-edge spectra of sulfide, sulfinate, and sulfonate ligands and their complexes as examples for the most reduced and most oxidized S-ligands, we developed a linear relationship to convert the coordination-based chemical shift to a correction of ligand-based integrals to obtain complex-based integrals.

As described earlier,[27] the tetrathiolatonickel(II) complex can be regarded as classical coordination compound in which the partially occupied orbitals and thus the M-L bond are dominantly metal-based. Therefore, any redox chemistry will primarily affect the metal. The previous interpretation of XAS data using the uncorrected I^C(Cu-SEt) dipole integral gave 33% S character for each of the LUMOs, which we estimate to be somewhat less (30%). However, in going from terminal thiolates in tetrahedral

coordination environment to covalently linked thiolates in the square planar $[Ni(nbdt)_2]^{2-}$ complex the pre-edge intensities go up from 0.56 to 1.28 eV (Table 2.4). Even with the increased dipole moment (I^C from Table 2.4) from 12.2 to 15.0 eV, the S 3p contribution goes up in the square planar complex to be more than 50%. This is an indication of inverted bonding, where the LUMOs become S-based and as a result, the electrophilic site shifts from the Ni to the S atoms. In a valence bond/ionic limit description, the formally Ni(II) center is effectively reduced to Ni(0) and the formally RS_2^{2-} ligands become radicalized anions ($RS_2^{\bullet -}$). This is a similar description to the dianionic, olefinic enedithiolate complex.[37] Our experimental S 3p values for the $[Ni(nbdt)_2]^{2-}$ and $[Ni(dmedt)_2]^{2-}$complexes are practically identical. This suggests that by covalently linking two donor atoms in 1,2 position either by a strained ligand system (as in $nbdt^{2-}$) or with a double bond (as in $dmedt^{2-}$) the S ↔ S repulsion within and in between the ligands can destabilize in energy the S-based donor orbitals above the acceptor metal d-orbital and thus trigger intramolecular electron-transfer. The latter is well facilitated by the efficient Ni-S overlap in the square planar complex relative to that in a tetrahedral complex. Using the saturated def2-TZVP basis set with respect to LUMO composition, the overlap integral as calculated from the product of overlap and density matrices drops from 0.086 to 0.006 per Ni-S bond in going from square planar to tetrahedral complexes. This is dominantly due to the 0.1 Å elongation of the Ni-S bonds in the latter in addition to the non-ideal alignments of the S donor and vacant Ni 3d orbitals.

Considering the $[Ni(dmedt)_2]^{2-}$ complex as a starting point for the series of enedithiolate complexes shown in Table 2.4, we can describe a chemically meaningful trend about Ni-S σ-bonding on the basis of experimental S covalency from XAS. The LUMO in the $[Ni(dmedt)_2]^{2-}$ complex has about 52% S 3p character, which corresponds to inverted bonding. Substituting one of the methyl groups in $dmedt^{2-}$ with a nitrile group as in $CNedt^{2-}$ the S contributions drops to about 45%. The second substitution leading to the mnt^{2-} ligand further drops the S character to 35%. This trend continues for the $[Ni(bdt)_2]^{2-}$ complex. This series nicely demonstrates the importance of correcting the transition dipole integral due to the large variation in Z_{eff}(S) between various S-ligands and furthermore the smaller adjustment as a result of metal coordination.

Keeping this in mind, it is then not surprising that for the $[Ni(bdt)_2]^{2-}$ complex we obtain such low S 3p values of about 27%. The EPR data used for the transition dipole integral and the free bdt^{2-} ligand salt define a exceptionally high S contribution (74%) for the out-of-plane π-orbital.[138] The corresponding S K-edge feature[73] has an intensity of 0.801 eV, while the adjacent feature from the in-plane σ-orbital with two electron holes has only 1.09 eV. Thus, the latter corresponds to about 0.545 eV intensity per electron hole, which is about 40% overall reduction of S covalency per hole. Even without a correction to the dipole integral for σ- *versus* σ + π-bonding the expected S character for the Ni(III) complex in the σ-hole is about 44%. The missing 17% S character from our estimated value for the Ni(II) complex is likely due to the use of the already covalent Li^+ salt of the bdt^{2-} free ligand. The protonated H_2bdt XAS data gives an even larger

deviation from the expected S character due to the higher energy position of the edge jump for the free ligand spectrum (Figure 2.16).

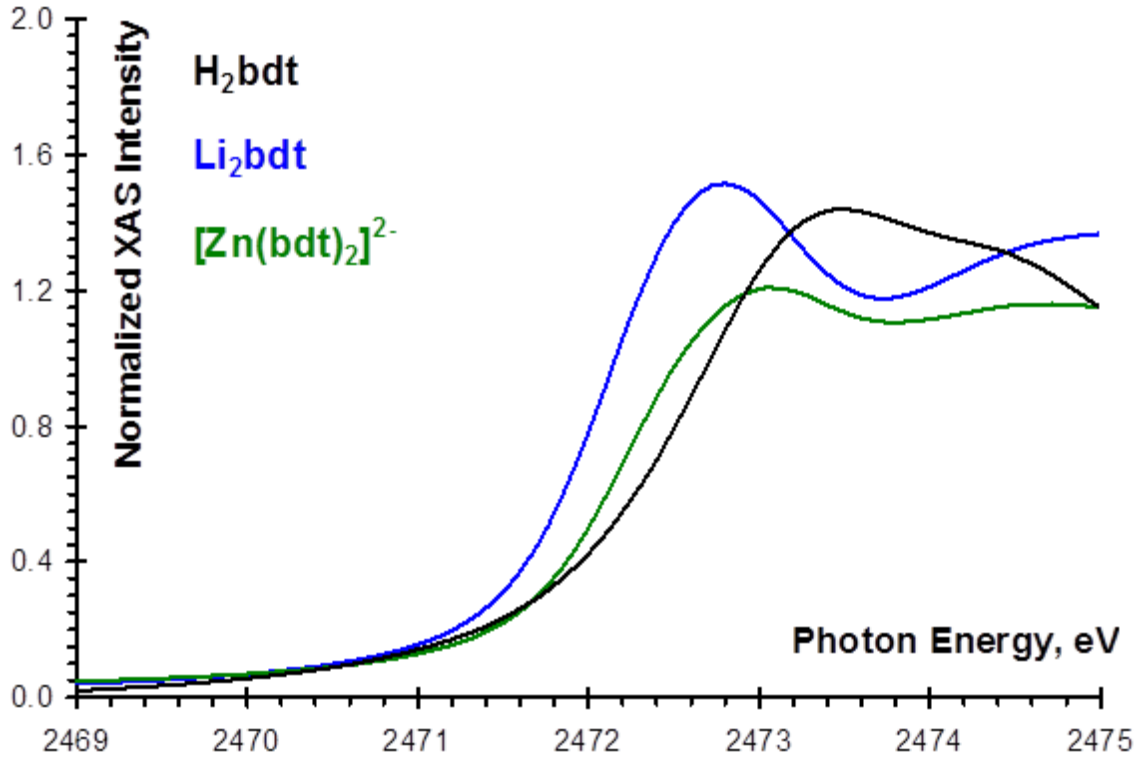

Figure 2.16 Data illustrating the covalent nature of the Li^+ salt and protonated H_2bdt ligand.

The dithiocarbamate and the thioether ligands, as the two least reduced S-ligands of the studied series, showed the most surprising S 3p characters for the experimentally probed LUMOs. The dtc^- ligand is particularly interesting with respect of the entire S-ligand series, since the intraligand S ↔ S repulsion is reduced by removing one electron relative to the dithiolate ligands despite the reduced S···S distance. Furthermore, from electronic structure calculations using the saturated def2-TZVP basis set, we found that in going from a 2.18 Å Ni-S bond length to 2.20 Å, as in $[Ni(dtme)_2]^{2-}$ relative to $[Ni(dtc)_2]$,

the Ni-S orbital overlap decreases by 3% per sulfur atom; while moving the sulfur atoms off axis by about 10° also decreased the overlap by about 4% per sulfur atom. As a consequence, while the [$Cu(dtc)_2$] complex in Table 2.3 was characterized by covalent bonding of about 48% S in the paramagnetic SUMO from EPR, the estimates for the [$Ni(dtc)_2$] complex from XAS is 31% (Table 2.4) despite the more intense pre-edge features (1.09 *versus* 1.60 eV, respectively). This is due to the non-linearity of the transition dipole integral as it considerably increases relative to the thiolates and enedithiolates. From Table 2.4, the I^C values for Cu(II) complex with thiolate, enedithiolate, and dithiocarbamate changes from 10.3, 17.8, to 27.4 eV, respectively. Due to the opening of the additional electron hole in the Ni(II) complex relative to the Cu(II), the energy of the edge position shifts up by 0.5 eV or 0.6 eV relative to the Cu(II) complex and the free ligand, respectively. These chemical shifts with a σ-slope value of about 24 from Table 2.4 give an I^C value that is above 30 eV, which defines about 31% S 3p character in the LUMO. The difference between the above two complexes suggests that we need to expect considerable bonding differences between the dithiocarbamate-coordinated Cu(II) and Ni(II) complexes, where Cu(II) has an inverted bonding, while Ni(II) displays classical coordination chemistry. By extending the series with additional metal complexes, such as Zn(II), Fe(II)/Fe(III), Mo(IV), we are currently investigating a broad family of dtc complexes.[129]

Equally interesting is the case of the Ni(II)-thioether complex. Compositionally it is a unique Ni(II) coordination compound, since normally thioether does not coordinate to late transition metals. This is due to the limited nucleophilicity of the S centers despite

the availability of S lone pair for coordination, which also means that the ionic interactions between the Ni(II) and the S centers were diminished relative to the anionic ligands. However, the ideal geometry of the tetrathiocrownether (ttctd) allowing for 90° S-Ni-S bite angles and the vicinity of the four sulfur donors allow for the formation of the Ni(II) complex. The Ni-S overlap is efficient as also witnessed by the strong color of the $[Ni(ttctd)]^{2+}$ complex due to the presence of a S → Ni charge transfer band with molar extinction coefficient of 370 $dm^3\ mol^{-1}\ cm^{-1}$ in GBL.[3] As mentioned in the introduction, this complex displays ligand-exchange-based thermochromic behavior in the 25–125 °C range. The estimated ΔH_{rxn} of 60 kJ mol^{-1} for the ligand-exchange reaction (Eqation 1.3) suggests that the Ni-S bond is only moderately covalent and has limited ionic character. Otherwise the reversible ligand-exchange thermochromism would not take place for $[Ni(II)(ttctd)]^{2+}$ as can be observed for all the enedithiolates, for example. This means that the experimental value of about 39% is a reasonable number for the S 3p character of the Ni-S bonds. This is actually a considerable electron donation from a neutral S-ligand to the Ni(II) in comparison to the similar S 3p values for the anionic tetrahedral tetrathiolate complex.

Without going into specific details for the performance of each and every density functional, we found that the previously described[55, 59, 60] transferability of a specific hybrid functional does not hold for $[Ni(II)S_4]$ complexes. The most peculiar finding is that all square planar $[Ni(II)S_4]$ complexes were described by a greatly covalent Ni-S bonding with close to 50% S character. While these values are reasonable for the enedithiolates and even the constrained 1,2-dithiolate ligands, it certainly deviates

considerably even from the upper limit of XAS values for the dtc^{-} and the ttctd complexes. As mentioned above, we need to be cautious with directly comparing the experimental and the computational results, since all computational models were only embedded in an isotropic polarizable continuum model and none included the potentially critical fine tuning effect of counter ions and adjacent molecules from the crystal packing environment. The systematic evaluation of these effects and the limitations of linear response theory-based TDDFT calculations are being investigated.

In conclusion, despite some uncertainties of employing quantitative XANES analysis for the S K-edge spectra of a spectrochemical series for $[Ni(II)S_4]$ complexes, we can still consider the experimental determination of the composition of unoccupied frontier orbitals from pre-edge and rising-edge features to be a very powerful approach that is worthwhile to continue developing. The current limitations of this approach come from the lack of complementary data sets for comparison and critical assessment of the data dependence of detection method and detector instrument, sample preparation and thickness, and data normalization procedures. Furthermore, the spectroscopists need to be critical in evaluating the peak fitting procedure since it can have a dramatic influence on the resulting covalency parameters. The computed electronic structures from the popular density functional theory showed serious discrepancies among each other as well as to the experimental XAS data. Therefore, one should not rely too heavily on any one functional or population analysis model. It is beyond any doubt that complementary experimental techniques and internal checks are needed for XAS data to obtain a reasonable experimental description of metal–ligand bond covalency.

The already available XAS and EPR data allow for a yet to be explored phenomena between the composition of the ligands and the magnitude of transition dipole integral. The notably higher transition dipole integrals in Table 2.4 and Figure 2.15C (teal dots) correspond with ligands that contain N substituents electronically interacting with the sulfur centers. The intensity enhancement of spectroscopic features by a heteroatom is the subject of our future XAS and RIXS studies.

Using the available experimental data we can classify the series of [Ni(II)S_4] homoleptic complexes into three categories. The tetrahedral tetrathiolate complex can be described with classical coordination chemical bonding description with the lowest unoccupied frontier orbitals being metal based. Constraining two negatively charged thiolates either by a ring system ($nbdt^{2-}$) or double bonds ($dmedt^{2-}$) induces inverted bonding description, where each ligand donates more than 0.5 electron per electron hole to the metal and thus effectively reduces the metal. In these dianionic complexes, the formal divalent metal is better described by a zero-valent metal that is stabilized by covalent and/or L-M-L superexchange interactions. The substitution of the enedithiolate ligand framework with strongly electron withdrawing groups, such as in $CNedt^{2-}$, mnt^{2-}, or bdt^{2-}, attenuates the S → Ni electron donation. The most unexpected finding is related to the two less reduced S-ligands, since despite their intense pre-edge features, they are best described by a covalent, but still normal bonding scenario. This is chemically quite reasonable, since in the [Ni(II)dtc_2] complex the vicinity of the two S donors, the difference in donor ability of the 1,1-dithiocarbamate *versus* a 1,2-dithiolate, and the reduced charge per S donor cannot allow for the same efficient ligand-to-metal electron

donation as in the enedithiolate complexes. Furthermore, the formation of the Ni(II) complex with the cyclic tetrathioether ligand is mainly possible due to the ideal S-Ni overlap despite the considerably reduced nucleophilicity of the S centers and the availability of a single S lone pair for Ni-S bond formation with only a modest ionic character.

CHAPTER THREE

ELECTRONIC STRUCTURE OF Ni(II), Co(II), AND Zn(II) THIOUREA COMPLEXES FROM SULFUR K-EDGE X-RAY ABSORPTION SPECTROSCOPY

Contributions of Authors and Co-Authors

Manuscript in Chapter 3

Author: Matt S. Queen

Contributions: Collected and worked up XAS data, carried out and analyzed DFT calculations.

Co-author: Farideh Jalilehvand

Contributions: Synthesized and purified thiourea coordination complexes

Co-author: Robert K. Szilagyi

Contributions: Assisted with the design and execution of the experiment and theoretical calculations. Discussed the results and edited the manuscript at all stages.

Manuscript Information Page

Authors: Matt S. Queen, Farideh Jalilehvand, Robert K. Szilagyi

Journal: Canadian Journal of Chemistry

Status of the manuscript:

_X_ Prepared for submission to a peer-reviewed journal
___ Officially submitted to a peer-reviewed journal
___ Accepted by a peer-reviewed journal
___ Published in a peer-reviewed journal

Publisher: NRC Research Press

CHAPTER THREE

ELECTRONIC STRUCTURE OF Ni(II), Co(II), AND Zn(II) THIOUREA COMPLEXES FROM SULFUR K-EDGE X-RAY ABSORPTION SPECTROSCOPY

Introduction

Thiourea (TU), as a ligand in coordination complexes, is notable due to both σ donor and π acid characters. The formally sp^2 hybridized thiocarbonyl group is not considered as a good donor, yet TU forms well-defined complexes with zinc(II), nickel(II), and cobalt(II). In $[Ni(TU)_6]^{2+}$, TU coordinates via sulfur lone pairs in σ interactions forming a close-to-octahedral ligand environment around the nickel(II). In the $[Co(TU)_4]^{2+}$ and $[Zn(TU)_4]^{2+}$ complexes, there is pseudo-σ/π donation of the sulfur lone pair forming distorted tetrahedral complexes. The thiocarbonyl coordination and corresponding ground state electronic structure of the nickel complex were previously investigated[139-141] using infrared spectroscopy. These studies showed that N-H symmetric and asymmetric stretching modes as well as the N-C-N bending modes were shifted to higher energy in coordinated TU relative to the free ligand. These blue shifts in IR spectra were attributed to an increase in the double bond character between the nitrogen and carbon upon TU binding to nickel, which translates to a shift from a thiocarbonyl to more thiolate like bonding (Scheme 1). In this study, we used sulfur K-edge X-ray absorption spectroscopy (S K-XAS) to directly evaluate the ground state electronic structure of free TU ligand and its complexes with zinc(II), nickel(II) and cobalt(II). In

addition, density functional theory-based (DFT) electronic structure calculations were carried out to aid the spectral assignments and interpretation of data.

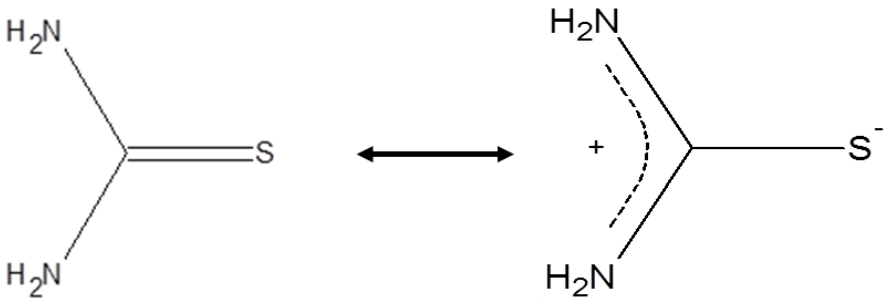

Scheme 1.

S K-XAS is an experimental technique used to evaluate M-S(ligand) bonding.[24] Tender X-ray radiation in the 2430-2700 eV energy range is used to excite sulfur 1s core electrons either into unoccupied sulfur 3p/4p-based molecular orbitals or to ionize the electrons into the continuum. Ionization gives rise to an edge jump feature, which is often superimposed with the highest detectable, bound-state excitations involving sulfur 4p orbitals. The X-ray photons with energy below the sulfur 1s ionization threshold give rise to intense, dipole-allowed excitations into unoccupied M-S(ligand) antibonding (pre-edge), and S-C antibonding (rising-edge) orbitals of the ligand. These transitions increase in intensity proportional to the sulfur 3p atomic orbital character present in an experimentally probed molecular orbital. The proportionality between pre-edge intensity and sulfur 3p orbital character can be expressed by the dipole expression[47]

$$D_0 = \frac{1}{3}\frac{h}{N} \propto^2 I(\text{S 1s} \rightarrow \text{3p}) \qquad (3.1)$$

where D_0 is the integrated normalized pre-edge intensity (eV), *h* is the number of electron holes probed, *N* is the number of sulfur absorbers per molecule, and the 1/3 factor is due to the angular dependence of the dipole integral. The term *I*(S 1s→3p) was termed as transition dipole integral[50] (eV),and α^2 (%S hole^{-1}) is the sulfur 3p atomic orbital character present in a molecular orbital per electron hole. In *Eq.(3.1), I*(S 1s→3p) takes the role of an empirical proportionality constant between the experimental peak intensity and orbital composition, therefore it needs to be experimentally determined for the sulfur absorbers in a given complex. In a recent work, as summarized in the previous chapter we outlined a general method for deriving transition dipole integral values experimentally using the concept of free ligand based dipole integrals.[142] The dipole integral has been historically related to the effective nuclear charge of the sulfur absorber seen by the 1s core orbital (Z_{eff}(S)).[48] The measure of Z_{eff}(S) in the free ligand, or in its complexed form, is the energy position of the S 1s→4p/edge jump feature. We established a second order relationship between the rising-edge inflection point or Z_{eff}(S) and the free ligand dipole integral (I^L) (Figure 2.15). At this point, the latter is only a theoretical value, since in the free ligand or ligand salt all possible orbitals that can be involved in metal-ligand bonding are doubly occupied and thus no excitation is possible into the valence 3p level. Further studies of S-based radical species may allow for assigning physical picture to I^L.[143] The shift of the 4p/edge energy position between the free and the coordinated ligand can be used to estimate the transition dipole integral for the complex (I^C). The mathematical relationships for I^L and the correction in going from I^L to I^C as a function of Z_{eff} (using

the relative edge inflection point to the Na_2S spectrum) are shown in Eqs. 1 and 3 in Figure 3.1.

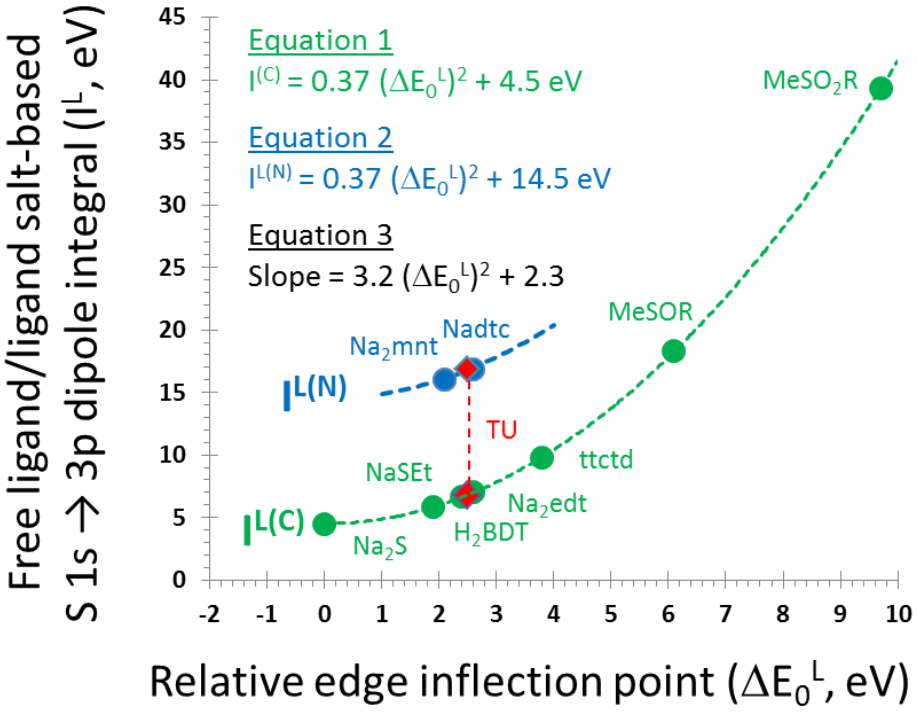

Figure 3.1 Correlation of edge positions relative to Na_2S edge-inflection point (2471.7 eV) and the S 1s→3p dipole integrals ($\Delta \mathbf{E_L^0}$versus $\mathbf{I^L}$)

It is important to emphasize that there is a need for a second (blue) relationship between $I^{L(N)}$ and $\Delta \mathbf{E_L^0}$ in Figure 3.1 that connects data points for sodium maleonitrile (Na_2mnt) and sodium dithiocarbamate (Nadtc) complexes. This emerged from the comparison of EPR and XAS investigations of the S 3p orbital character of complexes with ligands containing nitrogen. A plausible physical explanation of the above empirical relationships is the enhanced fluorescence or Auger electron yields due to the presence of extensive N-based conjugation in comparison to the hydrocarbon based ligands $I^{L(C)}$ (green curve).

The TU ligand with its conjugated nitrogen atoms offers an independent way to further investigate the need for multiple empirical relationships (green and blue lines in Figure 3.1) connecting the $I^{L(C)}/I^{L(N)}$ to I^{C} dipole integrals through $Z_{eff}(S)$.

In general, the S K-XAS derived experimental S 3p character can be directly correlated with orbital compositions from density functional theory (DFT) calculations. We have found in our earlier systematic DFT study that it generally overestimates the sulfur character in nitrogen containing sulfur ligands bound to metals resulting in an overly covalent M-S bonding picture.[142] This is expected for generalized gradient approximation (GGA) functionals; however, it is often less severe for most hybrid functionals that mix Hartree-Fock ionic exchange with covalent density functional exchange.[144] In this study we use a set of popular GGA, hybrid GGA, and metaGGA density functionals to evaluate their accuracy with respect to the S K-XAS results.

Materials and Methods

Preparation of Compounds

Samples were prepared according to established procedures[141] in the collaborator's laboratory (Prof. Farideh Jalilehvand, Department of Chemistry, University of Calgary, Calgary, Alberta, Canada)

X-ray Absorption Measurements

The S K-edge spectra for all complexes and the free TU ligand were measured at Stanford Synchrotron Radiation Lightsource, beamline 4-3 under storage ring (SPEAR 3) conditions of 500 mA current in top-off mode and 3GeV energy. Beamline 4-3 is a 20-

pole, 2.0 T Wiggler beamline, equipped with a liquid N_2 cooled Si(111) double-crystal monochromator. The beamline was optimized at 2740 eV using $Na_2S_2O_3 \cdot 5H_2O$ as calibrant with a maximum pre-edge feature at 2472.02 eV. Sulfur K-edge spectra were collected in the energy range of 2450 – 2740 eV using an unfocused beam, in a He-purged beam path, at room temperature, using a Passivated Implanted Planar Silicon (PIPS) fluorescence detector (CANBERRA). Solid samples were prepared in a glove box and diluted in boron nitride to minimize self-absorption. After repeated grinding, they were thinly pasted onto a sulfur-free Kapton tape. While these samples are not extremely air sensitive, they were protected from oxidation and moisture during sample mounting by a thin polypropylene window.

Data Normalization

Both free ligand and complex data were background subtracted and normalized using the Automated Data Reduction Protocol developed by D. Gardenghi.[76]

Data Fitting

The normalized S K-edge spectra were fit using Peak Fit v4.12 (SeaSolve) to obtain pre-edge peak intensities (A), energy positions (E_0), and linewidths (lw). All transitions were fit with a "Gaussian+Lorentzian Amplitude" function as shown in Eq. 3.2.

$$D_0 = A\left[\frac{\frac{(G:L)\sqrt{ln2}}{lw\sqrt{\pi}}e^{\left(-4ln2\left(\frac{E-E_0}{lw}\right)^2\right)}+\frac{1-(G:L)}{\pi lw\left[1+4\left(\frac{E-E_0}{lw}\right)^2\right]}}{\frac{(G:L)\sqrt{ln2}}{lw\sqrt{\pi}}+\frac{1-(G:L)}{\pi lw}}\right] \tag{3.2}$$

The Gaussian/Lorentzian ratio (G:L) was setting to 0.5 for individual excitations, which corresponds to a pseudo-Voigt line shape. All transition envelopes were fit using the same type of function with shared line widths and G:L mixing ratios. The edge jump was fit with an "Ascending Lorentzian Cumulative" arctangent function

$$D = \frac{A}{\pi}\left[tan^{-1}\left(\frac{E - E_0}{lw}\right) + \frac{\pi}{2}\right] \tag{3.3}$$

where A is the amplitude, E_0 is the energy position, and lw is the width of the step function. Fits were obtained stepwise by allowing for the linewidths, amplitudes, and lastly the energy positions to be varied. The final fits were obtained by relaxing all fit parameters except the Gaussian/Lorentzian mixing ratio.

In order to obtain reasonable error bars for fitting, the $[Ni(TU)_6]^{2+}$ and $[Co(TU)_4]^{2+}$ data were also fit using the free TU and $[Zn(TU)_4]^{2+}$ spectra, respectively. Fits to the spectra of the free ligand and zinc complex were converted into a user-defined functions (UDFs) in order to account for S-C σ*, π*, 4p and edge jump features in the $[Co(TU)_4]^{2+}$ and $[Ni(TU)_6]^{2+}$ spectra. For these fits, only the peak positions and amplitudes of the UDFs were optimized. Furthermore, an additional set of fits were guided by the IR study of the $[Ni(TU)_6]^{2+}$ complex[141] with regards of change in the valence bond picture of TU upon coordination to nickel(II). We performed a series of fits varying the ratio of the S-C π* to S-C σ* areas from 0.2 to 0.4 with at most 4% variation in the pre-edge intensity, which translate to a negligible contribution to S 3p orbital characters.

Electronic Structure Calculations and Vibrational Analysis Electronic structure calculations of free thiourea, $[Co(TU)_4]^{2+}$, $[Zn(TU)_4]^{2+}$, and $[Ni(TU)_6]^{2+}$ complexes were performed using Gaussian09 quantum chemical package[77] to determine the metal and ligand orbital characters of the frontier molecular orbitals. Since the complexes are charged, we carried out all calculations using the polarizable continuum model (PCM)[78, 82, 83, 145] with solvent parameters for acetonitrile ($\varepsilon = 35.5$) to avoid artifacts due to *in vacuo* modeling, PCM(CH_3CN). Crystal structures of all complexes[146-149] were used without structural optimization for electronic structure analysis. In all crystal structures the positions of the H atoms were also refined experimentally. BP86[56, 92], B3LYP [91, 102] and TPSS[99] exchange and correlation functionals were chosen as representative examples for the GGA, hybrid GGA, and metaGGA rungs for Perdew's ladder of functionals, respectively[89, 90].We chose the def2-TZVP[111] basis set from the EMSL Gaussian Basis Set Exchange[112, 150] that has been shown to be saturated with respect of electronic structure for Ni(II) complexes.[151] The theoretical sulfur 3p orbital composition of the unoccupied frontier orbitals corresponding to the M-S bonds were obtained from Bader's 'Atoms-in-Molecule' (AIM) population analysis[114-116] using the AIMAll program.[118] Specific atomic orbital contributions to the total atomic orbital character were solved for using Weinholds's natural population analysis (NPA)[120] as implemented in Gaussian09.

To be conceptually correct with respect to the theoretical IR spectra, crystal structure geometries were optimized using the BP86 functional and def2-TZVP basis set in the acetonitrile PCM environment (BP86/def2TZVP/PCM(CH_3CN)). Frequency calculations were performed on the stationary geometries to obtain theoretical IR spectra.

Results and Analysis

In order to extract experimental orbital compositions from S K-XANES pre-edge and rising-edge features, we first assigned the spectral features and the edge jump position for the free TU ligand and its Ni and Co complexes. This allowed for the estimation of transition dipole integrals for the free (I^L) and the coordinated ligands (I^C) in the complexes as described in the introduction for Figure 3.1. The fitting of the pre-edge and rising-edge spectral features results in normalized pre-edge peak intensities (D_0). Lastly *Eq.(3.1)* provides the S 3p contribution (α^2) to the covalent bonding in TU complexes.

Free Ligand Transition Dipole Integral (I^L) for sulfur atom in TU

The XANES region of the S K-edge spectra for thiourea is compared to sodium dithiocarbamate (Nadtc) and tetrathiocyclotetradecane (ttctd) in Figure 3.2 A along with the first (Figure 3.2 B) and second derivative spectra (Figure 3.2 C).

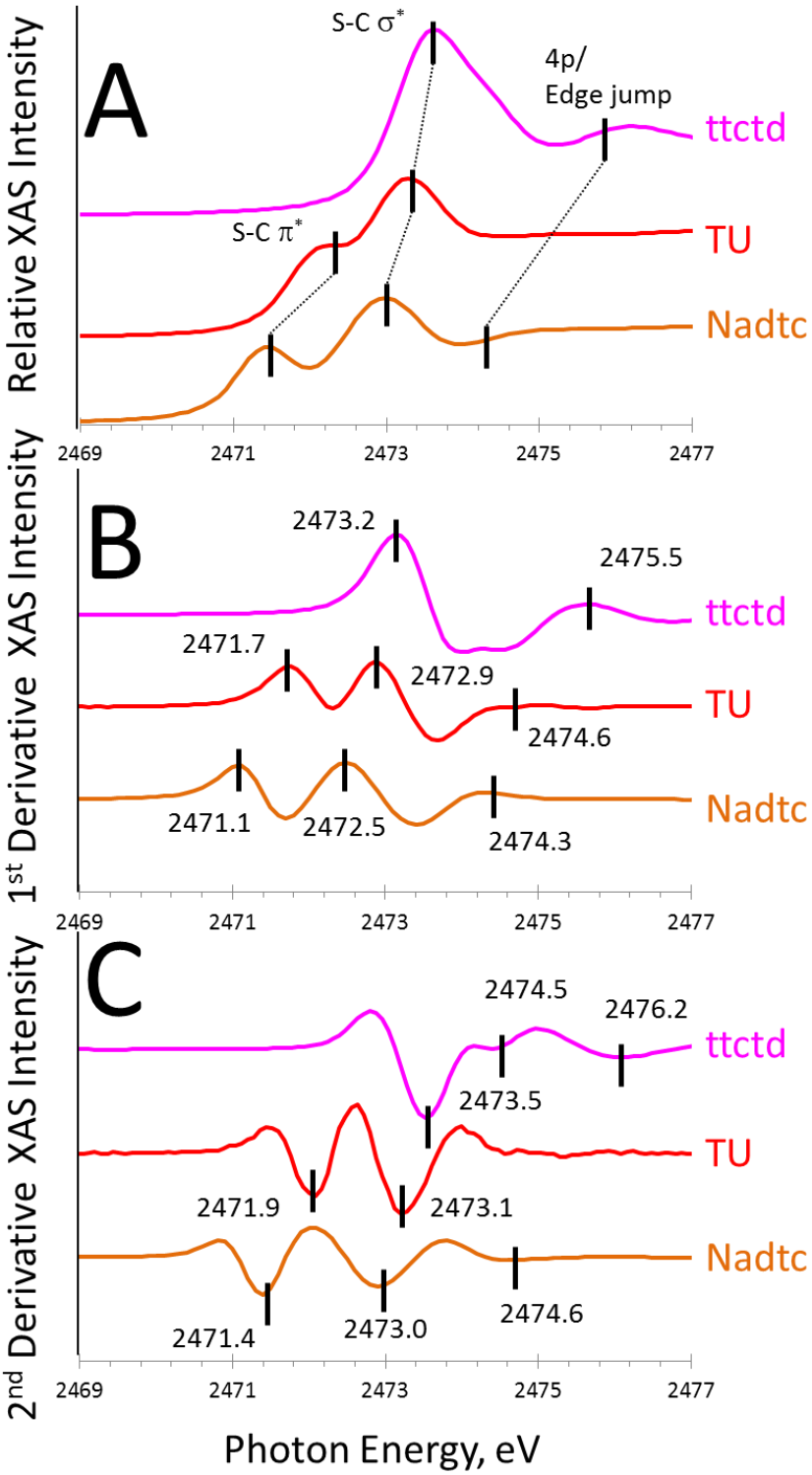

Figure 3.2 XANES spectra of the free ligands along with the first (B) and second (C) derivatives. All resolved peaks are marked based on the first and second derivative maximum and minimum positions, respectively.

At the rising edge region between 2474 and 2476 eV, there is a monotonous shift in sulfur 4p/edge jump energy position in the order Na(dtc) (2474.3 eV), TU (2474.6 eV), and then ttctd (2475.5 eV). Normally, the 4p/edge jump energy position would be assigned to the maximum of the first derivative after the last resolved feature;[142] however, the different chemical bonding for the three free ligands prevents this. Using the trend of the other two ligands (and an entire series from Reference 6) the edge transition is assigned for the first inflection point after the last resolved rising-edge feature/white line at 2474.6±0.5 eV. The error in the edge measurement is due to the limited resolution in the 4p/edge jump feature. Using a molecular orbital description of the free ligand the 1s→C-S π*, 1s→C-S σ* transitions can be assigned as indicated in Figure 3.2 A.

The second order relationship between $I^{L(N)}$ and edge position ($\Delta \mathbf{E_L^0}$) represented by the blue curve in Figure 3.1 is given by

$$I^{L(N)} = 0.37\text{eV}^{-1}(\Delta E_0^L)^2 + 14\ \text{eV} \tag{3.4}$$

The relative rising edge position (ΔE_0^L) is 2.9 eV in TU, which gives a free ligand dipole integral of 17.6±0.6 eV for free TU. This is 0.7 eV larger than the $I^{L(N)}$ of dtc (16.9 eV). However, the corresponding relationship for the hydrocarbon containing S-ligands, the $I^{L(C)}$, is 7.6±0.6 eV. This is 2.2 eV less than that of ttctd (9.8 eV). The agreement is chemically reasonable considering TU is a formally sp^2 hybridized sulfur. The edge position also determines the slope parameter used to account for the change of Z_{eff}(S) in going from the free to the complexes ligand to the metal center given by

$$slope = 3.2\ (\Delta E_0^L)^2 + 2.3 \tag{3.5}$$

For the free TU ligand, the slope parameter is 29.2, which is reasonable when compared to dtc at 23.9 and ttctd at 48.5. Table 3.1 summarizes the relevant free-ligand-based values for Nadtc, TU, and ttctd as discussed in this section.

Table 3.1 Summary of parameters used to estimate free ligand dipole integrals (I^{L}) for Nadtc, TU, and ttctd ligands

	edge position, eV	ΔE_L^0, eV	$I^{L(C)}$, eV	$I^{L(N)}$, eV	*slope*
Nadtc	2474.3	2.6	-	16.9	23.9
TU	2474.6	2.9	7.6	17.6	29.2
ttctd	2475.5	3.8	9.8	-	48.5

Transition Dipole Integral (I^{C}) Coordinated
Sulfur in $[Ni(TU)_6]^{2+}$, and $[Co(TU)_4]^{2+}$

The S K-XANES spectra for $[Co(TU)_4]^{2+}$, $[Zn(TU)_4]^{2+}$, and $[Ni(TU)_6]^{2+}$ are compared to the spectra of $[Ni(ttctd)]^{2+}$ and $[Ni(dtc)_2]^{+}$ along with their first and second derivatives in Figures 3.3A, B, and C. The new pre-edge features (relative to the free TU), seen at 2471.2 eV and 2471.1 eV for $[Co(TU)_4]^{2+}$ and $[Ni(TU)_6]^{2+}$ respectively are due to the sulfur 3p character of electron holes in the M-S σ^*/π^* orbitals. This feature is not present in the $[Zn(TU)_4]^{2+}$ complex because of its closed shell $3d^{10}$ electronic configuration. The rising edge and edge jump positions of all TU complexes shift by approximately 1 eV relative to the free TU.

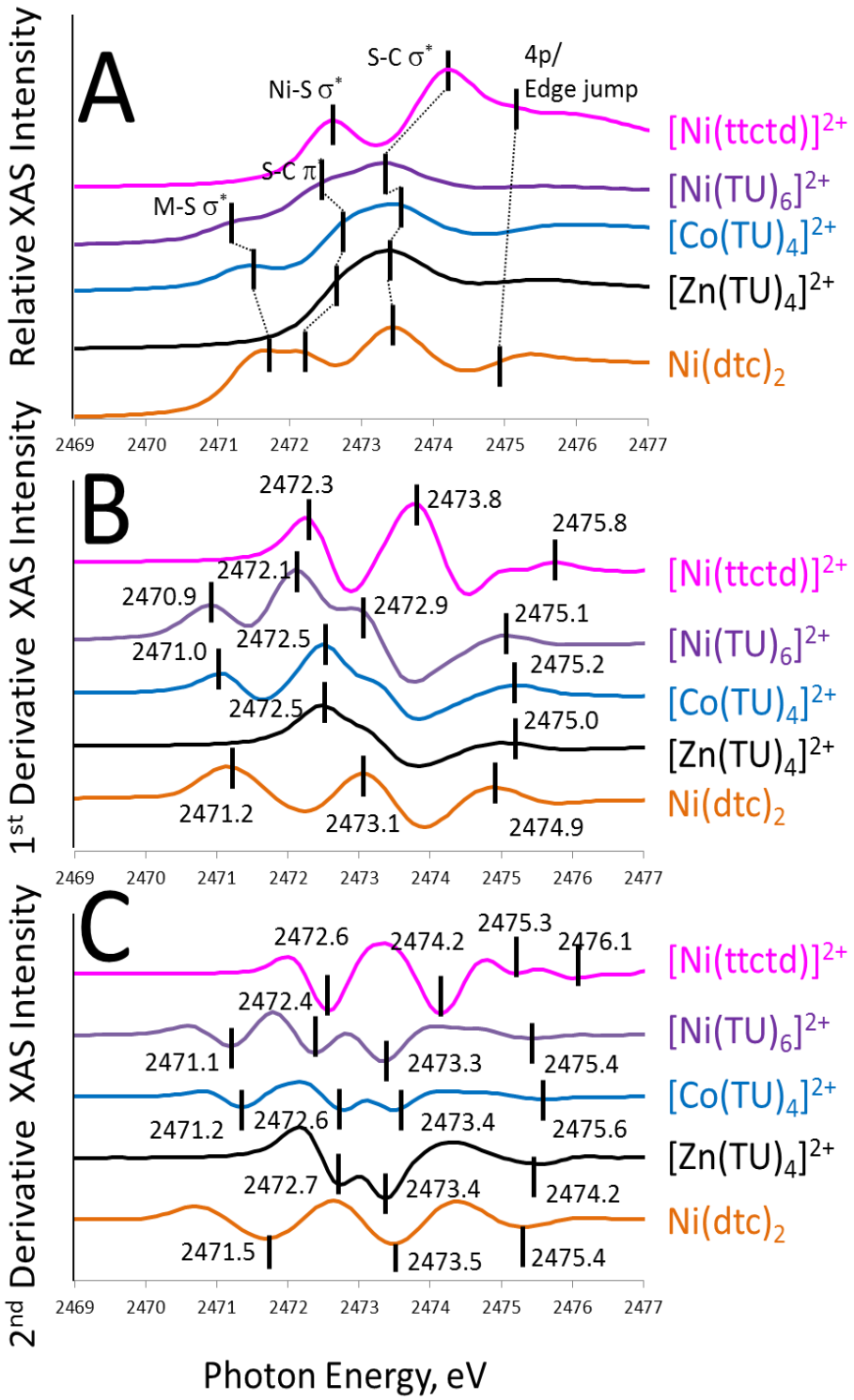

Figure 3.3 XANES spectra of selected $Ni^{(II)}$ coordination compounds along with the first (B) and second (C) derivatives. All resolved peaks are marked based on the first and second derivative maximum and minimum positions, respectively

The edge jump position of $[Ni(TU)_6]^{2+}$, although more resolved than the free TU, cannot be assigned without the aid of the $Ni(dtc)_2$ and $[Ni(ttctd)]^{2+}$ spectra. Interpolating the edge positions using these two spectra, an edge position of 2475.1±0.3 eV can be assigned for $[Ni(TU)_6]^{2+}$, which is 0.5 eV greater up than the edge jump energy position of the free TU (2474.6 eV). The shift is the direct measure of the increase in Z_{eff}(S) upon coordination to the Ni^{2+} ion.

Applying the correction for going from $I^{L(N)}$(TU) to $I^{C}([Ni(TU)_6]^{2+})$ a dipole integral value of 32.2 eV can be obtained for $[Ni(TU_6)]^{2+}$. This is a reasonable value when compared to the I^{C} for $[Ni(dtc)_2]$ (31.2 eV). When the lower value of $I^{L(C)}$(TU) is considered, the $I^{C}([Ni(TU)_6]^{2+})$ dipole integral is 22.2 eV which is again reasonable relative to $[Ni(ttctd)]^{2+}$ (23.3 eV), respectively. Similar analysis for the $[Co(TU)_4]^{2+}$ complex gave has an edge jump position of 2475.2±0.3 eV, which is 0.6 eV shift upon TU coordination relative to the free TU energy position. This shift results in dipole integrals I^{C} for the Co complex of 25.1 eV and 35.1 eV when the free ligand dipole integrals of $I^{L(C)}$ and $I^{L(N)}$) are considered, respectively..

Determination of Pre-Edge
Intensity (D_0) for Free Ligand

Figure 3.4 shows the pseudo Voigt line fits to the S1s→S-C π^*, S-C σ^*, S4p and a edge-jump fit of the sulfur 1s ionization transitions for the S K-edge spectrum of the free TU.

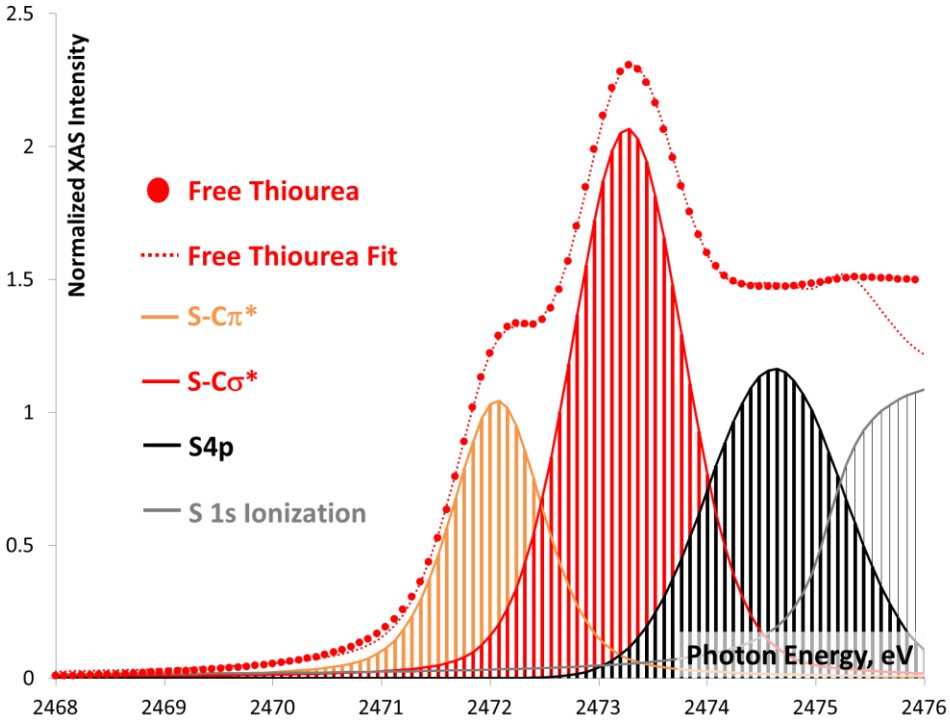

Figure 3.4 S K-edge spectrum of free TU with pseudo Voigt line fitting the S-C π^*, S-C σ^*, S 4p and an edge jump fit of the sulfur 1s ionization transitions

The fit shown in Figure 3.4 has a S-C π^* feature at 2472.1 eV with 1.33 eV intensity, and a S-C σ^* transition at 2473.3 eV with 2.92 eV intensity. Given that the TU has formally a σ- and a π-bond, the approximately double peak intensity for the latter should correspond to considerable larger S character in the antibonding C-S σ* orbital. However, as discussed later for the electronic structure analysis even the free ligand shows considerable mixing of the unoccupied valence bond orbitals, and thus the second feature cannot be purely assigned to C-S σ*-based excitations. Using the free TU ligand dipole integral $I^{L(C)}$ or $I^{L(N)}$ (7.6 or 17.6 eV), and Equation 3.1 the S 3p orbital character of the S-C π^* feature can be estimated. The sulfur 3p orbital character of 26% e^- $hole^{-1}$ and 11% e^- $hole^{-1}$ was obtained for the S-C π^*, respectively, which appears to be too low

considering the difference between the Z_{eff}(S) and Z_{eff}(C) that defines the antibonding, unoccupied orbitals to be dominantly S-based.

The fit to the free TU spectrum was converted to an analytical function, which can be used to account for the rising-edge features in spectra of the TU complexes by allowing the amplitude and energy position of the analytical free-ligand function to vary as needed.

Determination of Pre-Edge Intensity (D_0) for Coordinated Ligands Figures 3.5 A, B, and C show representative fits the spectra of $[Zn(TU)_4]^{2+}$ (A), $[Co(TU)_4]^{2+}$ (B), and $[Ni(TU)_6]^{2+}$ (C) using the free TU spectrum. All the spectra contain S-C π^*, S-C σ^* features that are poorly fit by the free TU ligand spectrum. This is the direct experimental indication that the electronic structure of the coordinated and free TU ligands are different as also suggested by the difference in the IR spectra. In addition, the S K-XAS spectra of $[Co(TU)_4]^{2+}$, and $[Ni(TU)_6]^{2+}$ have an additional pre-edge feature due to the S 1s$\rightarrow$M-S σ/π^* excitation. This pre-edge feature is not present in the $[Zn(TU)_4]^{2+}$ spectrum due to the Zn^{2+} ion's $3d^{10}$ electron configuration.

The integrated pre-edge intensities for the $[Co(TU)_4]^{2+}$ and $[Ni(TU)_6]^{2+}$ complexes are 0.54 and 0.59 eV, respectively.

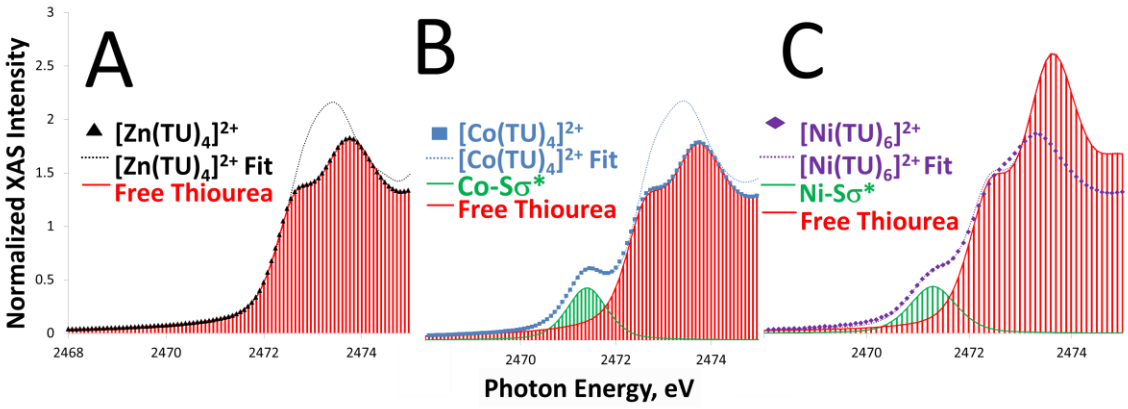

Figure 3.5 S K-edge spectra of $[Zn(TU)_4]^{2+}$ (A), $[Co(TU)_4]^{2+}$ (B), and $[Ni(TU)_6]^{2+}$ (C) fit using the free ligand spectrum as rising-edge correction

The energy positions and peak amplitudes of the S-C π^* and σ^* features within the free-ligand corrected fits as in Figure 3.5 were not allowed to change. This constraint does not reflect the experimentally observed differences between the free and coordinated TU IR and XAS spectra that are the result of a shift in the dominance of resonance structures from the neutral thione to the charged thiolate.

To improve fits along the rising-edge region and simultaneously investigate how these improvements affect the chemically most important pre-edge intensities, the S-C π^* feature was removed from the analytical free TU ligand spectrum and fitted with a separate pseudo-Voigt line. The new set of fits for the $[Zn(TU)_4]^{2+}$, $[Co(TU)_4]^{2+}$, and $[Ni(TU)_6]^{2+}$ complexes are shown in Figures 3.6 A, B, and C

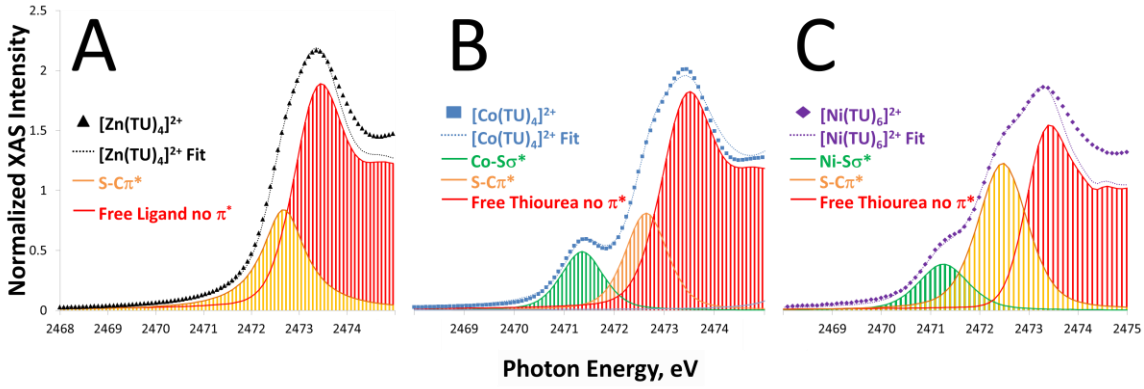

Figure 3.6 S K-edge spectra of $[Zn(TU)_4]^{2+}$ (A), $[Co(TU)_4]^{2+}$ (B), and $[Ni(TU)_6]^{2+}$ (C) fit using the modified free ligand spectrum without the S-C π^* feature

The new fits in Figure 3.6, with two linked pseudo-Voigt lines for the M-S σ^*/π^* and S-C π^* transitions, gave D_0 vales of 0.61 eV and 0.57 eV for $[Co(TU)_4]^{2+}$ and $[Ni(TU)_6]^{2+}$ respectively. Despite that these are practically identical values within the error bar of XAS data collection and analysis[117], they do not correspond to identical S 3p contributions since the $Co^{(II)}$ complex has 3 d electron holes and 4 absorbers, while the $Ni^{(II)}$ complex has 2 holes for 6 absorbers. The renormalized intensity values are now 0.8 and 1.7 eV $hole^{-1}$ for $[Co(TU)_4]^{2+}$ and $[Ni(TU)_6]^{2+}$ respectively, which are now clearly indicate a more double M-S bond covalency in the octahedral Ni vs. in the tetrahedral Co complex.

The improved fit with respect of the rising-edge features between the complete free-ligand (Figure 3.5) and the separated S-C π* free-ligand fits (Figure 3.6) is due to the change in the intensity ratio between the S-C π^* and S-C σ^* features. To evaluate the dependence of the M-S σ^*/π^* intensity as a function of the S-C π^*/ S-C σ^* intensity ratio from 0.4 (as in the free ligand, Figure 3.5) to 0.2 (as in the coordinated complex, Figure

3.6), a series of fits was carried out for the $[Ni(TU)_6]^{2+}$ complex (Figures 3.7A, B, and C) with all resolved features allowed to vary independently including those for the S 4p transition and the edge jump. The Ni-S σ^*-based transition was fit with integrated pre-edge intensities (D_0) of 0.50-0.53 eV. The less than 2% variation indicates that we can obtain a reasonable fit for the pre-edge intensities when the change in the C-S π^* spectral features is fit independently from the unresolved excitations that make up the rest of the rising-edge region.

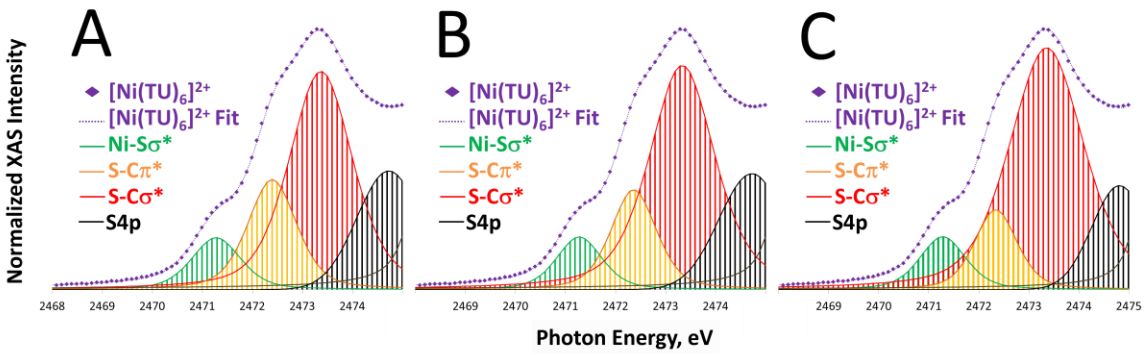

Figure 3.7 Multiple fits to the S K-edge spectra of $[Ni(TU)_6]^{2+}$ with pseudo-Voigt lines for the S 1s→S-C π^*, S-C σ^*, S 4p transitions and an edge-jump for the sulfur 1s ionization, where the ratio of S-C π^* to S-C σ^* intensity was varied from A) 0.4 B) 0.3, and C) 0.2

Figure 3.8 shows the unconstrained pre-edge and rising-edge fits with separate Co-S π/σ^*, S-C π^*, S-C σ^*, S 4p and edge jump features of $[Co(TU)_4]^{2+}$. This fit resulted in a well resolved Co-S π/σ^* -based transition with an intensity of 0.55 eV. This is less than the result obtained for the full analytical free ligand fit in Figure 3.4.

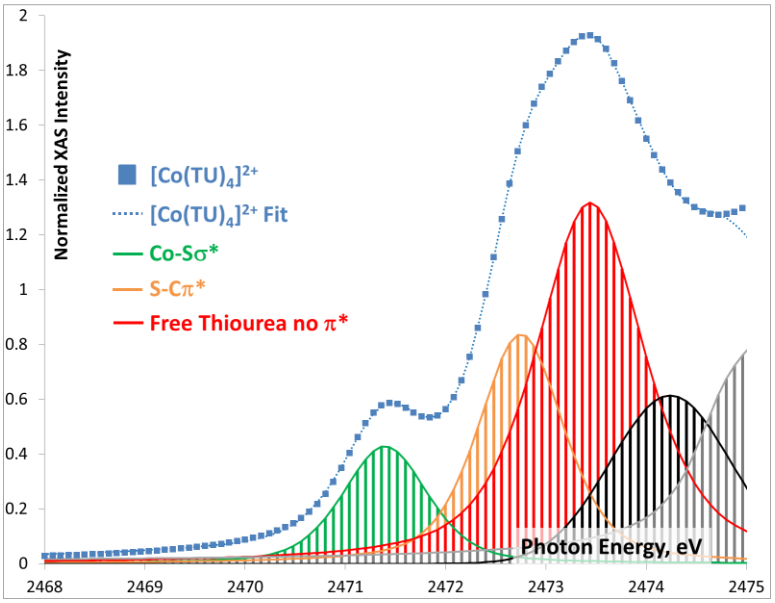

Figure 3.8 4 S K-edge spectrum of $[Co(TU)_4]^{2+}$ independent Co-S π/σ^*, S-C π^*, S-C σ^*, S 4p excitations and edge jump functions

It is also interesting to compare, the spectra of the two tetrahedral species. The $[Zn(TU)_4]^{2+}$ complex has a $3d^{10}$ filled d-manifold and thus all covalent bonding is limited to the 4s/4p set. The rising-edge features thus represent the overall effect of the ionic bonding between the Zn^{2+} ion and the TU ligands and the limited covalent interaction with the Zn 4s and 4p and the symmetry adapted linear combination of the TU orbitals. The similarly poor fit to rising-edge features in Figures 3.6A and B further support the benefit of using the spectrum of the $[Zn(TU)_4]^{2+}$ complex to obtain the most reasonable pre-edge feature intensities for the the $[Co(TU)_4]^{2+}$ complex. Similarly to the free ligand, an analytical function was created for the $[Zn(TU)_4]^{2+}$ spectrum, which was then used to obtain the fits shown in Figure 3.9.

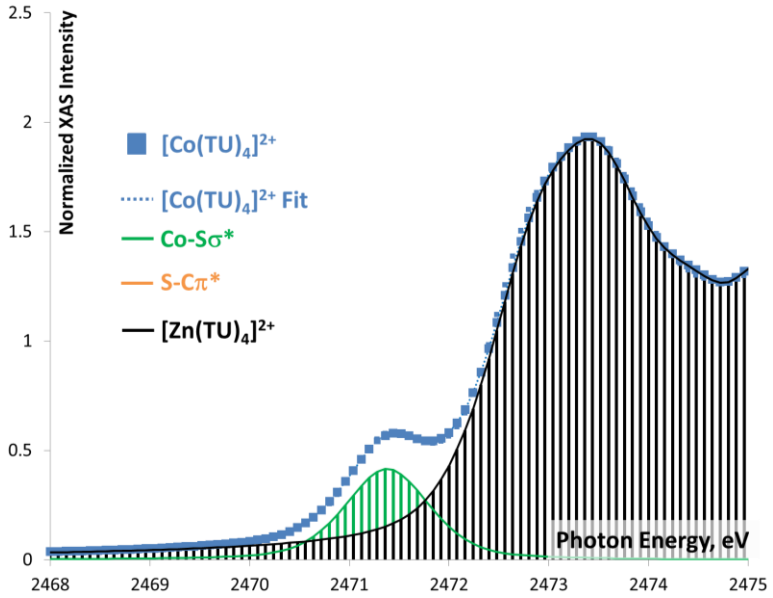

Figure 3.9: S K-edge spectrum of $[Co(TU)_4]^{2+}$ fit using the analytical fit function of $[Zn(TU)_4]^{2+}$

The use of the $[Zn(TU)_4]^{2+}$ spectrum provided a high quality fit to the $[Co(TU)_4]^{2+}$ giving practically no residual for the rising-edge region and 0.53 eV integrated pre-edge intensity, which upon renormalization corresponds to 0.7 eV $hole^{-1}$ for four S(TU) absorbers and three 3d electron holes.

Table 3.2 summarizes the parameters and the normalized peak from Figures 3.4-3.9.

Tabel 3.2 Peak amplitudes (A), energy positions (E_0), line widths (lw), Gaussian/Lorentzian ratios (G:L), and integrated peak intensity (D_0) for normalized spectra in Figures 3.4-3.9 (UDF stands for analytical fits of reference spectra)

		A, -	E_0, eV	lw, eV	(G:L)	D_0, eV
free TU Figure 3.4	S-C π^*	1.0	2472.1	1.0	0.5	1.33
	S-C σ^*	2.1	2473.3	1.2	0.7	2.92
	S 4p	1.2	2474.6	1.5	1.0	1.83
	edge jump	1.2	2475.1	0.3		
$[Zn(TU)_4]^{2+}$ Figure 3.5 A	TU UDF	1.8	2473.8			
$[Co(TU)_4]^{2+}$ Figure 3.5 B	Co-S π/σ^*	0.4	2471.4	1.0	1.0	0.54
	TU UDF	1.0	2472.6			
$[Ni(TU)_6]^{2+}$ Figure 3.5 C	Ni-S σ^*	0.4	2471.3	1.1	0.5	0.59
	TU UDF	1.1	2472.4			
$[Zn(TU)_4]^{2+}$ Figure 3.6 A	S-C π^*	0.84	2472.7	1.09	0.5	1.44
	TU UDF (No S-C π^*)	1.9	2473.5			
$[Co(TU)_4]^{2+}$ Figure 3.6 B	Co-S π/σ^*	48	2471.4	1.0	0.5	0.61
	C-S π^*	0.8	2472.6	1.0	0.5	1.02
	(No S-C π^*)	1.9	2473.5			
$[Ni(TU)_6]^{2+}$ Figure 3.6 C	Ni-S σ^*	0.4	2471.3	1.2	0.5	0.57
	S-C π^*	1.2	2472.5	1.2	0.5	1.82
	TU UDF (No S-C π^*)	0.6	2472.3			
$[Ni(TU)_6]^{2+}$ S-C π^*/S-C σ^* = 0.2 Figure 3.7 A	Ni-S σ^*	0.4	2471.3	1.1	0.5	0.51
	S-C π^*	0.6	2472.3	1.0	0.5	0.71
	S-C σ^*	1.7	2473.4	1.8	0.5	3.79
	S 4p	0.7	2474.8	1.3	1.0	1.00
	edge jump	1.0	2475.1	0.2		
$[Ni(TU)_6]^{2+}$ S-C π^*/S-C σ^* = 0.3 Figure 3.7 B	Ni-S σ^*	0.4	2471.3	1.1	0.5	0.50
	S-C π^*	0.7	2472.4	1.1	0.5	0.95
	S-C σ^*	1.6	2473.3	1.6	0.4	3.17
	S 4p	0.8	2474.7	1.6	1.0	1.33
	edge jump	1.0	2475.1	0.2		
$[Ni(TU)_6]^{2+}$ S-C π^* S-C σ^* = 0.4 Figure 3.7 C	Ni-S σ^*	0.4	2471.3	1.2	0.5	0.53
	S-C π^*	0.8	2472.4	1.2	0.5	1.12
	S-C σ^*	1.5	2473.4	1.5	0.5	2.90
	S 4p	0.8	2474.7	1.5	1.0	1.32
	edge jump	1.0	2475.1	0.2		
$[Co(TU)_4]^2$ Figure 3.8 This is not reasonable!	Co-S π/σ^*	0.4	2471.4	1.0	0.5	0.55
	S-C π^*	0.8	2472.8	1.0	0.4	1.09
	S-C σ^*	1.3	2473.4	1.27	0.3	2.28
	S 4p	0.6	2474.2	1.42	1.0	0.93
	edge jump	1.0	2474.6			
$[Co(TU)_4]^{2+}$ Figure 3.9	Co-S π/σ^*	0.4	2471.4	1.0	1.0	0.53
	$[Zn(TU)_4]^{2+}$ UDF	0.9	2472.8			

The final integrated pre-edge intensities corresponding to the S 1s→Co-S π/σ^* and Ni-S σ^* excitations were obtained from averaging the D_0 values from Table 3.2 for the most reasonable fits shown Figures 3.6-3.9. The free TU ligand-based fits in Figure 3.5 were excluded due to poor fitting of the S-C σ^* features. The resulting average Co-S π/σ^* and Ni-S σ^* intensities are 0.56±0.04 eV and 0.53±0.03 eV, respectively.

Determination of the M-S(TU) Bond Covalencies. Table 3.3 summarizes all the relevant ligand and complex parameters used to determine the S 3p character of the experimentally probed M-S unoccupied or partially occupied antibonding orbitals Equation 3.1 and transition dipole relationships shown in Figure 3.1.

Table 3.3 Relevant parameters used to obtain S 3p orbital character for the studied Co and Ni complexes of TU

	D_0 (eV)	E_0^L (eV)	I^L (eV)	ΔE (eV)	slope	I^C (eV)	S 3p (e^- hole^{-1})
$[Co(TU)_4]^{2+}$	0.56±0.4	2474.6±0.5	7.6±0.8	0.6	29.2	25.1	0.09±.04
			17.6±0.8			35.1	0.06±0.04
$[Ni(TU)_6]^{2+}$	0.53±0.3	2474.6±0.5	7.6±0.8	0.5	29.2	22.2	0.21±0.05
			17.6±0.8			32.2	0.15±0.05

As described above, the numerically comparable pre-edge intensities (D_0) will results in different S 3p contributions due to the different number of S absorbers. The Ni-S(TU) bonding is more than twice covalent than Co-S(TU) as a result of approximate octahedral coordination geometry which gives better M-L overlap[142] than the approximate tetrahedral geometry for the Co complex. The maximum predicted 21%

covalency per electron hole, still corresponds to a normal bonding sheme[152] where the metal orbitals are destabilized relative to the S-donor orbitals and the M-L overlap is limited.

Theoretical Geometry, Vibrational
Frequencies, and Ground State Electronic Structure

Molecular Geometry Using the TU crystal structures as a starting geometry, calculations at the BP86/def2-TZVP/PCM(CH_3CN) level were used to obtain optimized TU structure (Figure 3.10).

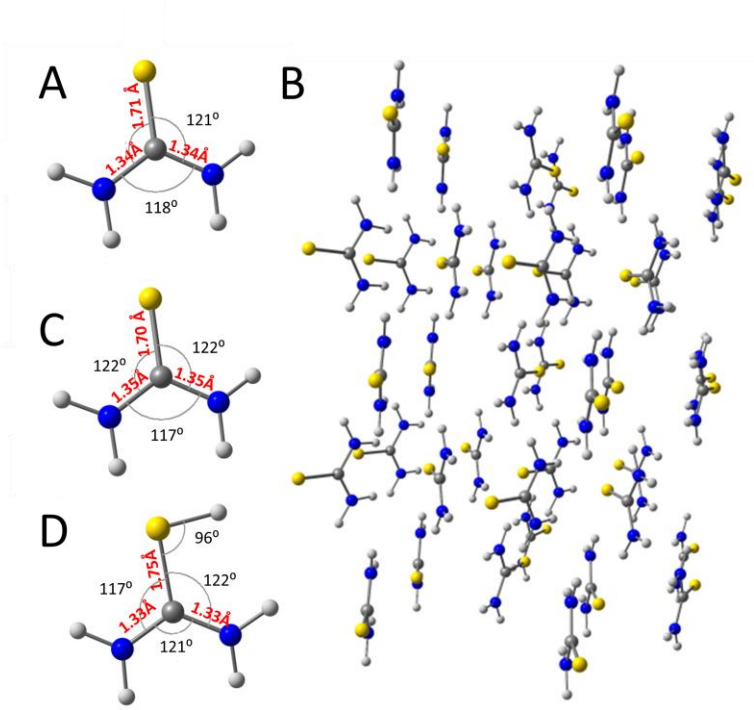

Figure 3.10 Comparison of the A) crystal structure, B) crystal packing effects, C) BP86/def2-TZVP/PCM(CH_3CN) optimized TU molecule and its protonated form at the S D)

The BP86/def2-TZVP/PCM(CH_3CN) optimization reproduces the geometry of the TU crystal structure to within 0.01 Å and 1° for bond lengths and bond angles respectively. Unexpectedly, the simulated acetonitrile dielectric environment mimics the stabilizing effects of the weak S…H-N hydrogen bonding that takes place in the packed TU crystal where the S-H hydrogen bonding distances are ~2.4 Å (Figure 3.10B). As discussed in more detail in Chapter 4 of this dissertation, we need to be cautious here because the specific combination of level of theory and limited computational model can results to error cancellations giving the experimentally correct structure for the wrong reason.

The sulfhydryl protonated TU is an approximation for shifting the resonance structure in Scheme 3.1 toward the thiolate form. The now formally single S-C bond bond length is elongated by 0.04 Å (1.75 Å vs. 1.71 Å) and the N-C-N bond angle changes by 3º (121 º vs. 118 º)

The calculated structure for the $[Ni(TU)_6]^{2+}$ complex at the BP86/def2-TZVP/PCM(CH_3CN) level shows poor agreement in bond lengths (0.04 Å), but acceptable for bond angles (2º). The crystal packing indicate that there is a H···Br interaction of 2.51 Å within the inner-sphere, which could lessen the S donation to the Ni(II) center. The only additional interaction is intramolecular hydrogen bonding between coordinated sulfur ligands and hydrogens on neighboring TU. This is an unbalanced interaction which when geomterically optimized in DFT is not present. There is a considerable elongation in the S=C bond in going from the free TU (1.71 Å) to the coordinated (as long as 1.75 Å). This corresponds to a shift in the preference of resonance structures from thion to thiolate (scheme3.1).

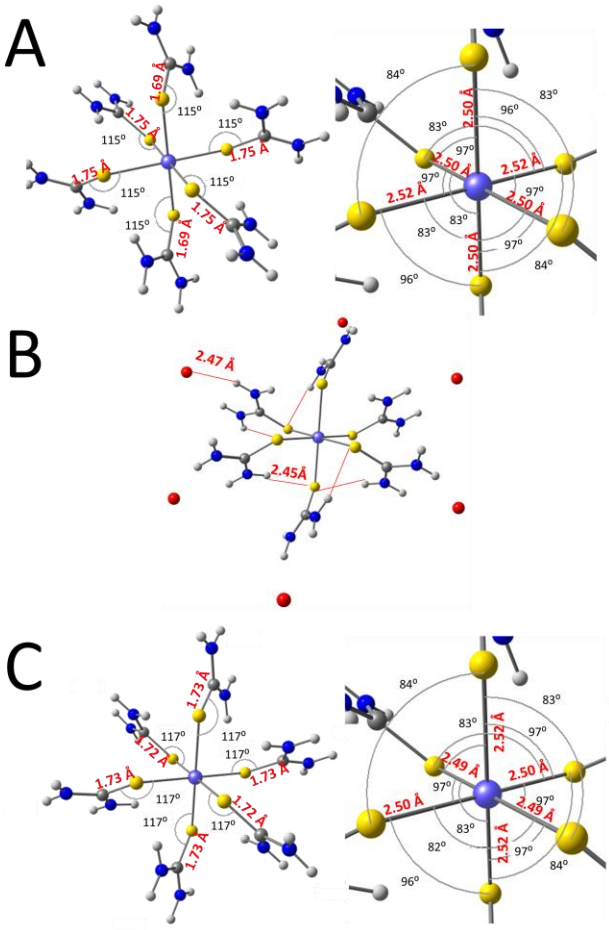

Figure 3.11 A) experimental crystal structure, B) crystal packing, and the C) BP86/def2-TZVP/PCM(CH_3CN) optimized structure of $[Ni(TU)_6]^{2+}$ with relevant bond lengths and bond angles

Figure 3.12 A and B compares the experimental and BP86/def2-TZVP/PCM(CH_3CN) optimized structures of $[Co(TU)_4]^{2+}$. The calculated bond lengths show good aggreament with the crystal structure deviating by less than 0.02 Å. The bond angles differ considerably by 15°. There is an axial compression in the calculated structures since the bond angle change from 92° and 95° (in the crystal structure) to 111° and 114° at DFT/def2-TZVP/PCM(CH_3CN). There is a repeating hydrogen bond in the crystal strucuture of $[Co(TU)_4]^{2+}$ where two S are 2.65 Å from a neighboring TU H.

When compared to structure the free TU ligand, we can observe an elongation of the S=C bond in the $[Co(TU)_4]^{2+}$ complex (1.73 Å vs. 1.70 Å), which is along the distortion coordinate between the thion and the thiolate resonance structures of TU (Scheme 3.1)

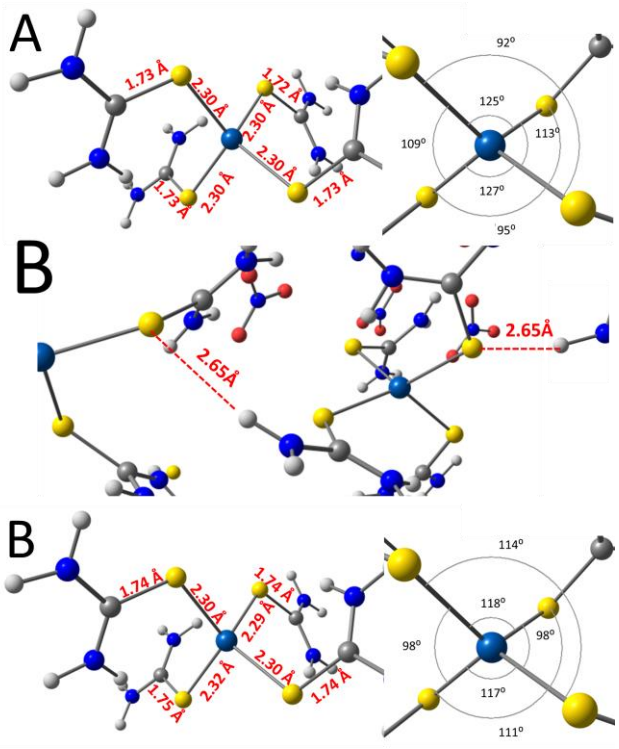

Figure 3.12 A) Experimental crystal structure, B) crystal packing, and C) DFT/def2-TZVP/PCM(CH_3CN) optimized structure of $[Co(TU)_4]^{2+}$

Vibrational Analysis.

Frequency calculations were performed at the BP86/def2-TZVP/PCM(CH_3CN) optimized structures for the free TU ligand, $[Ni(TU)_6]^{2+}$, and $[Co(TU)_4]^{2+}$. The calculated IR transition frequencies and their assignments are summarized in Table 3.4

Table 3.4 Calculated (BP86/def2-TZVP/PCM(CH_3CN)) and experimental[141, 153] IR frequencies for the free TU ligand, $[Ni(TU)_6]^{2+}$ and $[Co(TU)_4]^{2+}$ complexes

free TU, cm^{-1}		$[Ni(TU)_6]^{2+}$, cm^{-1}		$[Co(TU)_4]^{2+}$, cm^{-1}		
exp.	DFT	exp.	DFT	exp.	DFT	assignment
3380	3474	3400	3488	-	3480	N–H stretch (N–H)
1620	1600	1619	1586	-	3328	C-N–H bending deformation
1477	1432 1567	1483	1479	-	1470	N–C stretching vibration (N–C–N symetric)
1414	1431	1398	1347	1350	1351	NH_2 rocking, C–S stretching and N–C–N asymetric stretching
1082	1044	1089	1046	1049	1072	NH_2 rocking, mode C=S and C–N strethcing
730	728	710	710	700	684	C=S stretching vib (C=S)

The BP86/def2-TZVP/PCM(CH_3CN) calculated TU frequencies were in qualitative agreement with the eperimentally measured values; however absolute errors up to 100 cm^{-1} were observed The BP86/def2-TZVP calculated C=S stretching frequency in the $[Co(TU)_4]^{2+}$, and $[Ni(TU)_6]^{2+}$ complexes, 684 cm^{-1}, and 710 cm^{-1} respectively, where in good agreement with the experimental values (700 cm^{-1} and 710 cm^{-1} respectively). Both the experimental and calculated C=S stretches in the complexes were red shifted from their respective free ligand values by ~20-30cm^{-1}. This frequency shift indicates a weakening of the S=C bond upon coordination, which is in agreement with the elongated

S-C bond lenghts relative to the free ligand both in the experimental structures and in calculations. The$[Ni(TU)_6]^{2+}$ N-H stretching vibration blue shifted in both experiementally and computationally. In a previous study,[141] this was used as an indication that upon forming the S-M bonds the bond order of C-N bond increases and the S-C decreases.[141]

Ground State Electronic Structure. The crystal structure of the free TU was used to obtain the MO diagram shown in Figure 3.13A at the BP86/def2-TZVP/PCM(CH_3CN). The in-plane sulfur lone pair is the highest occupied molecular orbital (HOMO). This is followed by the lowest unoccupied molecular orbital (LUMO), which is an out-of-plane S-C π^* with considerable delocalization. One of the in-plane N-H antibonding orbitals follows LUMO which is not relevant to S K-edge experiments due to its less than 1% sulfur contribution. The next experimentally important orbital is the S-C σ^*. This orbital ordering supports the assignments seen in Figure 3.2.

The AIM analysis of the atomic orbital composition for the free TU ligand gives a delocalized LUMO or S-C $\pi*$ with only 0.26 e^-hole^{-1} sulfur character. The LUMO+2 or S-C $\sigma*$ orbital has 0.32 e^-hole^{-1} sulfur contribution. The ratio of the S-C $\pi*$ and $\sigma*$ orbitals support the assumption that more intense, higher energy feature of the rising-edge cannot be solely assigned to the S-C $\sigma*$ transition. Furthermore, using the dipole expression (Equation 3.1), the AIM calculated S orbital contributions, and the D_0 values for the S-C π^* transition, a sulfur free ligand integral of 7.8 eV can be calculated. Interestingly, this is remarkably close to the $I^{L(C)}$ value of 7.6 eV than to the $I^{L(N)}$ (17.6 eV). However, we must keep in mind that the GGA functionals, such as BP86 generally

provide too covalent electronic structure. For thioethers, a hybrid functional with close to 40% HF exchange was found to provide the most reasonable electronic structure in comparison to high level ab initio wave function methods.[63]

The MO diagram for the $[Ni(TU)_6]^{2+}$ obtained at BP86/def2-TZVP/PCM(CH_3CN) level for the S_6 symmetrized molecule from the crystal structure is presented in Figure 3.13 C. The sulfur-based free ligand HOMOs (e_g orbitals) are formed from the symmetry adapted linear combinations (SALC) of the six donor lone pairs (Figure 3.13 B). At higher energy, there are six S-C π^* orbitals, followed by six S-C σ^* orbitals. The energy difference between S-C π^* and S-C σ^* decreases form ~2.5 eV in the free ligand to ~0.8 eV when the ligands are brought into the coordination geometry with S_6 symetry. This reduced energy gap was also observed experimentally in the S K-XAS spectra (Table 3.2 and Figure 3.6).

In the coordinated $[Ni(TU)_6]^{2+}$ the e_g SALCs combine with the d_{z^2} and $d_{x^2-y^2}$ to form the single unoccupied molecular orbitals (SUMOs.) The next LUMO+3, LUMO+4, and LUMO+5 orbitals show evidence of backbonding interaction of the TU ligand and the occupied Ni orbitals due to approximately 30% e^- $hole^{-1}$ Ni character from AIM analysis. These MOs are followed by a S-C σ^* (LUMO+7) orbital 0.1 eV higher in energy than the highest S-C π^* orbital. Beyond these energies the orbitals mix with diffuse Rydberg orbitals and not presented here due to their negligible importance to covalent bonding.

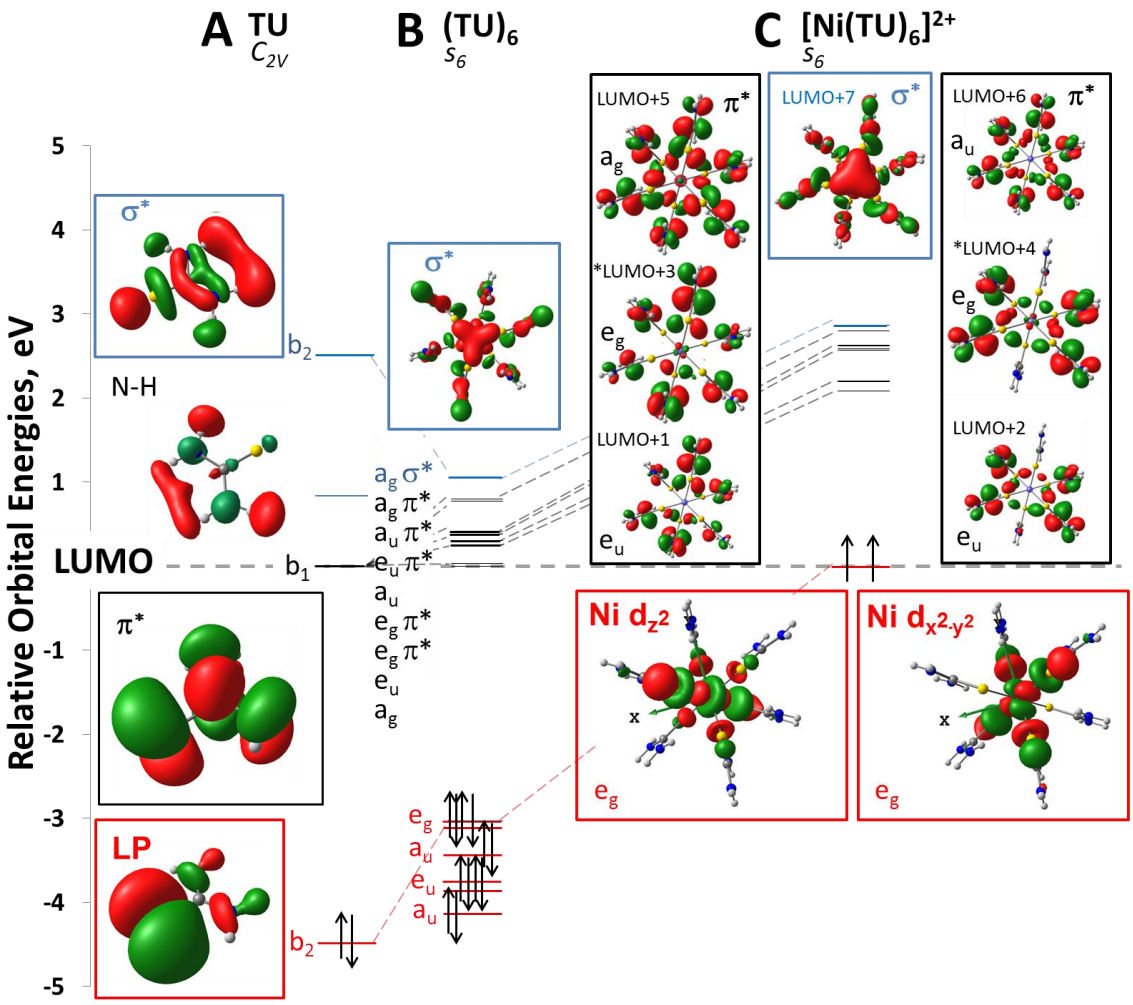

Figure 3.13 MO diagram calculated at the BP86/def2-TZVP/PCM(CH_3CN) of symmetrized C_{2v} X-ray structure of free thiourea (A), S_6 symmetrized $(TU)_6$ hexamer of free ligands without central metal ion (B), and S_6 $[Ni(TU)_6]^{2+}$ (C)

The MO diagram for the $[Co(TU)_4]^{2+}$ for the S_4 symmetrized crystal structure is presented in Figure 3.14 B, along with the symeterized S_4 symeterized free ligands showing the ligand-lignad repulsion energy.

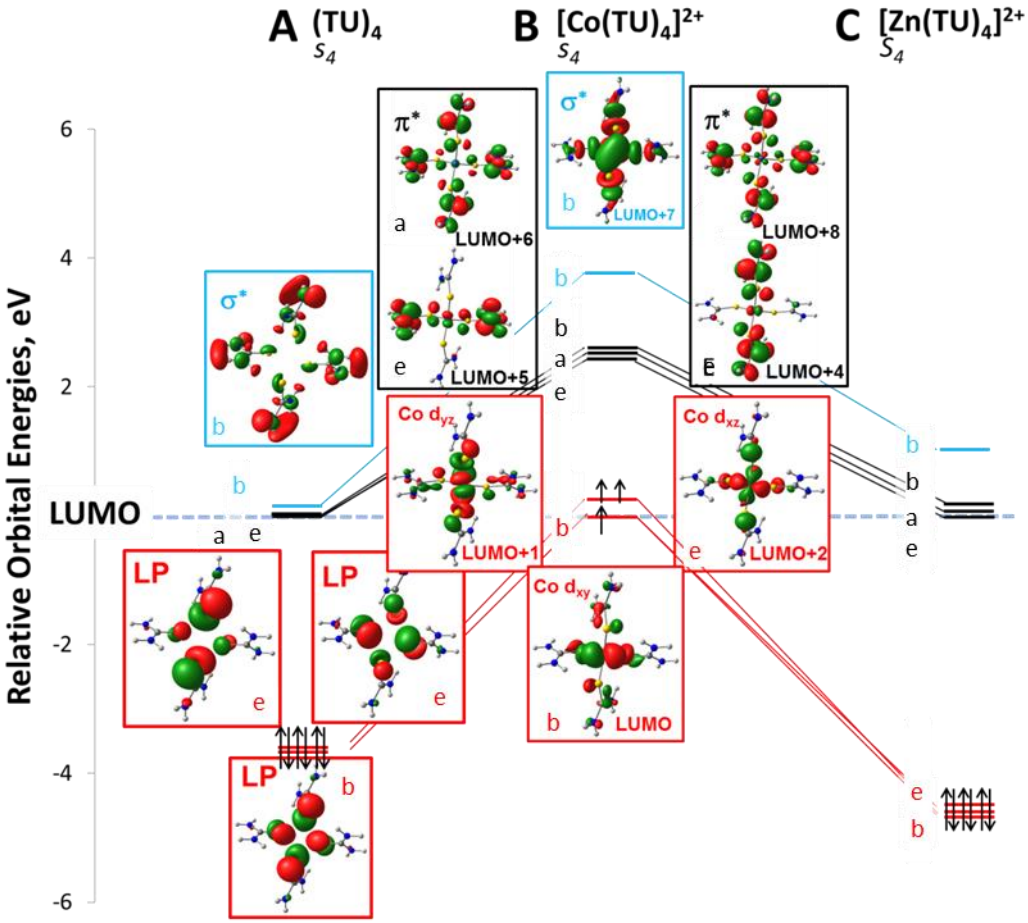

Figure 3.14 MO diagram calculated at the BP86/def2-TZVP/PCM(CH_3CN) level for symmetrized experimental geometries for A) S_4 symmetrized $(TU)_4$, B) $[Co(TU)_4]^{2+}$ and C) $[Zn(TU)_4]^{2+}$

In the cobalt complex, the e symmetry SALCs of the sulfur lone pairs (Figure 3.16A) donate to the degenerate Co $3d_{xz}$ and $3d_{yz}$ orbitals, while the b symmetry SALC (Figure 3.14 B and C) donates to the $3d_{xy}$ The SUMOs with e and b symmetry split by 9 meV; however, this is so small that the exchange interaction among the unpaired electrons overcomes the sum of the energy gain due to ligand field stabilization and energy loss due to electron pairing repulsion and thus resulting in the S = 3/2 spin ground state. As detected experimentally.[153] The Co 3d orbitals are followed by the S-C π*

orbitals. The LUMO+4 and LUMO+5 orbitals suggest backbonding due to considerable Co content of approximately 0.3 e^- $hole^{-1}$. The energy difference between the S-C π^* and the S-C σ^* is the same between the Co to the Zn complex that supports the use of the $[Zn(TU)_4]^{2+}$ spectrum for the most reasonable rising-edge correction of the $[Co(TU)_4]^{2+}$ spectrum. (Figure 3.9).

The sulfur contributions to the LUMOs of the TU complexes were calculated using three representative of density functional exchange and correlation functionals as outlined in the Methods section from AIM population analysis. Due to the energy separation of the 3s and 3p S orbitals the former do not contribute to a more than a few percent to the M-S covalent bonds, thus the total sulfur contribution practically corresponds to the experimentally measured S 3p character from S K-XAS. The results of the population analysis in Table 3.5 show similar trends with respect of the nature of density functional for both complexes. The GGA functional provide the most covalent picture, while the hybrid GGA with approximately 20% HF exchange has the most ionic bonding. The metaGGA position is somewhat disordered being closer to the pure GGA in the Ni complex and vice versa for the hybrid GGA method. The analysis of the S K-XAS spectra showed similar pre-edge intensities; however, after renormalization by the number of absorbers (6 vs. 4) and number of electron holes (2 vs 3), the S 3p covalency per 3d electronhole of the Ni complex is about 9/4 greater than that of the Co complex. None of the computational results approximates well this high experimental ratio.

Table 3.5 Summary of DFT/def2-TZVP/PCM(CH_3CN) calculated orbital character in electron per hole from AIM analysis for $[Ni(TU)_6]^{2+}$ (h = 2) and $[Co(TU)_4]^{2+}$ (h = 3).

		Ni	S	Co	S
GGA (BP86)	LUMO + 2 (S-Co d_{xy})	-	-	66%	24%
	LUMO + 1 (S-Ni d_{z^2}, S-Co d_{yz})	60%	30%	44%	18%
	LUMO (S-Ni $d_{x^2-y^2}$, S-Co d_{xz})	58%	34%	72%	20%
	average over all electron holes	59%	32%	61%	21%
	ratio of Ni/Co S character		32:21		
Hybrid GGA (B3LYP)	LUMO + 2 (S-Co d_{xy})	-	-	44%	19%
	LUMO + 1 (S-Ni d_{z^2}, S-Co d_{yz})	66%	21%	73%	16%
	LUMO (S-Ni $d_{x^2-y^2}$, S-Co d_{xz})	66%	25%	27%	18%
	average over all electron holes	66%	23%	48%	18%
	ratio of Ni/Co S character		23:18		
Meta GGA (TPSS)	LUMO + 2 (S-Co d_{xy})	-	-	69%	22%
	LUMO + 1 (S-Ni d_{z^2}, S-Co d_{yz})	63%	26%	58%	19%
	LUMO (S-Ni $d_{x^2-y^2}$, S-Co d_{xz})	62%	30%	57%	16%
	average over all electron holes	63%	29%	61%	19%
	ratio of Ni/Co S character		29:19		

The AIM derived S orbital character and average experimental D_0 form Table 3.3 through Equation 3.1 can be used to calculate DFT-based I^c values for $[Ni(TU)_6]^{2+}$, which are 14.9, 20.7, and 16.4 eV for BP86, B3LYP, and TPSS, respectively. The corresponding I^C values for $[Co(TU)_4]^{2+}$ are -9.9, -7.7 and -9.1 eV for the same set of functionals, respectively. These transition dipole integrals are all lower than the experimentally derived value from Table 3.1. However, the hybrid B3LYP functional provides Ni-S bond covalency (23% S) that is actually comparable to the experimentally derived S 3p character (21%) using the dipole integral $I^{L(C)}$. From a more extensive computational study for a large series of $[Ni^{(II)}S_4]$ complexes, we found that all DFT

functionals, including the hybrid B3LYP method, give too covalent Ni-S bonding picture. This suggests that the good agreement between the hybrid B3LYP and the S K-XAS result is only furtoitious. The calculated S 3p character should be lower than any of the numbers shown in Table 3.5. This would require that the transition dipole integral cannot be the the one used for the all hydrocarbon containing S-ligands. It may not be as high as those used for the Na_2mnt and Nadtc complexes; however, these results further support the need for an adjustable S 1s$\rightarrow$3p transition dipole integral as a function of ligand composition.

Conclusion

With the given combined S K-XAS and DFT study we have extend the series of conjugated nitrogen containing sulfur ligands previous investigated[142] (Na_2mnt, and dtc) to include the formally sp^2 hybridized TU ligand. The energy position of the S K-edge jump was assigned of the free TU ligand to be at 2474.6 eV (Figure 3.2). This energy was used to establish two limits for the free ligand-based transition dipole integrals (I^L) of the TU ligand to be 7.6 eV and 17.6 eV. The latter $I^{L(N)}$ includes correction for the presence of conjugated nitrogen atom of the TU ligand that accounts for the expected greater fluorescence intensity than corresponding unsubstituted hydrocarbon ligands as found earlier for the Na_2mnt and the Nadtc complexes (Figure 3.1). When the $I^{L(N)}$ value was used to quantitate the S 3p orbital character from the D_0 pre-edge intensities and edge positions shifts between the $[Co(TU)_4]^{2+}$ and $[Ni(TU)_6]^{2+}$ complexes and the free TU ligand values of 9% and 15% e^- $hole^{-1}$ were obtained.

As found for a series of $[Ni^{(II)}S_4]$ complexes, none of the GGA, hybrid, metaGGA density functionals used in the given study reproduced the above M-S bond covalencies. Fortuitiously the B3LYP functional gave good agreement with the S K-XAS results when the lower value of the hydrocarbon dipole integral was used $I^{L(C)}$. This aggreement between DFT and S K-XAS results and the observation that all functionals gave overly covalent bonding description suggest that a higher transition dipole integral is more reasonable to quantitate the S orbital character of the TU and its complexes. In order to further explore the intimate nature of transition dipole integral and the S-ligand composition, we need to evaluate the cause of the excess fluorescence emission channels in N-containing ligands relative to corresponding unsubstituted hydrocarbon ligands by resonant inelastic X-ray scattering at the ligand S K-edge energy region.

CHAPTER 4

A COMPUTATIONAL MODEL FOR THERMOCHROMIC LIGAND EXCHANGE OF NICKEL(II) COORDINATION COMPLEXES

Introduction

Chapter 2 quantitatively examined the S K-edge spectra of coordination compounds showing ligand exchange thermochromism (LETC) phenomena. The interpretation of the XAS data defined the experimental ground-state electronic structure of the tetrathiacyclotetradecane coordinated nickel(II) ($[Ni(ttctd)]^{2+}$) LETC chromophore. The current chapter tests the applicability of computational methodologies and techniques to the structural analysis of LETC chromophores. The analysis includes the molecular structure, both ground and excited-states, and the energetics of ligand exchange thermodynamics, calculated using density functional theory, semi-empirical methods and molecular mechanics. We evaluated the accuracy, adequacy, and robustness of various computational models for the LETC systems.

Scheme 4.1 presents the molecules and ions relevant to a formulation of the blue LETC film in Suntuitive™ "smart windows" given in Table 4.1. Both tertabutylammonium tetrabromonickelate ($(TBA)_2NiBr_4$) and dibromodi(1-pentylbenzimidazole)nickel(II) ($NiBr_2(Pbiz)_2$), were proposed to be the blue colored, high ε metal complex ($[M(h\varepsilon L)_4]^y$).

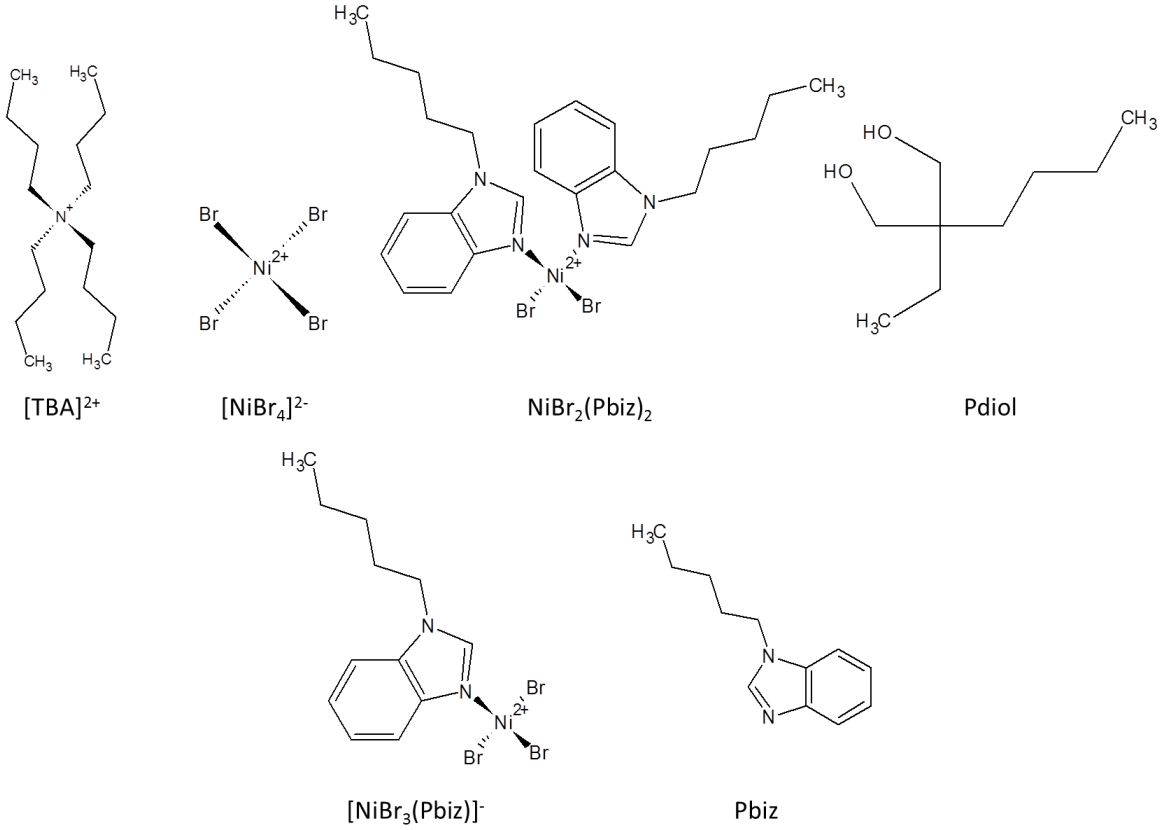

Scheme 4.1

To better understand the LETC system in the blue Suntuitive™ film, the system was first modeled starting at the structurally and compositionally well-defined ionic dissociation limit. At the ionic dissociation limit all complexes in the model are fully dissociated into their ligand, metal and counterion fragments. The concentration of each of the fragments in the model for the blue Suntuitive™ film can be seen in Table 4.1.

Table 4.1 Formulation of blue thermochromic polyvinylbutyral (PVB) Suntuitive™ window films.[154] Ionic dissociation limit fragment components, component concentrations, as well as the number of individual species found in a Ni^{2+} boundary box of volume 7550 Å^3.

	Concentration (mol dm^{-3})	Fragment (ionic limit)	Concentration at the ionic limit (mol dm^{-3})	Number of Fragments in Ni^{2+} Boundary Box
$NiBr_2(Pbiz)_2$	0.17	Ni^{2+}	0.17	1
		Pbiz	0.34	1 or 2
		Br^-	0.34	
$(TBA)_2NiBr_4$	0.04	Br^-	0.16	5
		Ni^{2+}	0.04	
		TBA^+	0.08	
TBABr	0.57	TBA^+	0.57	3
		Br^-	0.57	
Pdiol	1.10	Pdiol	1.1	5

The Ni^{2+} ion is the least concentrated species at the ionic dissociation limit; therefore, it was used to define a periodic boundary box. The volume of a Ni^{2+} periodic boundary box was calculated using Equation 4.1.

$$\frac{dm^3}{0.22\ moles\ Ni^{2+}} * \frac{1.0\times10^{27}Å^3}{dm^3} * \frac{1\ mole\ Ni^{2+}}{6.02\times10^{23} ions\ Ni^{2+}} = \frac{Å^3}{Ni^{2+} ion} \qquad (4.1)$$

The resulting volume of the Ni^{2+} boundary box is 7550 Å^3, which defines 19.6 Å or ~2 nm as the average distance between Ni^{2+} ions in the film at the fully mixed state of the ionic dissociation limit.

Figure 4.1 illustrates the process of finding the per molecule volumes available to the other ionic fragments and using it to solve for how many of each fragment appear in a Ni^{2+} boundary box.

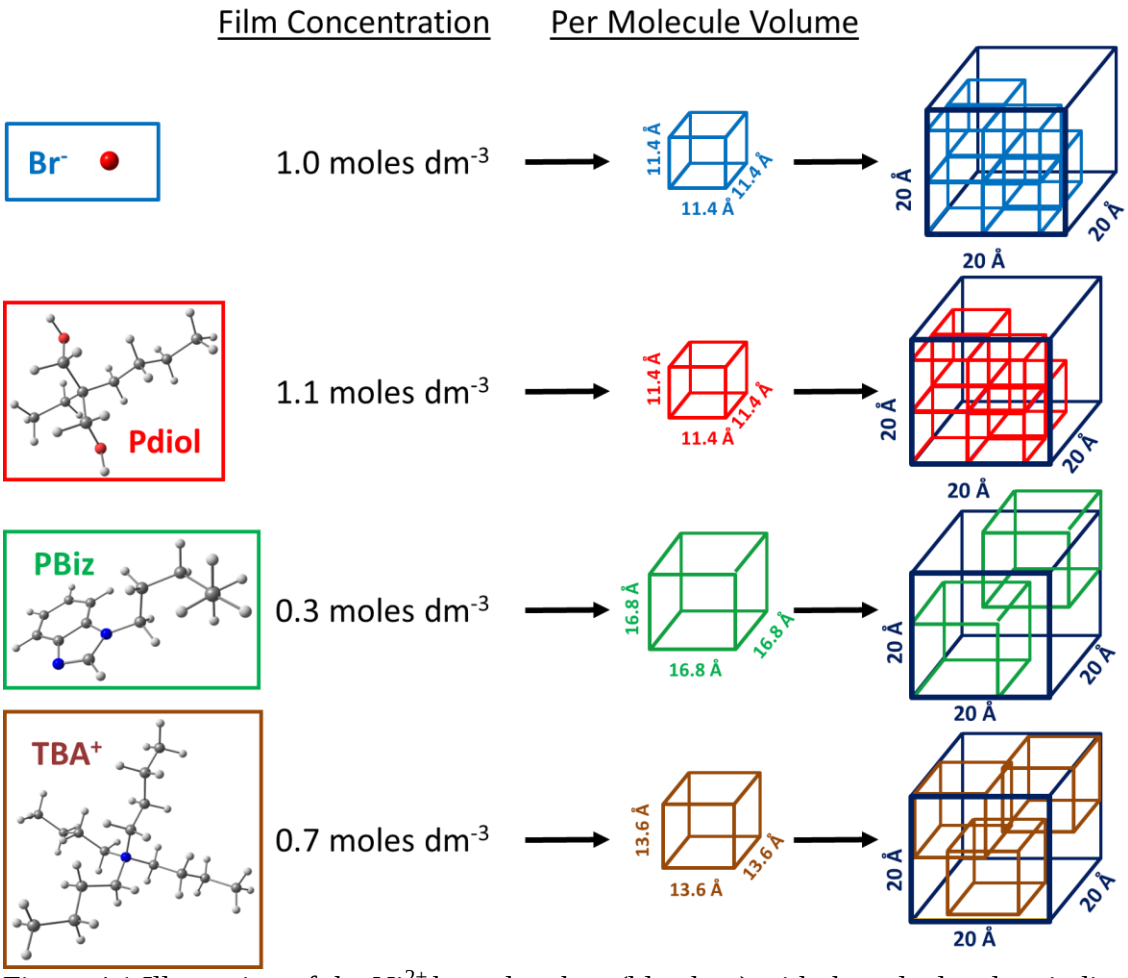

Figure 4.1 Illustration of the Ni^{2+} boundary box (blue box) with the calculated periodic boundary boxes for the Br^{-} (Blue), Pdiol (Red), Pbiz (Green), and TBA^{+}(Brown) fragments nested into the Ni^{+2} box.

The resulting number of each fragment present in a Ni^{2+} boundary box can be seen in Table 4.1.

To further improve a model for the chemical environment in the Ni^{2+} boundary box, the polymer matrix must be considered. Butvar B-90 is a thermoplastic polyvinyl butyral resin. It is composed of 18.5-20.5% polyvinyl alcohol, ~80% butyral, and a maximum of 2.5% acetate (Figure 4.2).[155]

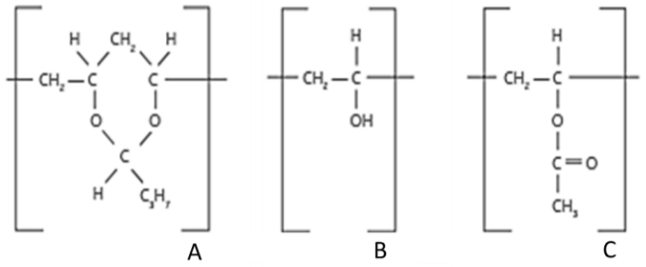

Figure 4.2 Structure of monomers that make up B-90 (PVB) resin. B-90 is ~80% polyvinyl butyral A, 18.5-20.5% polyvinyl alcohol B, and less than 2.5% polyvinyl acetate C.

Butvar B90 has an average molecular weight of 70 to 100 kg mole^{-1}. The 70 to 100 kg mol^{-1} range of molecular weights was used to define an average weight per polymer molecule (Equation 4.2)

$$\frac{85{,}000\ g\ Polymer}{mole\ Polymer} * \frac{1 mole\ Polymer}{6.02\times10^{23} strands} = \frac{g\ polymer}{polymer\ molecule} \qquad (4.2)$$

To represent the polymer, it is essential to know the number of each species of monomer (Figure 4.2) present in a given Ni^{2+} boundary box. The calculation was performed by first, solving for the number of each monomer component present in an average polymer unit using Equation 4.3.

$$\frac{85{,}000\ g\ Polymer}{mole\ Polymer} * \frac{g\ monomer}{g\ polymer} * \frac{1\ mole\ monomer}{g\ monomer} = \frac{monomer}{polymer} \qquad (4.3)$$

The fraction of an average polymer unit that fits into a Ni^{2+} boundary box was calculated using Equation 4.4

$$\frac{1\ mole}{85000\ g\ polymer} * \frac{1.10\ g\ polymer}{cm^3\ polymer} * \frac{1 cm^3}{1.0 \times 10^{24} Å^3} * \frac{6.02 \times 10^{23} units}{1 mole\ polymer} * \frac{7550\ Å^3}{Ni^{2+} boundary\ box} = \frac{Polymer\ molecule}{Ni^{2+} boundary\ box} \quad (4.4)$$

Each of the resulting monomer per polymer molecule values (Equation 4.3) was multiplied by the fraction of a single polymer unit in a Ni^{2+} boundary box (Equation 4.4) to get the number of times each monomer appears in a Ni^{2+} boundary box. On average each Ni^{2+} boundary box contains 22 poly(vinyl alcohol), 27 poly(vinyl butyral), and one poly(vinyl acetate).

The number of each fragment present in the 7550 $Å^3$ Ni^{2+} boundary box, reported in Table 4.1, allows for the formation of either the $[NiBr_4]^{2-}$, $NiBr_2(Pbiz)_2$, or even $[NBr_3(Pbiz)]^-$ chromophores in the film at high temperatures. The remaining fragments have the potential to form ion pairs (in the case of charged species TBA^+ with Br^-, $[NiBr_4]^{2-}$ or $[NiBr_3(Pbiz)]^-$) or coordination complexes (in the case of neutral species such as Pdiol and Pbiz).

Computational Methods

To organize the exploration of the balance between model size, level of theory, and accuracy required for a calculated system property (base of the tetrahedron in Figure 1.7), the methods used to calculate the system properties in this chapter are organized into a matrix representation (Figure 4.3). The matrix is organized such a way that the calculated properties of the model appear at the crossing of the methods used to

calculate electronic or geometric structure, and the methods for representing the chemical interactions within the computational model.

Model Composition (Size of Model)

Electronic and Geometric Structure Methods (Level of Theory)	Gas Phase / PCM	Charge Neutral	Periodic Boundary Box
DFT	• Optimized Geometry • Ground State • Electronic Structure • ΔH^0 , ΔS^0, ΔG^0 • Valence Excitations	• Optimized Geometry • Ground State Electronic Structure • ΔH^0 , ΔS^0, ΔG^0 • Valence Excitations	Computationally Prohibitive
Semi Empirical	• Optimized Geometry • Ground State Electronic Structure • ΔH^0	• Optimized Geometry • Ground State Electronic Structure • ΔH^0	• Ground State Electronic Structure • ΔH^0
Molecular Mechanics	• Optimized Geometry	• Optimized Geometry	• Optimized Geometry

Figure 4.3 Matrix representation of modeling efforts presented in this chapter.

Each section in this chapter will focus on a specific theoretical method, or level of theory, for calculating the electronic and geometric structures that are used to describe system properties. The following sections introduce the methods used to calculate electronic and geometric structure of LETC models and discuss the model composition that can be calculated by each.

Ab initio Wave Function Methods

Ab initio wave function methods can be used to calculate the electronic structure of model chemistry systems based on first principles. The Hartree Fock method

represents the wave function as a single Slater determinant of atomic orbitals. It then optimizes the linear combination of the atomic orbitals into molecular orbitals using the secular determinant given by

$$\begin{bmatrix} F_{11} - ES_{11} & \cdots & F_{1N} - ES_{1N} \\ \vdots & \ddots & \vdots \\ F_{N1} - ES_{1N} & \cdots & F_{NN} - ES_{NN} \end{bmatrix} = 0 \tag{4.5}$$

Where the matrix elements S_{ij} are overlap integrals in Equation 4.6

$$\int \varphi_i \varphi_j d\tau = 1 \tag{4.6}$$

and the matrix elements F_{ij} are given by Equation 4.7

$$F_{\mu\nu} = \left\langle \mu \middle| -\frac{1}{2}\nabla^2 \middle| \nu \right\rangle - \sum_{k}^{nucli} Z_k \left\langle \mu \middle| \frac{1}{r_k} \middle| \nu \right\rangle + \sum_{\lambda\sigma} P_{\lambda\sigma} \left[(\mu\nu|\lambda\sigma) - \frac{1}{2} (\mu\lambda|\nu\sigma) \right] \tag{4.7}$$

The first two terms on the r.h.s. of the equation are the so called "one-electron integrals" that calculate the electron kinetic energy and electron nuclear potential energy respectively. $P_{\lambda\sigma}$, within the second summation, is the density matrix, which uses the orbital coefficients to weigh the energy contribution from the so called "two-electron integral" terms within the brackets. These are the classical coulomb integral ($J_{\mu\nu}$) and the quantum exchange integral ($K_{\mu\nu}$) from left to right. A guessed density matrix is used to construct and solve the initial HF secular equation (Equation 4.5) which is in turn used to construct a new density matrix from the calculated occupied MOs. This is done via a self-consistent field calculation (SCF) until the new density matrix is sufficiently similar to the old.

HF calculations scale at N^4 where N is the total number of basis functions employed in a given calculation. Many computational codes use either Gaussian-type orbitals (GTO) basis functions for HF.[77, 156-158] Other basis set types include, Slater-type

orbitals and plane wave. Regardless of the type of basis set employed, a molecular calculation needs to use a basis set large enough that the addition of further basis functions does not affect the property under investigation, and only increases the computational cost.[159]

Density Functional Theory

DFT is built on the foundation of the Hohenberg-Kohn theorem[160] which states that a total electron density defines a unique external potential (position and charge of nuclei). The external potential determines the Hamiltonian of a system which in turn determines the wave function. If both the wave function and Hamiltonian of a system are known, the energy can be calculated. In other words, the electron density of a system determines its electronic energy. The Kohn-Sham (KS) equations[161] build on the density determines energy principle by representing the real electronic structure as a system of non-interacting electrons with the same total density. This identical total density ensures, via the Hohenberg-Kohn theorem, that both systems have the same total energy. The energy of the non-interacting system as a function of its density is broken down into the components in Equation 4.8

$$E[\rho(r)] = T_{ni}[\rho(r)] + V_{ne}[\rho(r)] + V_{ee}[\rho(r)] + \Delta T[\rho(r)] + \Delta V_{ee}[\rho(r)] \quad (4.8)$$

where the terms on the right hand side refer to the kinetic energy of the non-interacting electrons ($T_{ni}[\rho(r)]$), the nuclear–electron interaction($V_{ne}[\rho(r)]$), the classical electron–electron repulsion($V_{ee}[\rho(r)]$), the correction to the kinetic energy deriving from the interacting nature of the electrons($\Delta T[\rho(r)]$), and all non-classical corrections to the electron–electron repulsion energy respectively($\Delta V_{ee}[\rho(r)]$). These final two terms can

be combined into the so called exchange and correlation energy, $E_{xc}[\rho(r)]$. If an orbital representation of the density is used (Equation 4.9),

$$\rho = \sum_{i}^{N} \langle \chi_i | \chi_i \rangle \tag{4.9}$$

where the χ_i are the so called KS orbitals (orbitals in the single KS Slater determinant), a pseudoeigenvalue equation can be written (Equation 4.10).

$$h_i^{KS} \chi_i = \varepsilon_i \chi_i \tag{4.10}$$

In this equation h_i^{KS} is the KS one-electron operator given by

$$h_i^{KS} = -\frac{1}{2}\nabla_i^2 - \sum_{k}^{nuclei} \frac{Z_k}{|r_i - r_k|} + \int \frac{\rho(r')}{|r_i - r'|} dr' + \frac{\delta E_{xc}}{\delta_\rho} \tag{4.11}$$

where the fist three terms on the r.h.s. are the operators that determine the first three energies on the r.h.s. of Equation 4.11. The last term $\left(\frac{\delta E_{xc}}{\delta_\rho}\right)$ is the one electron operator whose expectation value, when operated on the KS Slater determinant, is the E_{xc}. The method for determining the KS orbital coefficients is analogous to solving for the orbital coefficients in HF using the secular determinant. The difference is the Fock operator in the $F_{\mu\nu}$ matrix element operating on the basis functions (given in equation 4.7) is replaced by the KS one-electron operator (given in equation 4.10).

DFT, as presented above, is exact in that it contains no approximations. The only term that is left ambiguous is the functional form of $E_{xc}[\rho(r)]$. The Hohenberg-Kohn theorem states that this functional form must exist, but provides no guidance as to what the form actually is. Because of this, considerable research has been done[162] to find functional forms that reasonably approximate this exact $E_{xc}[\rho(r)]$ functional. In an efforts to increase the accuracy of approximate $E_{xc}[\rho(r)]$ functionals in a non-empirical manner,

functionals were developed that contain energy as a function of the local density (Xα, and localize density approximation (LDA) functionals), as a function of the electron density gradient (generalized gradient approximations (GGA) functionals) and function of the electron density second derivatives (meta-GGA functionals). The LDA, GGA, and meta-GGA functionals form the lowest three rungs of a "Jacob's ladder"[163] for DFT (Figure 4.4).

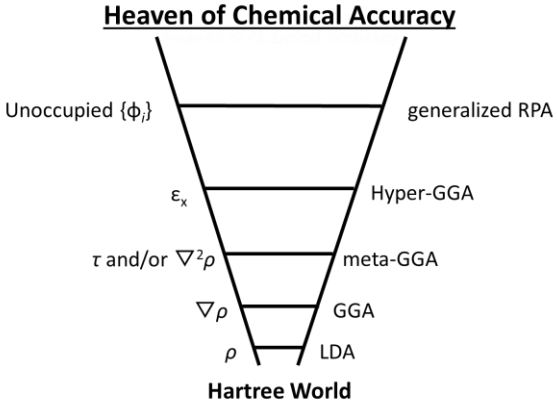

Figure 4.4 Perdew's Jacob's ladder[163] of density functional approximations to the exchange-correlation energy.

The ladder is organized vertically where each rung incorporates an increasingly more complex topology of the electron density into the calculation of the energy.[163] The highest two rungs are made up of the non-local hyper-GGA[99] and random phase approximations (RPA) with exact exchange functionals.[164] Hype-GGA and RPA methods, although highly accurate, are currently computationally too costly for coordination chemistry based applications. Therefore, the best option for calculating electronic structures for the chromophores in LETC systems is to calibrate lower rung functionals to experimental results as discussed above.

An alternative scheme introduced by Becke to approximate density functionals uses hybrid exchange expressions.[102] Hybrid methods mix exact Hartree-Fock exchange (HFX) and GGA or meta-GGA exchange functionals. From a coordination chemist perspective, this mixing is a tool for empirically tuning of the ionic vs. covalent nature of the calculated metal-ligand bonding. GGA functionals, such as BP86,[56, 92] often lead to overly covalent descriptions of ground state electronic structure. Hybrid functionals, such as B3LYP[102] which mixes in 18% exact HFX, can improve the accuracy of electronic structure calculations on coordination complexes.[55]

DFT can be used to calculate energy using the electron density which is a function of the three Cartesian coordinates. This should lead to N^3 scaling of the calculation. Unfortunately most DFT codes use a HF like algorithm that scales at N^4.[165] Despite the fact that this is similar scaling to HF one must consider that DFT is a correlated method that can provide accurate electronic structure calculations of up to 300 atoms with 2000 GTOs. This makes geometry optimizations of thermochromic chromophores computationally accessible (4 days for a Gaussian 09[77] B3LYP geometry optimization of gas phase $[Ni(Pdiol)_3]^{2+}$ consisting 298 electrons represented by 1428 GTOs using an 8 processor compute server), therefore DFT models cannot incorporate all the fragments in a given Ni^{2+} boundary box. DFT computational times limited calculations to the optimization of single chromophores and some truncated counterions.

Time Dependent Density Fucntional Theory The perceived colors of LETC chromophores are due to the absorption of photons, and promotions of electrons forming excited electronic states. Therefore, computational prediction of color is based on the

calculated energy difference between the ground and excited-states. A first order approximation to the excitation energies of a $[M(heL)_4]^{2-}$ complex can be made by taking the difference between the β occupied orbitals (including all metal ligand bonding, ligand non-bonding, and metal ligand antibonding orbitals) and the degenerate unoccupied β d_{xz}, d_{yz} orbitals. The error in the calculated excitation energies can be attributed to the fact that DFT does not optimize the unoccupied MOs during SCF cycles. To make ground state calculated excitation energies more chemically relevant, excited-state electron relaxations need to be considered. Excited-state relaxations can be accounted for by performing SCF calculations on a ground-state derived excited state formed by the promotion of one electron to a previously unoccupied orbital (in the case of the $[NiX_4]^{2-}$ the β d_{xz}, d_{yz} orbitals). The resulting energy difference between the SCF optimized excited-state and the ground-state is termed the ΔSCF. Systems with excited states that have the same spatial or spin symmetry as the ground-state they are derived from optimize back to the ground-state during the SCF procedure. This problem is known as variational collapse.

A more accurate method for calculating excitation energies, relative to ΔSCF calculations, is TD-DFT. TD-DFT allows for the simulation of valence or core electronic excitation spectra. As a molecule is subjected to a simulated fluctuating electric field, the resulting excitation can be approximated by:

$$\langle \alpha \rangle_\omega = \sum_{i \neq 0}^{states} \frac{|\langle \Psi_0 | r | \Psi_i \rangle|^2}{\omega - (E_i - E_0)} \tag{4.12}$$

where $\langle\alpha\rangle_\omega$ is the frequency-dependent probability of transition. The numerator is the transition dipole probability density and the denominator is the difference in frequency between the incident radiation and the ground and excited state energies. When the incident radiation frequency (ω) matches the difference in energy between the excited state and the ground state (E_i-E_0), the equation diverges (the denominator goes to zero), forming a pole in the frequency-dependent polarizability. Using propagator methodologies, poles can be determined without having to compute all the necessary excited-state wave functions. TD-DFT results are most reliable for, excitation energies that are significantly smaller than the molecular ionization potential of the molecule (note, excitations from orbitals below the HOMO are allowed), and for promotions that do not take place into orbitals with positive KS eigenvalues.[166] Neither of these constraints is an issue when calculating excitations in the visible energy region of interest in the LETC chromophores.

Semi-Empirical Methods

Semi-empirical methods contain empirically parameterized one and two electron integral values that are normally explicitly calculated in the HF secular determinant during an SCF cycle(Equation 4.7). Semi-empirical methods only consider valence electron interactions. Methods are differentiated based on the integrals that they parameterize or neglect in their respective Hamiltonians. Table 1.3 summarizes the types of Hamiltonians discussed in this section and their associated parameterizations.

Table 4.2 Summary of available semi-empirical methods and their parameterizations.

Method	Distinctive Neglected or Parameterized Interactions	Implementations
CNDO	Neglect of overlap between non-like basis functions	CNDO/1, CNDO/2, CNDO/BW
INDO	Parameterizes one center two electron integrals between non-similar basis functions	INDO/S
NDDO	Parameterizes two-center two-electron integrals	AM1, PM3,PM7

The first semi-empirical method was termed complete neglect of differential overlap (CNDO).[167, 168] The method sets the overlap between all non-similar basis functions equal to zero. This greatly reduces the number of matrix elements needed to calculate the secular determinant (Equation 4.5). The remaining two electron integrals (Coulomb and exchange integrals) and all diagonal one electron integrals (electron kinetic energy and electron nuclear potential) are set equal to empirically derived constants that are functions of atomic ionization potential and atomic electron affinity. The off-diagonal one-electron integrals are evaluated using an empirically derived constant, but the value is weighted by the evaluated overlap integral between the off-diagonal basis functions. CNDO methods are successful in predicting visible absorption spectra of organic molecules.[168] Because the method fails to distinguish between the orientations of unlike orbitals it is ineffective in geometry optimization.

The intermediate neglect of differential overlap (INDO) methods correct for the orientation of unlike orbitals problem by introducing parameterized values two electron interactions where the electrons are located on differing atomic orbitals at a given center.[169] INDO methods do not distinguish between interactions of similar or dissimilar

orbitals on neighboring atoms and therefore have poor performance in geometry optimizations.

The neglect of diatomic differential overlap (NDDO) methods further relaxes the constraints on two center, two electron integrals.[170, 171] The Austin Model 1 (AM1) parameterized the nuclear repulsion energy making reliable geometry optimization possible.[172, 173] The performance of AM1 was improved further when Parameterized Model 3 (PM3)[174, 175] was developed using a mathematical algorithm to simultaneously optimize the AM1 parameter set to reproduce heats of formation of an extensive test sets of molecules. Subsequent optimizations of PM3 parameters and modification of the way various quantum interactions were treated led to the development of the PM6[176] and PM7[177] methods. NDDO methods can be used to calculate molecular heats of formation by replacing atomic SCF values of the molecular SCF energy by experimental atomic heats of formation values. These semi-empirical molecular heats of formation can be used to optimize the geometries of LETC systems and calculate the resulting heats of reaction for systems of around 10,000 atoms at and accuracy of 33kJ $mole^{-1}$.[177]

Computational Thermochemistry

Thermochemistry allows for the calculation of reaction enthalpies, entropies, and thus free energies using optimized electronic structure and molecular geometry. A normal mode analysis is performed and the vibrational, and rotational mode energy levels are calculated. The ground state energy of all the normal modes are summed and added to the total electronic energy to calculate the zero point energy (E_{ZPE}) of the molecule. The molecular

partition function q, is used to determine which normal mode energy levels are thermally accessible (Equation 4.13).

$$q = \sum g_i e^{-\frac{\varepsilon_i}{kT}} \tag{4.13}$$

The partition functions for molecular translation, rotation, vibration and electronic motion are used to calculate total molecular entropy (S_{tot}) and internal thermal energy (E_{therm}), as seen in Equation 4.14 and 4.15 respectively

$$S_{tot} = R\left(ln(q_t q_e q_r q_v e) + T\left(\frac{\partial lnq}{\partial T}\right)_v\right) \tag{4.14}$$

$$E_{therm} = R\,T^2\left(\frac{\partial lnq}{\partial T}\right)_V \tag{4.15}$$

where R is the ideal gas constant, k_B is the Boltzmann constant, the partition functions are for molecular translation (q_x), electronic motion (q_e), molecular rotation (q_r), and molecular vibration (q_v) while T is the absolute temperature in Kelvin. The absolute entropy

Equation 4.16 is calculated by Gaussian using Equation 1.14 assuming 1 atm of pressure. The LETC systems consist of are solutes in solution with a 1 mole per liter ideal standard state. Compressing the 1 atm gas standard down to one mole per liter decreases the absolute entropy of each molecule by -26.58 J mol^{-1} K^{-1}. This creates an increase of 7.9 kJ mol^{-1} in the free energy of reaction per each molecule at 298K. This value needs to be added to all entropy calculations in this section.

The thermal enthalpy correction (H_{corr}) due to molecular motion of the system is calculated by adding k_BT to the E_{therm}.

$$H_{corr} = E_{therm} + k_B T \tag{4.16}$$

The H_{corr} term is added to the E_{ZPE} to calculate the absolute enthalpy of the molecule H_{tot}. The H_{tot} value is added to the S_{tot} in order to calculate the absolute free energy (Equation 4.17).

$$G = H_{tot} - TS_{tot} \tag{4.17}$$

The calculated H_{tot} and S_{tot} can be used along with Hess's law to calculate free energies of reaction. These calculations are accessible for systems whose largest chromophores have around 100-150 atoms, 400-450 electrons with around 1500 GTOs per molecule.

Polarizable Continuum Models The theoretical system properties from the previous sections are calculated for molecules in ideal gas-like molecular environments. Ignoring the influence of solvent/solute or solute/solute interactions poses a problem for LETC systems solvated in non-polar solvents.[20] Experimentally, varying a solvent can shift solute excitation spectra, the effect is known as solvotochromism.[178] The effect is due to either increased or decreased polarizability of the solute molecule in a given solution. The electrostatic solvent/solute interactions that lead to changes in a solutes polarizability can be considered implicitly by embedding the solute molecule within a polarizable continuum model
(PCM).[78, 80, 82, 83] In the PCM the solute molecule is placed a cavity, the surface of which, is made up of a grid of interacting finite dielectrics. The polarization of the dielectrics is self consistently adjusted in response to the changing charge distribution of the molecule during a molecular SCF calculation. Another method closely related to PMC is the conductor like screening model (COSMO).[179, 180] In COSMO based methods where the

continuum is modeled as a conductor-like picture where its polarization charges are derived from a scaled-conductor approximation.

To capture weak non-electrostatic solvent solute interactions such as Van der Waals or dispersion forces, explicit solvation modeling is needed. Explicit solvation models are created by surrounding the solute molecule with solvent molecules modeled at the same level of theory as the solute. Explicit solvation techniques are very useful in LETC systems with high ion and ligand concentrations that have the possibility for ion pairing. Experimentally ion pairing causes activity coefficients to deviate from the ideal value of one. Theoretically the deviation originates from the enthalpy of interaction between neighboring ions. Explicit modeling of ions pairs within explicit solvation models can quickly become computationally prohibitive with respect to model size. To explicitly account for the contribution of weak interactions to a systems free energy, lower levels of theory must be used.

Molecular Mechanics

Generally bond lengths and force constants between atoms transfer from one molecule to the next. The transferability allows the difference in energy of two isomers to be defined as the sum of the difference in their "strain" energies. Strain refers to a fictitious positive deviation from the zero energy of internal coordinates at equilibrium structural position. Molecular mechanics (MM) methods can be used to calculate strain energies of atoms in molecules by summing the deviation in their interactions from their equilibrium values and quantitatively evaluating those using parameterized classical potentials. The potentials are defined for parameterized atom types within a specified

molecular connectivity. Different MM methods are characterized by the force fields that are defined by the functional form of the energy potentials, the atom types, and the associated parameters. Some force fields are more holistic then others in that they provide less accurate results for a wider range of atom types, while others are more specialized providing accurate results for a small group of atom types.

Equation 4.18 shows the sum of potentials as part of the MM3 force field used in this dissertation

$$E_{total} = \sum E_S + \sum E_B + \sum E_{OOP} + \sum E_{SB} + \sum E_{BB} + \sum E_T + \sum E_{ts} + \sum E_V + \sum E_Q \quad (4.18)$$

Where the sums extend over all bonds, bond angles, torsion angles and non-bonded interactions between atoms not bound to each other of to a common atom. Table 1.4 list the symbols used in Equation 4.18 and their definitions.

Table 4.3 List of abbreviation used in Equation 4.18 and their definitions

Abbreviation	
ES	Energy of a bond stretched or compressed from its natural bond length
EB	energy of bending a bond angle from its natural value
EOOP	Energy of bending a planar atom out of its neighbors' plane
ESB	Energy of interaction between bond stretching and angle bending. Stretch bend is limited to angles at the end of a bond being stretched
EBB	Energy of interaction between two bending angles. Bend-bend is limited to the angles centered on a common atom
ET	Energy of twisting (torsion) about a bond
Ets	Energy of interaction between angle twisting and bond stretching. Torsion-stretch is limited to torsion about the bond being stretched
EV	Energy due to van der Waals non bonded interactions (also hydrogen bonding)
EQ	Energy due to electrostatic interactions between ions

Both bond stretching and bond bending energies in MM3 are calculated using modifications of the harmonic spring deformation potential. The torsional energy is calculated using Fourier series expansions. The cross term interactions E_{SB} , E_{ts}or E_{BB} are calculated using an empirical parameter multiplied by the product of the two deviations from their equilibrium values (i.e. deviation from equilibrium bond length and bond angle in E_{SB}). The van der Waals energy is calculated using a Hill potential

$$E_V = \epsilon^{\#}\left(1.84 \times 10^5 e^{-\frac{12R}{r_i + r_j}} - 2.25\left(\frac{r_i + r_j}{R}\right)^6\right) \quad (4.19)$$

Where $\varepsilon^{\#}$ is determined by the relative hardness of the two atoms, $r_{i,j}$ are the van der Walls radii of atoms i and j, and R is their effective interatomic distance. The electrostatic energy is calculated using the Coulomb potential.

The Newton–Raphson procedure is used to optimize geometries minimizing strain energies within a model. For LETC models of more than 1,000 atoms with many non-bonding interactions this method can lead to minimization of molecules into local minima. To avoid this, Monte-Carlo optimization methods are used to search potential energy surfaces for global minima that were started form a modest set of various initial geometries.

Parameterization of transition metal parameter is an area of current research.[181] This dissertation expands on this work by parameterizing the MM3 parameter set to optimize Ni(II) thermochromic systems for global geometric minima. Since the MM energy values are not suitable for deriving experimentally useful thermochemical

properties, we utilized the MM structures in subsequent semi-empirical PM7 calculations for obtaining enthalpy of reaction values.

Molecular mechanics allows for geometry optimizations of hundreds of thousands of atoms,[182] employing empirically parameterized force fields that are used to calculate forces between bonded and non-bonded atom types. As discussed in the introduction, a variety of force fields are available to optimize geometries of organic molecules, polymers, and biological systems, but most lack parameterizations for the diverse bonding of transition metals in coordination compounds. To optimize geometries for coordination compounds existing force field must be modified. We chose to modify the MM3[183] force field within the Tinker molecular mechanics package[184] due to its preexisting parameterizations for bromine found in organic molecules and nickel found in nickel oxides. The existing nickel and bromine parameters were modified to account for variation in their bonding within coordination compounds.

Experimental Blue Film Excited State Structure, and LETC Thermodynamics

Experimental Electronic Structure and Thermodynamics of Blue Suntuitive™ Film

Figure 4.5 shows the temperature dependent visible (VIS) spectrum of the blue LETC film created using the formulation in Table 4.1.

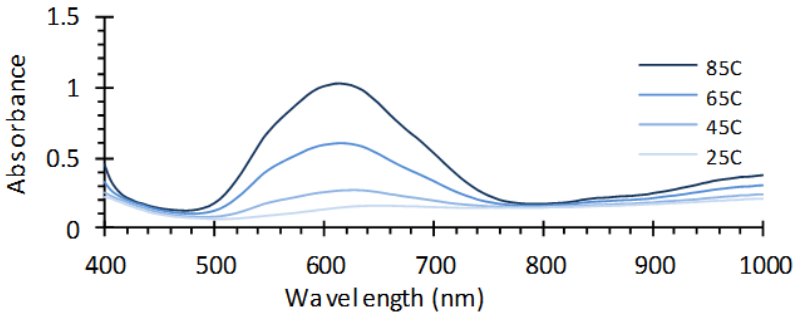

Figure 4.5 Temperature dependent VIS spectra of blue Suntuitive^{TM} LETC film composed of 0.04 m $(TBA)_2NiBr_4$, 0.17 m $NiBr_2(Pbiz)_2$, 0.57 m Pdiol, 3GO plasicizer, in PVB taken at Pleotint LLC.[154]

The blue film high temperature absorption band between 500 and 750 nm is broader and red shifted (λ_{max} = 605 nm) relative to the $NiBr_2(Pbiz)_2$ absorption (λ_{max} = 57 5nm) in GBL (purple line Figure 4.6). One possible reason for these differences is the variation in solvent environments in the PVB and more polar γ-Butyrolactone (GBL).[185] Another possibility is the presence of multiple chromophores. The UV-Vis spectra of another potential chromophore identified by the Ni^{2+} boundary box model, $[NiBr_4]^{2-}$ (λ_{max} = 575nm), is 30 nm red shifted relative to the blue film λ_{max}.

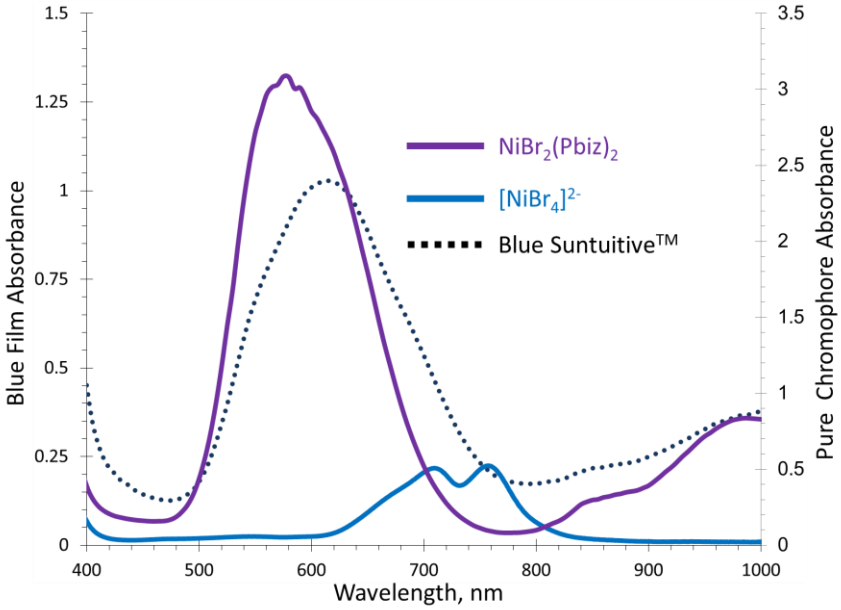

Figure 4.6 UV-Vis spectra of 20mM $NiBr_2(Pbiz)_2$ and 0.58 M Neopentyl Glycol in GBL at 85 °C used as a representative spectrum of pure $NiBr_2(Pbiz)_2$ (ε~220 mol L^{-1} cm^{-1}) recorded by Pleotint LLC.[154] 20mM $(TBA)_2[NiBr_4]$ in GBL. 85°C spectrum of blue Suntuitive™ LETC film with composition given in table 4.1 taken at Pleotint LLC.[154] (dotted blue line left Y axis)

The uncertainty in the number and identity of chromophores in the film make it difficult to experimentally determine equilibrium constants, and thus ΔH^0, and ΔS^0 for the LETC equilibrium. To better understand a reasonable range for the thermodynamics of the film an example system had to be examined.

A solution based LETC systems can be made by titrating lεL, trimethylolpropane (TMoP) (final concentration 80mM), into a GBL solution of $[NiBr_4]^{2-}$ (10mM $Ni(ClO_4)_2 \cdot 6H_2O$, and 100 mM TBABr) until the system is decolored. Figure 4.7 is a grouping of temperature-dependent UV-VIS-NIR spectra of the $[NiBr_4]^{2-}$ LETC system in GBL.

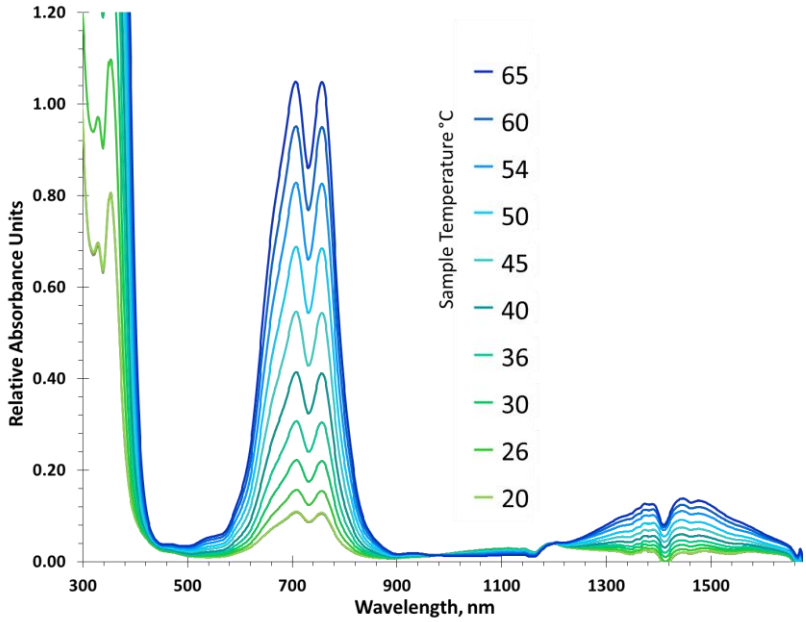

Figure 4.7 Temperature dependent UV-VIS-NIR spectra of LETC system with component concentrations of 10mM $Ni(ClO_4)_2 \bullet 6H_2O$, 80mM TMoP, and 100 mM TBABr

The lack of isosbestic points within the spectra indicate the increase in the concentration of a single species (the absorption of the $[Ni(TMoP)_2]^{2+}$ lεL complex is covered by the highly absorbing $[NiBr_4]^{2-}$ CT band at 350 nm). Therefore, the temperature dependent spectra can be used to monitor the concentration of the $[NiBr_4]^{2-}$ in solution via the prominent $^3T_1 \rightarrow {}^3T_1(P)$ transition (ε = 295 L mole^{-1} cm^{-1}). The relationship between temperature and changing chemical composition allows for experimental determination of the temperature dependent equilibrium constant (Figure 4.8 Equation B). Using a van't Hoff plot (Figure 4.8), the linear fit of the natural logarithm of the temperature dependent equilibrium constant plotted against the inverse temperature gives an experimental measure of the reaction enthalpy, and entropy thus free energy (Figure 4.8-Equation A).

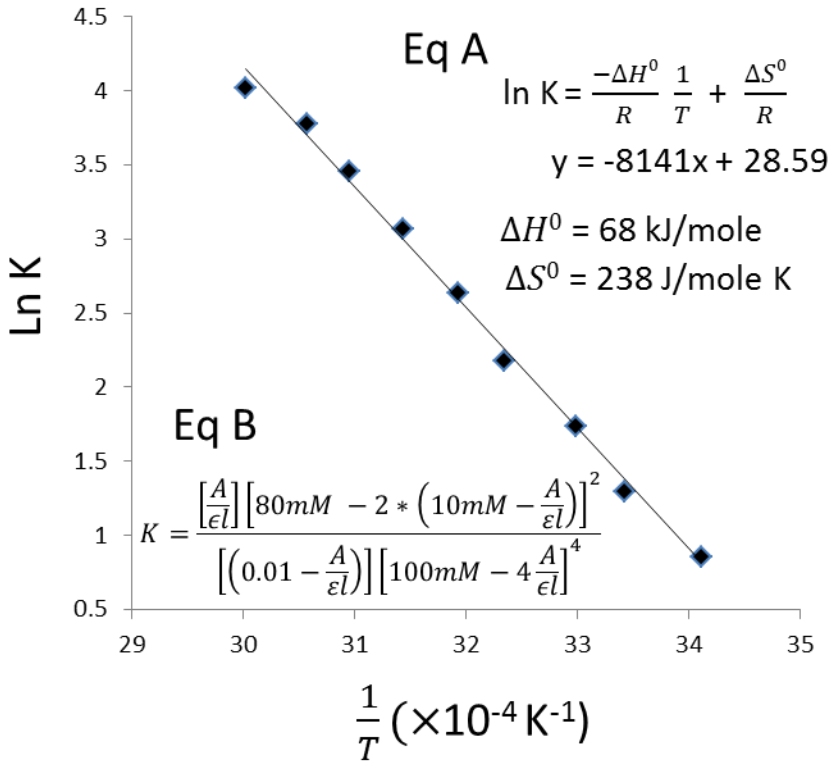

Figure 4.8 van't Hoff plot and thermodynamic parameters for $[NiBr_4]^{2-}$ LETC system A) Linear fit parameters Eq B) Method for solving for equilibrium constant for a given temperature based on the absorption intensity at 757 nm.

The ΔH^0 and ΔS^0 values determined in the van't Hoff plot are consistent with values found previously for similar LETC systems.[3]

The other factor to consider in the $[NiBr_4]^{2-}$ LETC free energy is the RTlnQ term. This is the portion of the free energy due to the systems deviation from the defined, infinitely dilute, standard state of reactants and products. To numerically access the energetic contribution of the RTlnQ term on the ΔG_{rxn} at a given temperature we need to first know what the system's equilibrium state (K_{eq}) is at that temperature. In the case of the $[NiBr_4]^{2-}$ system at 298 K, K_{eq} can be solved using the UV-VIS spectrum and the experimental concentration of $[NiBr_4]^{2-}$ in the same manner as the van't Hoff plot. In the

case of the $[NiBr_4]^{2-}$ system the K_{eq} at 298 K is 2.4, which makes the RTlnQ(293K) term +2.1 kJ mol^{-1}. At 298 K, K_{eq} = Q(293) and ΔG_{rxn}= 0 but once the temperature is increased $K_{eq} \neq$ Q(298K) and T[RlnQ(293K)] = T [0.025 kJ mol^{-1} K^{-1}] needs to be recalculated at the new temperature and the energy added to ΔG^0_{rxn} to determine spontaneity at the new temperature.

Normally non-linearity in van't Hoff plots would be a concern for non-ideal solutions like those assumed in thermochromic smart windows. In contrast most characterized LETC systems ΔH^0 values that are roughly constant across the temperature ranges that they operate in windows.[3]

Byker et al reported[3] the optimum range for smart window LETC system ΔH^0 and ΔS^0 is ~40-90 kJ mol^{-1} and ~60-315 J mol^{-1} K^{-1} respectively.[3] The systems previously examined in this dissertation fall within this range. The values are similar to those discussed in Chapter 2 for the thioether complex $[Ni(ttctd)]^{2+}$ (ΔH^0 = 60 kJ mol^{-1} and ΔS^0 = 190 J mol^{-1} K^1, in GBL with lεL = neopentyl glycol). The aqueous $[NiCl_4]^{2-}$ LETC system discussed in the introduction has a ΔH^0 = 167 kJ mol^{-1}, and ΔS^0= 470 J mol^{-1} K^{-1}. The increased value of ΔH^0 and ΔS^0 relative to the $[NiBr_4]^{2-}$ TMoP LETC system can be attributed to switching the low epsilon ligand (lεL) from a ligand to the solvent. The aqueous system therefore serves as an upper limit on the LETC systems enthalpy of reaction. The examples above support the range, and add an upper limit (ΔH^0 =167 kJ mol^{-1}) for reasonable values of the thermodynamics that will be calculated for the Blue Suntuitive™ LETC system film.

Density Functional Theory Models

Exchange and Correlation Functionals As Empirical Parameters The ground state DFT calculations of orbital character in Chapters 2 and 3 demonstrated the difficulty of finding a single exchange and correlation functional that performs well across the wide variety of available bonding in Ni(II) complexes. To ensure the accuracy of the calculated system properties of the blue LETC film, an exchange and correlation functional was chosen using chemically similar molecules to those potentially found in the blue film. With this in mind, the $[NiX_4]^{2-}$ series was used to survey, and ultimately empirically select an exchange and correlation functional based on its ability to reproduce experimental UV-VIS spectra.

The $[NiBr_4]^{2-}$ chromophore was used as an initial model to evaluate the performance of various excited state methods discussed in the introduction. Figure 4.9 shows the MO diagram of the BP86[56, 92] calculated ground state of a D_{2d} symmetrized $[NiBr_4]^{2-}$ complex with Ni-Br bond lengths of 2.46 Å and Br-Ni-Br angles of 111° and 106°. The valence excitation energies of the $[NiBr_4]^{2-}$ complex were first estimated by taking the difference between in the β occupied orbitals (including all metal ligand bonding, ligand non-bonding, and metal ligand antibonding orbitals) and the degenerate unoccupied β d_{xz}, d_{yz} orbitals.

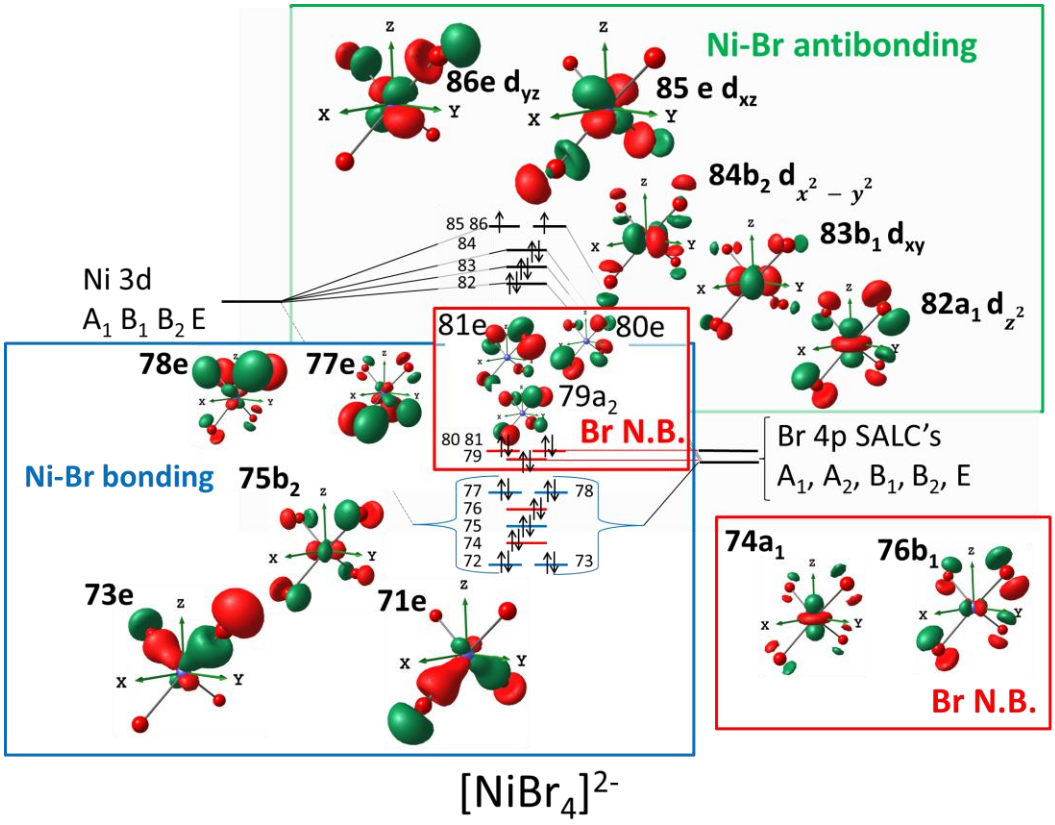

Figure 4.9 MO diagram of BP86/def2-TZVP/PCM(GBL)[78-80, 82, 83] optimized D_{2d} $[NiBr_4]^{2-}$ complex.

As discussed in the introduction, time dependent density functional theory (TD-DFT) is a linear response method that propagates the ground state density in response to a simulated external field. Figure 4.10 compares excitation energies calculated using BP86 TD-DFT to the experimental spectrum of $[NiBr_4]^{2-}$.

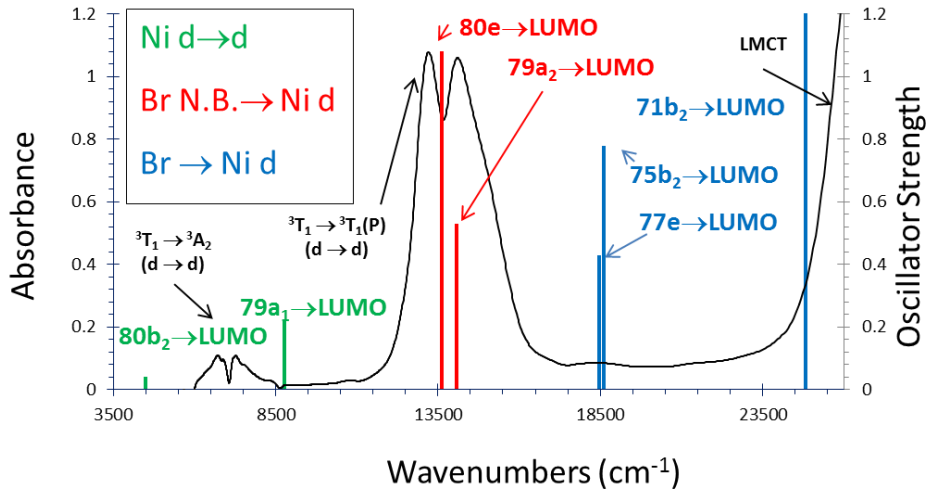

Figure 4.10 $[NiBr_4]^{2-}$ TD-DFT BP86/def2-TZVP/PCM(GBL) calculated transitions overlaid with UV-VIS-NIR spectrum of 10mM $TBA_2[NiBr_4]$.

The calculated CT states around 13500 cm^{-1} are lower in energy than experimentally predicted (25500 cm^{-1}). As discussed in the previous chapter, BP86 is known to calculate overly covalent ground states. This is also true for excited states, which results in lower energy transitions.

The hybrid B3LYP functional was used to calculate the TDDFT transitions shown in Figure 4.11. Upon initial inspection it seems as though the agreement has worsened in comparison to figure 4.10, but when the type of calculated transition is compared to the experimental assignment it can be seen that Figure 4.11 is actually an improvement. The B3LYP functional not only increased the energy of the CT transitions but also allowed for mixing of CT states into the d→d transitions (indicated by the coefficient to the left of each state).

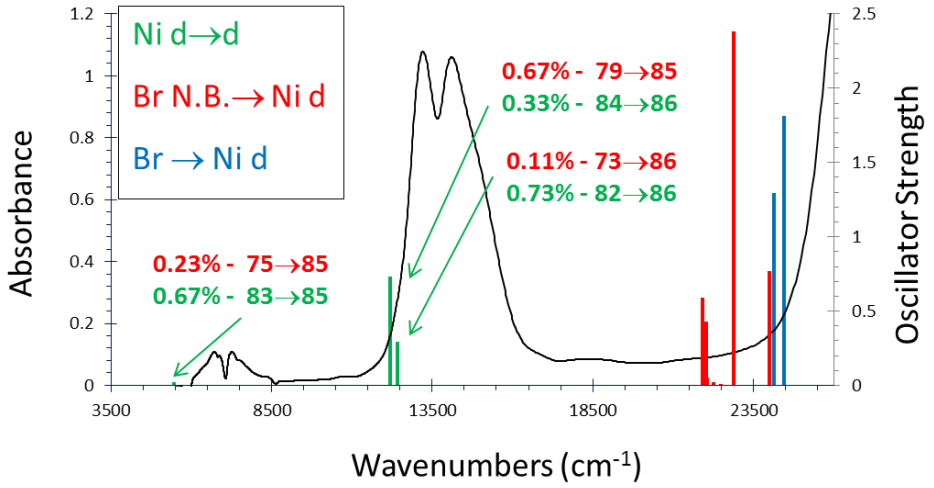

Figure 4.11 $[NiBr_4]^{2-}$ TD-DFT BP86/def2-TZVP/PCM(GBL) calculated transitions with mixing coefficients overlaid with UV-VIS-NIR spectrum of 10mM $TBA_2[NiBr_4]$.

Both the energy and composition (CT mixing) of the B3LYP calculated transitions supports the need for a hybrid functional to reproduce the proper excited state electronic structure.

Increases in accuracy, relative to the B3LYP functional, in this study were made by determining the appropriate mixing of HF exact exchange to be mixed with local and non-local density functionals creating a semi- empirical density functional. The $[NiBr_4]^{2-}$ test system was extended to incorporate the entire $[NiX_4]^{2-}$ series. GGA, meta-GGA, and hybrid GGA functionals, discussed in the introduction, were used within the user-defined model functionality in Gaussian 09[77] to calculate transition energies for the $[NiX_4]^{2-}$ series. The method in Gaussian 09 can incorporate any exchange and correlation functional and has the form

$$P_2E_x^{HF} + P_1\left(P_4E_x^{SLATER} + P_3\Delta E_X^{non-local}\right) + P_6E_C^{local} + P_5\Delta E_C^{non-local} \qquad (4.20)$$

where P_1 thru P_5 are coefficients that adjust the relative amount of exact, local, non-local exchange, and local, non-local correlation.[186]

The $[NiX_4]^{2-}$ time-dependent density functional survey was performed by Brett Patterson, MSU undergraduate student working under my guidance in three phases. During the first phase the correlation functional remained constant while the exchange was varied. During the second phase the exchange functional found to produce the best results, was held constant while varying the density functional correlation. For the HF mixing phase P_2 and P_1 (4.20) were adjusted, such that their total came to 100%, to find the best calculated spectral agreement across the entire halide series.

Figure 4.12 A shows the TD-DFT TPSSP86/6-311G+(d) /PCM(GBL) calculated $[NiX_4]^{2-}$ transitions done in phase 1 of the functional survey where the P86 correlation functional was held constant and the exchange was varied. The average error across all transitions for the $[NiX_4]^{2-}$ series calculated with the TPSSP86 functional was 1760 cm^{-1}. Comparing Figure 4.12 B with Figure 4.12 A shows the large change in transition energy due to changing the exchange while holding the correlation functional constant. A list of the average error across all transitions in the $[NiX_4]^{2-}$ series for all the exchange functionals tested in the phase 1 can be seen in Table 4.2.

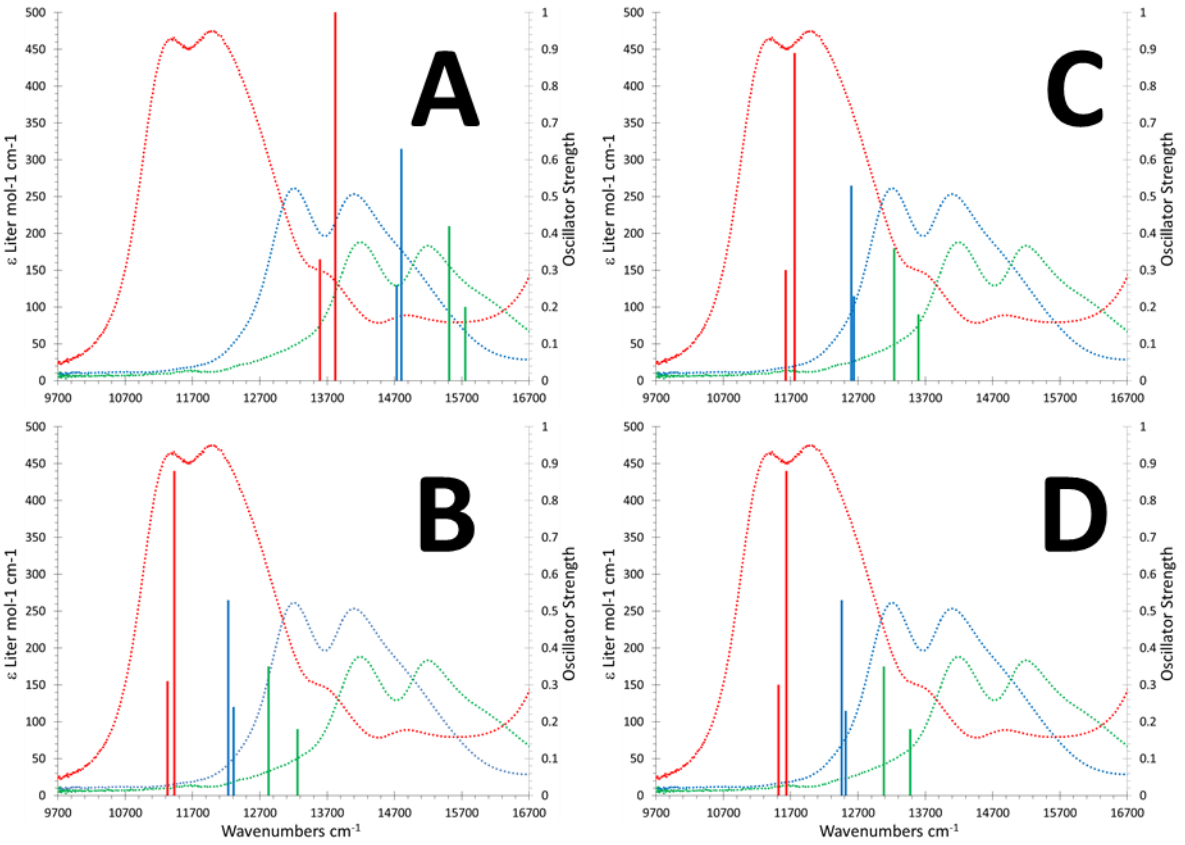

Figure 4.12 UV-VIS for $[NiX_4]^{2-}$ (X= Cl green, Br blue, I red) for d→d transitions with scaled oscillator strengths for A) TD-DFT TPSSP86/6-311G+(d) /PCM(GBL), B) TD-DFT PBEP86/6-311G+(d) /PCM(GBL), C) TD-DFT BPBE/6-311G+(d) /PCM(GBL) D) TD-DFT BTPSS/6-311G+(d) /PCM(GBL)

Figure 4.12 C and D show two sets of calculated $[NiX_4]^{2-}$ spectra done in phase 2 of the functional survey where the B88 exchange functional was held constant while the correlation was switched from meta GGA (TPSS) to GGA (PBE). Notice that changes in the correlation have less of an effect on the calculated excitation energies. Average error results from phase 2 can be seen in Table 4.2.

Table 4.4 The Average absolute error cm^{-1} in TD-DFT calculated $[NiX_4]^{2-}$ series excitation energies calculated in phase 1 and 2 of the exchange and correlation functional survey using 6-311G+(d)/PCM (ε=30.0).

	B88	PW91[97]	G96[96]	PBE[93]	O[91]	TPSS[99]
Phase 1: Average Absolute Error Across $[NiX_4]^{2-}$ Series cm^{-1}	1015	1086	1037	1129	1364	1726
	LYP	PW95[96]	PBE[93]	TPSS[99]	P86	
Phase 2: Average Absolute Error Across $[NiX_4]^{2-}$ Series cm^{-1}	1176	792	1000	1085	725	

The GGA exchange functional B88 performed the best across the entire $[NiX_4]^{2-}$ series with an average error of 1015 cm^{-1}. P86 was the best performing correlation functional, with an average absolute error of 725 cm^{-1}.

As the percent of HF mixed with the DFT exchange increases the energy of the transition increases (Figure 4.13). In phase three the percent of HF exchange mixing was varied for BP86 functional. From the shift in Figure 4.13 it can be estimated that an increase of 10% in the HF mixing moves the d→d transitions 800 cm^{-1}.

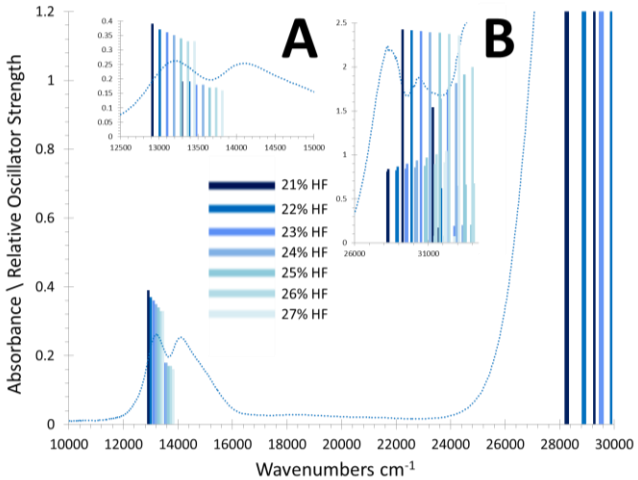

Figure 4.13 TD-DFT BXHFP86/6-311G+(d) /PCM(GBL) (X=%HF mixing) calculated excitation energies overlaid with the experimental $[NiBr_4]^{2-}$ spectrum.

The best functional to model the blue film was selected by finding the proper amount of exact exchange that gave the lowest absolute error across all transitions in the entire $[NiX_4]^{2-}$ series. The B23HFP86 functional was determined to be the most accurate functional and the excitations calculated for the $[NiX_4]^{2-}$ series can be seen in Figure 4.14 overlaid with the experimental UV-VIS data. The calculated $[NiBr_4]^{2-}$ transitions are red shifted (~600 cm^{-1}) from the experimental peak. Note, more HF could have been mixed in to reproduce the $[NiBr_4]^{2-}$ transitions exactly, but basing the selection on error across the entire $[NiX_4]^{2-}$ leads to a more acceptable calibration better suited to reproduce results for all the possible chromophores in the LETC equilibrium including $[Ni(Pdiol)_3]^{2-}$, $NiBr_2(Pbiz)_2$, and $[NiBr_3(Pbiz)]^-$.

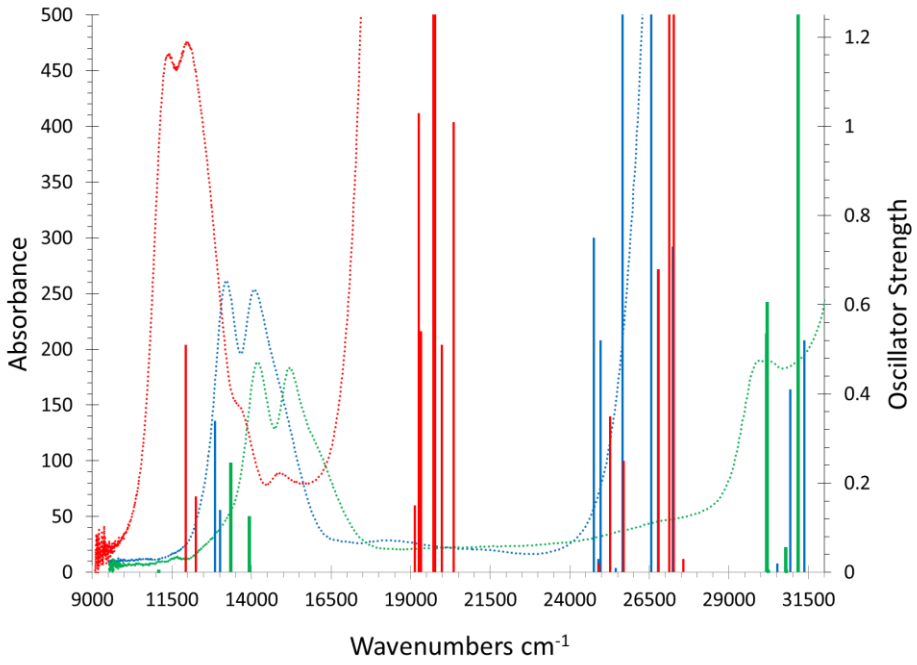

Figure 4.14 TD-DFT B23HFP86/6-311G+(d) /PCM(GBL) calculated oscillator strengths for $[NiX_4]^{2-}$ (X= Cl green, Br blue, I red) overlaid with experimental UV-VIS.

From the results shown in Figure 4.14 it was possible to establish an uncertainty range in the calculated transition energies of the B23HFP86 TD-DFT VIS d→d transitions. Experimentally, the $^3T_1$ feature between 9000, and 16500 cm^{-1} for the entire $[NiX_4]^{2-}$ series exhibits doublet in its spectra. The doublet structure is however not two separate d→d transitions but instead is due to spin/orbit coupling of the $^3T_1$ state with the S=1 spin state causing the 400 cm^{-1} split.[25] Since the TD-DFT calculations were not performed with a spin/orbit Hamiltonian, the doubling present in the calculated spectra cannot be correlated with the two calculated transitions that appear under the d→d excitations in the $[NiX_4]^{2-}$ series. Therefore, the average of the two experimental peaks is considered to be the experimental excitation energy (14,715, 13,643, and 11,694 cm^{-1} for $[NiCl_4]^{2-}$, $[NiBr_4]^{2-}$, and $[NiI_4]^{2-}$ respectively) and a weighted average of the two calculated transitions (13549, 12,914, and 12,043 cm^{-1} for $[NiCl_4]^{2-}$, $[NiBr_4]^{2-}$, and $[NiI_4]^{2-}$ respectively) is compared to it. The average error in calculated transition energy across the $[NiX_4]^{2-}$ series is 1,419 cm^{-1}.

Blue Film DFT Optimized Geometries The geometries of the components of the LETC blue film were optimized and the electronic structures were calculated using the empirical B23HFP86/def2-TZVP /PCM(GBL) method. The results of the calculations can be seen in Figures 4.15-4.21.

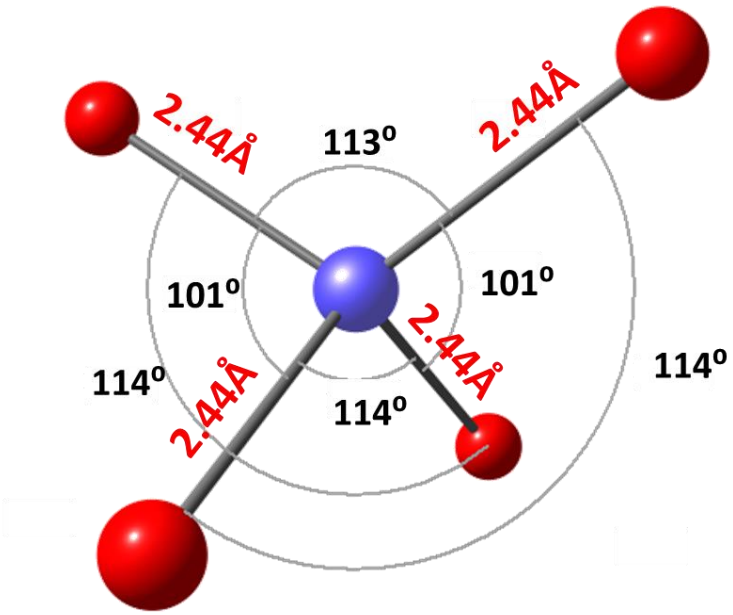

Figure 4.15 B23HFP86/def2-TZVP /PCM(GBL) optimized structure of $[NiBr_4]^{2-}$

Figure 4.15 shows the DFT optimized C_{2v} axially compressed (Br-Ni-Br bond angles of ~113^0 and 101^0) of the $[NiBr_4]^{2-}$ with bond lengths of 2.44 Å. This is just a 1^0 deviation in the 114^0 angle from a D_{2d} geometry.

Figure 4.16 shows the B23HFP86 optimized structure of the $NiBr_2(Pbiz)_2$ chromophore.

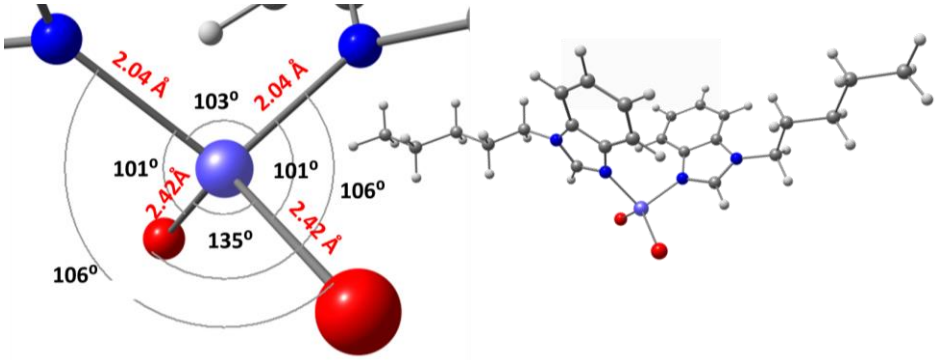

Figure 4.16 B23HFP86/def2-TZVP /PCM(GBL) optimized structure of $NiBr_2(Pbiz)_2$

The $NiBr_2(Pbiz)_2$ geometry is axially compressed in the same manner as the $[NiBr_4]^{2-}$. The Br-Ni-N bond angles are compressed to 101^0 (Figure 4.16) despite a widening in the remaining Br-Ni-Br bond relative to the angle in the $[NiBr_4]^{2-}$ (135^0). There is A negligible bond length change in the Ni-Br bond lengths in $NiBr_2(Pbiz)_2$ relative to the $[NiBr_4]^{2-}$ (2.44 Å and 2.42 Å respectively). The Ni-N bond in $NiBr_2(Pbiz)_2$ (2.04 Å) is considerably shorter than the Ni-Br bond (2.42 Å) suggesting better donation and thus a stronger bond. The 103^0 N-Ni-N bond angle in the $NiBr_2(Pbiz)_2$ maintains a C_{2v} coordination environment, seen in the $[NiBr_4]^{2-}$.

Figure 4.17 shows the B23HFP86/def2-TZVP /PCM(GBL) optimized geometry of the potential $[NiBr_3(Pbiz)]^-$ chromophore.

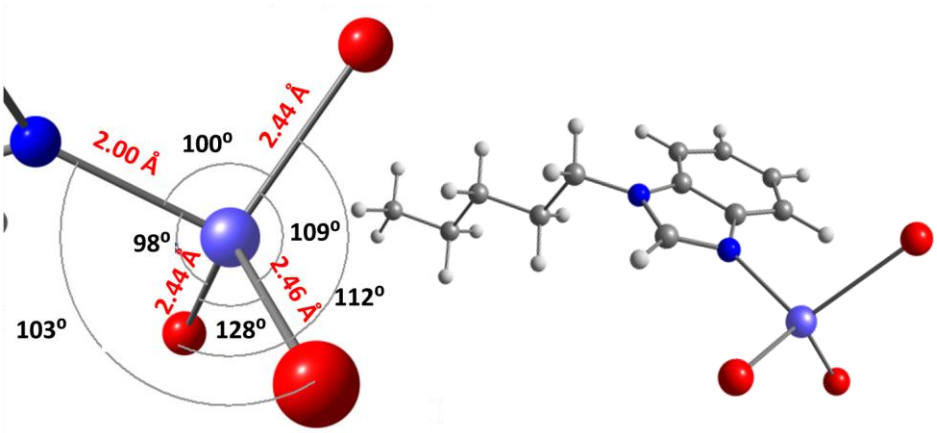

Figure 4.17 B23HFP86/def2-TZVP /PCM(GBL) optimized structure of $[NiBr_3Pbiz]^-$

The one elongated Ni-Br bond in $[NiBr_3(Pbiz)]^-$ (Figure 4.17) lowers its symmetry (relative to $NiBr_2(Pbiz)_2$) to C_3. The long Ni-Br bond is part of a 128^0 Br-Ni-Br bond angle, and a 98^0 Br-Ni-N bond angle that is compressed relative to the Br-Ni-N bond angels found in $NiBr_2(Pbiz)_2$.

Figure 4.18 shows the B23HFP86/def2-TZVP /PCM(GBL) optimized structure of the free Pbiz hεL.

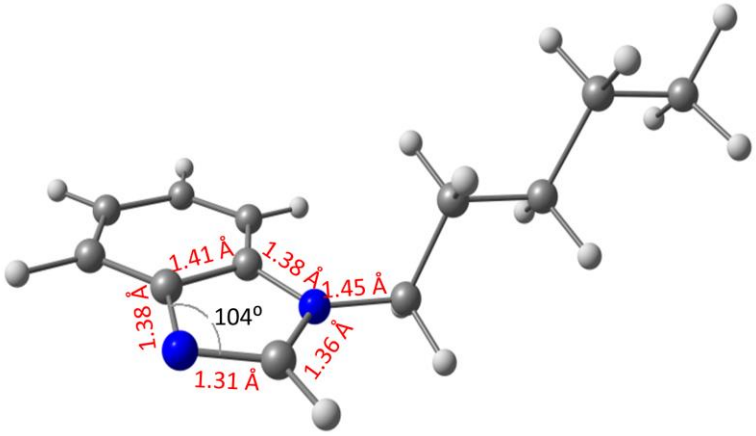

Figure 4.18 B23HFP86/def2-TZVP /PCM(GBL) optimized structure of Pbiz.

The free Pbiz ligand has N-C bond lengths of 1.38 (Figure 4.16). The C-N bond lengths are unchanged upon coordination to the nickel.

The B23HFP86/def2-TZVP /PCM(GBL) optimized geometry of the six coordinate lεL complex $[Ni(Pdiol)_3]^{2+}$ is shown in Figure 4.19.

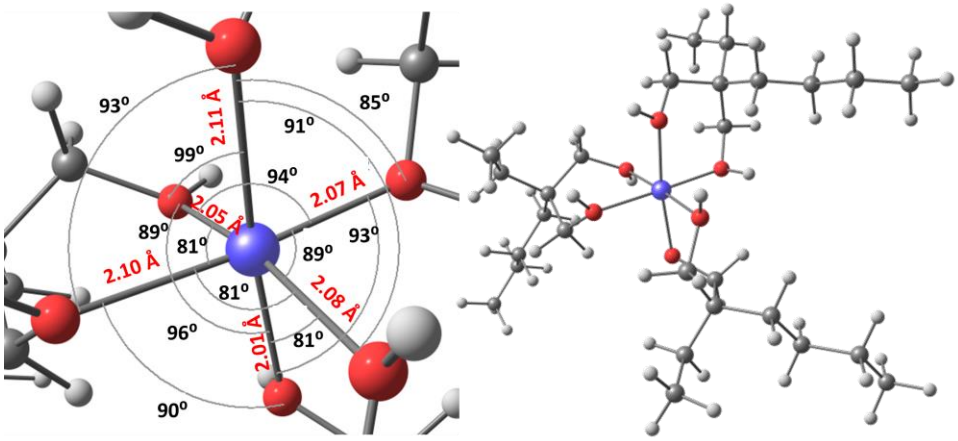

Figure 4.19 B23HFP86/def2-TZVP /PCM(GBL) optimized structure of $[Ni(Pdiol)_3]^{2+}$

The $[Ni(Pdiol)_3]^{2+}$ deviates from O_h symmetry due to bidentate ligand's bite angles. The O-Ni-O bite angle associated with each Pdiol is 81^0, 81^0, and 84^0; while O-Ni-O bond angle between oxygens on neighboring Pdiols are between 93^0 and 98^0. The ~2.10 Å Ni-O bond lengths in $[Ni(Pdiol)_3]^{2+}$ are longer than the Ni-N bonds (~2.0 Å) found in the hεL complexes but shorter than the Ni-Br bond distances (~2.4 Å) suggesting bonds more ionic in nature.

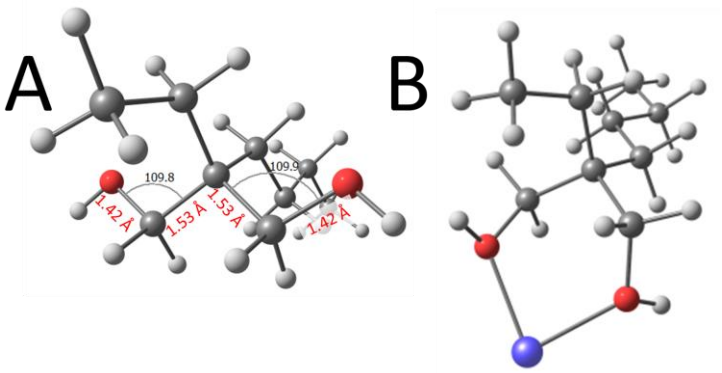

Figure 4.20 A) B23HFP86/def2-TZVP /PCM(GBL) optimized structure of free Pdiol ligand. B) Demonstration of the geometry perturbation necessary for Ni^{2+} coordination.

The B23HFP86/def2-TZVP /PCM(GBL) optimized structure of Pdiol in Figure 4.20 shows deviation from the geometry required to coordinate demonstrated in Figure 4.20B. The TBA^+ ion (Figure 4.21) has the potential to ion pair with negatively charged ions (Br^-, $[NiBr_4]^{2-}$, and $[NiBr_3(Pbiz)]^-$) in the system.

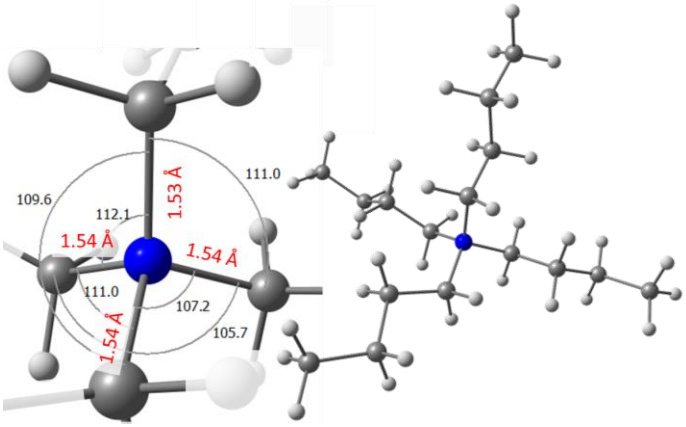

Figure 4.21 B23HFP86/def2-TZVP /PCM(GBL) optimized structure of TBA^+

The roughly tetrahedral cation has a total volume a estimated cubic volume of ~80 $Å^3$ determined from its longest H-H interatomic distance. This is ~25% of the volume allotted to the TBA^+ ion (314 $Å^3$) in the ionic limit model (Figure 4.1).

The $[Ni(Pdiol)_3]^{2-}$ complex has a pinched octahedral coordination environment with pinched bond angels (~85°) between connected hydroxyl groups. The diol pinching moves the bonds off center with the d orbitals decreasing spatial overlap (10% decrease in calculated overlap integral values relative to head coordination) and thus destabilizing the bond. The bonding destabilization is counteracted by the increased entropy due to the bidentate coordination of the ligand. The $[M(h\varepsilon L)_4]^y$ complexes are all pseudo-tetrahedral with Ni-Br bond distances ~2.45Å and Ni-N bond distances of ~2.00 Å. The longer nickel bromide bond distances indicate a weaker bond making the bromide more labile.

Blue Film DFT Calculated Ground State Electronic Structures Table 4.3 lists the spin density and charges calculated using natural population analysis as well as the natural population analysis (NPA)[120] MO composition analysis, introduced in chapter 2, to determine covalency.

Table 4.5 B23HFP86/def2-TZVP /PCM(GBL) and NPA optimized structures spin densities and charges of lεL and hεL complexes

	NPA Spin Density, e^-				NPA MO % Composition $orbital^{-1}$				NPA Charge			
	Ni	**O**			**Ni**	**1-O**	**2-O**		**Ni**	**O**		
$[Ni(Pdiol)_3]^{2+}$	1.60	0.03			85	4	5		1.41	-0.33		
	Ni	**Br**			**Ni**	**1-Br**	**2-Br**		**Ni**	**Br**		
$[NiBr_4]^{2-}$	1.60	0.10			90	5	1		1.05	-0.26		
	Ni	**Br**	**N**		**Ni**	**Br**	**N**		**Ni**	**Br**	**N**	
$NiBr_2(Pbiz)_2$	1.67	0.08	0.08		82	2	7		1.25	-0.28	-0.20	
	Ni	**1-Br**	**2-Br**	**N**	**Ni**	**1-Br**	**2-Br**	**N**	**Ni**	**1-Br**	**2-Br**	**N**
$[NiBr_3(Pbiz)]^-$	1.65	0.70	0.12	0.70	82	5	8	1	1.18	-0.26	-0.29	-0.21

The calculated ligand covalency for the molecules and ions in Table 4.3 are all under 5 % $bond^{-1}$. These orbital characters are low when compared to the 39% S e^- $hole^{-1}$ found in the $[Ni(ttctd)]^{2+}$ chromophore investigated in chapter 2. The coordination interactions are not covalent in nature, instead they come from the ionic interactions of the partial charges on the metal and its ligands. The oxygens in the $[Ni(Pdiol)_3]^{2+}$ has a calculated partial charge of -0.33 that interacts with a +1.41 charge at a distance of 2.07 Å. This results in ~ -3 J of potential between the atoms. The heL complexes in Table 4.3 tend to be more covalent than the $[Ni(Pdiol)_3]^{2+}$, but have reduced ionic interactions relative to the $[Ni(Pdiol)_3]^{2+}$. It is this balance between ionic and covalent that dictates the majority of the ΔH^0 in LETC.

<u>Excited State Electronic Structure</u> To investigate the species present in the blue film we now turn to an investigation of chromophore excited state electronic structures for which the exchange and correlation density functionals were empirically optimized.

The TD-DFT B23HFP86/def2-TZVP /PCM(GBL) calculated excitations of $[NiBr_4]^{2-}$ overlaid with experimental spectrum have already been presented in Figure 4.14. The calculated excitations are slightly red shifted (400 cm^{-1}) relative to the experimental peak. This discrepancy could be corrected with the mixing of ~5% more HF exact exchange, but this would jeopardize the models ability to represent the other types of bonding within the LETC system.

Figure 4.21 shows the TD-DFT B23HFP86/def2-TZVP /PCM(GBL) calculated transitions for $NiBr_2(Pbiz)_2$. The calculated transitions are red shifted (1000 cm^{-1}) relative to the experimental peak.

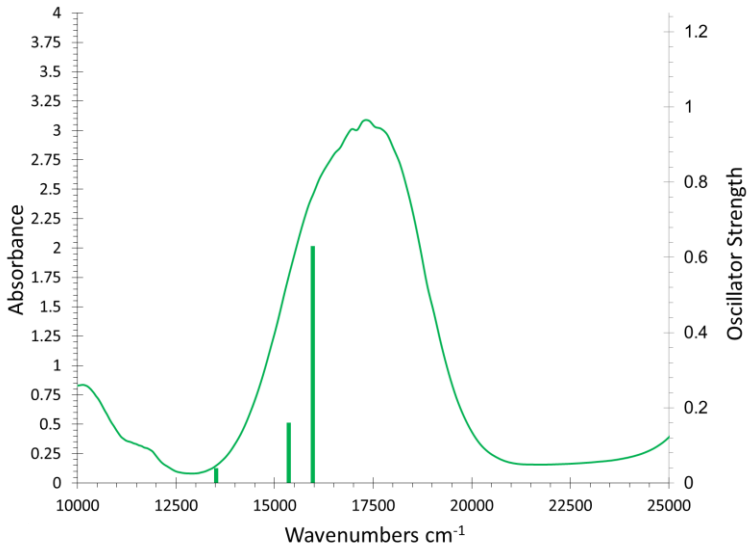

Figure 4.22 TD-DFT B23HFP86/def2-TZVP /PCM(GBL) calculated excitations for $NiBr_2(Pbiz)_2$ overlaid with UV-Vis spectra of 20mM $NiBr_2(Pbiz)_2$ and 0.58 M Neopentyl Glycol in GBL at 85 °C used as a representative spectrum of pure $NiBr_2(Pbiz)_2$ Recorded at Pleotint LLC.

In the $[NiBr(Pbiz)_2]^{2+}$ spectrum an increase of ~ 10% HF mixing could bring these transitions in line with the experimental observation.

Figure 4.23 shows the overlay of the 85° scan of the blue Suntuitive™ film and the calculated VIS transitions predicted by the TD- B23HFP86/def2-TZVP /PCM(GBL) calculated excitations for $[NiBr_4]^{2-}$, $[NiBr_3(Pbiz)]^-$, and $NiBr_2(Pbiz)_2$. The energy positions, accompanying error, and ability to empirically mix HF to increase transition energies show that all chromophores have the potential to be found in the blue Suntuitive™ LETC film in concentrations dictated by their respective free energies at high temperatures. To examine this possibility of multiple chromophores, calculated thermochemistry analysis is needed.

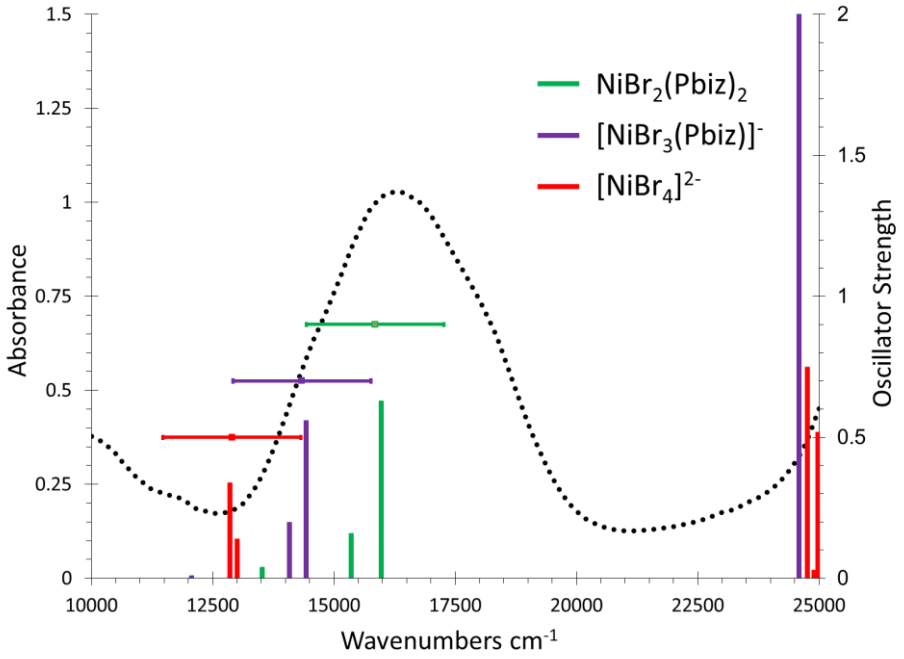

Figure 4.23 TD-DFT B23HFP86/def2-TZVP /PCM(GBL) calculated excitations for $[NiBr_4]^{2-}$, $[NiBr_3(Pbiz)]^-$, and $NiBr_2(Pbiz)_2$ overlaid with UV-VIS spectrum of blue Suntuitive™ LETC film composed of 1 unit $(TBA)_2NiBr_4$, 4 units $NiBr_2(Pbiz)_2$, 13 units Pdiol, 3GO plasicizer, in PVB taken at 85°C taken at Pleotint LLC. Calculated transitions are shown with error bars established in the functional search.

Blue Film DFT Calculated Thermodynamics Three possible equilibria in the blue film LETC system are given in Equations 4.21-4.23.

$$[Ni(Pdiol)_3]^{2+} + 4Br^- \leftrightarrow [NiBr_4]^{2-} + 3Pdiol \quad (4.21)$$

$$[Ni(Pdiol)_3]^{2+} + 2Br^- + 2Pbiz \leftrightarrow NiBr_2(Pbiz)_2 + 3Pdiol \quad (4.22)$$

$$[Ni(Pdiol)_3]^{2+} + 3Br^- + Pbiz \leftrightarrow [NiBr_3Pbiz]^- + 3Pdiol \quad (4.23)$$

The absolute enthalpy, entropy and thus free energy for each species was calculated according to statistical mechanics using the thermochemical analysis of quantum chemical results. Hess' law was used to calculate the overall reaction thermodynamics. The results of these calculations can be seen in Table 4.4

Table 4.6 DFT/def2-TZVP /Gas - PCM(GBL) calculated thermochemistry for the forward reactions in the equilibrium presented Equations 4.21-4.23

Equilibrium	Method	ΔH^0_{rxn} kJ mol^{-1}	ΔS^0_{rxn} J mol^{-1} K^{-1}	ΔG^0_{rxn} kJ mol^{-1}
$[NiBr_4]^{2-}$	Gas Phase BP86	-1024	185	-1078
Equation 4.21	PCM (ε=30.0) BP86	-140	239	-211
	PCM (ε=30.0) B3LYP	-68	223	-134
	PCM (ε=30.0) B23HFP86	-90	230	-158
$[NiBr_3(Pbiz)]^-$	Gas Phase BP86	-1257	135	-1298
Equation 4.22	PCM (ε=30.0) BP86	-168	178	-221
	PCM (ε=30.0) B3LYP	-125	158	-172
	PCM (ε=30.0) B23HFP86	-126	170	-177
$NiBr_2(Pbiz)_2$	Gas Phase BP86	-1195	60	-1213
Equation 4.23	PCM (ε=30.0) BP86	-186	129	-224
	PCM (ε=30.0) B3LYP	-152	121	-188
	PCM (ε=30.0) B23HFP86	-153	114	-186

All of the ΔH^0 values in Table 4.3 have the opposite sign when compared to the experimental ΔH^0_{rxn}. They are ~ 200kJ mol^- from the experimental value (~+40-170 kJ mol^{-1}). The ΔS^0_{rxn} values are within the experimental range despite the unfavorable stoichiometry (less product species than reactants). The meticulous calibration of the functionals and the subsequent agreement with the excited state electronic structure suggests that the problem in the calculated ΔH^0_{rxn} comes about not because of the failings of DFT as an electronic structure method, but instead, the incompleteness of the computational model. PCM does not calculate explicit solvation enthalpy. Explicit solvation energy due to explicit interaction with solvent molecules is thought to be one of the main contributors

DFT Model Summary The C_{2v} $[Ni(heL)_4]^y$ LETC chromophore have Ni-Br bond distances of ~2.40 Å and Ni-N bond distances of ~2.04 Å. The six coordinate $[Ni(Pdiol)_3]^{2+}$ has bond lengths of ~2.05 Å. The shorter nitrogen and oxygen bond distances are structural indications strong ionic bonds. The ionic bonding picture is supported by the NPA calculated high partial charges and low ligand orbital characters (Table 4.3). The TD-DFT calculations show each chromophores' calculated absortption to be in good agreement with experiment (< 1000 cm^{-1} energy difference). The results are considered to be accurate since TD-DFT calculations were used in the initial selection of the hybrid functional. The calculated electronic structure of various products and reactants leads to a balance of the ionic bonding strengths that predict large negative ΔH^0_{rxn} (~ -100kJ mol^{-1}) for all the equilibria investigated (Equations 4.21-4.23). Ultimately, the DFT results prove that experimental observations cannot be reproduced

using single molecule models and that intermolecular interactions play an important role in LETC. Given the complexity of these systems, this result does not come as a surprise.

Blue Film Semi-Empirical
Chromophore Geometry Calculations

The geometries of the components of the LETC blue film were optimized and the ground state electronic structure properties were calculated using the PM7[177] semi-empirical method, and a conductor-like screening model (COSMO)[179] with the same GBL dielectric used in the PCM in the DFT models (THF solvent parameters, dielectric = 30 to match the dielectric of GBL). We choose to work with the PM7 effective Hamiltonian due to its ability to reproduce the pseudo T_d , C_{2v} and O_h Ni^{2+} geometries found in the DFT calculation. None of the other effective MNDO Hamiltonians (PM3 or PM6) were able to reproduce the four coordinate geometry. PM3 failed because it does not contain d orbitals. PM6 failed only when counterions were added where organic ligands competed via hydrogen bonds with the ligands ionic and covalent coordination bonds in the chromophore.

The results of the PM7 optimizations can be seen in Figures 4.24-30.

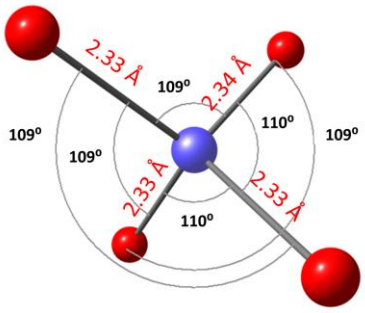

Figure 4.24 PM7/COSMO(GBL) optimization of the $[NiBr_4]^{2-}$ geometry.

The PM7 optimized geometry of $[NiBr_4]^{2-}$ (Figure 4.24) has shorter bond distances (2.33 Å) relative to the B23HFP86 def2-tzvp optimized structure (2.44 Å). In contrast to the C_{2v} geometry being the lowest energy state calculated by B23HFP86, PM7 has its minima in approximately T_d geometry.

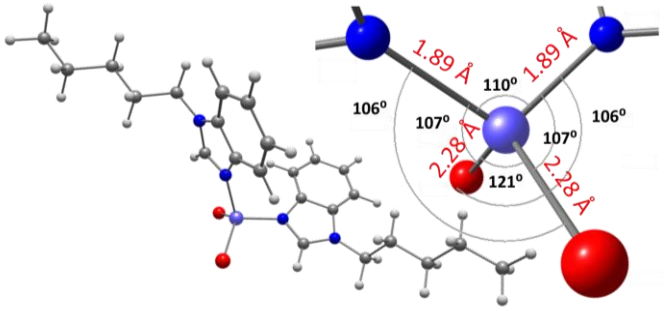

Figure 4.25 PM7/COSMO(GBL) optimization of the $NiBr_2(Pbiz)_2$ geometry.

The $NiBr_2(Pbiz)_2$ structure (Figure 4.25) has shortened Ni-Br and Ni-N bond distances (2.28 Å and 1.89 Å respectively) when compared to B23HFP86 def2-tzvp optimized structure (2.42 Å and 2.04 Å). The bond angles differ only in the axial compression. The DFT optimized structure is more axial compressed (Br-Ni-N angle of 101°) while the PM7 optimized structure is not (Br-Ni-N angle of 107°).

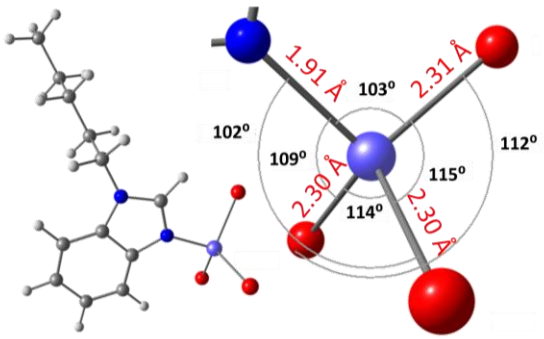

Figure 4.26 PM7/COSMO(GBL) optimization of the $[NiBr_3(Pbiz)]^-$ geometry.

The $[NiBr_3(Pbiz)]^-$ (Figure 4.26) structure has shortened Ni-Br and Ni-N bond distances (2.30 Å and 1.91Å respectively) relative to the B23HFP86 structure (~2.45 Å and 2.00 Å respectively). The PM7 optimized structure also lacks the single elongated Ni-4Br bond (2.46 Å) found in the B23HFP86 def2-tzvp optimized structure.

The bond lengths are systematically shorter in the PM7 structures compared to DFT. This could be improved through semi-empirical parameterization optimization along the lines of the UV-VIS TD-DFT survey in the DFT section.

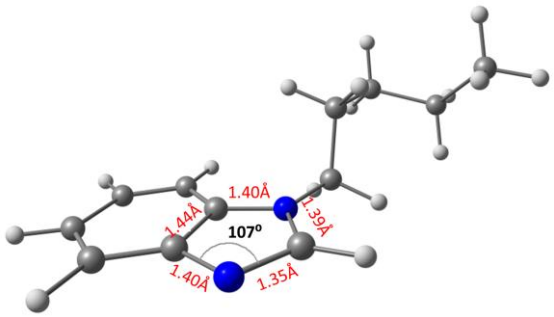

Figure 4.27 PM7/COSMO(GBL) optimization of the PBiz geometry.

The PM7/COSMO(GBL) PBiz (Figure 4.27) optimization reproduces the B23HFP86/def2-TZVP /PCM(GBL) optimization of the PBiz geometry to with 0.02 Å. This is expected because the majority of training molecules for PM7 are organic molecules.[177]

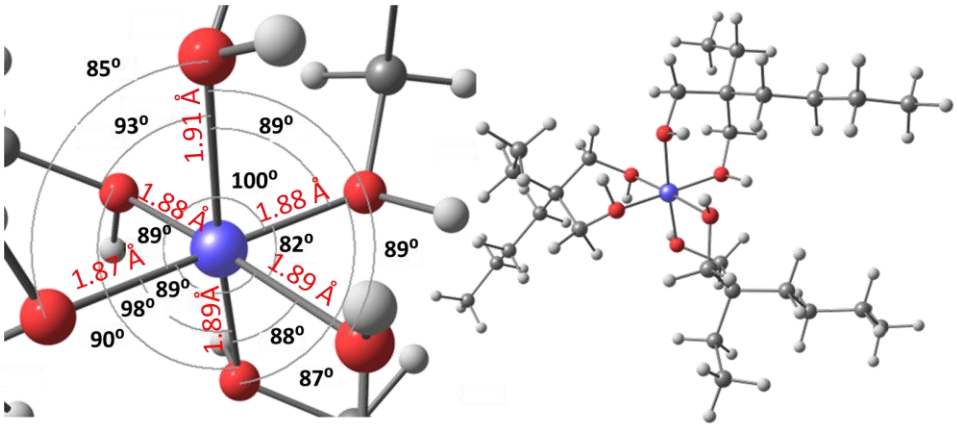

Figure 4.28 PM7/COSMO(GBL) optimization of the $[Ni(Pdiol)_3]^{2+}$ geometry.

The Ni-O bond distances in the PM7 optimized geometry of $[Ni(Pdiol)_3]^{2+}$ (Figure 4.28 ~1.90 Å) are shorter than those predicted by B23HFP86 def2-tzvp optimized structure (2.00-2.11 Å). The bidentate ligand bite angle opens up in the PM7 optimized structure (89°) relative to the B23HFP86 def2-tzvp structure (81°).

$[Ni(Pdiol)_3]^{2+}$ is a sizeable molecule. When the def2-tzvp basis set is used to represent its electrons 1428 basis functions have to be used. As discussed in the introduction, DFT optimizes orbital coefficients subsequent density matrix in a self-consistent manor to optimize the electronic structure. A single BP86 SCF cylcle takes 3 hours on an 8 processor compute node equipped with 2.4 gigahrtz Dual Core AMD Opteron(tm) Processor 880 while a single PM7 scf cycle takes 10 minutes on the identical node. These time differences become very significant when performing geometry optimizations that might take hundreds of SCF cycles.

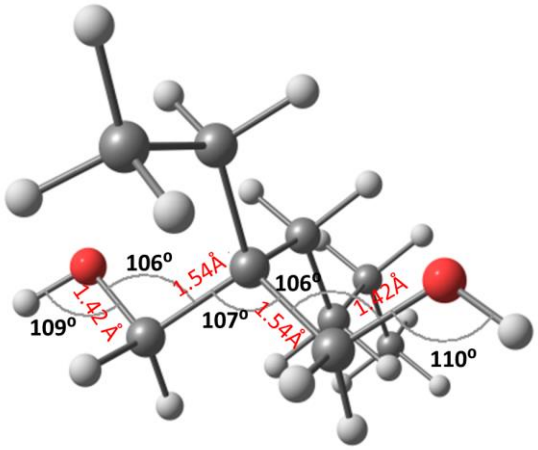

Figure 4.29 PM7/COSMO(GBL) optimization of the free Pdiol geometry.

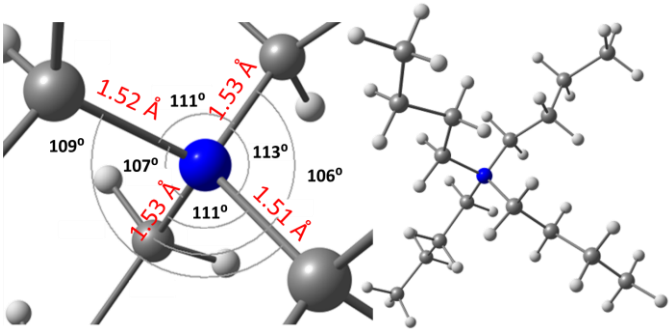

Figure 4.30 PM7/COSMO(GBL) optimization of TBA^+ geometry.

As with the organic Pbiz molecule, the PM7/COSMO(GBL) opitimzed geometry Pdiol, TBA^+ geometries (Figure 4.29 and 30 respectively) reproduce the B23HFP86/def2-TZVP /PCM(GBL) geometries. Neither structure varies by more than 0.01 Å.

Blue Film Semi-Empirical Chromophore Calculated Thermodynamics As discussed in the introduction, PM7 can be used to calculate empirically derived heats of formation. The heats of formation are parameterized to include the electronic energy, the

zero point energy, the vibrational energy at 298.15K, the rotational energy, and translational energy. The only thermodynamic value not included in the parameterization is the entropy. To calculate the entropy contributions to the free energy frequency calculations were performed on the PM7 optimized structure. The enthalpy and entropy values were used along with Hess's law to calculate $\Delta H^0_{rxn,}$ $DS^0_{rxn,}$ and DG^0 for the equilibria found in Equations 4.21-4.23 . The results of these calculations are presented in Table 4.5

Table 4.7 PM7 gas phase and COSMO (ε=30.0) calculated $\Delta H^0_{rxn,}$ $\Delta S^0_{rxn,}$ and ΔG^0_{rxn}

Equilibrium / $[M(heL)_4]^y$	Method	ΔH^0_{rxn} kJ mole^{-1}	ΔS^0_{rxn} J mole^{-1} K^{-1}	ΔG^0_{rxn} (298K) kJ mole^{-1}
Equation 4.21 / $[NiBr_4]^{-2}$	Gas Phase PM7	-52		
	COSMO PM7	-20	740	-242
Equation 4.22 / $NiBr2(Pbiz)_2$	Gas Phase PM7	-62		
	COSMO PM7	-46	530	-205
Equation 4.23 / $[NiBr_3(Pbiz)]^-$	Gas Phase PM7	-90		
	COSMO PM7	-82	310	-174

The ΔH^0_{rxn} predicted by PM7 are still exothermic, the opposite of the endothermic predicted by DFT. This was to be expected since no new intermolecular interactions were added to the system. In fact this is a positive result because we know that the individual molecules are being represented at the accuracy of the DFT methods.

Geometries of Charge Neutral PM7 and DFT Models To improve on the calculated enthalpies calculated thus far the model needs to be expanded to include the other species present in a Ni^{2+} centered boundary box. A first order approximation to increasing the completeness of the model is to form expanded charge neutral models of

the molecules and ions contained in a Ni^{2+} boundary box. This is comparable to exploring the interactions in the first solvation sphere.

To assess the accuracy of PM7 semi-empirical calculated ion pairing geometries and stabilization energies against those predicted by DFT the equilibrium in Equation 4.24 was modeled with both PM7 and DFT.

$$[Ni(Pdiol)_3]^{2+} \bullet (Br^-)_2 + 2(TMA^+ \bullet Br^-) \leftrightarrow (TMA^+)_2 \bullet [NiBr_4]^{2+} + 3Pdiol \qquad (4.24)$$

The two trimethylamonniums (TMA^+) were paired with $[NiBr_4]^{2+}$ and the model was optimized using both B23HFP86/def2-TZVP /PCM(GBL) (Figure 4.31 A) PM7/COSMO(GBL) (Figure 4.31 B). The TMA^+ ion is a truncation of the TBA^+ ion and was made so that the ion pair could be optimized and the resulting thermochemistry calculations could be made using both DFT and the results could be used to test the theoretical agreement between DFT and PM7 ion pairing energies.

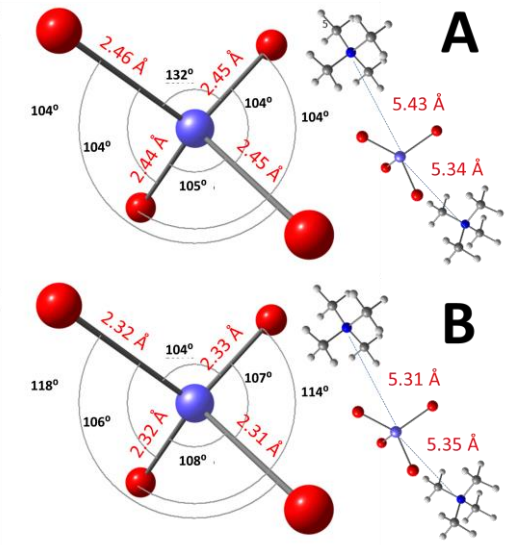

Figure 4.31 A) B23HFP86/def2-TZVP /PCM(GBL) and B) PM7/COSMO(GBL) optimization of the ($2TMA^+ + [NiBr_4]^{2+}$) geometry.

As in the other PM7/COSMO(GBL) optimizations the bond lengths in the DFT method are longer than those predicted by PM7/COSMO(GBL) (2.45 and 2.33 Å respectively) The real geometric difference relative to the unpaired ions are seen in the bond angles. The B23HFP86/def2-TZVP /PCM(GBL) optimized structure predicts an accentuation of the C_{2v} symmetry of the chromophore due to a 132^0 Br-Ni-Br angle. This bending is the result of the new, competing, ionic bond interaction formed between the bromide and the TMA. This result is also seen in the PM7 calculation but to lesser extent with a Br-Ni-Br angle of 118^0 . We would expect this effect to be smaller in the actual LETC system since TBA is used. The apolar side chains will better shield the positively charged nitrogen.

The PM7/COSMO(GBL) calculated enthalpy of pairing the TMA^+ and $[NiBr_4]^{2-}$ is -8 kJ mol^{-1} while B23HFP86/def2-TZVP /PCM(GBL) thermochemistry calculation predicts -46 kJ mol^{-1} stabilization.

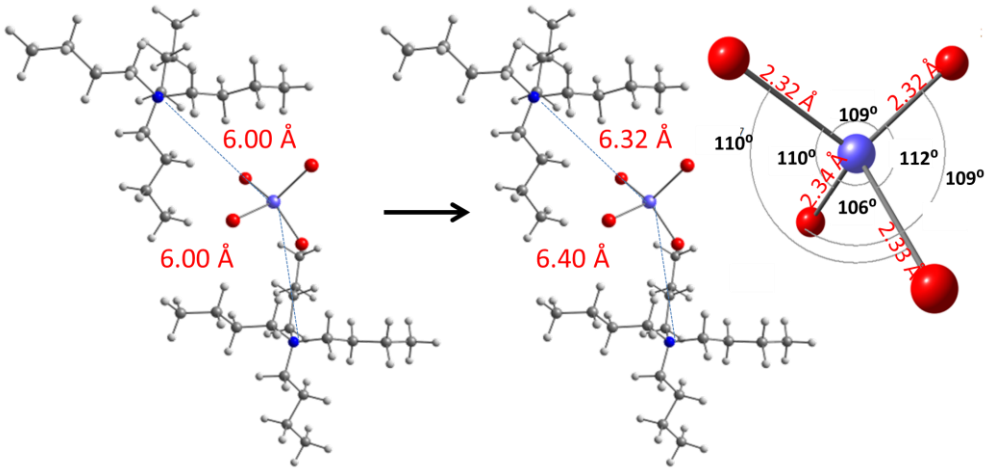

Figure 4.32 Starting and PM7/COSMO(GBL) optimized structure of the $2TBA^+$ $[NiBr_4]^{2-}$ ion pair.

As expected the Ni-N intermolecular distances are larger for the TBA^+ than they were for the TMA^+ in Figure 4.32. The symmetry breaking seen in the $2TMA^+$ $[NiBr_4]^{2-}$ ion pair is less pronounced in the optimized $2TBA^+$ $[NiBr_4]^{2-}$ ion pair. The stabilizing effect of pairing of the ions was calculated by subtracting the enthalpy of formation of the free $[NiBr_4]^{2-}$ and two TBA^+ and the result was 40 kJ mol^{-1} stabilization due to ion pairing.

The ion paired $[Ni(Pdiol)_3]^{2+}$ $2Br^-$ was optimized using both PM7/COSMO(GBL) and B23HFP86/def2-TZVP/PCM(GBL) (Figure 4.33 A and B respectively).

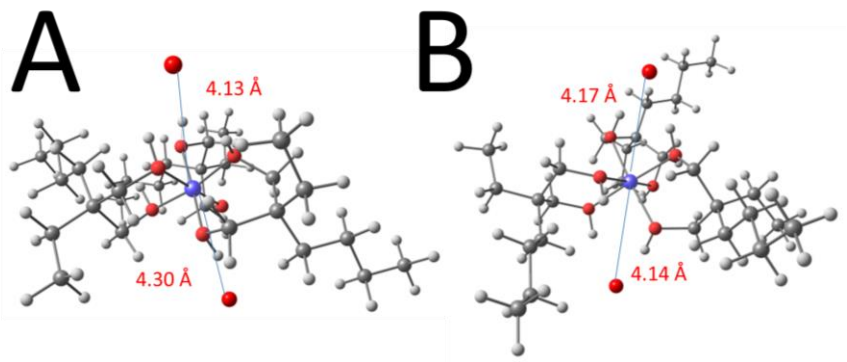

Figure 4.33 A) PM7/COSMO(GBL) B) B23HFP86/def2-TZVP/PCM(GBL) optimized geometries for $[Ni(Pdiol)_2]^{2+}$ 2 Br^-.

B23HFP86/def2-TZVP/PCM(GBL) gave a final optimized structure with ~4.17 Å Ni-Br distances. The PM7 optimized structure had final Ni-Br distances of ~4.13 and 4.30 Å. The stabilization predicted by B23HFP86/def2-TZVP/PCM(GBL) was -161 kJ mol^{-1} while PM7/COSMO(GBL) was -21kJ $mole^{-1}$. The large negative enthalpy of ion pairing in both PM7/COSMO(GBL) and B23HFP86/def2-TZVP/PCM(GBL) show that ion pairs are very likely, especially in concentrated solutions or polymer films.

The TMA bromide ion pair shown as a reactant in Equation 4.9 was optimized using both DFT and PM7 and the resulting geometry can be seen in Figure 4.34.

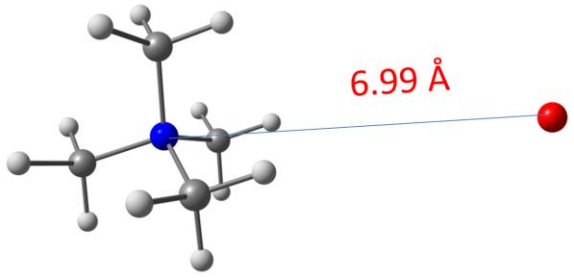

Figure 4.34 PM7/COSMO(GBL) optimized geometry for TMABr

The optimized structures (Figure 4.31-4.34) were used to calculate the $\Delta H^0_{rxn,}$ $\Delta S^0_{rxn,}$ and ΔG^0_{rxn} for the equilibrium in Equation 4.9 and the results are presented in Table 4.6

Table 4.8 PM7/COSMO(GBL) and B23HFP86/def2-TZVP/PCM(GBL) calculation of $\Delta H^0_{rxn,}$ $\Delta S^0_{rxn,}$ and ΔG^0_{rxn} of equalibrium in Equation 4.9

	ΔH^0_{rxn} kJ mol^{-1}	S^0_{rxn} J mol^{-1} K	ΔG^0_{rxn} kJ mol^{-1}
PM7/COSMO(GBL)	-47.8	-297	41
B23HFP86/def2-TZVP/PCM(GBL)	84	360	-26

The B23HFP86/def2-TZVP/PCM(GBL) thermochemistry calculations yield a ΔH^0_{rxn} that is within the range of experimentally predicted by Byker et al[3] and supported throughout this dissertation. The ionic stabilization due to ion pairing within this model is greater on

the reactants side of the equilibrium than on the products. For the reactants there are three ion pairing interactions ($2Br^-$ $[Ni(Pdiol)_3]^{2+}$ and two (TMA^+ Br^-)) while the products only have one ($2TMA^+$ $[NiBr_4]^{2+}$). This indicates that ion pairing does in fact play an important role in the spontaneity and ultimately the temperature dependence of LETC. It is also apparent that these interactions must be represented at the highest accuracy possible. It is interesting that despite the ΔH^0_{rxn} reproducing the endothermic nature of the reaction the reaction is still predicted to be spontaneous at 298 K. It appears that the ion pairing is not entropiclly favored.

The PM7/COSMO(GBL) calculations do not reproduce the experimentally predicted $\Delta H^0_{rxn,}$ which is most likely a result of the underestimation of the ion pairing energy within the PM7 models.

Charge neutral models for PM7 calculations were created using the species present in the Ni^{2+} boundary box. The starting structures along with the PM7/COSMO(GBL) optimized structures can be seen in Figures 4.35-4.36

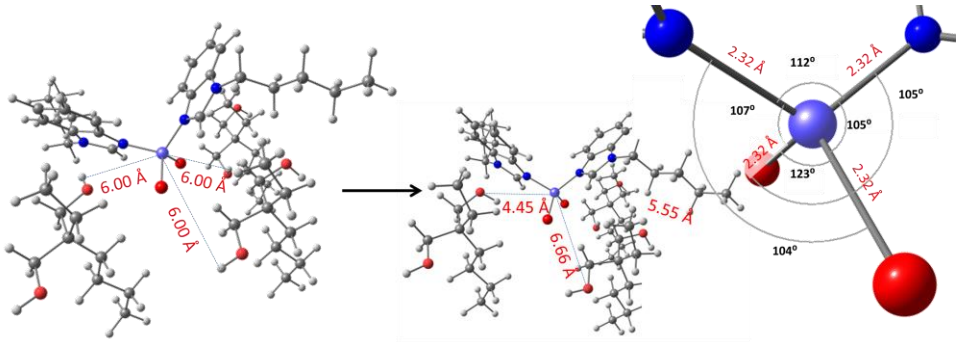

Figure 4.35 Starting and PM7/COSMO(GBL) optimized structures of the $NiBr_2(Pbiz)_2$ 2Pdiol charge neutral model

Figure 4.35 shows the effect of putting two neutral Pdiols in the proximity of the neutral $NiBr_2(Pbiz)_2$. The presence of the Pdiols has the effect of elongating all the Ni-N bonds relative to the chromophore in the PM7 optimized structure (2.32 Å and 1.89 Å respectively). The Ni-Br bond is elongated relative to the PM7 optimized structure as well (2.32 Å and 2.28 Å respectively). This is due to hydrogen bonding interactions with the Pdiols weakening the ionic bonding between the ligands and the Ni^{2+} .

The PM7/COSMO(GBL) optimized geometry of TBA^+ $[NiBr_3(Pbiz)]^-$ is presented in Figure 4.36.

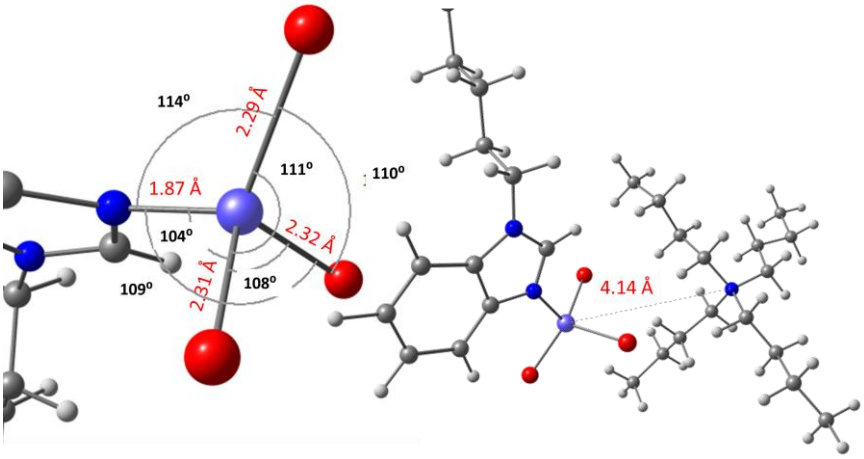

Figure 4.36 PM7/COSMO(GBL) optimized geometry of TBA^+ $[NiBr_3(Pbiz)]^-$

There is no meaningful perturbation to the geometry of the PM7/COSMO(GBL) optimized $[NiBr_3(Pbiz)]^-$ chromophore due to the presence of the TBA. This is peculiar considering the established ionic nature of the bonds in this chromophore.

The size of the ion pair models in Figures 4.35-4.36 prevented the use of frequency calculations so only the parameterized heats of formation were used to calculate the ΔH^0_{rxn} for the equilibria in equations 4.10-4.12 However, you could take

zero point energy corrections, thermal energy corrections etc. and get a reasonable estimate for the thermochemical contribution.

$$[Ni(Pdiol)_3]^{2+} \bullet (Br^-)_2 + 2(TBA^+ \bullet Br^-) \leftrightarrow (TBA^+)_2 \bullet [NiBr_4]^{2-} + 3Pdiol \quad (4.25)$$

$$[Ni(Pdiol)_3]^{2+} \bullet (Br^-)_2 + (TBA^+ \bullet Br^-) + Pbiz \leftrightarrow (TBA^+) \bullet [NiBr_3(Pbiz)]^- + 3Pdiol \quad (4.26)$$

$$[Ni(Pdiol)_3]^{2+} \bullet (Br^-)_2 + 2\ Pbiz \leftrightarrow 3\ Pdiol \bullet NiBr_2(Pbiz)_2 \quad (4.27)$$

The results of the ΔH_{rxn} calculations can be seen in Table 4.7.

Table 4.9 PM7 COSMO (ε=30.0) calculated ΔH^0_{rxn}

Equilibrium / $[M(heL)_4]^y$	ΔH_{rxn} kJ mole^{-1}
Equation 4.25 / $[NiBr_4]^{-2}$	-106
Equation 4.26 / $[NiBr_3(Pbiz)]^-$	-131
Equation 4.27 / NiBr2$(Pbiz)_2$	-179

Once again all the models wrongly predict exothermic reactions. The lack of success demonstrates the difficulty in modeling these non-ideal systems of weakly bound coordination complexes. One method of attempting to increase the accuracy of these models is to make them even larger, building them in such a way that all models include the same number of species on both sides of the equilibrium. This way the same total interaction energy exists on both sides of the modeled equilibrium.

Force Field Parameterization

Our interest in molecular mechanics calculations comes from our desire to expand the modeled network of weak interactions in LETC systems to include all the species

present in the Ni^{2+} periodic boundary box discussed in the introduction to this chapter. The MM3 force field includes parameters that model weak van der Waals (vdW) and hydrogen bonding interactions for all the atom types found in the LETC systems except the coordinated bromide and free bromide ions. Also the partial charges for coordinated nickel (in all chromophores), bromide (found in $[NiBr_4]^{2-}$, $NiBr_2(Pbiz)_2$, and $[NiBr_3(Pbiz)]^-$), oxygen (found in $[Ni(Pdiol)_3]^{2+}$), and nitrogen (found in $NiBr_2(Pbiz)_2$, and $[NiBr_3(Pbiz)]^-$) needed to be defined.

The NPA calculated partial charges from the B23HFP86/def2-TZVP/PCM(GBL) optimized geometries were used to parameterize the MM3 partial charges. To parameterize, the vdW interactions for the coordinated bromide atom type a model $[NiBr_4]^{2-}\cdot NH_3$ system was used (Figure 4.37). B23HFP86/def2-TZVP/PCM(GBL) was used to calculate the potential energy of the system at various Br-H interatomic distances.

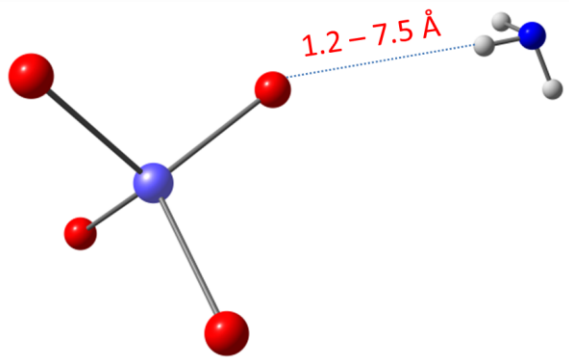

Figure 4.37 $[NiBr_4]^{2-}$ NH_3 VdW scan where the Br-H bond distance was varied from 1.2 to 7.5 Å.

The results of the DFT potential energy scan can be seen in Figure 4.37 (blue points). The DFT results are plotted with the MM3 total potential energies calculated using various values for the coordinated bromine vdW parameter.

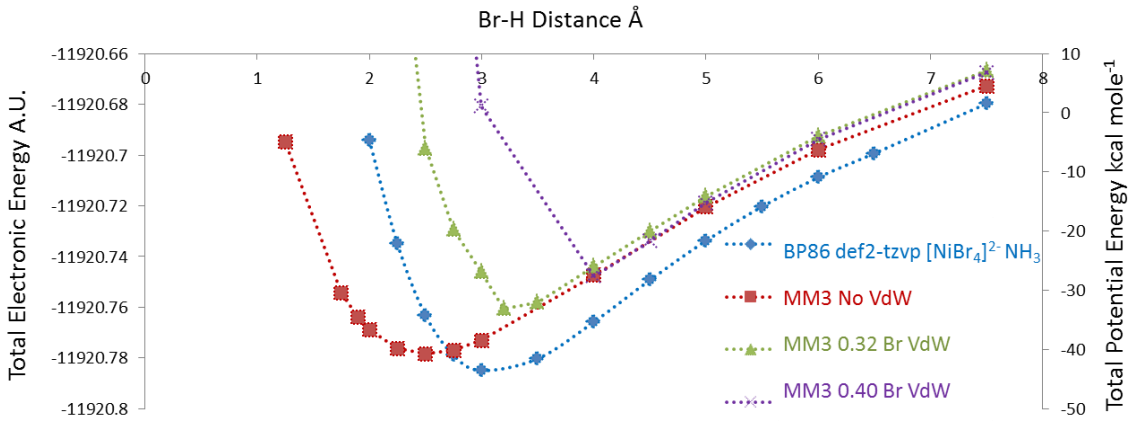

Figure 4.38 Graphical representation of $[NiBr_4]^{2-}$ NH_3 potential energy scan using different values for the coordinated bromine VdW parameters.

In Figure 4.38, it can be seen that when no vdW parameter is used (red data points) the calculated repulsive wall of the potential energy well moves unrealistically close Br-H interatomic distances. The value of 0.32 was found to best reproduce the DFT results moving the potential energy minimum to match the DFT value by less than a tenth of an angstrom.

To test of the optimized vdW and charge parameters a Ni^{2+} ion (with the partial charge present in the coordinated $[NiBr_4]^{2-}$) was placed in the center of four free bromide ions and the geometry was optimized using the new MM3 force field parameters. The resulting geometry can be seen in Figure 4.39. The optimized bond distances were ~0.5 Å longer and the axial compression seen in both the DFT and PM7 results was not observed, but the tetrahedral coordination with the other methods was reproduced.

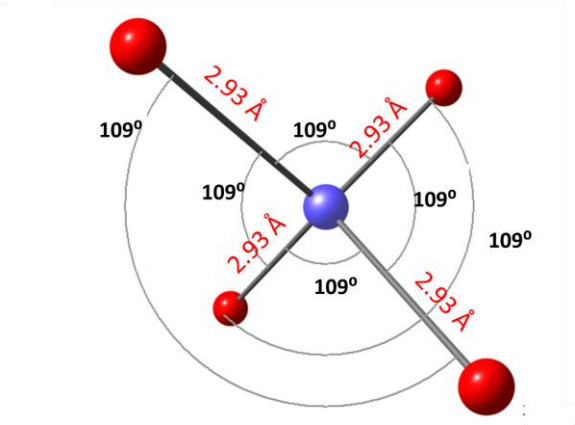

Figure 4.39 MM3 optimized free Ni^{2+} ion and Br^- ion.

The same free ligand procedure was used in an attempt to optimize and reproduce the tetrahedral coordination in $NiBr_2(Pbiz)_2$ but met with no success due to the dominating interligand interactions already parameterized within MM3. The reason the $[NiBr_4]^{2-}$ geometry was so succesfull is because its geometry is dictated almost entirely by Ni^{2+} -Br^- attraction and Br^- -Br^- repulsion.

To improve on the bond lengths seen in Figure 4.39 for the free Ni^{2+} and Br^- ions the bonding length and angle parameters between the two atom types were optimized to reproduce the DFT optimized chromophore geometries. The resulting parameters can be seen in Table 4.8 and the geometry of the optimized $[NiBr_4]^{2-}$ chromophore can be seen in Figure 4.40.

Table 4.10 Optimized MM3 parameters for four coordinate Ni^{2+} and coordinated bromide

	Atom Types	VdW Radi, Å	Hardness of atom kcal $mole^{-1}$
VdW	1Ni	2.20	0.02
VdW	1Br	2.22	0.32
		Equilibrium Bond Length, Å	Stretching Constant, mdyn $Å^{-1}$
Stretch	1Ni-1Br	2.46	6.00
		Bending Constant, mdyn Å rad^{-2}	Equilibrium Bond Angle, ^{0}
Bend	1Br-1Ni-1Br	3.19	105.3

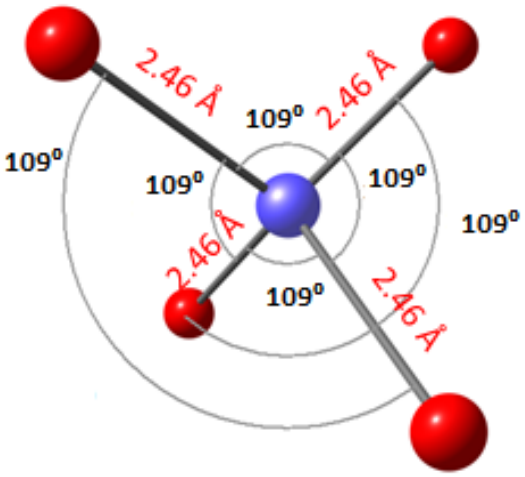

Figure 4.40 MM3 optimized $[NiBr_4]^{2-}$ structure.

The Br-Ni bond distances are less than 0.02 Å from the DFT values. The bond angles deviate from those seen in the DFT molecule replacing the C_{2V} geometry of DFT with a T_d geometry in the MM3. This is similar to the PM7 optimized molecule.

MM3 contained a set of sp^2 nitrogen parameters useful for calculating geometries of imidazoles. The existing parameters were modified with new bond and angle parameters to reproduce the nickel coordinated geometry of Pbiz in optimized DFT structures of $NiBr_2(Pbiz)_2$. Table 4.9 lists the parameters that varied from those existing

in the MM3 force field. Figure 4.41 shows the optimized MM3 geometry calculated using the modified parameters.

Table 4.11 Optimized MM3 parameters for the Ni, N, and Br in the $NiBr_2(Pbiz)_2$ chromophore.

	Atom Types	VdW Radi, Å	Hardness of atom kcal $mole^{-1}$
VdW	2Ni	2.22	0.02
VdW	1N	1.93	0.043
VdW	2Br	2.22	0.32
VdW	3Br	2.22	0.32
		Stretching Constant, mdyn $Å^{-1}$	Equilibrium Bond Length, Å
Bond	1N-2Ni	7	1.98
Bond	2Ni-2Br	6	2.42
Bond	2Ni-3Br	6	2.42
		Bending Constant, mdyn Å rad^{-2}	Equilibrium Bond Angle, ^{0}
Bend	sp2C-1N-2Ni	1.19	127
Bend	1C-1N-2Ni	1.19	127
Bend	2C-1N-2Ni	1.19	127
Bend	1N-2Ni-2Br	1.19	104
Bend	1N-2Ni-3Br	1.19	104
Bend	1N-2Ni-1N	1.19	104
Bend	2Br-2Ni-3Br	3.19	133
		2^{nd} order torsional constant, kcal mol^{-1}	Dihedral Angle, ^{0}
Torsion	sp2C-sp2C-1N-2Ni	10	180
Torsion	sp2N-sp2C-1N-2Ni	10	180
Torsion	sp2N-1C-1N-2Ni	10	180
Torsion	sp2N-2C-1N-2Ni	10	180
Torsion	H-sp2C-1N-2Ni	10	0
Torsion	H-1C-1N-2Ni	10	0
Torsion	H-2C-1N-2Ni	10	0

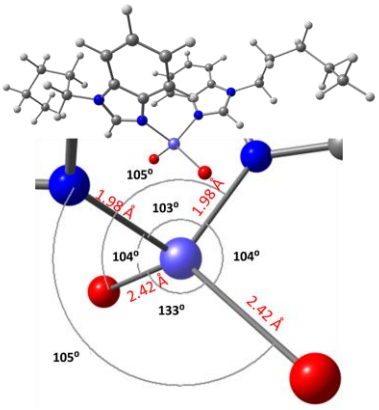

Figure 4.41 MM3 optimized structure of $NiBr_2(Pbiz)_2$

The Ni-Br distances in the $NiBr_2(Pbiz)_2$ are in match exactly the lengths in DFT. The Nitrogen bond distances vary by 0.06 Å. This is due to the difficulty in optimizing parameters when trying to counteract the interligand attraction of the Pbiz ligands.

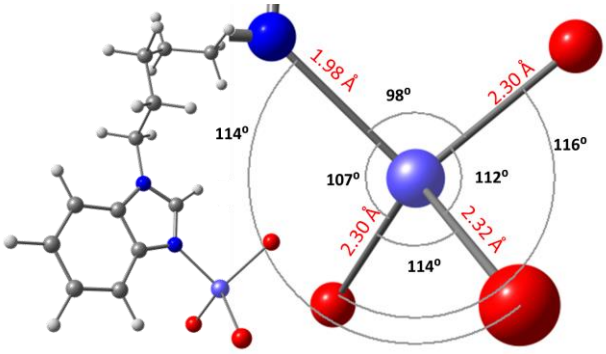

Figure 4.42 MM3 optimized structure of $[NiBr_3(Pbiz)]^-$

The $[NiBr_3(Pbiz)]^{2-}$ structure is in poor agreement with the DFT optimized structure. The bond lengths vary by more than 0.15 Å. This is because no special parameterization was made for the extra Br^- coordination in the structure. This shows that the non-explicit parameters leave too much room for error.

The parameters for the $[Ni(Pdiol)_3]^{2+}$ were optimized to reproduce the DFT optimized geometry and the results of this optimization Figure 4.43 shows the resulting MM3 optimized geometry.

Table 4.12 Optimized MM3parameters for the Ni, and O in $[Ni(Pdiol)_3]^{2+}$.

		Stretching Constant, md Å^{-1}	Equilibrium Bond Length, Å
Bond	1O-4Ni	7	2.086
Bond	2O-4Ni	7	2.086
Bond	3O-4Ni	7	2.086
		Bending Constant md Å rad^{-2}	Equilibrium Bond Angle, ^{0}
Angle	1O-4Ni-1O	1.19	180
Angle	1O-4Ni-2O	1.19	90
Angle	1O-4Ni-3O	1.19	90
Angle	sp3C-1O-4Ni	1.19	116
Angle	H-1O-4Ni	1.19	109
Angle	2O-4Ni-1O	1.19	90
Angle	2O-4Ni-2O	1.19	180
Angle	2O-4Ni-3O	1.19	90
Angle	sp3C-2O-4Ni	1.19	116
Angle	H-2O-4Ni	1.19	109
Angle	3O-4Ni-1O	1.19	90
Angle	3O-4Ni-2O	1.19	90
Angle	3O-4Ni-3O	1.19	180
Angle	sp3C-2O-4Ni	1.19	116
Angle	H-3O-4Ni	1.19	109

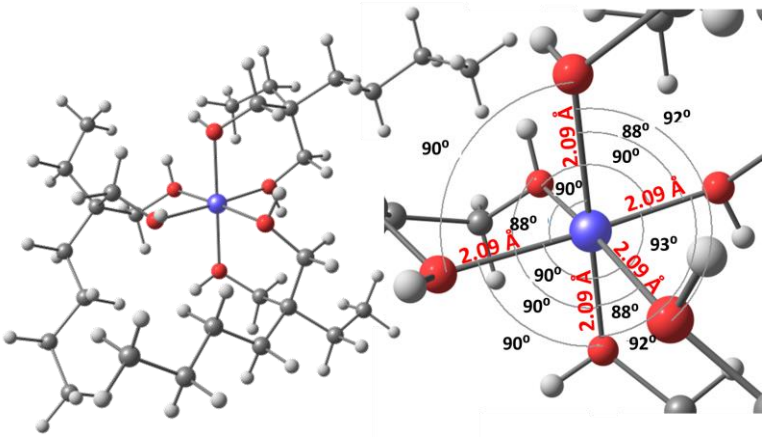

Figure 4.43 MM3 optimized $[Ni(Pdiol)_3]^{2+}$

The $[NiPdiol)_3]^{2+}$ has an optimized geometry that is in good agreement with the DFT optimized structure. Bond lengths vary by less than 0.02 Å, and bond angle by less than 4°.

Thermodynamics of MM3 Geometries

Charge Neutral Models As discussed in the introduction, molecular mechanics can be used to calculate strain energy relative to the equilibrium values for each of its parameterized potentials. The steric energy can be used to minimize geometries, but is not thermodynamically meaningful. To get thermodynamically relevant energies for MM3 optimized geometries PM7 single point calculations must be performed to get PM7 calculated heats of formation. Table 4.13 gives the calculated values of both heats of formation, enthalpy and entropy for the equilibria and compares those calculated using the PM7 and DFT optimized structures.

As the number of species present in a chemical model of LETC increases not only does it become more computationally expensive to calculate the interactions within the

model, but the potential energy surfaces becomes smoother. The smoother potential energy surface makes it easier to optimize models into local minimum as opposed to global. To find the global minima for LETC models a Monte Carlo (MC) optimization method was used.

The MC geometry optimization algorithm within the Tinker molecular mechanics package make a randomized 1Å perturbation of the Cartesian coordinated an atom in the starting geometry. The resulting geometry is then optimized using the standard Newton optimization scheme. Geometries with lower optimized steric energies are retained and a subsequent one angstrom perturbation is made to that geometry. The process is repeated for a designated number of steps. We always took performed 500k steps to assure a minim structure was found. To ensure that the MM3 MC optimization method was optimizing the charge neutral model geometries from (figures 4.31-34) were optimized with MC/MM and the PM7 heats of formation were calculated to ensure that the geometries were optimizing with respect to PM7.

Figure 4.44 shows the MM3 strain energies and corresponding PM7 calculated heats of formation for a ($TBA^{+} \cdot [\ NiBr_4]^{2-}$) geometry at points during an MM3 MC optimization.

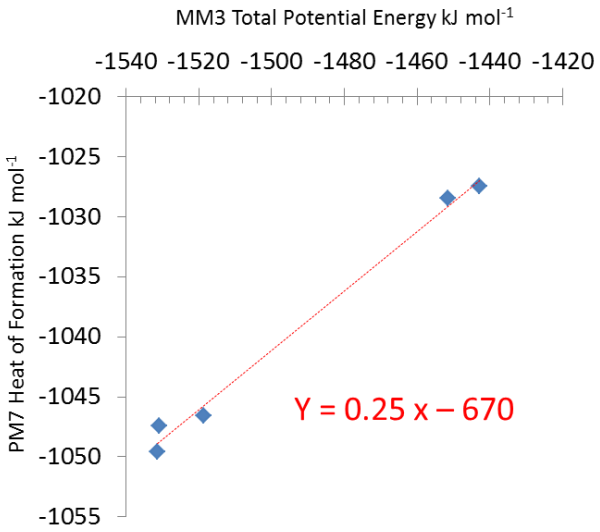

Figure 4.44 MC MM3 optimized structure calculated total potential energy vs PM7 calculated single point heats of formations

The linear relationship in Figure 4.43 ensures that as geometries are being optimized with respect to their calculated MM3 energy they are also being optimized with respect to the PM7 $H^0_{form.}$. If this was not true there would be no way to ensure MM3 was finding chemically meaningful minimum energy conformations.

The charge neutral models calculated in the PM7 section were optimized using 500k M.C. steps. Table 4.11 shows a comparison of intermolecular distances (measured between the Ni and N, O, or Br) for MM3 MC and PM7 optimized geometries.

Table 4.13 Comparison of average intermolecular distances for MM3 MC optimized and PM7 optimized of charge neutral chromophore models.

	MM3 MC Average Intermolecular Distance Å	PM7 Average Intermolecular Distance Å
$[Ni(Pdiol)_3]^{2+}$ $2Br^-$	3.76	4.50
$2TBA^{2+}$ $[NiBr_4]^{2-}$	4.75	6.35
$NiBr_2(Pbiz)_2$ 3Pdiol	3.50	5.00
TBA^+ $[NiBr_3(Pbiz)]^-$	4.69	6.25
TBA^+ Br^-	4.63	6.00

The inter ion distances are across the board shorter in MM3 optimizations. This means that MM3 will most likely overestimate ion stabilization due to ion pairing. The $NiBr_2(Pbiz)_2$ 3Pdiol is somewhat of a standout, probably due to the lack of formal charge on the oxygens in the Pdiol.

The heats of formation for the above structures were calculated using PM7 single points. The heats of formation and Hess's law were used to calculate ΔH^0_{rxn} for the equilibria in Equations 4.10-4.12 and the results can be seen, compared to the PM7 optimized values in Table 4.12.

Table 4.14 Comparison of heats of formation calculated for MM3 MC and PM7 optimized charge neutral chromophores.

	MM3 optimized PM7 Heat of Formation kJ mol^{-1}	PM7 Optimized Heat of Formation kJ mol^{-1}
$Ni(Pdiol)_3$ 2Br	-1605	-1911
2TBA $NiBr_4$	-1044	-1100
TBA $NiBr_3(Pbiz)$	-204	-594
$NiBr_2(Pbiz)_2$ 3Pdiol	-1156	-1879
TBABr	-432	-450
Pdiol	-546	-561
Pbiz	87	74

The heats of formation in Table 4.11 follow the trends of the PM7 optimizations and the values are always less stable, but the error in the stability is not systematic (Figure 4.45).

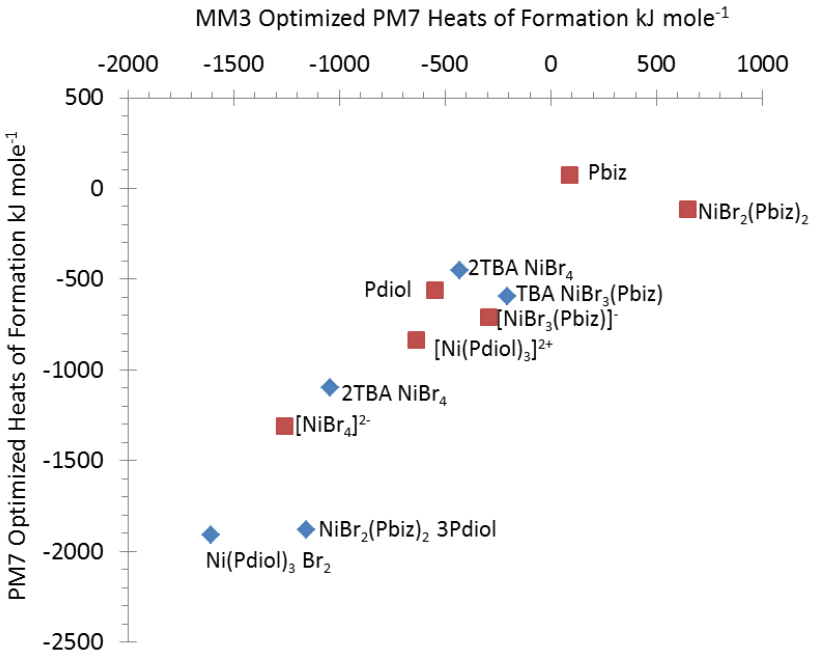

Figure 4.45 Comparison of heats of formation calculated using PM7 on PM7, and MM3 optimized geometries

The non-systematic error leads to MM3 predicted PM7 ΔH^0_{rxn} values calculated that are chemically unrealistic.

Full Ni^{2+} Boundary Box Models MM3 force field calculations can be used to optimize models that contain all the species present in the Ni^{2+} periodic boundary box. When putting together the full Ni^{2+} periodic boundary box models the configuration of molecules had to be considered so that the relative stability of ion pairing, or neutral molecules separating ions in the system could be accessed.

To better explain the rational used to build the Ni^{2+} boundary box models the $[NiBr_4]^{2-}$ chromophore will be used as an illustrative example. Figure 4.46 illustrates the one configuration of all the species present in a Ni^{2+} boundary box when the $[NiBr_4]^{2-}$ chromophore is present.

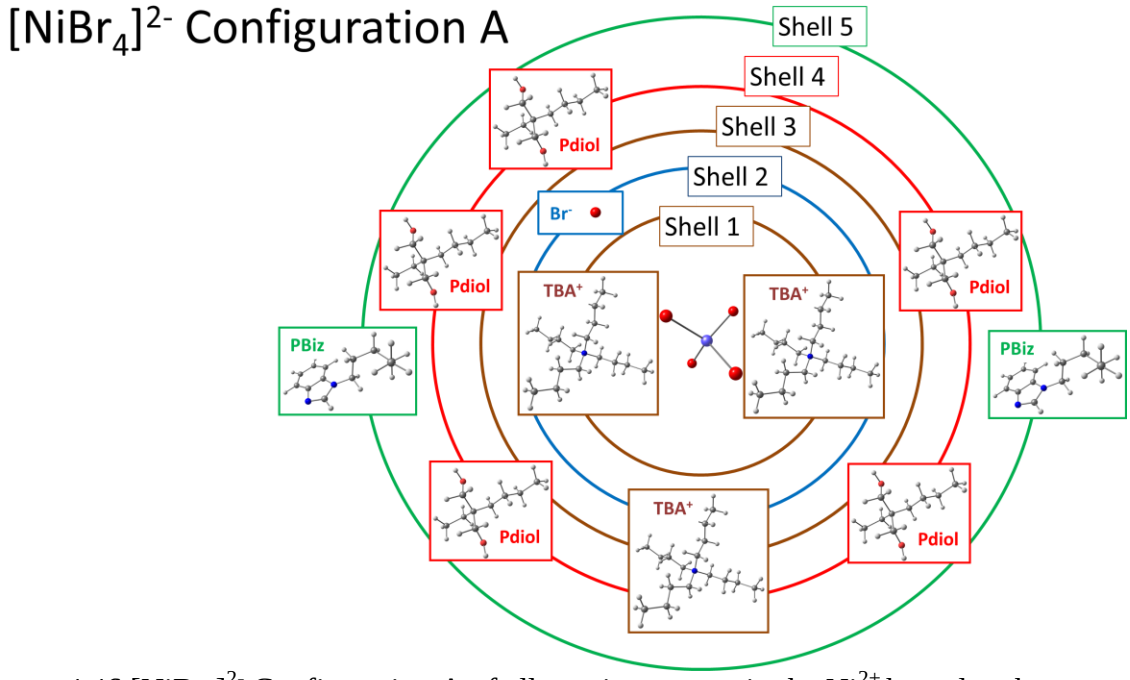

Figure 4.46 $[NiBr_4]^{2-}$ Configuration A of all species present in the Ni^{2+} boundary box with solvation shell definitions.

Each ring in Figure 4.46 represents a different "solvation shell". In the model represented by Figure 4.46 The TBA^+ and Br^- ions were placed around the charge neutral $2TBA^+$ $[NiBr_4]^{2-}$ model so as to optimize ion pairing interactions. The system was then optimized using 500k MC steps. Once the 500k MC steps were complete the species in the next shell (five Pdiols) were added one at a time so as to maximize hydrogen bonding, and another MM3 MC 500k step optimization was performed upon adding each leL. This process was repeated until all the chemically active species and their counterions in the Ni^{2+} boundary box were present.

The order of species that were added to the model was varied so as to test the importance of different weak interactions in the model.

Table 4.15 $[NiBr_4]^{2-}$ Configuration A, B, and C of all species present in the Ni^{2+} boundary box with solvation shell definitions.

Configuration	Shell 1 Species	Shell 2 Species	Shell 3 Species	Shell 4 Species	Shell 5 Species
A	2 TBA^+	Br^-	TBA^+	5 Pdiol	2 Pbiz
B	2 TBA^+	Br^-	TBA^+	2 Pbiz	5 Pdiol
C	2TBA^+	2Pbiz	5Pdiol	TBA^+	Br^-

Configuration B swaps the configuratiuon A's neutral ligands in the 4th and 5th shells. Configuration C places the charge neutral Pbiz ligands in the third shell, distancing the charged species (TBA^+ and Br^-) from the charged $[NiBr_4]^{2-}$ chromophore.

Once all the active species and their counterions were optimized using the MM3 MC method, the polymer monomers were added to the model in the quantities given in the introduction. The monomers were added in such a way as to maximize hydrogen bonding. The full Ni^{2+} model was then put through a final 10k step MM3 MC optimization. Figure 4.47 shows the MM3 MC optimized of the $[NiBr_4]^{2-}$ Configuration A with polymer monomers surrounding it.

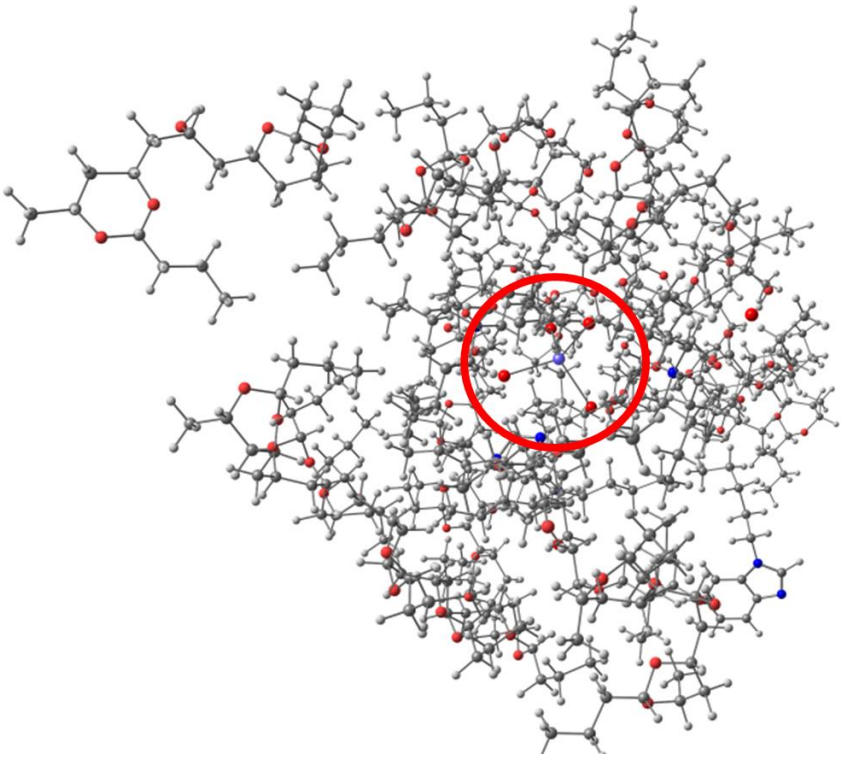

Figure 4.47 Full Ni^{2+} boundary box model of $[NiBr_4]^{2-}$ (highlighted in red circle) of Configuration A.

With the MM3 MC optimization complete the polymer species were removed from the model and PM7 single point calculations were performed on the resulting geometries to get PM7 heats of formation.

The initial MM3 MC optimized geometries were also used as a starting point for PM7 optimizations. A single PM7 optimization step of the full Ni^{2+} boundary box models, which contain 380 atoms, took ~10-15 hours on a two processor compute node with an Intel Xeon CPU 3.00GHz processor. The smoothness of the potential energy surface necessitated the development of an optimization cutoff criteria that differed from the gradient < 0.1 that is default in the MOPAC's Newton Minimization method. All optimizations reached at least 250 steps. To extrapolate minimum heat of formation

values from the optimizations the last 30 values for the gradient were fit with a line. The line was extrapolated out to the gradient equal zero step. A line was also fit to the last 30 heat of formation values. The heat of formation line was then evaluated at the step predicted by the zero gradient linear fit extrapolation (Figure 4.48).

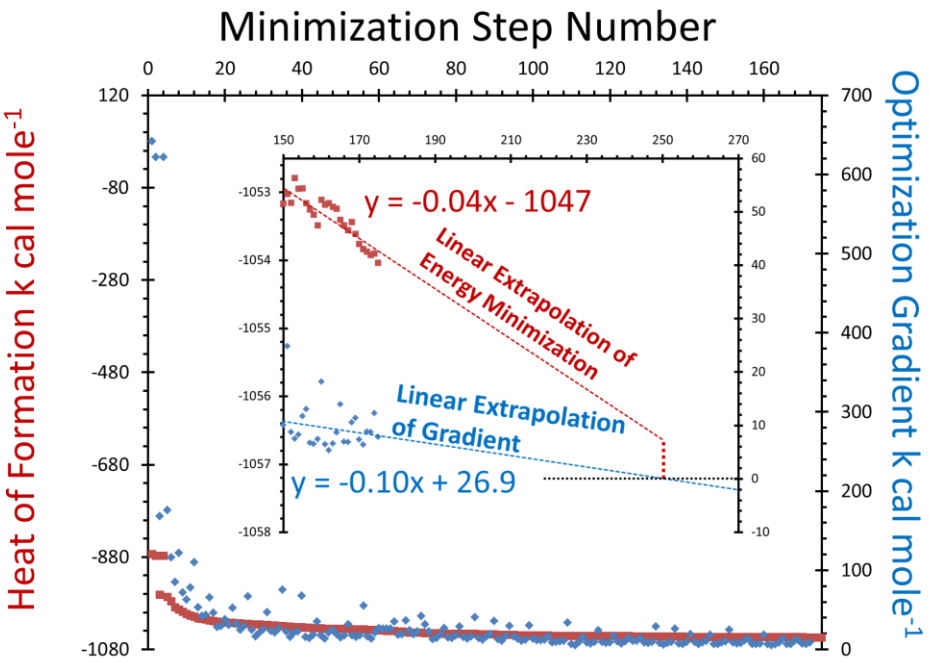

Figure 4.48 Illustrates the extrapolation method used to determine optimized PM7 heats of formation for the full Ni^{2+} boundary box models.

The MM3 MC optimized heats of formation as well as PM7 optimized heats of formation for the three previously shown $[NiBr_4]^{2-}$ boundary box calculations are given in Table 4.14.

Table 4.16 MM3MC and PM7 optimized Heats of formation for the $[NiBr_4]^{2-}$ configurations in the Ni^{2+} boundary box.

	MM3 Intermolecular Distances Å					PM7 Intermolecular Distances Å				
Configuration	MM3 Heat of Formation kJ mole^{-1}	Ni - N (TBA)	Ni N (Pbiz)	Br - H (Pdiol)	Br - N (TBA)	MM3 Heat of Formation kJ mole^{-1}	Ni - N (TBA)	Ni N (Pbiz)	Br - H (Pdiol)	Br - N (TBA)
A	-865	5.07	9.40	3.06	4.19	-1102	5.19	8.99	2.98	4.07
B	-856	4.99	3.03	3.05	4.31	-1084	5.17	4.13	3.65	4.18
C	-866	5.38	2.98	3.01	4.50	-1102	5.31	4.39	3.10	4.20

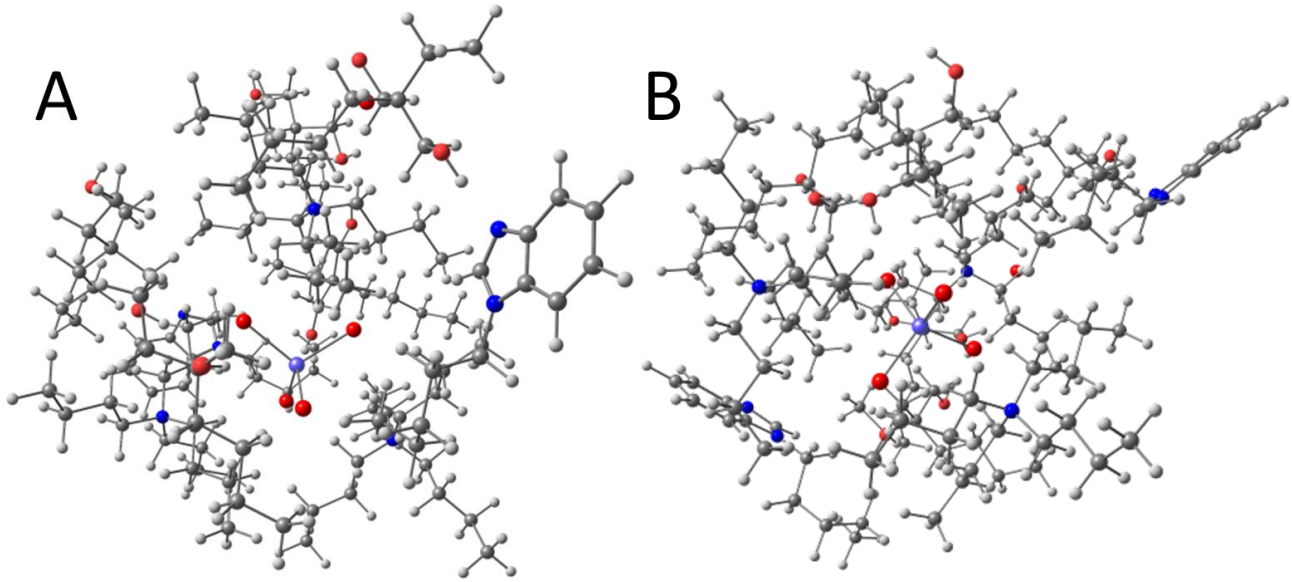

Figure 4.49 MM3 MC (A) and PM7 (B) optimized models of $[NiBr_4]^{2-}$ Configuration A

Note that the PM7 structures are all at least 200kJ $mole^{-1}$ more stable than those optimized using the MM3 MC method. Both methods predict the most stable configurations to be A and C. The PM7 optimizations increase the energy discrepancy between configuration B and A,C (~20kJ $mole^{-1}$). When comparing the intermolecular distances it can be seen that the MM3 MC optimized structures were more compact with shorter intermolecular distances. The trend in model compactness between MM3 MC and PM7 was seen for all chromphore models as well as the trend in energy differences between MM3 and PM7 models.

Table 4.15 lists the different model configurations for all the potential chromophores in the blue film LETC equilibrium.

Table 4.17 Definitions of A, B, and C configurations the of $[Ni(Pdiol)_3]^{2+}$, $[NiBr_3(Pbiz)]^-$ and$NiBr_2(Pbiz)_2$ full Ni^{2+} boundary box with solvation shell definitions.

Configuration	Shell 1 Species	Shell 2 Species	Shell 3 Species	Shell 4 Species	Shell 5 Species
$[Ni(Pdiol)_3]^{2+}$					
A	2 Pdiol	2 Pbiz	5 Br^-	3 TBA^+	
B	2 Br^-	3 TBA^+	3 Br^-	2 Pbiz	2 Pdiol
C	2 Br^-	2 Pbiz	2 Pdiol	3Br^-	3 TBA^+
$[NiBr_3(Pbiz)]^-$					
A	5 Pdiol	Pbiz	3TBA^+	3 Br^-	
B	TBA^+	5 Pdiol	Pbiz	2 TBA^+	2 Br^-
$NiBr_2(Pbiz)_2$					
A	3 TBA^+	3 Br^-	5 Pdoil		
B	5 Pdiol	3 TBA^+	3 Br^-		

Table 4.16 presents the single point PM7 H_f^0 calculated for the MC/MM3 optimized structure. The second column lists the PM7 optimized H_f^0.

Table 4.18 PM7 Heats of formation for the MC/MM3/SP optimized models of all configurations of the potential chromophores present in the blue Suntuitive™ film.

	Configuration	MM3 MC Optimized PM7/SP H_f^0 kJ mole^{-1}	PM7 Optimized H_f^0 kJ mole^{-1}
$[NiBr_4]^{2-}$	A	-3621	-4611
	B	-3582	-4535
	C	-3625	-4607
$[Ni(Pdiol)_3]^{2+}$	A	-3292	-4431
	B	-3317	-4422
	C	-3232	-4347
$[NiBr_3(Pbiz)]^-$	A	-3624	-3718
	B	-3627	-4617
$NiBr_2(Pbiz)_2$	A	-3507	-4632
	B	-3510	-4640

From the energies associated with the configurations shown in Table 4.14, it can be seen that the models that initially place opposite charges closest to each other are consistently the lowest energy systems. This builds on the picture that the DFT and PM7 calculations painted, where the coordination chemistry is dominated by ionic interactions.

The lowest energy heat of formations for the model configurations were used with Hess' law to calculate ΔH^0_{rxn} values for the equilibria between $[Ni(Pdiol)_3]^{2+}$ and all three possible chromophores. The results can be seen in Table 4.17.

Table 4.19 ΔH^0rxn for the equilibria connecting the most stable Ni^{2+} boundary box models for the three potential chromphores in blue Suntuitive™ LETC film

	MM3 MC optimized PM7 ΔH^0rxn kJ mole^{-1}	PM7 Optimized ΔH^0rxn kJ mole^{-1}
$[NiBr_4]^{2-}$	-308	-180
$[NiBr_3(Pbiz)]^-$	-310	-186
$NiBr_2(Pbiz)^2$	-193	-209

Yet again none of the systems produced endothermic reactions. This is a function of the flatness of the potential energy surface being investigated in the MM3 model study. There are too many interactions in the system to be able to find a global minimum.

Discussion

The computational modeling study of the Blue Suntuitive film that is based on the Ni^{2+} boundary box model showed that the empirically developed B23HFP86 density functional acceptably well reproduces UV-Vis spectral features of the film using potential film chromophores relative to other, more commonly used functionals. Despite the calibration efforts, it does not reproduce the spectral features to the degree required to determine what chromophores are present.

All but the charge neutral DFT model incorrectly predict exothermic LETC reactions with ΔH^0 values of ~ -50-100 kJ mol^{-1}. The exothermic prediction from the charge neutral model suggests ion pairing as being an important factor in LETC equilibrium. Due to the inconsistency in the ΔH^0 value predicted by the PM7 calculation for the same model, we believe the model still fails to capture the complexity of the ligand exchange process that takes place within the film at a molecular level.

The $[Ni(Pdiol)_3]^{2-}$ to $[NiBr_4]^{2-}$ reaction shown in the Equation 4.9 can be used as an example to demonstrate the complexity of thermochemistry we need to consider. The high and low temperature equilibrium constant for the reaction are given by Equations 4.28 and 4.29 respectively

$$K(T_H) = e^{-\frac{\Delta H^0}{RT_H}+\frac{\Delta S^0}{R}} \tag{4.28}$$

$$K(T_L) = e^{-\frac{\Delta H^0}{RT_L}+\frac{\Delta S^0}{R}} \tag{4.29}$$

$$\frac{K(T_H)}{K(T_L)} = e^{-\frac{\Delta H^0}{R}*\left(\frac{1}{T_L}-\frac{1}{T_H}\right)} \tag{4.30}$$

Equations 4.28 and 4.29 give the temperature dependence of the two equilibrium constants. Neglecting the temperature dependence of the standard enthalpy and entropy, the ratio of the two equilibrium constant is shown in Equation 4.30. The complexity of the LETC system can be seen when the equilibrium constant from Equation 4.31 is expressed using the molar concentrations and activity coefficients

$$K_{eq} = \frac{\gamma_{NiBr_4{}^{2-}}\left[NiBr_4{}^{2-}\right] * \gamma^3{}_{Pdiol}[Pdiol]^3}{\gamma_{Ni(Pdiol)_3{}^{2+}}\left[Ni(Pdiol)_3{}^{2+}\right] * \gamma^4{}_{Br^-}[Br^-]^4} \tag{4.31}$$

The activity coefficients in equation 4.31 are not independent of each other or temperature. As the temperature increases the reaction proceeds in the forward direction, and the concentration of Br^- ion decreases. This decrease affects the ionic strength of the solution and changes the activity coefficient associated with the $[Ni(Pdiol)_3]^{2+}$. These

affects are thought to be large in a system as concentrated and therefore manifest non-ideal solution behavior in the blue LETC film. Given that none of the computational models can reasonably well reproduce the standard free energy values required for functioning thermochromism, it is plausible that the temperature dependent activity coefficients will also contribute to change of the sign of enthalpy that at a single molecule level was calculated to be $\Delta H^0 < 0$.

All but the truncated charge neutral PM7 models predict the correct sign for the ΔS^0. This is especially interesting considering that the entropy in these systems is calculated using the ideal gas model approximation without consideration of the ion solvation entropies. The absolute entropies of all species are dominated by vibrational term (~50-70 % of total entropy) followed closely by the translational entropy (~15-25 % of total entropy) and least important contribution from the rotational entropy (~5-10 % of total entropy). The translational entropy calculations can be considered as being overestimated due to the difference in movement of molecules in gas phase vs. condensed phase medium that restricts their mean free path.[187] If the LETC master equation is examined (Equation 1.3) for a Pdiol lεL complex

$$[M(l\varepsilon L)_3]^x + 4\ h\varepsilon L^y \leftrightarrow [M(h\varepsilon L)_4]^z + 3\ l\varepsilon L \qquad (4.32)$$

The entropy correction would be require -7.8 kJ mol^{-1} to be removed from the free energy at 298 K due to an imbalance in the number of species on the left and right hand side.

To better understand our computational results of with this study further experimentation is needed. The experimental determination of the effects of temperature on activity is crucial to understanding the role that ion pairing plays in modeling these LETC systems.

CHAPTER 5

CONCLUSION

Bridging the macroscopic observation of LETC materials, and their molecular level description requires the integration of theoretical and experimental techniques. It is this integrated approach that guided the initial research into developing the structure-function relationships that stand to contribute to the design and improvement of current materials in smart window technology.

In Chapter 2 the S K-edge analysis of a spectrochemical series for [Ni(II)S_4] complexes allowed for the determination of the composition of the unoccupied frontier orbitals using the pre-edge, and rising edge features. Already available XAS and EPR data allowed us to explore the relationship between the composition of the ligands and the magnitude of S 1s$\rightarrow$3p transition dipole integral. There were notably higher transition dipole integrals found for ligands that contain N substituents electronically interacting with the sulfur centers.

The computed electronic structures from the popular density functional theory showed discrepancies with the experimental X-ray absorption spectroscopy (XAS) data. We concluded that when dealing with nickel(II) coordination complexes one should not rely too heavily on any one functional or population analysis model unless the functional is selected based on its experimental agreement with a system as chemically similar to the system in question as possible.

We can classified the series of [Ni(II)S_4] complexes into three categories. There were the tetrahedral tetrathiolate complexes that can be described with a classical coordination chemical bonding description where the lowest unoccupied frontier orbitals are metal based. There were the complexes that constrained two negatively charged thiolates either through a ring system ($nbdt^{2-}$) or double bonds ($dmedt^{2-}$). This constraint induced an inverted bonding description, where each ligand donated more than 0.5% e^{-1} $hole^{-1}$ to the metal, effectively reducing the metal. The most unexpected finding in the study was that the two more oxidized S-ligands ($Ni(dtc)_2$, and $[Ni(ttctd)]^{2+}$), with intense pre-edge features, were best described by a normal bonding scenario with 31, and 39% e^- $hole^{-1+}$ respectively. This covalency supports a picture of the ttctd hεL ligand bonded to nickel because of an ideal S-Ni overlap and only modest ionic character.

In Chapter 3 the S K-XAS and DFT study extended the series of conjugated nitrogen containing sulfur ligands, previously found to have inhanced pre-edge intensity, to include the formally sp^2 hybridized thiourea (TU) ligand. The edge-jump energy of the free TU was used to establish two limits for the free ligand-based S 1s→3p transition dipole integrals. The larger one included the dipole correction for the presence of conjugated nitrogen atoms. This dipole correction accounts for the expected increase in fluorescence intensity relative to unsubstituted hydrocarbon ligands found earlier for the Na_2mnt and the Nadtc complexes. When the nitrogen corrected value was used to quantitate the S 3p orbital character from the pre-edge intensities (D_0) and edge positions shifts between the $[Co(TU)_4]^{2+}$ and $[Ni(TU)_6]^{2+}$ complexes the Ni-S bond characters were found to be 9% and 15% e^- $hole^{-1}$.

Similarly to those obtained for the $[Ni^{(II)}S_4]$ complexes, none of the GGA, hybrid, metaGGA density functionals used in the study reproduced the Ni-S(TU) bond covalencies. It is worth mentioning that the B3LYP functional gave good agreement fortuitously with the S K-XAS results when the lower value of the hydrocarbon dipole integral was used. This agreement between DFT. S K-XAS results, and the Chapter 2 observation that all functionals gave overly covalent bonding descriptions suggesting that the corrected transition dipole integral is more accurate in the quantitation of the S orbital character of the Ni(II) and Co(II) TU complexes.

The Chapter 3 results were used to motivate a time dependent density functional theory based survey of density functionals in Chapter 4. The search looked for a functional that could reproduce the $[NiX_4]^{2-}$ (X= Cl, Br, and I) series UV-Vis excitations. The selected B23HFP86 functional was then used to calculate transitions of potential chromophores within the blue Suntuitive® film. The results were inconclusive as to the actual chromophores present in the film.

Most of the thermochemistry computational modeling of the potential equilibria in the LETC film incorrectly predicted exothermic reactions with ΔH^0 values of ~ -50-100 kJ mol^{-1}. The truncated charge neutral $[Ni(Pdiol)_3]^{2+} \bullet (Br^-)_2 \rightarrow (TBA^{2+})_2 \bullet [NiBr_4]^{2-}$ equilibrium (Equation 4.25) gave the correct endothermic result. This endothermic result suggests the importance of ion pairing in LETC equilibrium. Despite this positive result we still believe the model fails to capture the complexity of the ligand exchange process that takes place within the film. To better understand the computational results presented

in this study, further experimentation into the effects of temperature on ionic strength is needed.

REFERENCES CITED

1. D. Arasteh, S. S., J. Apte, M. LaFrance Zero Energy Windows. In ACEEE Summer Study on Energy Effciency in Buildings, Pacific Grove, Ca, 2006; Pacific Grove, Ca, 2006.

2. Svensson, J. S. E. M.; Granqvist, C. G. Electrochromic Coatings For "Smart Windows". 1984; 1984; Vol. 0502; pp 30-37.

3. Byker, H. J.; Ogburn, P. H.; Vander Griend, D. A.; Veldkamp, B. S.; Winkle, D. D. Ligand exchange thermochromic, (LETC), systems US 7,525,717 b2, April 28, 2009.

4. McQuarrie, D. A. R. P. A. G. E. B., *General chemistry*. University Science Books: Mill Valley, CA, 2011.

5. Araujo, R. J.; Hares, G. B.; Kerko, D. J.; Morgan, D. W.; Morse, D. L. Ultraviolet absorbing photochromic glass of low silver content. US 4,549,894, October 29, 1985.

6. Deniz, E.; Tomasulo, M.; Sortino, S.; Raymo, F. M., Substituent Effects on the Photochromism of Bichromophoric Oxazines. *J. Phys. Chem. C* **2009**, 113, 8491-8497.

7. Ercole, F.; Davis, T. P.; Evans, R. A., Comprehensive Modulation of Naphthopyran Photochromism in a Rigid Host Matrix by Applying Polymer Conjugation. *Macromolecules* **2009**, 42, 1500-1511.

8. Momoda, J.; Kawabata, Y.; Tanaka, N.; Iwata, A. Chromene compound. US 7,521,004 April 21, 2009.

9. Perrott, C. M.; Pidgeon, K. J. A photochromic light-transmissible article. WO 1,996,018,927 A1, 1996.

10. Lin, J. S., Interaction between dispersed photochromic compound and polymer matrix. *Eur. Polym. J.* **2003**, 39, 1693-1700.

11. Lee, E. S.; Pang, X. F.; Hoffmann, S.; Goudey, H.; Thanachareonkit, A., An empirical study of a full-scale polymer thermochromic window and its implications on material science development objectives. *Sol. Energy Mater. Sol. Cells* **2013**, 116, 14-26.

12. Granqvist, C. G., Electrochromic tungsten oxide films: Review of progress 1993-1998. *Sol. Energy Mater. Sol. Cells* **2000**, 60, 201-262.

13. Deb, S. K., Opportunities and challenges in science and technology of WO3 for electrochromic and related applications. *Sol. Energy Mater. Sol. Cells* **2008**, 92, 245-258.

14. Bechtel, J. H.; Byker, H. J. Improved automatic rearview mirror system for automotive vehicles. US 4,917,477 A, April 17, 1990.

15. Tang, H.; MacLaren, D. C.; White, M. A., New insights concerning the mechanism of reversible thermochromic mixtures. *Can. J. Chem.* **2010**, 88, 1063-1070.

16. Schönberg, A.; Mustafa, A.; Asker, W., Some Adsorption Colors and their Significance for Thermochromic and Tautomeric Effects. II.1 Experiments with Spiropyrans and with 1,3-Diketohydrindene. *J. Am. Chem. Soc.* **1951**, 73, 2876-2879.

17. Day, J. H., Thermochromism. *Chem. Rev.* **1963**, 63, 65-80.

18. Sone, K.; Fukuda, Y., *Inorganic thermochromism*. Springer-Verlag: 1987.

19. Miessler, G. L.; Tarr, D. A., *Inorganic Chemistry*. Pearson Prentice Hall: 2010.

20. Griffith.Tr; Scarrow, R. K., Effects of Cations Upon Absorption Spectra .2. Formation of Tetrahedral Tetrachloronickelate(II) in Aqueous Solution *J. Chem. Soc. Faraday Trans* **1969**, 65, 1727-&.

21. Solomon, E. I.; Lever, A. B. P., *Inorganic Electronic Structure and Spectroscopy: Applications and case studies*. Wiley: 1999.

22. Bohr, N., On the Constitution of Atoms and Molecules. *Philos. Mag.* **1913**, 26, 1-25.

23. Moseley, H. G. J., The High-Frequency Spectra of the Elements. *Philos. Mag.* **1913**, 26, 1024-1034.

24. Solomon, E. I.; Hedman, B.; Hodgson, K. O.; Dey, A.; Szilagyi, R. K., Ligand K-edge X-ray absorption spectroscopy: covalency of ligand-metal bonds. *Coord. Chem. Rev.* **2005**, 249, 97-129.

25. Lever, A. B. P., *Inorganic Electronic Spectroscopy*. Elsevier: Amsterdam, 1984; Vol. 33

26. Silver, A.; Koch, S. A.; Millar, M., X-Ray Crystal-Structures of a Series of [M(Ii)(Sr)4]2- Complexes (M = Mn, Fe, Co, Ni, Zn, Cd and Hg) with S4 Crystallographic Symmetry. *Inorg. Chim. Acta* **1993**, 205, 9-14.

27. Williams, K. R.; Hedman, B.; Hodgson, K. O.; Solomon, E. I., Ligand K-edge X-ray absorption spectroscopic studies: metal-ligand covalency in transition metal tetrathiolates. *Inorg. Chim. Acta* **1997**, 263, 315-321.

28. McCleverty, J. A., *Metal 1,2-Dithiolene and Related Complexes*. John Wiley & Sons, Inc.: Hoboken, NJ, USA, 1968; Vol. 10, p 49–221.

29. Schrauzer, G. N., Coordination Compounds with Delocalized Ground States . Transition Metal Derivatives of Dithiodiketones and Ethylene(1,2) Dithiolates (Metal Dithienes). *Accounts Chem. Res.* **1969**, 2, 72-80.

30. Eisenberg, R., *Structural Systematics of 1,1- and 1,2-Dithiolato Chelates*. John Wiley & Sons, Inc.: Hoboken, NJ, USA, 1970; Vol. 12, p 295–369.

31. Maki, A. H.; Davison, A.; Edelstein, N.; Holm, R. H., Electron Paramagnetic Resonance Studies of Electronic Structures of Bis(Maleonitriledithiolato)Copper)2) -Nickel)3) -Cobalt)2) + -Rhodium)2) Complexes. *J. Am. Chem. Soc.* **1964**, 86, 4580-4587.

32. Shupack, S. I.; Williams, R.; Gray, H. B.; Billig, E.; Clark, R. J. H., Electronic Structures of Square-Planar Metal Complexes .V. Spectral Properties of Maleonitriledithiolate Complexes of Nickel Palladium + Platinum. *J. Am. Chem. Soc.* **1964**, 86, 4594-4602.

33. Schrauzer, G. N.; Mayweg, V. P., Preparation Reactions and Structure of Bisdithio-Alpha-Diketone Complexes of Nickel Palladium and Platinum. *J. Am. Chem. Soc.* **1965**, 87, 1483–1489.

34. Baker, J. R.; Hermann, A.; Wing, R. M., Mechanism of Oxidative Cycloaddition of Olefins to Metal Dithiolenes. *J. Am. Chem. Soc.* **1971**, 93, 6486–6489.

35. Wang, K.; Stiefel, E. I., Toward separation and purification of olefins using dithiolene complexes: An electrochemical approach. *Science* **2001**, 291, 106-109.

36. Bachler, V.; Olbrich, G.; Neese, F.; Wieghardt, K., Theoretical evidence for the singlet diradical character of square planar nickel complexes containing two omicron-semiquinonato type ligands. *Inorg. Chem.* **2002**, 41, 4179-4193.

37. Szilagyi, R. K.; Lim, B. S.; Glaser, T.; Holm, R. H.; Hedman, B.; Hodgson, K. O.; Solomon, E. I., Description of the ground state wave functions of Ni dithiolenes using sulfur K-edge X-ray absorption spectroscopy. *J. Am. Chem. Soc.* **2003**, 125, 9158-9169.

38. Kaim, W.; Schwederski, B., Non-innocent ligands in bioinorganic chemistry-An overview. *Coord. Chem. Rev.* **2010**, 254, 1580-1588.

39. Eisenberg, R., Trigonal prismatic coordination in tris(dithiolene) complexes: Guilty or just non-innocent? *Coord. Chem. Rev.* **2011**, 255, 825-836.

40. Schmitt, R. D.; Maki, A. H., Electronic Ground State of Bis(Maleonitriledithiolene)Nickel Monoanion . Sulfur-33 Hyperfine Interaction. *J. Am. Chem. Soc.* **1968**, 90, 2288-2292.

41. Huyett, J. E.; Choudhury, S. B.; Eichhorn, D. M.; Bryngelson, P. A.; Maroney, M. J.; Hoffman, B. M., Pulsed ENDOR and ESEEM study of [bis(maleonitriledithiolato)nickel](-): An investigation into the ligand electronic structure. *Inorg. Chem.* **1998**, 37, 1361-1367.

42. Lim, B. S.; Fomitchev, D. V.; Holm, R. H., Nickel dithiolenes revisited: Structures and electron distribution from density functional theory for the three-member electron-transfer series [Ni(S(2)C(2)Me2)(2)](0,1-,2-). *Inorg. Chem.* **2001**, 40, 4257-4262.

43. Fomitchev, D. V.; Lim, B. S.; Holm, R. H., Electron distribution in the nonclassical bis(dithiolene) electron transfer series [M(CO)(2)(S2C2Me2)(2)](0/1-/2-) (M = Mo, W): Assessment by structural, spectroscopic, and density functional theory results. *Inorg. Chem.* **2001**, 40, 645-654.

44. Rosen, W.; Busch, D. H., Nickel(II) Complexes of Cyclic Tetradentate Thioethers. *J. Am. Chem. Soc.* **1969**, 91, 4694-4697.

45. Veldkamp, B. S.; Vander Griend, D. A.; Byker, H. J., In; West Olive, MI, 2012, p personal communication.

46. Hedman, B.; Hodgson, K. O.; Solomon, E. I., X-Ray Absorption-Edge Spectroscopy of Ligands Bound to Open-Shell Metal-Ions - Chlorine K-Edge Studies of Covalency in Cucl42. *J. Am. Chem. Soc.* **1990**, 112, 1643-1645.

47. Shadle, S. E.; Hedman, B.; Hodgson, K. O.; Solomon, E. I., Ligand K-Edge X-Ray-Absorption Spectroscopic Studies - Metal-Ligand Covalency in a Series of Transition-Metal Tetrachlorides. *J. Am. Chem. Soc.* **1995**, 117, 2259-2272.

48. Neese, F.; Hedman, B.; Hodgson, K. O.; Solomon, E. I., Relationship between the dipole strength of ligand pre-edge transitions and metal-ligand covalency. *Inorg. Chem.* **1999**, 38, 4854-4860.

49. Boysen, R. B.; Szilagyi, R. K., Development of palladium L-edge X-ray absorption spectroscopy and its application for chloropalladium complexes. *Inorg. Chim. Acta* **2008**, 361, 1047-1058.

50. Shadle, S. E.; Pennerhahn, J. E.; Schugar, H. J.; Hedman, B.; Hodgson, K. O.; Solomon, E. I., X-Ray Absorption Spectroscopic Studies of the Blue Copper Site - Metal and Ligand K-Edge Studies to Probe the Origin of the Epr Hyperfine Splitting in Plastocyanin. *J. Am. Chem. Soc.* **1993**, 115, 767-776.

51. Rose, K.; Shadle, S. E.; Glaser, T.; de Vries, S.; Cherepanov, A.; Canters, G. W.; Hedman, B.; Hodgson, K. O.; Solomon, E. I., Investigation of the electronic structure of 2Fe-2S model complexes and the Rieske protein using ligand K-edge X-ray absorption spectroscopy. *J. Am. Chem. Soc.* **1999**, 121, 2353-2363.

52. Izumi, Y.; Glaser, T.; Rose, K.; McMaster, J.; Basu, P.; Enemark, J. H.; Hedman, B.; Hodgson, K. O.; Solomon, E. I., Ligand K-edge and metal L-edge X-ray absorption spectroscopy and density functional calculations of oxomolybdenum complexes with thiolate and related ligands: Implications for sulfite oxidase. *J. Am. Chem. Soc.* **1999**, 121, 10035-10046.

53. George, S. D.; Basumallick, L.; Szilagyi, R. K.; Randall, D. W.; Hill, M. G.; Nersissian, A. M.; Valentine, J. S.; Hedman, B.; Hodgson, K. O.; Solomon, E. I., Spectroscopic investigation of stellacyanin mutants: Axial ligand interactions at the blue copper site. *J. Am. Chem. Soc.* **2003**, 125, 11314-11328.

54. Sarangi, R.; George, S. D.; Rudd, D. J.; Szilagyi, R. K.; Ribas, X.; Rovira, C.; Almeida, M.; Hodgson, K. O.; Hedman, B.; Solomon, E. I., Sulfur K-edge X-ray absorption spectroscopy as a probe of ligand-metal bond covalency: Metal vs ligand oxidation in copper and nickel dithiolene complexes. *J. Am. Chem. Soc.* **2007**, 129, 2316-2326.

55. Szilagyi, R. K.; Metz, M.; Solomon, E. I., Spectroscopic calibration of modern density functional methods using [CuCl(4)](2-). *J. Phys. Chem. A* **2002**, 106, 2994-3007.

56. Becke, A. D., Density-Functional Exchange-Energy Approximation with Correct Asymptotic-Behavior. *Phys. Rev. A* **1988**, 38, 3098-3100.

57. Gewirth, A. A.; Cohen, S. L.; Schugar, H. J.; Solomon, E. I., Spectroscopic and Theoretical-Studies of the Unusual Electron-Paramagnetic-Res Parameters of Distorted Tetrahedral Cupric Sites - Correlations to X-Ray Spectral Features of Core Levels. *Inorg. Chem.* **1987**, 26, 1133-1146.

58. Didziulis, S. V.; Cohen, S. L.; Gewirth, A. A.; Solomon, E. I., Variable Photon Energy Photoelectron Spectroscopic Studies of Copper Chlorides - an Experimental Probe of Metal-Ligand Bonding and Changes in Electronic-Structure on Ionization. *J. Am. Chem. Soc.* **1988**, 110, 250-268.

59. Szilagyi, R. K.; Solomon, E. I., Electronic structure and its relation to function in copper proteins. *Curr. Opin. Chem. Biol.* **2002**, 6, 250-258.

60. Solomon, E. I.; Szilagyi, R. K.; George, S. D.; Basumallick, L., Electronic structures of metal sites in proteins and models: Contributions to function in blue copper proteins. *Chem. Rev.* **2004**, 104, 419-458.

61. Rokhsana, D.; Dooley, D. M.; Szilagyi, R. K., Structure of the oxidized active site of galactose oxidase from realistic in silico models. *J. Am. Chem. Soc.* **2006**, 128, 15550-15551.

62. Rokhsana, D.; Dooley, D. M.; Szilagyi, R. K., Systematic development of computational models for the catalytic site in galactose oxidase: impact of outer-sphere residues on the geometric and electronic structures. *J. Biol. Inorg. Chem.* **2008**, 13, 371-383.

63. Rokhsana, D.; Howells, A. E.; Dooley, D. M.; Szilagyi, R. K., Role of the Tyr-Cys Cross-link to the Active Site Properties of Galactose Oxidase. *Inorg. Chem.* **2012**, ASAP, DOI: 10.1021/ic2022769.

64. Solomon, E. I.; Gorelsky, S. I.; Dey, A., Metal-thiolate bonds in bioinorganic chemistry. *J. Comput. Chem.* **2006**, 27, 1415-1428.

65. Solomon, E. I., Spectroscopic methods in bioinorganic chemistry: Blue to green to red copper sites. *Inorg. Chem.* **2006**, 45, 8012-8025.

66. Sarangi, R.; Gorelsky, S. I.; Basumallick, L.; Hwang, H. J.; Pratt, R. C.; Stack, T. D. P.; Lu, Y.; Hodgson, K. O.; Hedman, B.; Solomon, E. I., Spectroscopic and density functional theory studies of the blue-copper site in M121SeM and C112SeC azurin: Cu-Se versus Cu-S bonding. *J. Am. Chem. Soc.* **2008**, 130, 3866-3877.

67. Szilagyi, R. K.; Winslow, M. A., On the accuracy of density functional theory for iron - Sulfur clusters. *J. Comput. Chem.* **2006**, 27, 1385-1397.

68. Harris, T. V.; Szilagyi, R. K. Nitrogenase Structure and Function Relationships by Density Functional Theory. In *Methods in Molecular Biology: Nitrogen Fixation*, Ribbe, M., Ed.; Springer: 2011; Vol. 766, pp 267-291

69. Pandey, A. S.; Harris, T. V.; Giles, L. J.; Peters, J. W.; Szilagyi, R. K., Dithiomethylether as a ligand in the hydrogenase H-cluster. *J. Am. Chem. Soc.* **2008**, 130, 4533-4540.

70. So, J.-H.; Boudjouk, P.; Hong, H. H.; Weber, W. P. Hexamethyldisilathiane. In *Inorganic Synthesis*, Grimes, R. N., Ed.; John Wiley & Sons, Inc.: Hoboken, NJ, USA, 1992; Vol. 29, pp 30-32.

71. Hendrickson, A. R.; Martin, R. L.; Rohde, N. M., Dithiocarbamates of Nickel in Formal Oxidation-States I-Iv - Electrochemical Study. *Inorg. Chem.* **1975**, 14, 2980-2985.

72. Fox, S.; Wang, Y.; Silver, A.; Millar, M., Viability of the [Ni(III)(SR)4]- Unit in Classical Coordination-Compounds and in the Nickel Sulfur Center of Hydrogenases. *J. Am. Chem. Soc.* **1990**, 112, 3218-3220.

73. Ray, K.; George, S. D.; Solomon, E. I.; Wieghardt, K.; Neese, F., Description of the ground-state covalencies of the bis(dithiolato) transition-metal complexes from X-ray absorption spectroscopy and time-dependent density-functional calculations. *Chem.-Eur. J.* **2007**, 13, 2783-2797.

74. Szilagyi, R. K.; Frank, P.; George, S. D.; Hedman, B.; Hodgson, K. O., High covalence in $CuSO_4$ and the radicalization of sulfate: An X-ray absorption and density functional study. *Inorg. Chem.* **2004**, 43, 8318-8329.

75. Pickering, I. J.; George, G. N.; Yu, E. Y.; Brune, D. C.; Tuschak, C.; Overmann, J.; Beatty, J. T.; Prince, R. C., Analysis of sulfur biochemistry of sulfur bacteria using X-ray absorption spectroscopy. *Biochemistry* **2001**, 40, 8138-8145.

76. Gardenghi, D. J. http://computational.chemistry.montana.edu/ADRP/: Bozeman, MT, 2011.

77. M.J.T. Frisch, G. W., H.B. Schlegel, G.E. Scuseria, M.A. Robb, J.R. Cheeseman, G.; Scalmani, V. B., B. Mennucci, G.A. Petersson, H. Nakatsuji, M. Caricato,; X. Li, H. P. H., A.F. Izmaylov, J. Bloino, G. Zheng, J.L. Sonnenberg, M.; Hada, M. E., K. Toyota, R. Fukuda, J. Hasegawa, M. Ishida, T. Nakajima,; Y. Honda, O. K., H. Nakai, T. Vreven, J.A. Montgomery Jr., J.E. Peralta, F.; Ogliaro, M. B., J.J. Heyd, E. Brothers, K.N. Kudin, V.N. Staroverov, R.; Kobayashi, J. N., K. Raghavachari, A. Rendell, J.C. Burant, S.S. Iyengar, J.; Tomasi, M. C., N. Rega, N.J. Millam, M. Klene, J.E. Knox, J.B. Cross, V. Bakken,; C. Adamo, J. J., R. Gomperts, R.E. Stratmann, O. Yazyev, A.J. Austin, R.; Cammi, C. P., J.W. Ochterski, R.L. Martin, K. Morokuma, V.G. Zakrzewski,; G.A. Voth, P. S., J.J. Dannenberg, S. Dapprich, A.D. Daniels, Ö. Farkas, J.B.; Foresman, J. V. O., J. Cioslowski, D.J. Fox, *Gaussian 09*, Revision C.1; Gaussian, Inc.: Wallingford, CT,, 2009.

78. Miertus, S.; Scrocco, E.; Tomasi, J., Electrostatic Interaction of a Solute with a Continuum - a Direct Utilization of Abinitio Molecular Potentials for the Prevision of Solvent Effects. *Chem. Phys.* **1981**, 55, 117-129.

79. Pascual-ahuir, J. L.; Silla, E.; Tuñon, I., GEPOL: An improved description of molecular surfaces. III. A new algorithm for the computation of a solvent-excluding surface. *J. Comput. Chem.* **1994**, 15, 1127–1138.

80. Tomasi, J., Selected features of the polarizable continuum model for the representation of solvation. *Wiley Interdiscip Rev Comput Mol Sci* **2011**, 1, 855-867.

81. Tomasi, J.; Mennucci, B.; Cammi, R., Quantum mechanical continuum solvation models. *Chem. Rev.* **2005**, 105, 2999-3093.

82. Mennucci, B.; Tomasi, J., Continuum solvation models: A new approach to the problem of solute's charge distribution and cavity boundaries. *Journal of Chemical Physics* **1997**, 106, 5151-5158.

83. Cossi, M.; Barone, V.; Cammi, R.; Tomasi, J., Ab initio study of solvated molecules: A new implementation of the polarizable continuum model. *Chemical Physics Letters* **1996**, 255, 327-335.

84. Sellmann, D.; Funfgelder, S.; Knoch, F.; Moll, M., Transition-Metal Complexes with Sulfur Ligands .76. Redox and Addition-Reactions of Nickel-Complexes with Multidentate Thioether-Thiolato Ligands - X-Ray Structure Determinations of (Nme4)2[Ni('S2')2] and [Ni('S4-C3')(Pme3)] 'S2'2- = 1,2-Benzoldithiolat - 'S4-C3'2- = 1,3-Bis(2-Mercaptophenylthio)Propan(2-). *Z.Naturforsch.(B)* **1991**, 46, 1601-1608.

85. Fourmigue, M.; Bertran, J. N., [Ni(edt-CN)(2)](-center dot), a novel paramagnetic nickel dithiolene complex analog of Ni(mnt)(2)(-center dot) with two cyano groups only. *Chem. Commun.* **2000**, 2111-2112.

86. Mahadevan, C.; Seshasayee, M.; Radha, A.; Manoharan, P. T., Structure of Bis(Tetraethylammonium) Bis[Dimercaptomaleodinitrilato(2-)-S,S']-Nickelate(Ii), [N(C2h5)4]2[Ni(C4n2s2)2]. *Acta Crystallogr. Sect. C-Cryst. Struct. Commun.* **1984**, 40, 2032-2034.

87. Kuppusamy, P.; Manoharan, P. T., Hyperfine and Exchange Interactions in Tetraethylammoniumbis(Maleonitriledithiolato)Cuprate(Ii), [Net4]2[Cu(Mnt)2]. *J. Indian Chem. Soc.* **1986**, 63, 95-100.

88. Husain, A.; Nami, S. A. A.; Singh, S. P.; Oves, M.; Siddiqi, K. S., Anagostic interactions, revisiting the crystal structure of nickel dithiocarbamate complex and its antibacterial and antifungal studies. *Polyhedron* **2011**, 30, 33-40.

89. Perdew, J. P.; Ruzsinszky, A.; Constantin, L. A.; Sun, J. W.; Csonka, G. I., Some Fundamental Issues in Ground-State Density Functional Theory: A Guide for the Perplexed. *Journal of Chemical Theory and Computation* **2009**, 5, 902-908.

90. Staroverov, V. N.; Scuseria, G. E.; Tao, J.; Perdew, J. P., Tests of a ladder of density functionals for bulk solids and surfaces. *Physical Review B* **2004**, 69.

91. Lee, C. T.; Yang, W. T.; Parr, R. G., Development of the Colle-Salvetti Correlation-Energy Formula into a Functional of the Electron-Density. *Physical Review B* **1988**, 37, 785-789.

92. Perdew, J. P., Density-Functional Approximation for the Correlation-Energy of the Inhomogeneous Electron-Gas. *Phys. Rev. B* **1986**, 33, 8822-8824.

93. Adamo, C.; Barone, V., Exchange functionals with improved long-range behavior and adiabatic connection methods without adjustable parameters: The mPW and mPW1PW models. *Journal of Chemical Physics* **1998**, 108, 664-675.

94. Molawi, K.; Cohen, A. J.; Handy, N. C., Left-right and dynamic correlation. *Int. J. Quantum Chem.* **2002**, 89, 86-93.

95. Hoe, W. M.; Cohen, A. J.; Handy, N. C., Assessment of a new local exchange functional OPTX. *Chemical Physics Letters* **2001**, 341, 319-328.

96. Perdew, J. P.; Burke, K.; Wang, Y., Generalized gradient approximation for the exchange-correlation hole of a many-electron system. *Physical Review B* **1996**, 54, 16533-16539.

97. Perdew, J. P.; Chevary, J. A.; Vosko, S. H.; Jackson, K. A.; Pederson, M. R.; Singh, D. J.; Fiolhais, C., Atoms, Molecules, Solids, and Surfaces - Applications of the Generalized Gradient Approximation for Exchange and Correlation. *Phys. Rev. B* **1992**, 46, 6671-6687.

98. Zhao, Y.; Truhlar, D. G., A new local density functional for main-group thermochemistry, transition metal bonding, thermochemical kinetics, and noncovalent interactions. *Journal of Chemical Physics* **2006**, 125.

99. Tao, J. M.; Perdew, J. P.; Staroverov, V. N.; Scuseria, G. E., Climbing the density functional ladder: Nonempirical meta-generalized gradient approximation designed for molecules and solids. *Phys. Rev. Lett.* **2003**, 91.

100. Dahlke, E. E.; Truhlar, D. G., Improved density functionals for water. *J. Phys. Chem. B* **2005**, 109, 15677-15683.

101. Becke, A. D., Density-functional thermochemistry .4. A new dynamical correlation functional and implications for exact-exchange mixing. *Journal of Chemical Physics* **1996**, 104, 1040-1046.

102. Becke, A. D., Density-Functional Thermochemistry .3. the Role of Exact Exchange. *Journal of Chemical Physics* **1993**, 98, 5648-5652.

103. Becke, A. D., A New Mixing of Hartree-Fock and Local Density-Functional Theories. *Journal of Chemical Physics* **1993**, 98, 1372-1377.

104. Lynch, B. J.; Fast, P. L.; Harris, M.; Truhlar, D. G., Adiabatic connection for kinetics. *J. Phys. Chem. A* **2000**, 104, 4811-4815.

105. Zhao, Y.; Truhlar, D. G., Hybrid meta density functional theory methods for thermochemistry, thermochemical kinetics, and noncovalent interactions: The MPW1B95 and MPWB1K models and comparative assessments for hydrogen bonding and van der Waals interactions. *J. Phys. Chem. A* **2004**, 108, 6908-6918.

106. Schultz, N. E.; Zhao, Y.; Truhlar, D. G., Density functionals for inorganometallic and organometallic chemistry. *J. Phys. Chem. A* **2005**, 109, 11127-11143.

107. Cohen, A. J.; Handy, N. C., Dynamic correlation. *Mol. Phys.* **2001**, 99, 607-615.

108. Zhao, Y.; Truhlar, D. G., The M06 suite of density functionals for main group thermochemistry, thermochemical kinetics, noncovalent interactions, excited states, and transition elements: two new functionals and systematic testing of four M06-class functionals and 12 other functionals. *Theor. Chem. Acc.* **2008**, 120, 215-241.

109. Zhao, Y.; Truhlar, D. G., Density functional for spectroscopy: No long-range self-interaction error, good performance for Rydberg and charge-transfer states, and better performance on average than B3LYP for ground states. *J. Phys. Chem. A* **2006**, 110, 13126-13130.

110. Zhao, Y.; Truhlar, D. G., Comparative DFT study of van der Waals complexes: Rare-gas dimers, alkaline-earth dimers, zinc dimer, and zinc-rare-gas dimers. *J. Phys. Chem. A* **2006**, 110, 5121-5129.

111. Weigend, F.; Ahlrichs, R., Balanced basis sets of split valence, triple zeta valence and quadruple zeta valence quality for H to Rn: Design and assessment of accuracy. *Phys. Chem. Chem. Phys.* **2005**, 7, 3297-3305.

112. Feller, D., The Role of Databases in Support of Computational Chemistry Calculations. *J. Comput. Chem.* **1996**, 17, 1571-1586.

113. Schuchardt, K. L.; Didier, B. T.; Elsethagen, T.; Sun, L.; Gurumoorthi, V.; Chase, J.; Li, J.; Windus, T. L., Basis Set Exchange: A Community Database for Computational Sciences. *J. Chem. Inf. Model.* **2007**, 47, 1045-1052.

114. Bader, R. F. W., Atoms in Molecules. *Accounts Chem. Res.* **1985**, 18, 9-15.

115. Corts-Guzman, F.; Bader, R. F. W., Complementarity of QTAIM and MO theory in the study of bonding in donor-acceptor complexes. *Coord. Chem. Rev.* **2005**, 249, 633-662.

116. Bader, R. F. W., Definition of Molecular Structure: By Choice or by Appeal to Observation? *Journal of Physical Chemistry A* **2010**, 114, 7431-7444.

117. Giles, L. J.; Grigoropoulos, A.; Szilagyi, R. K., Electron and Spin Density Topology of the H-Cluster and Its Biomimetic Complexes. *Eur. J. Inorg. Chem.* **2011**, 2677-2690.

118. Keith, T. A. TK Gristmill Software: Overland Park KS, USA, 2011.

119. Mulliken, R. S., Electronic Population Analysis on Lcao-Mo Molecular Wave Functions .1. *Journal of Chemical Physics* **1955**, 23, 1833-1840.

120. Foster, J. P.; Weinhold, F., Natural Hybrid Orbitals. *J. Am. Chem. Soc.* **1980**, 102, 7211-7218.

121. Shadle, S. E.; Hedman, B.; Hodgson, K. O.; Solomon, E. I., Ligand K-Edge X-Ray-Absorption Spectroscopy as a Probe of Ligand-Metal Bonding - Charge Donation and Covalency in Copper-Chloride Systems. *Inorg. Chem.* **1994**, 33, 4235-4244.

122. George, S. J.; Lowery, M. D.; Solomon, E. I.; Cramer, S. P., Copper L-Edge Spectral Studies - a Direct Experimental Probe of the Ground-State Covalency in the Blue Copper Site in Plastocyanin. *J. Am. Chem. Soc.* **1993**, 115, 2968-2969.

123. Kirmse, R.; Stach, J.; Dietzsch, W.; Hoyer, E., S-33 Hyperfine Interactions in Single-Crystal Esr-Spectra of (N-Bu4n)2[Cu-63(Mnt)2]. *Inorg. Chim. Acta* **1978**, 26, L53-L55.

124. Plumlee, K. W.; Hoffman, B. M.; Ibers, J. A.; Soos, Z. G., Weak Exchange in Heisenberg Linear-Chain - Structure and Epr of [N(N-Bu)4]2[Cu(Mnt)2]. *Journal of Chemical Physics* **1975**, 63, 1926-1942.

125. Snaathorst, D.; Doesburg, H. M.; Perenboom, J.; Keijzers, C. P., Structural, Electron-Paramagnetic-Res, and Magnetic Studies of a Nonplanar Copper(Ii) Maleonitriledithiolate Complex. *Inorg. Chem.* **1981**, 20, 2526-2532.

126. Stach, J.; Kirmse, R.; Dietzsch, W.; Olk, R. M.; Hoyer, E., Single-Crystal Electron-Paramagnetic-Res Spectra of (N-Bu4n)2[Cu-63(Dmit)2]. *Inorg. Chem.* **1984**, 23, 4779-4780.

127. Reijerse, E. J.; Thiers, A. H.; Kanters, R.; Gribnau, M. C. M.; Keijzers, C. P., Electron-Spin Echo Envelope Modulation Study of Bis(Tetrabutylammonium) Bis(Maleonitriledithiolato)Nickelate(Ii) Doped with Copper(Ii). *Inorg. Chem.* **1987**, 26, 2764-2769.

128. Kirmse, R.; Solovev, B. V., S-33 and C-13 Hyperfine Interactions in Single-Crystal Epr-Spectra of Cu(Ii)-63 Bis(Diethyl-Dithiocarbamate). *J. Inorg. Nucl. Chem.* **1977**, 39, 41-44.

129. Towey, B. D.; Szilagyi, R. K., S K-edge X-ray absorption spectroscopy of dithiocarbamate complexes. *Inorg. Chem.* **2012**, manuscript in preparation.

130. Sriskandakumar, T.; Petzold, H.; Bruijnincx, P. C. A.; Habtemariam, A.; Sadler, P. J.; Kennepohl, P., Influence of Oxygenation on the Reactivity of Ruthenium-Thiolato Bonds in Arene Anticancer Complexes: Insights from XAS and DFT. *J. Am. Chem. Soc.* **2009**, 131, 13355-13361.

131. Karunakaran-Datt, A.; Kennepohl, P., Redox Photochemistry of Methionine by Sulfur K-edge X-ray Absorption Spectroscopy: Potential Implications for Cataract Formation. *J. Am. Chem. Soc.* **2009**, 131, 3577-3582.

132. Martin-Diaconescu, V.; Kennepohl, P., Effects of Hyperconjugation on the Electronic Structure and Photoreactivity of Organic Sulfonyl Chlorides. *Inorg. Chem.* **2009**, 48, 1038-1044.

133. Sarode, P. R.; Ramasesha, S.; Madhusudan, W. H.; Rao, C. N. R., Relation between Effective Atomic Charge and Chemical-Shifts in X-Ray Absorption-Spectra of Transition-Metal Compounds. *Journal of Physics C* **1979**, 12, 2439-2445.

134. Manthiram, A.; Sarode, P. R.; Madhusudan, W. H.; Gopalakrishnan, J.; Rao, C. N. R., X-Ray Spectroscopic Study of Chromium, Nickel, and Molybdenum Compounds. *Journal of Physical Chemistry* **1980**, 84, 2200-2203.

135. Khadikar, P. V.; Mangelson, N. F.; Pandharkar, S. P., Effective Nuclear-Charge and Chemical-Shifts in X-Ray Absorption-Spectra of Polymeric Copper(Ii) Salicylhydroxamates. *Jpn. J. Appl. Phys.* **1989**, 28, 709-712.

136. Katare, R. K.; Joshi, S. K.; Shrivastava, B. D.; Pandeya, K. B.; Mishra, A., K-Absorption spectral studies of some copper(II) mixed-ligand complexes. *X-Ray Spectrometry* **2000**, 29, 187-191.

137. El Khoury, L.; Journel, L.; Guillemin, R.; Carniato, S.; Stolte, W. C.; Marin, T.; Lindle, D. W.; Simon, M., Resonant inelastic x-ray scattering of methyl chloride at the chlorine K edge. *Journal of Chemical Physics* **2012**, 136.

138. Kirmse, R.; Stach, J.; Dietzsch, W.; Steimecke, G.; Hoyer, E., Single-Crystal Electron-Paramagnetic-Res Studies on Nickel(Iii), Palladium(Iii), and Platinum(Iii) Dithiolene Chelates Containing the Ligands Isotrithionedithiolate, Ortho-Xylenedithiolate, and Maleonitriledithiolate. *Inorg. Chem.* **1980**, 19, 2679-2685.

139. Yamaguchi, A.; Penland, R. B.; Mizushima, S.; Lane, T. J.; Curran, C.; Quagliano, J. V., Infrared Absorption Spectra of Inorganic Complexes ,14 Infrared Studies of Some Metal Thiourea Complexes. *J. Am. Ceram. Soc.* **1958**, 80, 527-529.

140. Kumler, W. D.; Fohlen, G. M., The dipole moment and structure of urea and thiourea. *Journal of the American Chemical Society* **1942**, 64, 1944-1948.

141. El-Bahy, G. M. S.; El-Sayed, B. A.; Shabana, A. A., Vibrational and electronic studies on some metal thiourea complexes. *Vibrational Spectroscopy* **2003**, 31, 101-107.

142. Queen, M. S.; Towey, B. D.; Murray, K. A.; Veldkamp, B. S.; Byker, H. J.; Szilagyi, R. K., Electronic structure of [Ni(II)S4] complexes from S K-edge X-ray absorption spectroscopy. *Coordination Chemistry Reviews* **2013**, 257, 564-578.

143. Kennepohl, P.; Wasinger, E. C.; George, S. D., X-ray spectroscopic approaches to the investigation and characterization of photochemical processes. *J. Synchrotron Radiat.* **2009**, 16, 484-488.

144. Szilagyi, R. K.; Metz, M.; Solomon, E. I., Spectroscopic calibration of modern density functional methods using CuCl4 (2-). *Journal of Physical Chemistry A* **2002**, 106, 2994-3007.

145. Pascualahuir, J. L.; Silla, E.; Tunon, I., Gepol - an improved description of the molexular surfaces .3. A New Algorithm for the Computation of Solvent-Excluding. *Journal of Computational Chemistry* **1994**, 15, 1127-1138.

146. Weininger, M. S.; O'Connor, J. E.; Amma, E. L., Crystal and molecular structure of hexakis(thiourea)nickel(II) bromide. *Inorg. Chem.* **1969**, 8, 424-431.

147. Spofford, W. A., III; Amma, E. L., Crystal and molecular structure of tetrakisthiourea cobalt (II) nitrate monohydrate, C4H16CoN8S4 2+,2NO 3 − ,H2O. *Journal of Crystal and Molecular Structure* **1976**, 6, 235-258.

148. Kutoglu, A.; Scheringer, C.; Meyer, H.; Schweig, A., Experimental and Theoretical Difference and densities for Thiourea. *Acta Crystallogr. Sect. B* **1982**, 38, 2626-2632.

149. Vega, R.; Lopez-Castro, A.; Marquez, R., Structure of tetrakis(thiourea)zinc(II) nitrate. *Acta Crystallographica Section B* **1978**, 34, 2297-2299.

150. Schuchardt, K. L.; Didier, B. T.; Elsethagen, T.; Sun, L. S.; Gurumoorthi, V.; Chase, J.; Li, J.; Windus, T. L., Basis set exchange: A community database for computational sciences. *Journal of Chemical Information and Modeling* **2007**, 47, 1045-1052.

151. Klamt, A.; Schuurmann, G., COSMO - A New Approach to Dielectric Screening in Solvents with Explicit Expressions for the Screening Energy and its Gradient. *J. Chem. Soc., Perkin Trans. 2* **1993**, 799-805.

152. Szilagyi, R. K. Structural Origins of Noninnocent Coordination Chemistry. In *Encyclopedia of Inorganic Chemistry, Second Edition (EIR-2)*, King, B. R., Ed.; John Wiley & Sons, Ltd: 2009, pp 1-13.

153. Cotton, F. A.; Faut, O. D.; Mague, J. T., Molecular and Electronic Structures of Some Thiourea Complexes of Cobalt(II). *Inorg. Chem.* **1964**, 3, 17-21.

154. Byker, H., In; email, 2013.

155. Solutia, In; Vol. Pub. No. 2008161A.

156. Neese, F., The ORCA program system. *Wiley Interdisciplinary Reviews: Computational Molecular Science* **2012**, 2, 73-78.

157. M.S.Gordon, M. W. S., *Advances in electronic structure theory: GAMESS a decade later*. Elsevier: Amsterdam, 2005.

158. M.W.Schmidt, K. K. B., J.A.Boatz, S.T.Elbert, M.S.Gordon, J.H.Jensen, S.Koseki, N.Matsunaga, K.A.Nguyen, S.Su, T.L.Windus, M.Dupuis, J.A.Montgomery J. , General Atomic and Molecular Electronic Structure System. *Comput. Chem* **1993**, 14, 1347-1363.

159. Foresman, J. B.; Frisch, A. E.; Gaussian, I., *Exploring chemistry with electronic structure methods*. Gaussian, Inc.: 1996.

160. Hohenberg, P.; Kohn, W., Inhomogeneous Electron Gas

Phys. Rev. B **1964**, 136, B864-+.

161. Kohn, W.; Sham, L. J., Self-Consistent Equations Including Exchange and Correlation Effects *Phys. Rev.* **1965**, 140, 1133-&.

162. Parr, R. G.; Yang, W. T., Density-Functional Theory of the Electronic-Structure of Molecules *Annu. Rev. Phys. Chem.* **1995**, 46, 701-728.

163. Perdew, J. P.; Schmidt, K. Jacob's ladder of density functional approximations for the exchange-correlation energy. In *Density Functional Theory and Its Application to Materials*, VanDoren, V.; VanAlsenoy, C.; Geerlings, P., Eds.; 2001; Vol. 577, pp 1-20.

164. Bartlett, R. J.; Grabowski, I.; Hirata, S.; Ivanov, S., The exchange-correlation potential in ab initio density functional theory. *J. Chem. Phys.* **2005**, 122.

165. Cramer, C. J., *Essentials of Computational Chemistry: Theories and Models*. Wiley: 2005.

166. Casida, M. E.; Jamorski, C.; Casida, K. C.; Salahub, D. R., Molecular excitation energies to high-lying bound states from time-dependent density-functional response theory: Characterization and correction of the time-dependent local density approximation ionization threshold. *J. Chem. Phys.* **1998**, 108, 4439-4449.

167. Pople, J. A.; Santry, D. P.; Segal, G. A., Approximate Self-Consistent Molecular Orbital Theory .I. Invariant Procedures *J. Chem. Phys.* **1965**, 43, S129-+.

168. Pople, J. A.; Segal, G. A., Approximate Self-Consistent Molecular Orvital Theory .2.2 Calculations with Complete Neglect of Differential Overlap. *J. Chem. Phys.* **1965**, 43, S136-+.

169. Pople, J. A.; Beveridg.Dl; Dobosh, P. A.,

Approximate Self-Consistent Molecular Orvital Theory .5. Calculations with Intermediate Neglect of Differential Overlap

J. Chem. Phys. **1967**, 47, 2026-&.

170. Dewar, M. J. S.; Thiel, W., Ground-States of Molecules .38. MNDO Method - Approximations and Parameters. *J. Am. Chem. Soc.* **1977**, 99, 4899-4907.

171. Dewar, M. J. S.; Thiel, W., Ground-States of Molecules .39. MNDO Results for Molecules Containing Hydrogen, Carbon, Nitrogen, and Oxygen. *J. Am. Chem. Soc.* **1977**, 99, 4907-4917.

172. Dewar, M. J. S.; Storch, D. M., The Development and Use of Quantum Molecular-Models .75. Comparative Tests of Theoretical Procedures for Studying Chemical-Reations. *J. Am. Chem. Soc.* **1985**, 107, 3898-3902.

173. Dewar, M. J. S.; Zoebisch, E. G.; Healy, E. F.; Stewart, J. J. P., The Development and Use of Quantum-Mechanical Molecular-Models .76. AM1 - A New General Purpose Quantum Mechanical Molecular Model. *J. Am. Chem. Soc.* **1985**, 107, 3902-3909.

174. Stewart, J. J. P., Optimization of Parameters for Semiemperical Methods .1.1 Method. *J. Am. Chem. Soc.* **1989**, 10, 209-220.

175. Stewart, J. J. P., Optimization of Parameters for Semiempirical Methods .2. Applications. *J. Comput. Chem.* **1989**, 10, 221-264.

176. Stewart, J. J. P., Optimization of parameters for semiempirical methods V: Modification of NDDO approximations and application to 70 elements. *J. Mol. Model.* **2007**, 13, 1173-1213.

177. Stewart, J. J. P., Optimization of parameters for semiempirical methods VI: more modifications to the NDDO approximations and re-optimization of parameters. *J. Mol. Model.* **2013**, 19, 1-32.

178. Buncel, E.; Rajagopal, S., Solovotochromism and Solubility Scales. *Acc. Chem. Res.* **1990**, 23, 226-231.

179. Klamt, A.; Schuurmann, G., COSMO A New Approach to Dielectric Screening in Solvents with Explicit Expressions for the Screening Energy and its Gradient. *J. Chem. Soc., Perkin Trans. 2* **1993**, 799-805.

180. Klamt, A., Calculation of UV/Vis spectra in solution. *J. Phys. Chem.* **1996**, 100, 3349-3353.

181. Deeth, R. J.; Anastasi, A.; Diedrich, C.; Randell, K., Molecular modelling for transition metal complexes: Dealing with d-electron effects. *Coord. Chem. Rev.* **2009**, 253, 795-816.

182. Sun, H., COMPASS: An ab initio force-field optimized for condensed-phase applications - Overview with details on alkane and benzene compounds. *J. Phys. Chem. B* **1998**, 102, 7338-7364.

183. Allinger, N. L.; Yuh, Y. H.; Lii, J. H., MOLECULAR MECHANICS - THE MM3 FORCE-FIELD FOR HYDROCARBONS .1. *J. Am. Chem. Soc.* **1989**, 111, 8551-8566.

184. Ponder, J. W. *TINKER – Software Tools for Molecular Design*, Version 6.3; 1990-2014.

185. Moomaw, W. R.; Skinner, J. F., Vibronic Spectra and Energy Levels of Polyatomic Molecules - Physical Chemistry Expriment. *J. Chem. Educ.* **1971**, 48, 304-&.

186. Frisch, M. J. T., G. W.; Schlegel, H. B.; Scuseria, G. E.; Robb, M. A.; Cheeseman, J. R.; Scalmani, G.; Barone, V.; Mennucci, B.; Petersson, G. A.; Nakatsuji, H.; Caricato, M.; Li, X.; Hratchian, H. P.; Izmaylov, A. F.; Bloino, J.; Zheng, G.; Sonnenberg, J. L.; Hada, M.; Ehara, M.; Toyota, K.; Fukuda, R.; Hasegawa, J.; Ishida, M.; Nakajima, T.; Honda, Y.; Kitao, O.; Nakai, H.; Vreven, T.; Montgomery, Jr., J. A.;

Peralta, J. E.; Ogliaro, F.; Bearpark, M.; Heyd, J. J.; Brothers, E.; Kudin, K. N.; Staroverov, V. N.; Kobayashi, R.; Normand, J.; Raghavachari, K.; Rendell, A.; Burant, J. C.; Iyengar, S. S.; Tomasi, J.; Cossi, M.; Rega, N.; Millam, N. J.; Klene, M.; Knox, J. E.; Cross, J. B.; Bakken, V.; Adamo, C.; Jaramillo, J.; Gomperts, R.; Stratmann, R. E.; Yazyev, O.; Austin, A. J.; Cammi, R.; Pomelli, C.; Ochterski, J. W.; Martin, R. L.; Morokuma, K.; Zakrzewski, V. G.; Voth, G. A.; Salvador, P.; Dannenberg, J. J.; Dapprich, S.; Daniels, A. D.; Farkas, Ö.; Foresman, J. B.; Ortiz, J. V.; Cioslowski, J.; Fox, D. J. Gaussian, Inc.: Wallingford CT, 2009.

187. Okuda, Y.; Szilagyi, R. K.; Mori, S.; Nishihara, Y., The origin of exo-selectivity in methyl cyanoformate addition onto the C=C bond of norbornene in Pd-catalyzed cyanoesterification. *Dalton Transactions* **2014**, 43, 9537-9548.